Theoretical and Experimental Characterization of Single-Screw Expanders for ORC Applications

Theoretische en experimentele karakterisering van enkele-schroefexpanders voor ORC-toepassingen

Davide Ziviani

Promotoren: prof. dr. ir. M. De Paepe, prof. dr. M. van den Broek
Proefschrift ingediend tot het behalen van de graad van
Doctor in de ingenieurswetenschappen: werktuigkunde-elektrotechniek

UNIVERSITEIT
GENT

Vakgroep Mechanica van Stroming, Warmte en Verbranding
Voorzitter: prof. dr. ir. J. Vierendeels
Faculteit Ingenieurswetenschappen en Architectuur
Academiejaar 2017 - 2018

ISBN 978-94-6355-047-5
NUR 961, 978
Wettelijk depot: D/2017/10.500/82

Members of Examination Board

Voting members:

Chair:	Prof. Rik Van de Walle (Dean)
Faculty reading committee:	Prof. Andreas Brümmer (Technische Universität Dortmund, Germany) Prof. Dieter Fauconnier (EA08) Prof. Eckhard A. Groll (Purdue University, West Lafayette, USA) Prof. Vincent Lemort (Université de Liège)
Other members:	Prof. Jan Vierendeels (EA03), **Secretary**

Members ineligible to vote:

Supervisors:	Prof. Michel De Paepe Prof. Martijn van den Broek

Universiteit Gent
Faculteit Ingenieurswetenschappen en Architectuur
Vakgroep Mechanica van Stroming, Warmte en Verbranding

Promotoren: Prof. dr. ir. Michel De Paepe
Prof. dr. Martijn van den Broek

Universiteit Gent
Faculteit Ingenieurswetenschappen en Architectuur

Vakgroep Mechanica van Stroming, Warmte en Verbranding
Sint-Pietersnieuwstraat 41, B-9000 Gent, België

Tel.: +32-9-264.32.88
Fax.: +32-9-264.35.75

Proefschrift tot het behalen van de graad van
Doctor in de ingenieurswetenschappen:
werktuigkunde - elektrotechniek
Academiejaar 2017-2018

”Never say never, because limits, like fears, are often just an illusion.”

— MICHAEL J. JORDAN

To my wife and family

Dankwoord

Before acknowledging any of the individuals that influenced, inspired and supported me while accomplishing this PhD work, I must say a huge thank you to my wife, Yuan-Fan. We started this journey together 4 years ago and you have always been there for me even though I had limited time to spend with you. You constantly sacrificed your time, sometimes happiness, weekends, vacations to support me on this major challenge of my life. I was not always there as husband and, I know, I was not able to give you all the attentions you needed. Yet, you were willing to stand beside me and supporting my (often) questionable decisions. I owe you a lot and I could not make it through without you.

Next, I need to thank my co-promotors, Prof. Martijn van den Broek and Prof. Michel De Paepe, for the opportunity given me at the beginning of the this work and for the freedom that allowed me to establish my research. I would like also to thank all the Members of the Examination Board for the thorough reviews and all the useful remarks.

During this PhD, I had the privilege of working with extraordinary people that truly inspired me and set the bar for high quality research. It is not possible to name and thank all of you here, but I am deeply grateful.

I wish to acknowledge and thank my colleague and friend Sergei Gusev. We have been working together since the beginning and throughout the years, your deep knowledge and experience on thermal systems helped me a lot. I value the time spent in the lab., the discussions about thermodynamics in front of multiple beers or with a cup of coffee on early morning. I consider the design and construction of our Blue machine one of the best example of successful team work. I will always remember your positive, hard-working and selfless mind set.

I am immensely grateful to Prof. Eckhard Groll and Prof. James Braun. You gave me the opportunity to work on numerous projects that helped me improving my research skills. Your vast knowledge of positive displacement machines shaped this contribution. I am looking forward to keep working at the Ray W. Herrick Laboratories.

I would like to acknowledge Prof. Vincent Lemort. I started working on ORCs by reading your papers and during these years I had the opportunity to work with you. All my visits at your lab. have been extremely useful. I would like to extend the acknowledgments to all the colleagues and friends of the Thermodynamic Lab.

at ULg.

I thought I knew some thermodynamics until I met Ian Bell and Brandon Woodland. I need to thank you, Ian, for getting me started with compressor modeling and the Herrick Lab. culture. It was because of you that I had the opportunity to work extensively Prof. Eckhard Groll, Prof. James Braun and Prof. Travis Horton. It has been a mind blowing experience that paved my way towards accomplishing my research goals for this work and beyond. To me, you set the bar for really high quality research. Brandon, I would like to thank you for all the time spent on discussing thermodynamics of ORCs, the time spent on modeling and the numerous occasions in which you gave me a useful advice. You are a truly great researcher and person.

I would like to thank Feilong Liu for you friendship and numerous discussions about the manufacturing of single-screw rotors. Your help was instrumental to understand the meshing pair kinematics. I miss your Xi'an burgers so much! I had great time in Belgium also because of you.

I would also like to thank Claudio Pavan. Our first 3D scan of the single-screw opened up my research on this machine. We have spent ours understanding the manufacturing, reconstructing the housing and designing new concepts. The accomplishments in this work are certainly also because of you.

Joke and Brecht, thank you for the opportunity of working with single-screw machines and for the help in many occasions.

There are a number of colleagues and friends at HLAB that I need to thank. Xinye, it is a pleasure working with you. You are an incredible fast learner and your help with code debugging was vital. Nelson, thank you for the discussions on flooded-expansion and optimization. And,of course, Orkan! Dude! I owe you a lot. You helped be throughout my multiple trips to the US.

To Ward and Susana, you became our extended Belgian family and I value our friendship. I will never forget all the help and support you gave to me but especially to Eva, as she went through a very difficult time. I would like to extend the thoughts also to Nhu and Koen. Countless times you have helped us and I treasure your friendship.

Niccolo and Azzurra I need to thank you for the help in very difficult times of my family. Being away from home, and having people like you to count on has been of tremendous importance.

Last but not least, I have to thank my family - Mom, Dad and my brother, Nicola. I have been away to pursue my academic career for several years and I was not there when you needed me the most. I thank you for the constant support, the Facetime calls on weekends and for the joy you gave me every time I was coming back home. Thank you to my mother in law Chih-Ling. You have always been so kind to me and encouraged me throughout my PhD. This work is especially for you, Dad. You taught me how to be disciplined, to have values and work ethic. I will be always immensely in debt with you.

Gent, September 2017
Davide Ziviani

Table of Contents

List of Figures

List of Tables

Nomenclature

A	area	m^2
A_{thr}	throat flow area	m^2
c_{p}	specific heat capacity at constant pressure	$J/(kgK)$
c_{v}	specific heat capacity at constant specific volume	$J/(kgK)$
C_D	valve drag coefficient	-
C_{flow}	flow coefficient	-
C_{lump}	thermal capacitance	J/K
$d_{\mathrm{sw,sr}}$	distance between rotor and starwheel	m
D	diameter	m
D_h	hydraulic diameter	m
E	total energy	J
E	Young's modulus	Pa
f	friction factor	-
f_{F}	Fanning friction factor	-
F	force	N
g	gravitational constant	m/s^2
G	mass flux	$kg/(m^2s)$
Gr	Grashof number	-
h	convective heat transfer coefficient	$W/(m^2K)$
h	specific enthalpy	J/kg
i	meshing pair engaging ratio	-
I	moment of inertia	m^4
k	thermal conductivity	$W/(mK)$
k	adiabatic exponent	-
k_{valve}	valve stiffness	N/m
L	length	m
m	mass	kg
$\dot{m}$	mass flow rate	kg/s
$\mathbf{M}$	rotation matrix	-
N	rotational speed	rpm
Nu	Nusselt number	-
p	pressure	Pa

Pr	Prandtl number	-
q	heat flux	W/m^2
$\dot{Q}$	heat transfer rate	W
r_p	pressure ratio	-
r_v	specific volume ratio	-
$r_{\mathrm{v,built-in}}$	geometric internal volume ratio	-
R	radius	m
R_ab	thermal resistance	K/W
Re	Reynolds number	-
Ra	Rayleigh number	-
s	specific entropy	$J/(kgK)$
S	slip ratio	-
T	temperature	K
t	time	s
u	specific internal energy	J/kg
U	internal energy	J
U	overall heat transfer coefficient	W/m^2K
v	specific volume	m^3/kg
v	velocity	m/s
V	volume	m^3
V_c	velocity in the minimum cross sectional flow area	m/s
$\dot{V}$	volume flow rate	m^3/s
w	specific work	J/kg
	tooth width	m
$\dot{W}$	power	W
x	mass fraction	-
$\mathbf{x}$	general vector	-
x, y, z	coordinates	m
X	Lockhart-Martinelli parameter	
z_sr	number of grooves	-
z_sw	number of teeth	-
z	height	-

Greek symbols

α	void fraction	-
α	angle	rad
β_s, β_d	suction and discharge angles	rad
δ_{gap}	leakage gap size	m
Δ	difference	-
	groove tip thickness	-
γ	angle	rad
ϵ	effectiveness	-
η_{s}	isentropic efficiency	-
$\eta_{\text{II,finite}}$	Second Law efficiency for finite heat capacity heat source	-
η_{ORC}	ORC thermal efficiency	-
φ_{FF}	filling factor	-
ϕ	phase multiplier	
μ	dynamic viscosity	$Pa \cdot s$
ν	kinematic viscosity	m^2/s
τ	mechanical torque	Nm
θ	crank angle	rad
ρ	density	kg/m^3
σ	contraction ratio	-
ω	rotational speed	rad$/s$
ω_n	natural frequency	$1/s$

Subscripts

ad	adiabatic
amb	amb
c	cold
cd	condenser
cf	condenser
calc	calculated
crit	critical
des	desired
dis	discharge
el	electrical
ex	exhaust
exp	expander
eng	engaged
ev	evaporator
fr	friction
g	saturated gas property
	groove
G	primary working fluid
h	hot
hf	hot fluid
in	inlet
int	internal
isoth	isothermal
JB	journal bearing
l	saturated liquid property
L	secondary liquid (e.g. oil)
leak	leakage
loss	losses
meas	measured
mech	mechanical
mix	mixture
oa	overall
opt	optimal
out	outlet
pp	pump
r	refrigerant
ref	reference

s	isentropic
sh	shaft
sr	screw rotor
su	supply
sw	starwheel
th	theoretical
TB	thrust-bearing
w	wall
∞	free stream
V	volume
2ϕ	two-phase
0	dead state

Acronyms

CFD	Computational Fluid Dynamics
CNC	Computer Numerical Control
CV	Control Volume
MCEMP	multi-column envelope meshing pair
OEB	Overall Energy Balance
ORC	Organic Rankine Cycle
PD	Positive Displacement
PDSim	Positive Displacement Simulation Framework
SLEMP	straight-line envelope meshing pair
SSC	Single-Screw Compressor
SSE	Single-Screw Expander

Nederlandse Samenvatting –Summary in Dutch–

Recuperatie van restwarmte op lage en middelhoge temperatuur uit industrile processen kan een antwoord bieden op de het broeikasgasprobleem en de vraag naar efficintere thermische systemen. Organische-Rankinecycli (ORCs) zijn een gekende technologie om restwarmte om te zetten in waardevolle elektrische stroom. Niettegenstaande er al enkele decennia onderzoek naar ORC-technologie wordt verricht, is verder onderzoek in cyclusconfiguraties, werkmedia en componenten noodzakelijk om de thermodynamische prestaties en het gebruik van ORCsystemen in een breder aantal toepassingen te verhogen.

De omzetting van thermische energie naar mechanische energie, en vervolgens in elektrische energie, gebeurt in een ORC via de expander. Meestal is deze component van het waaiertype, denk aan een radiale of axiale turbine, of van het verdringertype (of volumetrische type), zoals zuiger-, scroll- en schroefexpanders. Vooral voor ORCs van klein of middelgroot elektrisch vermogen zijn verdringerexpanders aanbevolen omwille van hun gunstige prijs-prestatie-verhouding.

Minstens twee overwegingen dienen gemaakt te worden bij de selectie van een verdringerexpander voor ORC-toepassingen. Eerst is er de afstemming van de interne volumeratio van de expander met de optimale drukverhouding van het ORC-systeem. Verder zijn er de inwendige verliezen in de expander, meer specifiek de afweging tussen lek- en wrijvingsverliezen, die afhangen van het specifieke type van de machine.

Om de invloed van de interne volumeratio op het rendement van het ORC-systeem te kunnen evalueren, is een thermodynamisch cyclusmodel ontwikkeld samen met een semi-empirisch expandermodel. Het expandermodel groepeert mechanische, lek- en warmteverliezen. Omdat ORC-systemen gewoonlijk geoptimaliseerd worden voor een hogere drukverhouding (om meer vermogen te kunnen onttrekken), hebben expanders met een grotere interne volumeratio - zoals die van het schroeftype - de voorkeur omdat hun isentroop rendement een kleiner verval vertoont in het gebied van onderexpansie. Op basis van de randvoorwaarden opgelegd door een e warmte- en koudebron, werd de theoretisch matching van een verdringerexpander met een ORC-systeem bekomen. Hiervoor werd gebruik gemaakt van de maximalisatie van het rendement van de cyclus volgens de tweede-hoofdwet, dat wil zeggen ten opzichte van de gerelateerde Carnotcyclus.

Een ander aspect waarmee moet worden rekening gehouden is de beschikbaarheid van een bepaald expandertype. Omdat er weinig commercieel beschikbare expanders zijn, wordt er in het onderzoek naar verdringermachines dikwijls bestaande maar aangepaste compressortechnologie gebruikt uit de dampcompressie-industrie. In het ultra-lage tot lage vermogensbereik (1 tot 10 kWe), hebben scrollexpanders de voorkeur omwille van het hoge bereikbare rendement. In het middenvermogengebied zijn de expanders van het schroeftype de gangbare technologie. Van de familie van schroefexpanders worden tegenwoordig de dubbele en enkele schroef industrieel ingezet. Dubbele-schroefexpanders zijn onderzocht geweest in de literatuur en vertoonden een isentroop rendement hoger dan 80%. Enkele-schroefmachines, die ook worden toegepast bij het comprimeren van lucht en in de koeltechniek, worden gekenmerkt door het in -elkaar-grijpen van één centrale rotor en twee tandwielen. Deze configuratie leidt tot een symmetrisch werkingsproces wat voordelen biedt in vergelijking met de traditionele dubbele-schroeftechnologie. Er is een verminderde belasting voor de lagers en minder geluid en trillingen. Het maken van enkele-schroefmachines is een bijzondere uitdaging en vergt geavanceerde en specifiek ontworpen CNC-machines. Dubbele-schroefmachines krijgen meestal de voorkeur omwille van hun hogere volumetrische en isentrope rendement. Beide schroeftypes echter kunnen overweg met deellastomstandigheden dankzij interne capaciteits- of drukratioregelingen, wat erg gewenst is bij de werking van ORCs.

Het huidige onderzoek naar de bepaling van de prestaties van enkele-schroefexpanders voor ORC-toepassingen staat nog maar aan het begin. Het merendeel van de beschikbare literatuur is beperkt tot perslucht als werkmedium. Een veel kleiner aantal gepubliceerde studies behandelen de inbouw van een enkele-schroefexpander in een ORC-systeem en zijn dan ook nog eens beperkt tot de studie van één enkel werkmedium, bijvoorbeeld R123.

Om de prestaties van een enkele-schroefexpander te kunnen karakteriseren zijn zowel numerieke methoden als experimentele gegevens nodig om de prestaties te voorspellen. Ten behoeve van de numerieke simulatie is een alomvattend mechanistisch model opgesteld, gebaseerd op de geometrische beschrijving van de enkele-schroefexpander en op een open-controlevolumeformalisme. Dit model omvatte de effecten van inwendige lekken, warmteoverdracht en wrijvingsverliezen. Er werd aangetoond dat de kernstructuur van het simulatiemodel toepasbaar was op het merendeel van de verdringermachines, zowel expanders als compressoren.

Een geschaald prototype van een industrile ORC met een 11 kWe-generator werd gebruikt om experimentele data van een enkele-schroefexpander te verzamelen. Deze enkele-schroefexpander was een geconverteerde luchtcompressor die met R245fa en SES36 werd getest. De inlaattemperatuur aan de warmtebron werd vastgelegd op 125 °C. In totaal werden 102 steady-state punten opgemeten. De expander bereikte een maximaal veralgemeend isentroop rendement van 0.65 bij een drukverhouding van 8.83 met SES36 als werkmedium. De experimentele resultaten werden dan gebruikt voor de validatie van het expandermodel en voor de calibratie van het semi-empirische model.

Deze experimentele studie bracht aan het licht hoe de prestaties van een enkele-schroefexpander worden benvloed door slijtage aan het aangrijpprofiel, meer specifiek door de groter wordende lekopeningen, en door de maximum druk waaronder de behuizing kan werken. Toleranties in het ontwerp van het ingrijpend paar en onvoldoende smering werden aangewezen als mogelijke oorzaken voor het afslijten van de tandprofielen. Het semi-empirische model werd gebruikt om de interne verliezen in de expander te ontleden en om de impact van ontwerpverbeteringen op de prestaties te evalueren. De vermindering van mechanische verliezen en lekstromen resulteerde in een maximaal isentroop rendement van 72.5%.

De ervaringen met het operationele ORC-systeem vormden de basis van de optimalisatie van de werking van de enkele-schroefexpander via de analyse van de afstemming tussen expander- en systeemprestaties.

In dit werk worden enkele aanbevelingen gegeven voor een nieuw ontwerp van de behuizing, die kunnen worden meegenomen in verdere ontwikkelingen en onderzoeksvragen, in het bijzonder voor expansie van twee-fasenstroming.. De kennis van kinematische vergelijkingen die de het ingrijpend paar beschrijven kan gebruikt worden om correcte gridgeneratiealgoritmes in bvb CFD te ontwikkelen die toepasbaar zijn op complexe rotorgeometrieën.

English summary

Medium to low grade waste heat recovery from industrial processes is of particular interest to address both environmental concerns and the need of more efficient thermal systems. Organic Rankine cycles (ORCs) have been demonstrated to be a viable solution to convert waste heat into valuable electric power. Although the research on the ORC technology has been pursued for decades, further advancements on cycle architectures, working fluids and components are still required to increase the thermodynamic performance and the adoption of such systems to a larger variety of applications in order to valorize wasted heat.

In an ORC, the conversion of thermal energy into mechanical energy and, successively, into electrical energy occurs by means of an expander. Such a device is usually of a dynamic type, e.g., radial or axial turbine, or a positive displacement type, e.g., reciprocating, scroll, screw. In particular, positive displacement expanders have been identified as key components in the medium to low power range ORCs because of the trade-off between cost and performance.

The selection of a positive displacement expander for ORC applications involves at least two main fundamental aspects. The first one is related to the matching between expander design internal volume ratio and the ORC system optimum pressure ratio, and the second one is expander internal losses, e.g., trade-off between leakage and friction, which are tied to the specific type of machine.

To evaluate the impact of the expander internal volume ratio on the ORC system efficiency, a thermodynamic cycle model with a semi-empirical expander model was developed. The expander model included lumped mechanical, leakage and heat losses. As ORC systems are usually optimized for higher pressure ratios in order to extract more power, expanders with larger internal volume ratios, e.g., screw type, are favored because their isentropic efficiency shows a lower decay in the under-expansion region. For given heat source and sink conditions, the theoretical matching between a positive displacement expander and the ORC system was obtained by maximizing the cycle Second Law efficiency defined with respect to the associated Carnot cycle.

The availability of a certain expander type is another aspect to be taken into account. Due to the fact that commercially available expanders are very limited, the research on positive displacement machines is often conducted by modifying existing compressor technologies used in vapor compression industry. In the ultra-low and low power range (1 to 10 kWe), scroll expanders are usually preferred due to high efficiency achievable. In the medium power

range, screw-type of expanders represent main technology to be employed. Under the screw family of positive displacement machines, twin-screw and single-screw are currently employed industrially. Twin-screw expanders have been investigated in literature and showed isentropic efficiency above 80%. Single-screw type of machines, which are also employed in air-compression and refrigeration applications, are characterized by a meshing pair of central rotor and two starwheels. Such configuration leads to a symmetrical working process which presents advantages compared to traditional twin-screw technology because of reduced loads on bearings, noise and vibrations. The manufacturing of single-screw machines is particularly challenging and requires advanced and custom-made CNC machines. Twin-screw machines are usually preferred due to higher volumetric and isentropic performance. However, both screw-type of machines are able to handle part-load conditions by means of internal capacity or pressure ratio control mechanisms which is ideal for the ORC operations.

The current research on evaluating the performance of single-screw expanders for ORC applications is still at the beginning and the majority of the literature available is limited to compressed-air as working fluid. Fewer studies have been published on the integration of a single-screw expander into an ORC system and always limited to a single working fluid, e.g., R123.

In order to characterize the single-screw expander performance, numerical methods to predict its performance as well as experimental data were necessary. To address the numerical simulation part, a comprehensive mechanistic model based on a detailed geometry description of the single-screw expander and an open-control volume formulation was developed. The model included effects of internal leakage, heat transfer and friction losses. The core structure of simulation model was demonstrated to be applicable to the majority of positive displacement machines, either expanders or compressors. A scaled-down prototype of an industrial ORC with an 11 kWe generator was used to collect experimental data on a single-screw expander. In particular, a single-screw expander converted from an air-compressor unit was tested with R245fa and SES36. The hot source inlet temperature was fixed at 125 °C. A total of 102 steady-state points were obtained. The expander achieved a maximum overall isentropic efficiency of approximately 65% at a pressure ratio of 8.83 with SES36 as working fluid. The experimental results were used to carry out a preliminary validation of the expander model and to calibrate a semi-empirical model.

The experimental analysis revealed how the performance of the single-screw expander were affected by the deterioration of the meshing profile, i.e., larger leakage gaps, and by the maximum pressure at which the housing was able to work. Design tolerances of the meshing pair and non-sufficient lubrication were identified as possible causes of the wearing of the tooth profile. The semi-empirical model was used to break-down the internal losses of the expander and further exercised to evaluate the impact of design improvements on the performance. The reduction of mechanical losses and leakage flows results in a maximum isentropic efficiency of 72.5%.

Based on the experience gained by running the ORC system, the operation

of the single-screw expander with the system was optimize by analyzing the matching between expander and system performance. As a result of this work, recommendations are made on a new housing design that could be considered for further developments and research opportunities especially regarding two-phase flow expansion. Moreover, the knowledge gained during the present work, especially related to meshing pair geometry model, led to obtain preliminary transient CFD results which has not been addressed yet in the open-literature due to the complexity of the meshing process. The knowledge of the meshing pair kinematics equations could be used to develop proper grid generation algorithms applicable to complex rotor geometries.

The simulation framework for positive displacement machines employed and enhanced in this work is a powerful tool for both research and teaching purposes. In particular, its structure will allow the integration of other important modeling aspects such as gas pulsations as well as transient operating cycles to be found for example in linear compressors.

1 Introduction

1.1 Organic Rankine Cycles and Waste Heat Recovery

The increase in both global energy demand and environmental concerns push the research towards renewable energies as well as to more efficient ways of utilizing existing technologies [1]. A great variety of heat source profiles and capacities exist that are potentially suitable for waste heat recovery (WHR) technologies [2]. Medium to low grade (80-200 °C) waste heat recovery has gained attention and importance as conventional high temperature Rankine cycles are economically unfeasible in such range of temperatures [3]. In particular, the residual or waste heat from industrial processes is usually not efficiently recovered as it falls into the medium to low temperature range [4].

During recent years, organic Rankine cycle (ORC) systems have gained maturity, becoming a widely accepted technology to convert low to medium grade heat into higher quality type of energy, e.g., electricity [5–7] due to their adaptability to be designed to match different heat sources and heat sinks conditions.

The research on ORC systems progresses on several aspects such as environmentally-friendly working fluids, thermo-economic optimizations, cycle and components modeling as well as control strategies [8–10]. Especially at lower power range (below 50 kWe), thermo-economic aspects have to be included while investigating potential cycle improvements because of the absence of an

economy of scale of such systems. Lecompte et al. [11] analyzed several advanced thermodynamic cycle configurations for future developments and concluded that ORCs with partial evaporation and two-phase expansion have high potential for low-grade waste heat recovery.

The design of efficient, environmental-friendly, and cost effective ORC systems is still an open challenge nowadays. Although ORC systems are rather easy to operate and the components are mostly available from the refrigeration industry, the overall efficiency is still quite low compared to other traditional energy conversion technologies.

As aforementioned, one of the key aspects of WHR is the conversion of heat into higher quality type of energy by means of an expansion device. As a consequence, the optimization of so called expander plays an important role in the frame of maximizing the power output and improving the overall efficiency. Different expander technologies have been proposed and analyzed during recent years [12]. In general, expanders can be classified into two main categories: (i) dynamic or velocity-based type, e.g., axial and radial turbine expanders; (ii) positive displacement or volumetric type, e.g., scroll, screw, rotary, reciprocating [13]. Limitations of both technologies have been addressed by Quoilin et al. [14].

Positive displacement expanders have been proven to be cost-effective in the low to medium power range, as outlined by Imran et al. [12] in their comprehensive review. The performance of a volumetric expander is affected by internal losses (typically leakage, friction and heat losses) and the operating condition at which it operates in terms of applied pressure ratio. Because of the fixed internal volume ratio (usually in the range 2-7), also referred as built-in volume ratio, the volumetric expander has to be chosen to match with the system optimal pressure ratio. As a consequence, in most of the cases, the volumetric expanders work in the under-expansion area, i.e. the specific volume ratio applied is higher than the built-in one, because the over-expansion losses are significantly more detrimental and the ORC systems are usually optimized for a higher evaporating pressure depending on the working fluid selected [8].

1.2 Positive Displacement Expanders for ORC applications

In the selection process of an expander for a certain ORC application several desirable parameters can be listed and grouped in different categories:

(i) performance parameters: isentropic efficiency, pressure ratio, power output, working temperature, inlet vapor quality;

(ii) design parameters: lubrication requirements, clearances, rotational speed, capacity, noise and vibrations;

(iii) other general parameters: reliability, costs, safety.

The current research efforts suggest that each volumetric expander type has a certain range of capacity and therefore more appropriate applications [12]. However, on a commercial point of view, only turbine, screw and scroll expanders are widely used. This aspect represents a fundamental difference compared to vapor compression systems.

Scroll-expanders are a well known technology for small-scale ORC applications [15]. Other positive displacement machines have been proposed and investigated, such as rotary and reciprocating piston expanders. For instance, Bao et al. [16] proposed a detailed overview of available expander technologies and selection criteria for ORC systems. In particular, it appears clear that one-stage radial inflow turbines are attractive under isentropic efficiency point of view (48-85%), lower flow rate and higher pressure ratios compared to axial turbines. Screw expanders is a mature technology in the ORC systems with an isentropic efficiency in the range of 26-85%, but in many cases gear boxes and lubrication systems are required and they are mainly employed in the medium to large power range. Such wide range of efficiency is related to the size and operating conditions of the screw expanders. In fact, leakages and machining tolerances are important aspects during the design process. Scroll expanders present a more complicated geometry with a fixed built-in volume ratio which can cause under and over expansion issues. This type of machine is suitable for limited expansion ratios compared to turbines, and lower power range, which makes this technology the main candidate for small ORC systems (below 10 kW). The isentropic efficiency ranges between 10 and 77%. Reciprocating piston expanders are used in the heat recovery from internal combustion engine exhaust. The presence of intake and exhaust valves as well as large amount of moving parts, affect the reliability and the performances of such displacement machine. The maximum value of the isentropic efficiency reported in literature was slightly above 60%. Rotary vane expanders have some advantages such as wide range of tolerance of vapor qualities, simpler structure which limits manufacturing costs and flat operating efficiency curves. Low rotational speeds allow to couple the expander to a generator without gearboxes. Wear and sealing are major issues and a consequent lubrication system is required. In fact, leakages have been found to be the main contributor in performance loss. The capacity of the rotary vane expander is limited (below 10 kW) and the isentropic efficiency is in many cases below 55%.

Under the category screw type, different configurations exist that defined the type of machine. In particular, twin-screw and single-screw types, shown in Figure 1.1 and in Figure 1.2 respectively, are the most common ones and widely used in commercial and industrial applications. As it can be seen from Figure 1.2, the single-screw machine represents an improvement over twin-screw because of balanced loads on the main screw rotor. In fact, the compression or expansion

process occurs simultaneously with respect to the main shaft rotation axis which reduces also the vibrations leading to improved working life for the bearings.

During the selection and design of a positive displacement expander for ORC applications, two major aspects must be considered and analyzed:

- expander losses (friction losses, heat losses, leakages, other irreversibilities);
- matching between ORC system optimum pressure ratio and fixed expander built-in volume ratio.

A general overview of the typical expander internal losses is given in Section 1.2.1. Whereas, the matching between ORC system and a positive displacement expander is discussed in Section 1.2.2.

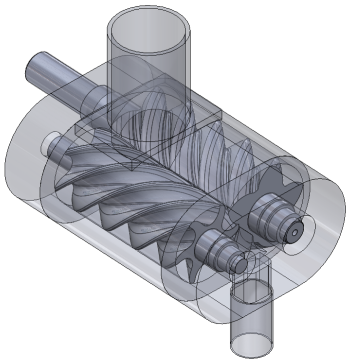

Figure 1.1: Assembly of a twin-screw compressor or expander machine.

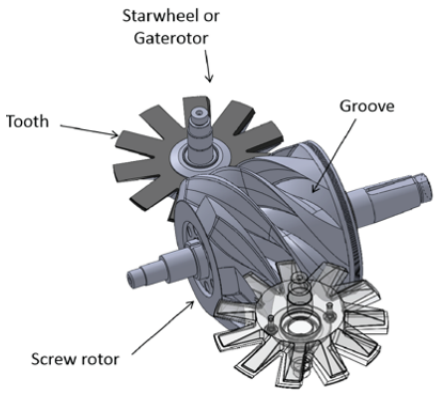

Figure 1.2: Assembly of a single-screw compressor or expander machine.

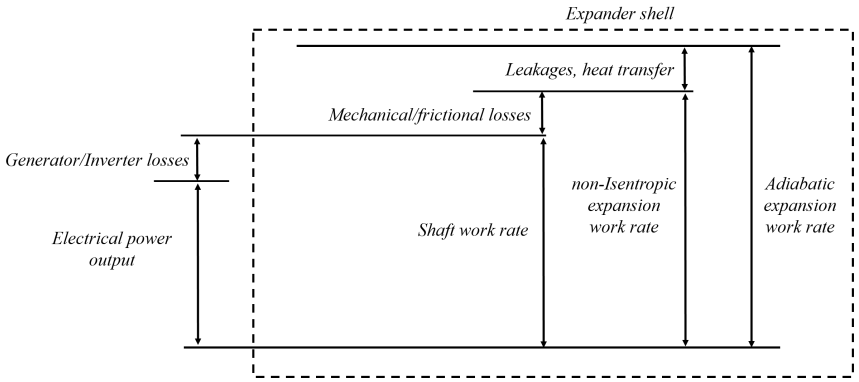

Figure 1.3: Definition of the internal losses of an open-drive expander. Adapted from Chen et al. [17].

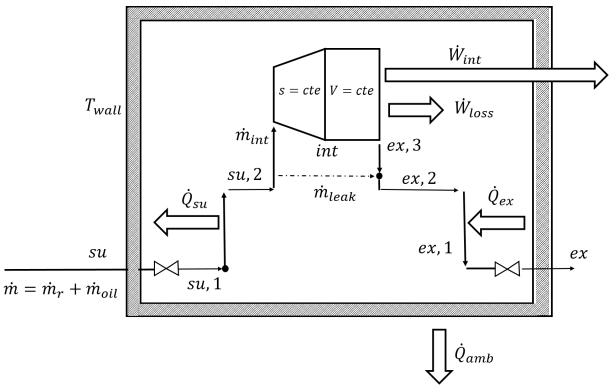

Figure 1.4: Break down of the internal physical phenomena occurring inside a positive displacement expander.

1.2.1 Expander internal losses

The performance of a positive displacement expander is affected by fixed internal volume ratio, mismatch with the applied pressure ratio, pressure drops during suction and discharge processes, heat losses, leakages, presence of lubricant oil and friction losses. Similar considerations can be readily extended to positive displacement compressors. The general energy flow chart of an open-drive positive displacement expander is shown in Figure 1.3.

A conceptual schematic of an expander can be considered to describe in a general way the evolution of the working fluid and lubricant oil through the machine and, thus, identify the different loss terms. In particular, the widely documented approach [18–20] of decomposing the expansion process into several

steps is adopted. By referring to Figure 1.4, the following physical-based steps can be recognized:

- adiabatic supply pressure drop;
- isobaric supply cooling;
- fictitious internal leakage;
- adiabatic reversible expansion to the internal pressure ratio imposed by the built-in volume ratio of the expander;
- adiabatic expansion at a constant volume;
- adiabatic mixing between the flow exiting the expansion chamber and the internal leakage flow;
- isobaric exhaust heat transfer;
- adiabatic discharge pressure drop.

The actual expansion process is divided into two steps, i.e. an isentropic expansion to the internal pressure, $p_{int,exp}$, corresponding to the built-in volume ratio and an adiabatic expansion at constant machine volume ($V=V_{dis}$), to the discharge pressure (condensing pressure). Therefore, the internal specific work is expressed as

$$w_{\mathrm{int,exp}} = w_{\mathrm{s,exp}} + w_{\mathrm{V,exp}} \tag{1.1}$$

where, the two contribution terms are given by

$$w_{\mathrm{s,exp}} = h_{\mathrm{su2,mix,exp}} - h_{\mathrm{int,mix,exp}} \tag{1.2}$$

$$w_{\mathrm{V,exp}} = v_{\mathrm{int,mix,exp}} \left(p_{\mathrm{int,exp}} - p_{\mathrm{ex3,exp}} \right) \tag{1.3}$$

and it is assumed that the working fluid and lubricant oil are in thermal and mechanical equilibrium, which implies that they are treated as an homogeneous mixture (subscript *mix*) with same temperature and velocity. To be noted is that in the case of reciprocating expanders, a re-compression step needs to be accounted for due to the presence of a clearance volume, as shown by Dumont et al. [21].

The mass flow rate through a positive displacement expander is typically related to pressure drops and heat transfer during the suction process and internal leakages. The theoretical mass flow rate through the expander is calculated as:

$$\dot{m}_{\mathrm{th,exp}} = \frac{\dot{V}_{\mathrm{swept,exp}}}{v_{\mathrm{su,mix,exp}}} \tag{1.4}$$

where $\dot{V}_{\mathrm{swept,exp}}$ is the volumetric flow rate displaced by the expander. Due to the aforementioned losses during filling process, it follows that the actual mass flow rate displaced can be expressed as:

$$\dot{m}_{\mathrm{exp}} = \dot{m}_{\mathrm{int,exp}} + \dot{m}_{\mathrm{leak,exp}} \tag{1.5}$$

where $\dot{m}_{\mathrm{int,exp}}$ is the internal mass flow rate that produces work and $\dot{m}_{\mathrm{leak,exp}}$ is the lumped leakage flow rate.

The expander shaft power is obtained by subtracting the mechanical losses associated with friction and bearing losses to the internal power, i.e. p-V work. That is:

$$\dot{W}_{\mathrm{sh,exp}} = \dot{W}_{\mathrm{int,exp}}\eta_{\mathrm{mech}} = \dot{m}_{\mathrm{int,exp}} w_{\mathrm{int,exp}} - \dot{W}_{\mathrm{loss,mech}} \tag{1.6}$$

As the expansion process is not adiabatic, the expander shell temperature increases leading to potential heat losses to the ambient. An overall energy balance on the expander is imposed to account for heat losses through the housing:

$$\dot{m}_{\mathrm{exp}} \left(h_{\mathrm{su,mix,exp}} - h_{\mathrm{ex,mix,exp}}\right) = \dot{W}_{\mathrm{sh,exp}} + \dot{Q}_{\mathrm{amb}} \tag{1.7}$$

The ambient heat rate losses are calculated as follows:

$$\dot{Q}_{\mathrm{amb}} = U A_{\mathrm{amb}} \left(T_{\mathrm{shell}} - T_{\mathrm{amb}}\right) \tag{1.8}$$

where the shell temperature of the expander is given as the average temperature between inlet and outlet conditions.

The performance of a volumetric expander can be fully characterized by defining an expander overall isentropic efficiency and a filling factor. The expander overall isentropic efficiency, $\eta_{\mathrm{oa,exp}}$, is affected by the pressure ratio across it (i.e., volume ratio - pressure ratio mismatch), by internal leakage losses, by thermodynamic irreversibilities as well as mechanical and friction losses. As outlined by Lemort et al. [22], the overall isentropic efficiency can be expressed as the product of four terms:

$$\eta_{\mathrm{oa,exp}} = \eta_{\mathrm{leak}}\, \eta_{\mathrm{int}}\, \eta_{\mathrm{mech}}\, \eta_{\mathrm{s,th}} \tag{1.9}$$

$$= \underbrace{\frac{\dot{m}_{\mathrm{int,exp}}}{\phi_{\mathrm{leak}}\phi_{\mathrm{P,T}}\phi_{\mathrm{O}}}\dot{m}_{\mathrm{exp}}}_{\varphi_{\mathrm{FF}}} \frac{\dot{W}_{\mathrm{int,exp}}}{\dot{W}_{\mathrm{pV,th,exp}}} \frac{\dot{W}_{\mathrm{sh,exp}}}{\dot{W}_{\mathrm{int,exp}}} \frac{\dot{W}_{\mathrm{pV,th,exp}}}{\dot{W}_{\mathrm{th,s,exp}}} \tag{1.10}$$

where η_{leak} is the reciprocal of the filling factor, φ_{FF}, and quantifies the leakage losses, η_{int} is the internal efficiency or "diagram factor" and quantifies all the irreversibilities associated with the actual indicated work rate (i.e. irreversibilities that deform the indicated diagram) with respect to the theoretical indicated work rate, $\dot{W}_{\mathrm{pV,th,exp}}$, η_{mech} is the expander mechanical efficiency and $\eta_{\mathrm{s,th}}$ is the theoretical isentropic efficiency that quantifies the impact of under/over-expansion/compression losses. The filling factor is a strong function of the rotation speed and a weak function of the pressure ratio [23] and it can be decomposed into three terms: ϕ_{leak} quantifies the impact of internal leakages and it is always larger than unity, $\phi_{\mathrm{P,T}}$ accounts for the impact of supply pressure drop and heat

transfer on the inlet specific volume and it is less than unity if the pressure losses are predominant and ϕ_{O} is equal to unity for all the machines that do not have a clearance volume. Furthermore, the volumetric performance of an expander is influenced by both manufacturing tolerances and working conditions. Its modeling requires a more mechanistic approach or experimental testing.

The theoretical isentropic power is given as:

$$\dot{W}_{\mathrm{th,is,exp}} = \dot{m}_{\mathrm{th,exp}} \left(h_{\mathrm{su,mix}} - h_{\mathrm{ex,mix,s}} \right) \tag{1.11}$$

The contribution of each term affecting the expander efficiency is shown in Figure 1.5(a). The maximum expander efficiency occurs when the imposed specific volume ratio matches the internal volume ratio of the machine and both suction and discharge pressure drops are neglected. To be noted is that usually the actual internal (or indicated) work differs from the theoretical one because of other irreversibilities than over/under expansion losses (for example leakages and heat losses) [22]. The terms η_{int} and η_{mech} are related to the internal leakages and mechanical losses of a specific machine and are functions of pressure ratio and rotational speed. Only for illustration purposes, the product $\eta_{\mathrm{int}}\eta_{\mathrm{mech}}$ has been assumed constant and equal to 0.6 in order to be representative of a general expander. Both contributions should be correlated to the actual behavior of the expander under different operating conditions.

In Figure 1.5(b) it is possible to see the effect of the pressure ratio on the expander isentropic efficiency. As the internal volume ratio increases, the effect of the under-expansion is less detrimental. The lower volume ratio expander efficiency curve resembles the one from a scroll-type of expander [24]. The curves at higher volume ratios are characteristic of screw-type expanders [23, 25].

1.2.2 Matching between ORC and Expanders

As described in the previous section, the actual expansion process deviates greatly from the ideal adiabatic and reversible process. One aspect that has not been analyzed previously is the pressure drops. The pressure ratio imposed externally to the expander differs from the internal pressure ratio applied to the working chambers. The difference is related to the fixed internal volume ratio, which has been discussed previously in terms of over- and under-expansion, and pressure drops at the inlet and outlet of the machine, filling of the chambers, internal piping. It follows that in order to optimize the performance of the expander, the system pressure ratio, the internal pressure ratio and the built-in volume ratio are closely related.

The matching between ORC systems and expanders has been analyzed [2, 24, 26]. For a given set of operating conditions and expander type, it is possible to determine the expander volume ratio at which both the cycle efficiency and

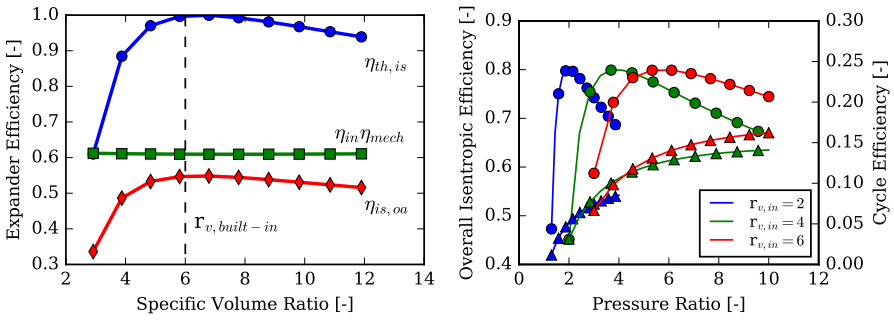

Figure 1.5: (a) Breakdown of the contributions to the expander overall isentropic efficiency. Plot generated for R245fa and an expander built-in volume ratio of 6. The mechanical efficiency is assumed to be 0.7; (b) influence of the expander built-in volume ratio on overall isentropic efficiency (circle markers) and cycle efficiency (triangle markers) at different pressure ratios with R245fa. Pressure drops at suction and discharge ports of the expander are not considered as they are machine specific.

the expander efficiency are maximized. For a fixed expander capacity, i.e., N_{exp} =fixed, the isentropic efficiency can be considered to be a function of only the expansion volume ratio, i.e., $\eta_{\mathrm{is,oa}} \simeq f_{\mathrm{exp}}\left(r_{\mathrm{v,exp}}\right)$. In fact, the filling factor is almost independent from the expander pressure ratio but it is a function of the expander rotational speed which is related to the capacity. Therefore, it is possible to maximize the Second Law efficiency for a heat source having a finite heat capacity [26, 27] as a function of the expansion volume ratio and the expander isentropic efficiency, i.e., $\eta_{\mathrm{II,finite}} = f_{\mathrm{ORC}}\left(r_{\mathrm{v,exp}}, \eta_{\mathrm{is,oa}}\right)$. In the case of ORCs, the Second Law efficiency for a heat source having a finite heat capacity is written as:

$$\begin{aligned}\eta_{\mathrm{II,finite}} &= \frac{\dot{W}_{\mathrm{net}}}{\dot{m}_{\mathrm{hf}} \int_0^{\mathrm{hf,in}} \left(1 - \frac{T_0}{T}\right) \delta q} \\ &= \frac{\dot{W}_{\mathrm{exp}} - \dot{W}_{\mathrm{pp}}}{\dot{m}_{\mathrm{hf}}\big[\left(h_{in}\left(T_{\mathrm{hf,in}}, p_{\mathrm{hf,in}}\right) - h_0\left(T_0, p_{\mathrm{hf,in}}\right)\right) \\ &\qquad -T_0\left(s_{in}\left(T_{\mathrm{hf,in}}, p_{\mathrm{hf,in}}\right) - s_0\left(T_0, p_{\mathrm{hf,in}}\right)\right)\big]}\end{aligned} \tag{1.12}$$

where the denominator represents the thermal exergy of the heat source with a finite heat capacity. The integral of the Carnot efficiency over the heat source profile limits has been calculated neglecting the contributions of kinetic energy and potential energy. Thus, since the thermal oil used as hot source is incompressible, any contribution associated to the pressure being slightly higher than the atmospheric one is neglected (the piping system is not pressurized). The

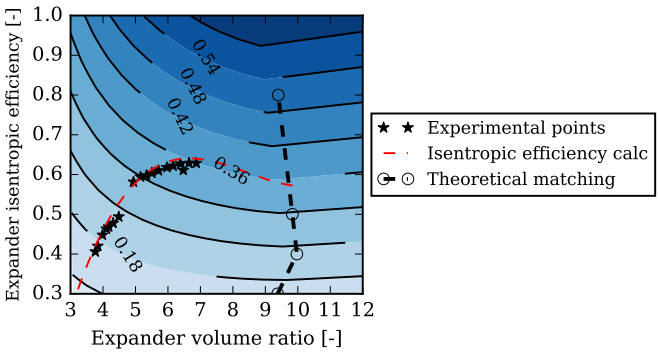

Figure 1.6: Theoretical match between expander and ORC cycle efficiency for R245fa. Contour shows lines at constant Second Law efficiency $\eta_{\mathrm{II,Carnot}}$. The hot source inlet temperature is fixed at 125 °C. The experimental data is overlaid for reference. The red dashed line represents the points that satisfy the Pacejka equation, as reported in [26].

dead state temperature, T_0, is chosen to be the coldest temperature within the ORC system, i.e., the cooling medium entering the condenser, $T_{\mathrm{cf,in}}$. If the heat source is fixed, then the denominator of Equation 1.12 is independent of the cycle configuration or working fluid, which allows to fairly compare the performance of a certain system with different working fluids. To be noted is that, for a fixed heat source, maximizing $\eta_{\mathrm{II,finite}}$ also means maximizing $\dot{W}_{\mathrm{net}}$.

A constraint is introduced regarding the isentropic efficiency of the expander. Woodland et al. [24], assumed that the expander efficiency must follow the trend of the obtained experimental data of the chosen expander. However, if the aim is to investigate the influence of both expansion ratio and maximum isentropic efficiency achievable with a certain expander type, the optimization can be constrained by imposing the desired value of the isentropic efficiency, $\eta_{\mathrm{is,des}}$. If a single value is considered, at the optimum point $(r_{\mathrm{v,opt}}, \eta_{\mathrm{is,opt}})$:

$$\left.\frac{d\eta_{\mathrm{II,finite}}}{dr_{\mathrm{v,exp}}}\right|_{\mathrm{opt}} = \left.\frac{\partial f_{\mathrm{ORC}}\left(r_{\mathrm{v,exp}}, \eta_{\mathrm{is,oa}}\right)}{\partial r_{\mathrm{v,exp}}}\right|_{\mathrm{opt}} = \left.\frac{d\eta_{\mathrm{is,oa}}}{dr_{\mathrm{v,exp}}}\right|_{\mathrm{opt}} = \left.\frac{\partial f_{\mathrm{exp}}\left(r_{\mathrm{v,exp}}\right)}{\partial r_{\mathrm{v,exp}}}\right|_{\mathrm{opt}} = 0 \tag{1.13}$$

with $\eta_{\mathrm{is,opt}} = \eta_{\mathrm{is,des}}$. If an array of values are posed as constraint, $\boldsymbol{\eta}_{\mathrm{is,des}}$, then a line of optimum points are obtained, representing the current design limit for the expander technology selected.

By taking as an example the performance of a single-screw expander, an optimization can be carried out to determine the theoretical expander that should be designed for the given set of boundary conditions in order to match the maximum isentropic efficiency with the maximum Second Law efficiency defined

with respect to the associated Carnot cycle:

$$\eta_{\mathrm{II,Carnot}} = \frac{\eta_{\mathrm{ORC,net}}}{\eta_{\mathrm{Carnot}}} \tag{1.14}$$

where $\eta_{\mathrm{Carnot}} = 1 - T_{\mathrm{in,cd,cf}}/T_{\mathrm{in,ev,hf}}$ with $T_{\mathrm{in,cd,cf}}$ and $T_{\mathrm{in,ev,hf}}$ are the inlet temperatures in Kelvin of heat sink and heat source, respectively. The upper limit of the desired single-screw expander isentropic efficiency is set equal to 0.8, which is a reasonable upper bound value for screw type of expanders [12]. The results of the optimization for a heat source inlet temperature of 125 °C is shown in Fig. 1.6. Under the specified boundary conditions, the contour shows the Second Law efficiency, $\eta_{\mathrm{II,Carnot}}$, calculated by varying the isentropic efficiency of the expander from 0.3 to 1 (ideal case) and by increasing the pump frequency up to 49 Hz. The experimental points (black stars), which are representative of the current expander performance range at 3000 rpm, are overlaid to highlight the possible performance improvements when compared with the theoretical black dashed line corresponding to the points where the maximum cycle efficiency is obtained at the maximum expander isentropic efficiency. If the operating conditions could be adjusted toward the black dashed line, an increase in expander isentropic efficiency would always result in an increase in cycle efficiency. The installed expander has a built-in volume ratio slightly higher than 5. Typically, the maximum isentropic efficiency occurs for a specific expansion ratio close to the built-in volume ratio. The optimization suggests that the hypothetical expander should have a high specific expansion ratio (above 9). However, the maximum reported built-in volume ratio for a single-screw compressor is around 7. As a consequence, additional experimental results should be obtained to better characterize the decrease of the isentropic efficiency at higher specific expansion ratio, i.e., between 7 to 10. In fact, usually, by increasing the pressure ratio across the expander, the power output still increases because the under-expansion is less detrimental than the over-expansion. There is a trade off between the decrease of expander isentropic efficiency due to under-expansion and the increase of cycle efficiency due to the increase of power produced by the expander at higher pressure ratios.

1.3 Motivation and objectives of the study

Organic Rankine cycle systems have the potential to recover waste heat at higher cycle efficiency as the development and research advance. As pointed out by Lecompte [28], the component selection, layout and sizing is among the major research topics on ORCs. The expansion device represents the core of the ORC system as it allows to generate useful work output. Up to know, commercially available positive displacement expanders are limited and often

tailored to particular applications. As for the working fluids, it is not possible to select one expander type for all the applications and capacities.

In medium to low power range, screw expanders are regarded as the most suitable technology among positive displacement machines. Single-screw expanders are gaining attention due to their favorable mechanical configuration compared to twin-screw type. Although, a number of works in literature can be found on such expander, the experimental characterization is often limited to compressed air or a single working fluid.

In order to assess the potential of single-screw expanders as volumetric expanders for ORC applications, a more in-depth characterization of their performance is required. Currently, several aspects have not been addressed yet in the open-literature. The most important ones, but not limited to, are:

- performance behavior of SSE with different working fluids in an ORC installation;
- relationship between the geometric built-in volume ratio and the applied system pressure ratio as well as the specific expansion ratio;
- quantify the major single-screw expander internal losses and identify design improvements;
- impact of lubricant oil on leakage path and friction losses;
- absence of available experimental data of single-screw expanders employed in ORC systems with different working fluids.

Furthermore, as aforementioned, numerous studies in literature focus on expander modeling. Yet, the detailed models are usually developed for a specific machine. The comparison of different positive expander types is an important aspects when designing an ORC. The availability of tools in the open-literature is still limited. An effort is made in this work to extend a generalized modeling approach to both positive displacement expanders and compressors.

The objective of this work is to characterize the performance of a single-screw expander for ORC applications in waste heat recovery both numerically and experimentally. The following aspects are addressed:

- development and validation of a generalized positive displacement simulation framework;
- development and validation of a single-screw mechanistic model
- experimental characterization of a single screw expander with two working fluids, i.e., SES36 and R245fa.

1.4 Outline

The structure of the thesis follows the objectives above.

In **Chapter 2**, a generalized approach to the modeling of positive displacement compressors and expanders is introduced and applied to show its flexibility.

In **Chapter 3**, the geometric features of a single-screw machine are described and proper models are formulated to obtain the geometric curves necessary to undertake the task of developing a mechanistic model.

The general approach outlined in Chapter 2 and the geometry model obtained in Chapter 3 are utilized in **Chapter 4** to complete the mechanistic model of the single-screw expander. Particular attention is given to model leakage flows, heat transfer rate within the working chambers, frictional losses and overall energy balance.

In **Chapter 5**, the performance of a single-screw expander with a 120 mm main rotor is evaluated experimentally. In particular, the expander is installed in an 11 kWe ORC which is a scaled-down version of a real commercial ORC, designed for waste heat recovery under low heat source temperatures. SES36 and R245fa are employed as working fluids.

In **Chapter 6**, the mechanistic model is validated with the experimental data and the operation of the single-screw expander integrated in ORC system is optimized.

References

[1] *BP Statistical Review of World Energy June 2015*. Technical report, BP, 2015.

[2] Y. Zhu, L. Jiang, V. Jin, and L. Yu. *Impact of built-in and actual expansion ratio difference of expander on ORC system performance*. Applied Thermal Engineering, 71:548–558, 2014.

[3] H. Zhai, Q. An, L. Shi, V. Lemort, and S. Quoilin. *Categorization and analysis of heat sources for organic Rankine cycle system*. Renewable and Sustainable Energy Reviews, 2016.

[4] G. Oluleye, M. Jobson, R. Smith, and S. J. Perry. *Evaluating the potential of process sites for waste heat recovery*. Applied Energy, 161:627–646, 2016.

[5] S. Quoilin, M. van den Broek, S. Declaye, P. Dewallef, and V. Lemort. *Techno-economic survey of Organic Rankine Cycle (ORC) systems*. Renewable and Sustainable Energy Reviews, 22:168–186, 2013.

[6] J-C Chang, T-C Hung, Y-L He, and W. Zhang. *Experimental study on low-temperature organic Rankine cycle utilizing scroll type expander*. Applied Energy, 155:150–159, 2015.

[7] T. Li, Z. Zhang, J. Lu, J. Yang, and Y. Hu. *Two-stage evaporation strategy to improve system performance of organic Rankine cycle*. Applied Energy, 150:323–334, 2015.

[8] D. Maraver, J. Royo, V. Lemort, and S. Quoilin. *System optimization of subcritical and transcritical organic Rankine cycles (ORC) constrained by technical parameters in multiple applications*. Applied Energy, 117:11–29, 2014.

[9] S. Lecompte, H. Huisseune, M. van den Broek, and M. De Paepe. *Methodical thermodynamic analysis and regression models of organic Rankine cycle architectures for waste heat recovery*. Energy, 87:60–76, 2015.

[10] A. Pezzuolo, A. Benato, A. Stoppato, and A. Mirandola. *The ORC-PD: A versatile tool for fluid selection and Organic Rankine Cycle unit design*. Energy, 102:605–620, 2016.

[11] S. Lecompte, H. Huisseune, M. van den Broek, B. Vanslambrouck, and M. De Paepe. *Review of organic Rankine (ORC) architectures for waste heat recovery*. Renewable and Sustainable Energy Reviews, 47:448–461, 2015.

[12] M. Imran, M. Usman, Park B-S, and D-H Lee. *Volumetric expander for low grade heat and waste heat recovery applications*. Renewable and Sustainable Energy Reviews, 57:1090–1109, 2016.

[13] G. Qiu, H. Liu, and S. Riffat. *Expanders for micro-CHP systems with organic Rankine cycle*. Applied Thermal Engineering, 21:381–390, 2011.

[14] S. Quoilin, S. Declaye, and V. Lemort. *Expansion machine and fluid selection for the Organic Rankine Cycle*. In 7th International Conference on Heat Transfer, Fluid Mechanics and Thermodynamics (HEFAT), 2010.

[15] P. Song, M. Wei, S. Shi, S. N. Danish, and C. Ma. *Review of scroll expanders for organic Rankine cycle systems*. Applied Thermal Engineering, 75:54–64, 2015.

[16] J. Bao and Li. Zhao. *A review of working fluid and expander selections for organic rankine cycle*. Renewable and Sustainable Energy Reviews, 24:325–342, 2013.

[17] Y. Chen, N.P. Halm, E.A. Groll, and J.E. Braun. *Mathematical Modeling of Scroll Compressor. Part II- Overall scroll compressor modeling*. Int. J. Refrig., 25:751–764, 2002.

[18] E. Winandy, C. Saavedra, and J. Lebrun. *Simplified modeling of an open-drive reciprocating compressor*. International Journal of Thermal Sciences, 42:183–192, 2002.

[19] A. Giuffrida. *Modelling the performance of a scroll expander for small organic Rankine cycles when changing the working fluid*. Applied Thermal Engineering, 70:1040–1049, 2014.

[20] D. Ziviani, B. J. Woodland, E. Georges, E. A. Groll, J. E. Braun, W. T. Horton, M. van den Broek, and M. De Paepe. *Development and validation of a charge sensitive organic Rankine cycle (ORC) simulation tool*. Energies, 9:389, 2016.

[21] O. Dumont, R. Dickes, and V. Lemeort. *Extrapolability and limitations of a semi-empirical model for the simulation of volumetric expanders*. Energy Procedia, 129:315–322, 2017.

[22] E. Macchi and M. Astolfi, editors. *Organic Rankine Cycle (ORC) Power Systems*. Woodhead Publishing, 2016. Chapter 12 - Positive displacement expanders for Organic Rankine Cycle systems, Lemort, V., Legros, A., pp. 361-396.

[23] D. Ziviani, S. Sergei, S. Lecompte, E. A. Groll, J. E. Braun, W. T. Horton, M. van den Broek, and M. De Paepe. *Characterizing the performance of a single-screw expander in a small-scale organic Rankine cycle for waste heat recovery*. Applied Energy, 181:155–170, 2016.

[24] B. J. Woodland, J. E. Braun, E. A. Groll, and W. T. Horton. *Experimental Testing of an Organic Rankine Cycle with Scroll-type Expander*. In International Refrigeration and Air Conditioning Conference at Purdue, number 2505, 2012.

[25] K. C. Ng, T. Y. Bong, and T. B. Lim. *A thermodynamic model for the analysis of screw expander performance*. Heat Recovery & CHP, 10:119–133, 1990.

[26] D. Ziviani, S. Sergei, S. Lecompte, E. A. Groll, J. E. Braun, W. T. Horton, M. van den Broek, and M. De Paepe. *Optimizing the performance of small-scale organic Rankine cycle that utilizes a single-screw expander*. Applied Energy, 189:416432, 2017.

[27] B. J. Woodland, J. E. Braun, E. A. Groll, and W. T. Horton. *Methods of Increasing Net Work Output of Organic Rankine Cycles for Low-Grade Waste Heat Recovery*. In 15th Int.Refrigeration and Air Conditioning Conf. at Purdue, number 2190, 2014.

[28] S. Lecompte. *Performance Evaluation of Organic Rankine Cycle Architectures: Application to Waste Heat Valorisation*. PhD thesis, Ghent University, 2016.

2

Mechanistic model of positive displacement machines:PDSim

2.1 Introduction

The deterministic or mechanistic simulation of positive displacement compressors and expanders, also referred to as chamber models, is of great interest both academically and industrially. Simulation programs are typically developed in order to conduct computer-based prototyping. Once the mechanistic model is properly validated and calibrated, it allows to accurately predict the performance of the machine at conditions for which the machine has not been tested previously. In contrast, semi-empirical models are typically valid within the calibrated range and the limits of extrapolability should be assessed [1]. Moreover, design improvements can also be analyzed which potentially reduces the experimental work.

One of the shortcomings of many of the documented simulation codes for positive displacement machines is that they are highly specific, generally having been developed for a particular type of machine (scroll, reciprocating, etc.) and are typically structured in a way that limit their flexibility. Furthermore, most of such models are not readily available in the open-literature due to highly proprietary modeling information. As a result, duplicate efforts can be found especially in the academic research.

By conducting a literature review, the fundamentals of computer simulation of positive displacement compressors were described by Prof. Soedel and Prof.

Hamilton from the Ray W. Herrick Laboratories at Purdue University in their short courses [2, 3]. Such approach was applied systematically to different compressor types, such as reciprocating, rolling piston, sliding vane as well as screw [4, 5], and a general methodology was developed. Throughout decades of research, this methodology allowed to develop tailor-made simulation models with focus on a particular type of positive displacement machine. A selection of the simulation codes developed at the Ray W. Herrick Laboratories over the last few decades is summarized here:

- Scroll compressor and expander [6–11]
- Bowtie compressor [12]
- Linear compressor [13, 14]
- Rotary compressor [15, 16]
- Z-compressor [17]
- Reciprocating compressor [18, 19]
- Screw compressor and expander [20–22]
- Spool compressor [16, 23]

With the knowledge gained by modeling different types of compressors and expanders, it was possible to identify a general structure in the construction of their models and to develop a tool that was able to include the common features shared amongst all positive displacement types:

- Control volumes, which form the heart of the device and the model. These control volumes (working chambers) have volume profiles governed by the geometry. The change in volume of the working chambers results in compression (with power input) or expansion (with power recovery). The control volumes exchange heat and mass with the elements with which it communicates, as shown in Figure 2.1.
- Flow models, used to connect tubes, chambers, and other components in the machines. As the complexity of the machine increases, the permutations of the chambers that may communicate through flow increases significantly.
- Electrical motor losses and heat transfer. The machine itself is usually driven with an electrical motor (alternatively drives a generator in the case of an expander), which may in turn be cooled by suction or discharge gas.
- Mechanical losses, and the commensurate heat transfer, that arise. These include friction generated by bearings, seals, and other relative motion between parts.
- The numerical challenges that typically arise in simulating these devices (numerical stiffness, step size selection, etc.) are common to all types of positive displacement machines, as is their resolution.

As a result, a generalized positive displacement simulation tool called PDSim was developed [24] by including reciprocating and scroll machines as examples.

Up to now, there has never been a generalized simulation code developed for all types of positive displacement compressors and expanders. The code is implemented in the programming language Python with the core structure compiled in Cython and it takes advantage of the highly object orient features that allow for easy modifications and extensions. Thus, the high-level nature of Python can be maintained while obtaining computational speeds close to low-level programming such as $C++$.

The scope of this chapter is provide a background on the aforementioned framework, to extend the compressor library and core components and to demonstrate its flexibility by investigating some of the challenges involved in simulating different positive displacement machines. In particular, the following major improvements have been accomplished:

- extend the core of PDSim in order to handle two-phase expansion/compression, homogeneous oil-flooded compression/expansion, two-fluids compression/expansion;
- add vibration mode valve dynamics, detailed leakage flow models and heat transfer library;
- integrate multi-lumped overall energy balance solution scheme;
- implement an extended library of compressor and expander models, i.e., rolling-piston, multi-cylinder reciprocating, Z-compressor.

A Z-compressor will be used as an example of comprehensive compressor modeling. Furthermore, PDSim will be also used to carry on the modeling of the single-screw expander which is the object of the present work.

The development of such generalized tool will be beneficial for both teaching and research purposes on positive displacement compressors and expanders.

2.2 Systematic approach to the modeling of positive displacement compressors and expanders

As previously outlined, mechanistic models of positive displacement (PD) machines present a systematic structure that accounts for the different physical phenomena occurring inside the machine during the entire compression or expansion process. The general approach is based upon a system of conservation equations within each of the working chambers of the PD machine that is a function of the parameters of PD technology considered such as volume of the chamber, rate of change of volume and thermodynamic state. The assumptions that are made to derive such system of equations are general enough that are applicable to different types of compressors or expanders. Besides the geometric parameters that defines a certain PD machine, physical phenomena such as leakage flow, heat transfer and mechanical or friction losses along with design details, e.g.,

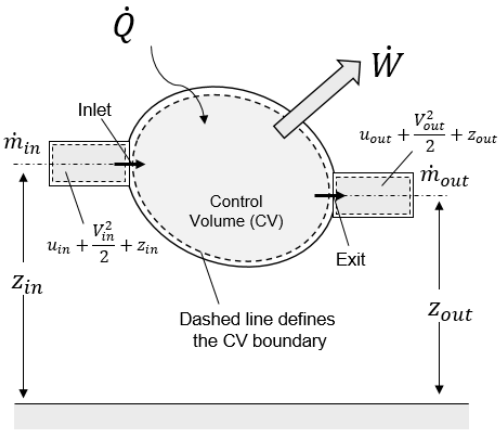

Figure 2.1: Schematic of the thermodynamic concept of a control volume. Adapted from [25].

presence of valves, hermetic or open-drive configurations, define the particular type of machine. The general structure of a compressor or expander model in PDSim is illustrated in Figure 2.2. The pseudo-code structure is not meant to be comprehensive but it serves to the purpose of highlighting the possible different modules that are needed in order to create a simulation code. As the complexity of a model can vary depending on the purpose of the simulation and the PD type, some modules may be optional as indicated by the dotted boxes.

Compression and expansion processes in PD machines are transient thermodynamic transformations. Therefore, to be studied, a system of transient conservation equations is necessary. Each working chamber is described in a thermodynamic way by means of open control volumes (CV), as shown in Figure 2.1. In each control volume, it is assumed that the thermodynamic properties are uniform which implies also quasi-equilibrium conditions. Such approach has been proven to be accurate enough to predict the performance of PD machines [2]. Non-uniformity of the thermodynamic properties within the chamber volume can be accounted for by means of Computational Fluid Dynamics (CFD) methods.

The conservation of mass for a generic control volume can be written as:

$$\frac{dm_{\mathrm{CV}}}{dt} = \sum_i \dot{m}_{\mathrm{i}} \tag{2.1}$$

where $\mathrm{m_{CV}}$ is the mass of working fluid within the chamber (or CV) and $\dot{m}_{\mathrm{i}}$ represents the mass flow rate of the *i-th* flow path entering or exiting the control volume (positive if flows into the CV). The flow interactions are usually referred to as leakage flows.

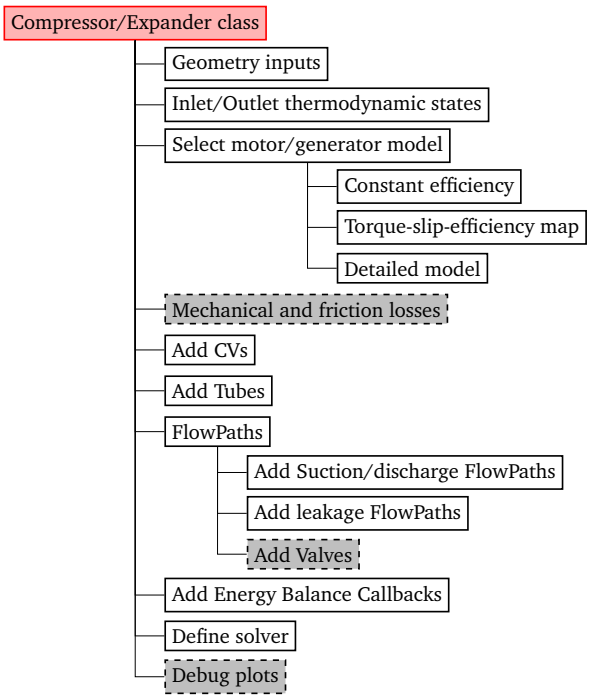

Figure 2.2: General structure of a positive displacement machine simulation code with PDSim.

The conservation of total energy is given by:

$$\frac{dE_{\mathrm{CV}}}{dt} = \dot{W}_{\mathrm{CV}} + \dot{Q}_{\mathrm{CV}} + \sum_i (\dot{m}e)_{\mathrm{i}} \tag{2.2}$$

where the first two terms on the right hand of Equation 2.2 refer to the boundary work rate of control volume and heat transfer rate of the control volume, respectively. The term $(\dot{m}e)_{\mathrm{i}}$ is associated with the energy flows across the boundaries of the CV. The total energy $\mathrm{E_{CV}}$ includes the contribution of internal energy, $\mathrm{U_{CV}}$, kinetic energy, $\mathrm{KE_{CV}}$, potential energy, $\mathrm{PE_{CV}}$ and other source terms. It is assumed that the kinetic energy of the control volume and gravitational effects are negligible compared to the effect of change in internal energy. It follows that Equation 2.2 can be rewritten as:

$$\frac{dU_{\mathrm{CV}}}{dt} = \frac{d(mu)_{\mathrm{CV}}}{dt} = \sum_i (\dot{m}h)_{\mathrm{i}} + \dot{W}_{\mathrm{CV}} + \dot{Q}_{\mathrm{CV}} \tag{2.3}$$

where $(\dot{m}h)_{\mathrm{i}}$ is the enthalpy flow term for the *i-th* flow path. In the case of positive

displacement machines, the boundary work rate term is usually given by

$$\dot{W}_{\mathrm{CV}} = -p_{\mathrm{CV}} \frac{dV}{dt} \tag{2.4}$$

where p_{CV} is pressure inside the control volume.

The system of equations developed describes a dynamic model of a PD machine that needs to be integrated over time. Such formulation is general enough that can be applied to both mechanistic models of PD machines that are crank-motion driven (e.g., reciprocating, rotary, etc.) as well as dynamic linear compressors, in which the stroke is determined by electro-mechanical forces. The dynamic simulation accounts for transients. As the integration over time progresses the system will reach a steady-periodic solution. Usually, in the case of PD machines having a crank-motion, the steady-periodic solution is of particular interest (unless transients such as start-up or shut-down are considered). The steady-periodic solution corresponds to a complete working cycle of the PD machine that is typically identified as a function of the rotation angle. For this reason, it is convenient to express the system of differential equations as function of the crank angle by recalling that $\theta = \omega t$. That is,

$$\begin{aligned} \frac{dm_{\mathrm{CV}}}{d\theta} &= \frac{1}{\omega} \sum_i \dot{m}_{\mathrm{i}} \\ \frac{d(mu)_{\mathrm{CV}}}{d\theta} &= \frac{1}{\omega} \sum_i (\dot{m}h)_{\mathrm{i}} - p_{\mathrm{CV}} \frac{dV}{d\theta} + \frac{\dot{Q}_{\mathrm{CV}}}{\omega} \end{aligned} \tag{2.5}$$

In the case of nonuniform crank rotational speed, proper equations describing the characteristics of the motor need to be coupled to the system of equations 2.5, as shown in Figure 2.2.

By analyzing the system of Equations 2.5, it can be observed that to reduce the unknowns to only two independent variables, i.e., two thermodynamic properties, additional models for the volume of the chambers, heat transfer rate and leakage interactions are necessary. Each sub-model can be defined to describe a particular machine and then the system of differential equations can be integrated simultaneously for each of the working chambers until one rotation is completed.

While present work will focus only on steady-periodic modeling of PD machines with the aim of developing the necessary theoretical background to analyze the single-screw expander, the extension of PDSim to dynamic modeling of a linear compressor can be found in Ziviani et al. [26] and Zhang et al. [27].

2.3 Control volume analysis and conservation equations

Control volume (CV) analysis applied to a PD machine requires the derivation of mathematical expressions for the conservation of mass and energy based upon the selection of two independent thermodynamic properties that fully define the thermodynamic state of the working fluid. This is true as long as pure (or pseudo-pure) fluids are considered. If lubricant oil or other secondary fluids are present within the working chamber, the CV analysis needs to be extended to fully determine the state of the homogeneous (or heterogeneous) mixture. Furthermore, during expansion or compression processes, there are situations where working fluid liquid and vapor phases are present at the same time. For example, a pure (or pseudo-pure) fluids can undergo phase-change during the expansion process, e.g., flash expansion [28], or slugging problems can occur in compressors [15]. As the working fluid becomes a liquid-vapor mixture, the governing equations should account for the change in quality. In this section, the CV analysis is extended to define proper thermodynamic governing equations that are able to be applied to the following cases of interest in PD modeling:

- Single-phase super-heated working fluid
- Two-phase working fluid
- Homogeneous mixture of working fluid and secondary fluid
- Two-fluid heterogeneous model.

2.3.1 Single-Phase governing equations

The most common set of control volume governing equations deals with dry compression or expansion processes, meaning a pure (or pseudo-pure) working fluid being compressed or expanded in the superheated region. Additionally, such model is suitable to handle vapor injection in compressors. Two independent thermodynamic properties need to be selected to derive the conservation equations of mass and energy. In literature, different thermodynamic property pairs have been adopted, such as (m, u) [29], (T, p) [16] , (v, T) [19]. Each thermodynamic pair leads to different set of property derivatives due to chain rule that has to be estimated numerically which contributes to numerical challenges. Furthermore, depending on the equation of state adopted, computational time also varies. As CoolProp library [30] is implemented in PDSim, Helmholtz equation of state (HEOS) is adopted for the majority of working fluids which explicit in temperature and density. For this reason, (T, ρ) is chosen as pair and the governing equations are explicit in temperature and total mass of the control volume. For each control

volume, the general conservation of mass equation can be written as:

$$\frac{d(\rho V)_{CV}}{d\theta} = \frac{1}{\omega}\sum_i \dot{m}_i \tag{2.6}$$

The general conservation of energy in each chamber of the compressor can be expressed as:

$$\omega\frac{d}{d\theta}(\rho u V)_{CV} = \dot{Q} + \dot{W}_{CV} + \sum_i (\dot{m}h)_i \tag{2.7}$$

where the specific internal energy is obtained as $u = h - pv$, the boundary work rate of the control volume can be expressed as $\dot{W}_{CV} = -\omega p(dV/d\theta)$ and $\dot{Q}$ is the heat transfer rate interactions between the components of the compressor chambers and the working fluid. By expanding the left hand side of Equation 2.7 according to [11], the derivative of temperature with respect to the crank angle can be obtained:

$$m_{CV}c_v\frac{dT}{d\theta} = -T\left(\frac{\partial p}{\partial T}\right)_v\left[\frac{dV}{d\theta} - v\frac{dm_{CV}}{d\theta}\right] - h\frac{dm_{CV}}{d\theta} + \frac{\dot{Q}}{\omega} + \frac{1}{\omega}\sum_i (\dot{m}h)_i \tag{2.8}$$

where the mass in the control volume is given by $m_{CV} = (\rho V)_{CV}$.

2.3.2 Single-fluid two-phase governing equations

Under the circumstances that the working fluid within the control volume is a wet vapor or undergoes flashing, temperature and quality are necessary to define the thermodynamic state. In this case, a quasi-equilibrium condition is assumed and the thermodynamic properties are calculated as mass fraction-weighted saturated two-phase mixture. Furthermore, such formulation can be applied to model slugging phenomena in compressors as well as two-phase injection or liquid injection of the same working fluid. Secondary fluids such as lubricant oil cannot be accounted for. The conservation of mass and energy given by Equations 2.5 can still be applied to the CV of the saturate two-phase mixture. However, further mathematical steps are necessary to explicit the dependency from the quality. In particular, the specific enthalpy of the working fluid is then given by:

$$h = x_g h_g + (1 - x_g)h_l \tag{2.9}$$

where the saturated properties are only functions of temperature. By differentiating the specific enthalpy with respect to temperature and quality:

$$\frac{dh}{d\theta} = \left(\frac{\partial h}{\partial T}\right)_{x_g}\frac{dT}{d\theta} + \left(\frac{\partial h}{\partial x}\right)_T\frac{dx_g}{d\theta} = \left[x_g\frac{dh_g}{dT} + (1 - x_g)\frac{dh_l}{dT}\right]\frac{dT}{d\theta} + (h_g - h_l)\frac{dx_g}{d\theta} \tag{2.10}$$

Therefore, the derivative of the specific internal energy becomes:

$$\frac{du_{CV}}{d\theta} = \frac{dh_{CV}}{d\theta} - p_{CV}\frac{dv_{CV}}{d\theta} - v_{CV}\frac{dp_{CV}}{d\theta} = \\ = \left[x_g\frac{dh_g}{dT} + (1-x_g)\frac{dh_l}{dT}\right]\frac{dT}{d\theta} + (h_g - h_l)\frac{dx_g}{d\theta} - \frac{p(\theta)}{m_{CV}}\frac{dV}{d\theta} + \frac{pV}{m_{CV}^2}\frac{dm_{CV}}{d\theta} \tag{2.11}$$

By recalling that the specific volume of the two-phase working fluid is equal to the volume to mass ratio of the working fluid, or:

$$x_g v_g + (1-x_g)v_l = \frac{V}{m_{CV}} = v_{CV} \tag{2.12}$$

and by differentiating each side with respect to the crank angle θ, the derivative of the quality with respect to the crank angle, $dx_g/d\theta$, can be obtained:

$$\frac{dx_g}{d\theta} = \frac{1}{v_g - v_l}\left\{\frac{1}{m_{CV}}\frac{dV}{d\theta} - \frac{V}{m_{CV}^2}\frac{dm_{CV}}{d\theta} - \left[x_g\frac{dv_g}{dT} + (1-x_g)\frac{dv_l}{dT}\right]\frac{dT}{d\theta}\right\} \tag{2.13}$$

Last, the derivative of the specific internal energy with respect to the crank angle is determined by substituting Equation 2.13 into Equation 2.11,

$$\frac{du_{CV}}{d\theta} = \left[x_g\frac{dh_g}{dT} + (1-x_g)\frac{dh_l}{dT} - v\frac{dp}{dT}\Big|_{sat}\right]\frac{dT}{d\theta} + (h_g - h_l)\frac{dx_g}{d\theta} \\ - \frac{p(\theta)}{m_{CV}}\frac{dV}{d\theta} + \frac{pV}{m_{CV}^2}\frac{dm_{CV}}{d\theta} \tag{2.14}$$

can be combined with the conservation of energy (Equation 2.5) and solved for $dT/d\theta$:

$$\frac{dT}{d\theta} = \frac{1}{A}\left\{\frac{dQ}{d\theta} - \frac{h_g - h_l}{v_g - v_l}\frac{dV}{d\theta} + \left(v\frac{h_g - h_l}{v_g - v_l} - h\right)\frac{dm_{CV}}{d\theta} + \sum_i (\dot{m}h)_i\right\} \tag{2.15}$$

with

$$A = m_{CV}\left[x\left(\frac{dh_g}{d\theta} - \frac{h_g - h_l}{v_g - v_l}\frac{dv_g}{d\theta}\right) + (1-x)\left(\frac{dh_l}{d\theta} - \frac{h_g - h_l}{v_g - v_l}\frac{dv_l}{d\theta}\right) - v\frac{dp}{dT}\Big|_{sat}\right] \tag{2.16}$$

2.3.3 Homogeneous mixture governing equations

In PD machines, lubricant oil (or other liquids) is often used to seal leakage gaps, reduce friction losses as well as achieve a more isothermal process [31]. If the lubricant oil and the refrigerant are in thermal and mechanical equilibrium throughout the process, a simple ideal mixture model can be used to calculate

the mixture properties which also allows to treat the mixture as a pseudo-pure fluid. While mechanical equilibrium is usually valid, the assumption of thermal equilibrium should be verified. If thermal equilibrium does not apply, mass and energy balance equations should also be included for the lubricant oil, for example in oil-injected screw compressor [32]. Such model is described in sub Section 2.3.4. By assuming thermal and mechanical equilibrium of mixture during the expanson or compression process, for each CV, the conservation of total mass, energy and lubricant oil mass are imposed. Three state variables are needed to fully fix the thermodynamic state of the mixture. The approach presented here considers temperature, total mass and oil mass fraction as the independent variables [11]. Other formulations can be considered. For example, Zaytsev [33] proposed a homogeneous model formulation using pressure, temperature liquid mass fraction for a water-ammonia wet compression process in a twin-screw compressor. The conservation of total mass for the general CV is given by:

$$\frac{dm_{CV}}{d\theta} = \frac{1}{\omega}\sum_i \dot{m}_i, \tag{2.17}$$

The conservation of oil mass is similar to Equation 2.17 but it accounts for the oil mass fraction of each flow paths of the CV:

$$\frac{dm_L}{d\theta} = \frac{1}{\omega}\sum_i (\dot{m}x_L)_i, \tag{2.18}$$

where the mass of oil in the CV can be expressed as $m_L = x_L m_{CV}$. By differentiating m_L with respect to m_{CV} and x_L and by diving by $d\theta$, the left hand side of Equation 2.17 becomes:

$$\frac{dm_L}{d\theta} = x_L\frac{dm_{CV}}{d\theta} + m_{CV}\frac{dx_L}{d\theta} \tag{2.19}$$

which yields to the conservation of oil mass fraction in differential form:

$$\frac{dx_L}{d\theta} = \frac{1}{m_{CV}}\left[\frac{1}{\omega}\sum_i \dot{m}_i x_{L,i} - x_L\frac{dm_{CV}}{d\theta}\right] \tag{2.20}$$

The specific internal energy of the CV can differentiated with respect to temperature, specific volume and oil mass fraction utilizing the chain rule:

$$du_{CV} = \frac{\partial u_{CV}}{\partial T}dT + \frac{\partial u_{CV}}{\partial v}dv + \frac{\partial u_{CV}}{\partial x_L}dx_L \tag{2.21}$$

By introducing the proper simplifications, the derivative of specific internal energy for the CV can be rearranged as:

$$du_{CV} = c_{v,mix}dT + \left[T\left(\frac{\partial p}{\partial T}\right)_v - p\right]dv + (u_L - u_g)\,dx_L \tag{2.22}$$

By expanding the left hand side term of Equation 2.5 as

$$m_{CV}\frac{du_{CV}}{d\theta}+u\frac{dm_{CV}}{d\theta}=\frac{\dot{Q}}{\omega}-p\frac{dV}{d\theta}+\frac{1}{\omega}\sum_i(\dot{m}h)_i, \tag{2.23}$$

as well as the derivative of chamber volume with respect to the crank angle as

$$\frac{dV}{d\theta}=m_{CV}\frac{dv}{d\theta}+v\frac{dm_{CV}}{d\theta} \tag{2.24}$$

and by integrating Equation 2.22, the derivative of the temperature with respect to the crank angle can be obtained:

$$\frac{dT}{d\theta}=\frac{1}{m_{CV}c_{v,mix}}\left\{-T\left(\frac{\partial p}{\partial T}\right)_v\left[\frac{dV}{d\theta}-v_{mix}\frac{dm_{CV}}{d\theta}\right]-m_{CV}(u_L-u_g)\frac{dx_L}{d\theta}\right.$$
$$\left.-h_{mix}\frac{dm_{CV}}{d\theta}+\frac{\dot{Q}}{\omega}+\frac{1}{\omega}\sum_i(\dot{m}h)_i\right\}, \tag{2.25}$$

which represents the conservation of energy in differential form [11].

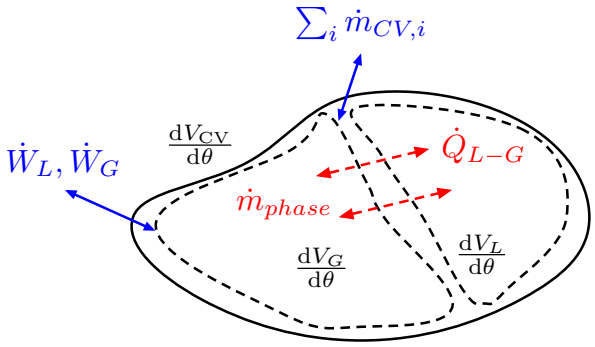

Figure 2.3: Two-fluid control volume schematic.

2.3.4 Heterogeneous model governing equations

In the general case that liquid and gas phases are at non-equilibrium conditions, a heterogeneous model formulation is required. Such model admits that the temperatures of each phase can be different as well as the concentration could different from those at equilibrium conditions, but the pressure is the same within the CV. By referring to Figure 2.3, a general CV, which corresponds to the actual geometry of the working chamber, is divided into two parts: gas phase (G)

and liquid phase (L). The volume occupied by each phase can be estimated by introducing the void fraction α [34]:

$$\alpha = \frac{1}{1 + \frac{x_L}{1-x_L} S \frac{v_L}{v_G}} \tag{2.26}$$

$$V_{CV} = \alpha V_{CV} + (1-\alpha) V_{CV} = V_G + V_L \tag{2.27}$$

where S is the slip ratio. A slip model between the phases can be introduced which requires the calculation of the fluid velocities at the interface. If mechanical equilibrium is enforced, then slip ratio is equal to unity. The gas volume derivative with respect to the crank angle is obtained as:

$$\frac{dV_G}{d\theta} = \frac{dV_{CV}}{d\theta} - \frac{dV_L}{d\theta} \tag{2.28}$$

where dV_{CV} is known from the control volume geometry. The volume of the liquid phase needs to be calculated.

Separate governing equations are required for each phase along with sub-models for heat and mass transfer between the phases, heat transfer between each phase and the CV boundary walls as well as flow models, as described by Zaytsev [33]. The conservation of mass for the gas phase is given as:

$$\frac{dm_G}{d\theta} = \frac{1}{\omega} \left[\sum_i \dot{m}_{G,i} + \frac{dm_{\text{phase}}}{d\theta} \right] \tag{2.29}$$

where dm_G is the variation of total gas phase mass in the CV, $\dot{m_{G,i}}$ is the mass flow rate of gas in and out the CV and m_{phase} is the mass of gas that is evaporating from the liquid phase (positive) or condensing from the gas phase (negative). Similarly, the conservation of mass for the liquid phase presents the same form:

$$\frac{dm_L}{d\theta} = \frac{1}{\omega} \left[\sum_i \dot{m}_{L,i} - \frac{dm_{\text{phase}}}{d\theta} \right] \tag{2.30}$$

Since the model is heterogeneous, besides the conservation of mass, also the conservation of concentration needs to be added for each of species, e.g., refrigerant and liquid. The conservation of concentrations can be expressed in a general form as:

$$\frac{d(mx)_{\text{ref}}}{d\theta} = \frac{1}{\omega} \left[\sum_i (\dot{m}x)_{\text{ref,i}} + \frac{dm_{\text{ref,phase}}}{d\theta} \right], \tag{2.31}$$

and

$$\frac{d(mx)_{\text{liq}}}{d\theta} = \frac{1}{\omega} \left[\sum_i (\dot{m}x)_{\text{liq,i}} + \frac{dm_{\text{liq,phase}}}{d\theta} \right] \tag{2.32}$$

where the subscripts *ref* and *liq* refer to refrigerant and liquid, respectively. The terms $dm_{\text{ref,phase}}$ and $dm_{\text{liq,phase}}$ represent the mass of refrigerant and liquid

evaporated or condensed which depend on the equilibrium concentration of the saturated refrigerant gas at liquid temperature and the equilibrium concentration of saturated liquid at gas temperature. At this point, the derivative of the liquid volume dV_L can be conveniently expanded to explicit the dependency from liquid phase temperature T_L and concentration x_L. In particular,

$$\frac{dV_L}{d\theta} = v_L \frac{dm_L}{d\theta} + m_L \frac{dv_L}{d\theta} \tag{2.33}$$

By assuming that the specific volume of liquid does not depend on pressure and by introducing proper expressions for dm_L and dv_L, Equation 2.33 results in:

$$\frac{dV_L}{d\theta} = v_L \left[\sum_i \left(\frac{dm_L}{d\theta} \right)_i - \frac{dm_{\text{phase}}}{d\theta} \right] + m_L \left[\left(\frac{\partial v_L}{\partial T_L} \right)_x \frac{dT_L}{d\theta} + \left(\frac{\partial v_L}{\partial x_L} \right)_T \frac{dx_L}{d\theta} \right] \tag{2.34}$$

The conservation of energy for the gas phase and liquid phase can be written as:

$$\frac{d(mu)_G}{d\theta} = \frac{1}{\omega} \left[\sum \dot{Q}_{G,b} + \sum_i (\dot{m}h)_{G,i} + h_G^{"} \frac{dm_{\text{phase}}}{d\theta} + \sum \dot{W}_{G,b} - \dot{Q}_{G-L} \right] \tag{2.35}$$

$$\frac{d(mu)_L}{d\theta} = \frac{1}{\omega} \left[\sum \dot{Q}_{L,b} + + \sum_i (\dot{m}h)_{L,i} + h_G^{"} \frac{dm_{\text{phase}}}{d\theta} + \sum \dot{W}_{L,b} + \dot{Q}_{G-L} \right] \tag{2.36}$$

where for each of the phases $\dot{Q}_b$ is heat transfer rate through the boundary of the control volume, $\dot{W}_b$ is the boundary work rate, $\dot{Q}_{G-L}$ is heat transfer rate between the two phases and it is considered positive transferred from gas to liquid and $h_G^{"}$ is the specific enthalpy of the saturated gas at liquid temperature and equilibrium concentration. Equation 2.35 and Equation 2.36, can be reworked to obtain the expressions for $dT_G/d\theta$ and $dT_L/d\theta$. Furthermore, the boundary work rate of each phase can be expressed as $V_G(dp/d\theta)$ and $V_L(dp/d\theta)$.

Equations 2.28, 2.29, 2.30, 2.31, 2.32, 2.34, 2.35, 2.36 are the governing equations of the heterogeneous model to be solved simultaneously.

The heterogeneous model can be applied to the case in which the liquid phase is a lubricant oil and the gas phase is the refrigerant. with the following assumptions :

- the refrigerant (G) can change phase and the saturated vapor and liquid phases are denoted as g and l, respectively;
- refrigerant and lubricant oil are treated as separate fluids. Oil-refrigerant interaction occurs through heat transfer. The flashing of oil is neglected. Mass transfer can be considered if a correlation for the solubility is available;
- refrigerant and oil thermodynamic states are homogeneous throughout the control volume at any moment;
- the kinetic and potential energy term are neglected. Therefore, the total energy of the control volume is $E_{CV} \simeq (mu)_{CV}$.

The lubricant oil is treated as incompressible and in mechanical equilibrium with the refrigerant. The volume of oil within the CV is obtained by integrating the conservation of mass for the oil [35]:

$$\frac{dV_L}{d\theta} = \frac{1}{\rho_L \omega} \sum_i \dot{m}_{L,i} \tag{2.37}$$

where $\dot{m}_{L,i}$ is the oil mass flow rate through the *i-th* flow path in or out the CV. The refrigerant volume is calculated as a difference between the total geometric volume of the CV and oil volume as:

$$V_G = V_{CV} - V_L \tag{2.38}$$

An example of two-phase expansion of R245fa and lubricant oil ACD100FY with a single-screw expander is proposed. The expander inlet conditions were specified in terms of temperature and quality, 100 °C and 0.6. The lubricant oil mass fraction was set to 0.05. The results of the two-phase expansion are shown in Figure 2.4. At each step size taken by the solver, the quality of the working fluid is updated by considering the actual volume occupied by the working fluid and its mass:

$$x_g = \frac{\frac{V_G}{m_G} - v_{G,l}}{v_{G,g} - v_{G,l}} \tag{2.39}$$

If $x_g < 0$ or $x_g > 1$, the working fluid is considered subcooled or superheated, respectively. Once x_g is calculated, its derivative $dx_g/d\theta$ can be evaluated. The evolution of pressure and quality with respect to of the crank angle are reported in the top-left chart of Figure 2.4. During the expansion process, the quality of R245fa increases from 0.60 to 0.87 which corresponds to a specific volume ratio of approximately 17. Thus, the majority of the quality change occurs during the filling process and at the beginning of the closed expansion. As a result, the built-in volume ratio of the machine needs to be lower than the expansion volume ratio to avoid over-expansion and other internal losses. In the case of twin-screw machines, Smith et al. [36] reported that the built-in volume ratio should be around 20-30% of the overall expansion volume ratio. Under the considered two-phase expansion conditions, shown in the T-s diagram (top-right chart of Figure 2.4), the built-in volume ratio of the single-screw expander should be between 3.4 and 5.1. This result is in line with the geometry of the existing expander showing potential to explore two-phase expansion and partial-evaporating ORC.

The chamber model has the ability to estimate the temperature evolution of both working fluid and lubricant oil. Different models of heat transfer term $\dot{Q}_{L-G}$ can be applied depending on the data availability, oil-injection parameters etc. [37] . In this case, the oil is pre-mixed with the working fluid prior entering the expander by means of a static mixer. Ideally, the static mixer creates an homogeneous fluid structure and therefore it is reasonable to assume an average oil droplet size to

estimate the heat transfer. The heat transfer coefficient at the oil droplet surface is given by:

$$h_{L-G} = \frac{k_L}{D_{d,L}} \left[2 + 0.6\mathrm{Re}^{0.6}\mathrm{Pr}^{0.33}\right] \tag{2.40}$$

where k_L is the thermal conductivity of the oil, $D_{d,L}$ is the mean oil droplet diameter, Re and Pr represent the Reynolds and Prandtl numbers for the oil, respectively. In particular, the Prandtl number is calculated by knowing the thermophysical properties of the oil. Whereas the Reynolds number is approximated by considering the mean oil droplet diameter and the average peripheral speed of the groove (a similar approach was used by Stosic et al. [29, 37]). In this case, mixing phenomena occurring inside the groove are not considered since the aim of the example is to show the capabilities of the two-fluid model. More detailed studies could be conducted to actually evaluate the correct definition of the Reynolds number of the oil within a groove of the single-screw expander. The thermal behaviors of the working fluid and the oil droplet are shown in Figure 2.4. The thermal inertia of the two fluids is different and the temperature drop experienced by the working fluid is significantly higher under the two-phase conditions. However, the expansion process in the single-screw is quite fast (pressure variations are in the order of 8-9 ms/cycle) and in order to account for phenomena such heat transfer between oil and working fluid as well as oil and the chamber walls, more accurate equations should be developed based on experimental results. The chamber model is general enough to account for primary and secondary thermal effects.

2.4 Tube models

A tube is a component of the simulation that allows for pressure drop and heat transfer. It is modeled as being quasi-steady, and either the outlet or the inlet state is fixed. The following assumptions are employed:

- steady-state and steady flow;
- fixed wall temperature, fixed wall heat transfer flux, or user-defined heat transfer model;
- viscous effects present.

The calculation of the pressure drop through the tube depends on the phase of the working fluid. At first single-phase flow is considered. The flow through the tubes is generally turbulent, and thus the friction factor can be given by the form from Churchill [38],

$$f = 8\left[(8/\mathrm{Re})^{12} + (A+B)^{-1.5}\right]^{\frac{1}{12}} \tag{2.41}$$

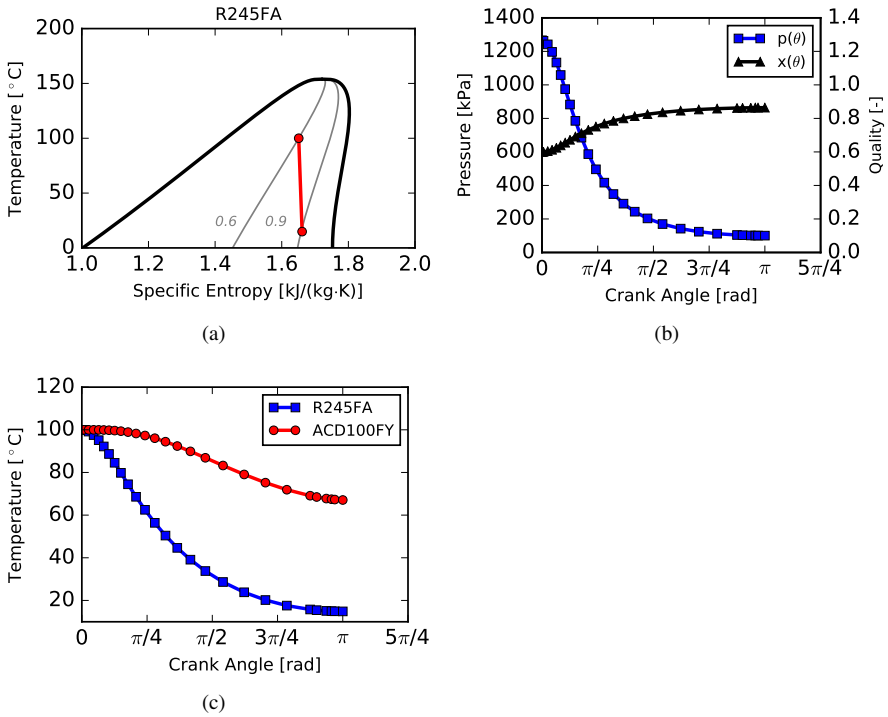

Figure 2.4: Example of two-phase expansion of R245fa with lubricant oil ACD100FY with the following boundary conditions: T_{su} = 100 °C, $x_{g,su}$=0.6, p_{ex} = 150 kPa, x_L = 0.05. The mean oil droplet size is 50 µm.

$$A = \left(2.457 \ln\left[(7/\mathrm{Re})^{0.9} + 0.27\,(\epsilon/D)\right]^{-1}\right)^{16} \tag{2.42}$$

$$B = (37530/\mathrm{Re})^{16}\,. \tag{2.43}$$

The heat transfer coefficient can be given by the equation of Gnielinski [39],

$$\alpha = \frac{k}{D}\frac{(f/8)(\mathrm{Re}-1000)\mathrm{Pr}}{1+12.7\sqrt{f/8}(\mathrm{Pr}^{2/3}-1)}. \tag{2.44}$$

The properties are evaluated at the known state. The Reynolds number is given by $\mathrm{Re} = GD/\mu$, where G is the mass flux given by $G = \dot{m}_{\mathrm{tube}}/A_{\mathrm{tube}}$ and A_{tube} is the cross-sectional flow area of the tube given by $A_{\mathrm{tube}} = \pi D^2/4$. If the inlet state of the tube is given and the wall temperature is known, the outlet temperature can be calculated from

$$T_{\mathrm{out}} = T_{\mathrm{wall}} - (T_{\mathrm{wall}} - T_{\mathrm{in}})\exp\left(-\frac{\pi D L \alpha}{\dot{m}_{\mathrm{tube}} c_{\mathrm{p}}}\right) \tag{2.45}$$

and the change in pressure by

$$\Delta p = -\frac{fG^2L}{2\rho D}, \tag{2.46}$$

which yields the outlet pressure of $p_{\mathrm{out}} = p_{\mathrm{in}} + \Delta p$.

If instead the outlet state is known, the inlet temperature can be calculated from Equation 2.45. The inlet pressure is calculated from $p_{\mathrm{in}} = p_{\mathrm{out}} - \Delta p$.

In the case of two-phase conditions through the tube, the frictional pressure drop gradient is calculated by using Lockhart-Martinelli [34] correlation which is a function of the quality. In particular, the frictional pressure drop based on the actual flow for each phase is given by

$$-\left(\frac{\mathrm{d}p}{\mathrm{d}z}\right)_l = \frac{2f_lG^2(1-x)^2v_l}{D} \tag{2.47}$$

$$-\left(\frac{\mathrm{d}p}{\mathrm{d}z}\right)_g = \frac{2f_gG^2x^2v_g}{D} \tag{2.48}$$

where f_l and f_g are the friction coefficients for each phase. Once the Lockhart-Martinelli parameter, X, is calculated along with the gas phase and liquid phase multipliers, ϕ_l and ϕ_g, the pressure drop gradient is calculated as:

$$-\left(\frac{\mathrm{d}p}{\mathrm{d}z}\right)_{f,2\phi} = \begin{cases} -\left(\frac{\mathrm{d}p}{\mathrm{d}z}\right)_g \phi_g & -\left(\frac{\mathrm{d}p}{\mathrm{d}z}\right)_g \phi_g > -\left(\frac{\mathrm{d}p}{\mathrm{d}z}\right)_l \phi_l \\ -\left(\frac{\mathrm{d}p}{\mathrm{d}z}\right)_l \phi_l & -\left(\frac{\mathrm{d}p}{\mathrm{d}z}\right)_g \phi_g < -\left(\frac{\mathrm{d}p}{\mathrm{d}z}\right)_l \phi_l \end{cases} \tag{2.49}$$

Thus, the average frictional pressure drop over a range of qualities $[x_1, x_2]$,

$$\overline{\Delta_{f,2\phi}} = \frac{1}{x_2 - x_1}\int_{x_1}^{x_2} -\left(\frac{\mathrm{d}p}{\mathrm{d}z}\right)_{l,2\phi} dx \tag{2.50}$$

is obtained by integrating Equation 2.49 with Simpson's rule.

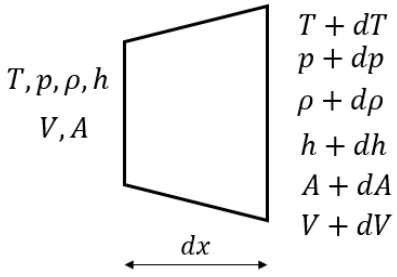

Figure 2.5: Differential element of a general leakage path (Adapted from Bell et el. [40]).

2.5 Flow path models

By referring to the general structure of positive displacement machine in Figure 2.2, after defining the control volumes and tubes, flow paths are required to connect different nodes within each element. These flow nodes could be control volumes, or they could be the inlet or an outlet for a tube section. In a flow path, the upstream state is fully specified and, in general, the downstream pressure is known. The flow path model is then used to predict the mass flow rate through the flow path. For certain path having a gap δ_{gap} and hydraulic diameter $D_{\mathrm{h,path}}$, as shown in Figure 2.6, the functional form of a general mass flow model is given as,

$$\dot{m}_{\mathrm{path}} = f\left(T_{\mathrm{up}}, p_{\mathrm{up}}, p_{\mathrm{down}}, C_{\mathrm{flow}}, A_{\mathrm{path}}\left(\delta_{\mathrm{gap}}, D_{\mathrm{h,path}}\right)\right) \tag{2.51}$$

where C_{flow} is a flow coefficient. Two flow path modeling aspects are of particular interest: leakage flows and valve models which will be described in Section 2.5.1 and Section 2.5.2.

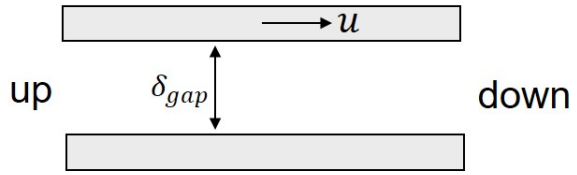

Figure 2.6: Schematic of a flow path.

2.5.1 Flow models

There is a wide range of flow models that can be employed for a flow path. Flow models are used to describe suction and discharge processes as well as leakage flows. The flow model selected for a particular flow path depends on the geometry, flow type, and other parameters such if the flow can be treated compressible flow or not. Modeling leakage flows is usually of particular challenge because the gaps are not constant and the flow is compressible, frictional and flow path has variable area and length. The flow paths are usually relatively long compared to the cross-sectional area. Moreover, lubricant oil can also be present in gaps. It is of general practice to adopt simple models such the isentropic nozzle model to calculate mass flow rates through paths. However, such simple models lead to discrepancies when compared to more detailed leakage flow models. For the isentropic compressible nozzle model, the fluid through a path is treated as an ideal gas with compressibility taken into account without friction. Upstream temperature and pressure, downstream pressure and throat area are usually known and the model is used to predict the mass flow rate. The mass flow rate from the

isentropic nozzle model is given by

$$\dot{m}_{\text{nozzle}} = A_{\text{thr,nozzle}}\sqrt{p_{\text{up}}\rho(T_{\text{up}}, p_{\text{up}})}\sqrt{\frac{2k}{k-1}\left(p_{\text{r}}^{2/k} - p_{\text{r}}^{(k+1)/k}\right)} \tag{2.52}$$

where $k = c_p/c_v$ is evaluated at the upstream conditions, and the pressure ratio, p_r is obtained as function of the critical pressure ratio that yields sonic conditions at the nozzle throat:

$$p_r = \begin{cases} p_{\text{r,crit}} & \text{if } p_{\text{down}}/p_{\text{up}} \leq p_{\text{r,crit}} \\ p_{\text{down}}/p_{\text{up}} & \text{if } p_{\text{down}}/p_{\text{up}} > p_{\text{r,crit}} \end{cases} \tag{2.53}$$

with

$$p_{\text{r,crit}} = \left(1 + \frac{k-1}{2}\right)^{k/(1-k)} \tag{2.54}$$

To improve the leakage flow predictions, a detailed 1-D flow with friction analysis can be employed to obtain mass flow rate estimations across each path. By considering the differential element dx along a general leakage path as shown in Figure 2.5, the conservation equations of mass, momentum and energy, can be coupled together. Under the assumptions of no heat transfer and mass transfer across the boundary of the differential element, no oil, compressible flow with real gas properties, a general expression for the system of differential equations along the leakage path can be expressed as [17, 40]:

$$\begin{bmatrix} 0 & 0 & 1/V & 0 & 1/\rho \\ 0 & 1 & \rho V & 0 & 0 \\ 0 & 0 & V & 1 & 0 \\ -\left(\frac{\partial h}{\partial T}\right)_\rho & 0 & 0 & 1 & -\left(\frac{\partial h}{\partial \rho}\right)_T \\ -\left(\frac{\partial \rho}{\partial T}\right)_\rho & 1 & 0 & 0 & -\left(\frac{\partial p}{\partial \rho}\right)_T \end{bmatrix} \begin{bmatrix} dT/dx \\ dp/dx \\ dV/dx \\ dh/dx \\ d\rho/dx \end{bmatrix} = \begin{bmatrix} -\frac{1}{A}\frac{dA}{dx} \\ -\frac{\rho V^2}{2}\frac{4f_F}{D_h} \\ 0 \\ 0 \\ 0 \end{bmatrix} \tag{2.55}$$

where f_F is the Fanning friction factor for flow between infinite plates [40] and V is the mean fluid velocity.

For a general leakage path having a flow area expressed as

$$A = 2\pi\delta_{\text{gap}}x \tag{2.56}$$

with x varying between two radii r_1 and r_2, it is possible to compare the isentropic nozzle flow model with the detailed 1-D flow model with friction. The calculation is performed by selecting two working fluids, in this case Nitrogen and R245fa, and by fixing upstream pressure and temperature values and gap size. A downstream pressure is varied by carrying out a sweep of the pressure ratio. The results are shown in Figure 2.7. To be noted is that, in both cases, the

isentropic flow model over predicts significantly the mass flow rate through the leakage path. Thus, the use of correction flow coefficients become important to fine tune a mechanistic model of a compressor or expander. However, in most cases, the isentropic flow model is not the most suitable to model leakage flows.

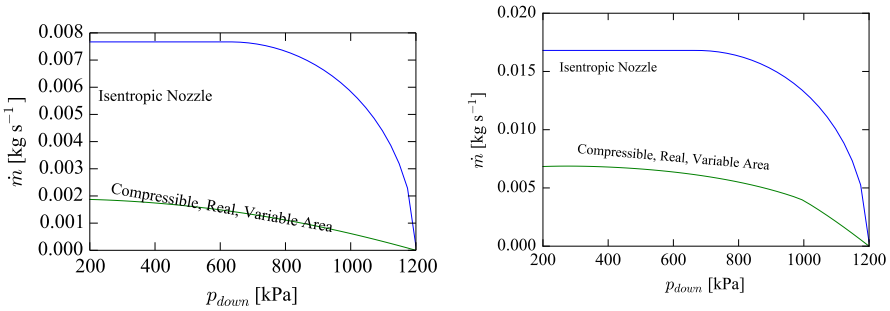

Figure 2.7: Comparison between mass flow predictions through a 10 µm gap: (a) Nitrogen;(b) R245fa.

As several leakage paths can be identified in a positive displacement machine, solving the system of Equations 2.55 within a comprehensive model would result in possible numerical issues with convergence as well as significantly higher computational time. These numerical issues are solved by determining the correction factor between the mass flow rate of leakage using the detailed flow with friction model and the mass flow rate predicted using an isentropic flow model. For a given configuration, the ratio of the isentropic nozzle mass flow rate prediction to that of the detailed model is defined by

$$M = \frac{\dot{m}_{\text{nozzle}}}{\dot{m}_{\text{fr}}} = f\left(Re, L^*, \delta^*\right) \tag{2.57}$$

where the dimensionless characteristic length and dimensionless gap width are given by $L^* = L/L_0$ and $\delta^* = \delta/\delta_0$ with L_0 and δ_0 being the reference length and gap width values. For a given path, the detailed model can be used to generate a large amount of mass flow predictions for different gap sizes, boundary conditions and working fluids upon which a correlation can be fitted. An example of generated points is shown in Figure 2.8.

In PDSim, both the isentropic flow model and flow model with friction are implemented. In Table 2.1,a list of single phase flow models that have been used in the past in literature is proposed.

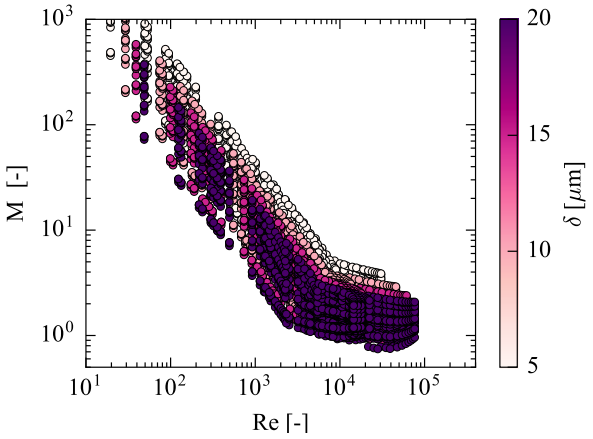

Figure 2.8: Generated points for Nitrogen, CO_2, R134a, R410A, R245fa.

2.5.2 Valve Models

In some machine types, valves are required to ensure that the flow goes in the desired direction (e.g., piston compressors and expanders). In others (e.g., high pressure-ratio scroll compressors), valves are employed to reduce the re-expansion losses due to under-compression.

There are a number of different types of valves that exist in positive displacement machines, the most common type are dynamic reed valves because they are straightforward to fabricate. Kinematic valves (poppet valves) driven by the kinematics of the machine are also possible; kinematic valves are more straightforward to analyze as their opening and closing profiles are deterministic and are not governed by dynamics.

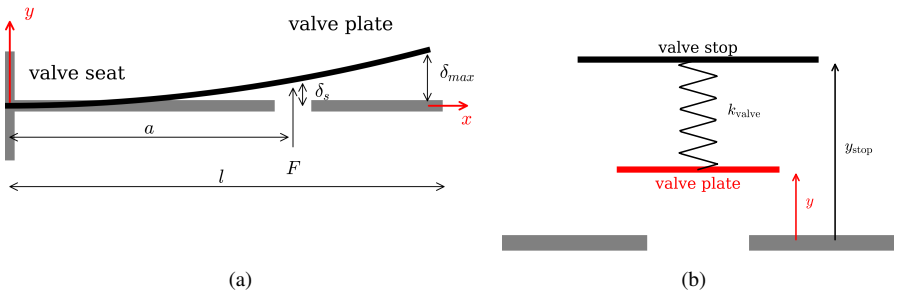

Figure 2.9: (a) Schematic of a reed valve (adapted from [27]); (b) Schematic of a plate valve.

Both poppet or plate valves and reed valves can be be described as a

Type	Reference	Compressible	Friction	Notes
Isentropic nozzle	[40]	Yes	No	Most common model, overpredicts flow rate, simple to implement
Incompressible pipe flow	[41]	No	Yes	
Fanno flow	[42]	Yes	Yes	
Couette flow	[16]	Yes	Yes	
Nozzle/Fanno combination	[43]	Yes	Yes	
Two-phase compressible flow	[34]	Yes	Yes	
Superposition method	[44]	No	Yes	
Hybrid leakage	[40]	Yes	Yes	Very computationally efficient, intended only for leakage

Table 2.1: List of some flow models used in literature

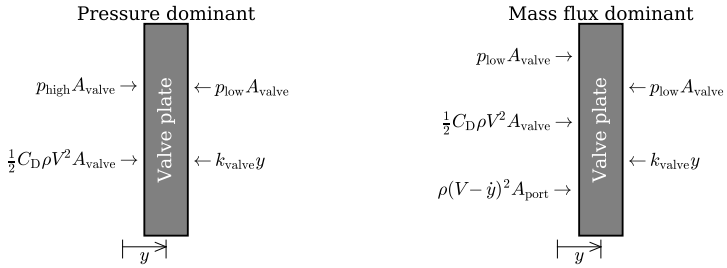

Figure 2.10: Free-body-diagrams for the valve plate of a dynamic reed valve in pressure-dominant and mass-flux dominant modes.

one-degree-freedom system as seen in Figure 2.9(a) and Figure 2.9(b) [12, 13]. However, such method may not be accurate enough in the case of reed valve since the valve deformation may not be the same in each part of the valve. A forced-vibration method can be adopted to describe the dynamics of reed valves [45, 46]. Both approaches are integrated within PDSim and further described in this section.

Reed valves are most often analyzed as one-degree-of-freedom, lumped element, vibrational systems. The reed valve is modeled as an equivalent lumped mass on a rigid plate for which the general equation of motion given by

$$m_{\text{valve}}\ddot{y} + c\dot{y} + k_{\text{valve}}y = \text{F}(t) \tag{2.58}$$

where m_{valve} is the equivalent mass of the reed valve, c is a damping factor, k_{valve} is the equivalent spring stiffness, and $\mathrm{F}(t)$ is the force on the valve exerted by the flow. The equivalent mass of the valve is related to the valve stiffness and its natural frequency ω_n:

$$m_{\mathrm{valve}} = \frac{k_{\mathrm{valve}}}{\omega_n^2} \tag{2.59}$$

The formulation of the natural frequency can be chosen according to the valve type and the natural modes of vibrations of the valve plate [45–47].

Two modes of operation are considered, i.e., mass-flux dominant or pressure dominant, and the free-body-diagrams for the valve plate in each mode are shown in Figure 2.10. The summation of the forces in the y direction gives the forcing term $\mathrm{F}(t)$ in Equation 2.58. The transition between the mass-flux-dominant and pressure dominant domains can be determined from the transitional displacement

$$y_{\mathrm{tr}} = \frac{1}{4}\frac{D_{\mathrm{port}}^2}{D_{\mathrm{valve}}} \tag{2.60}$$

where D_{valve} is the valve width or valve diameter in the case of a circular reed valve. If $y > y_{\mathrm{tr}}$, the valve is operating in the pressure dominant mode, otherwise in the mass-flux dominant mode.

The second-order differential equation in y that governs the valve motion can be decoupled into two differential equations, one for y and another for $\dot{y}$, where $\dot{y}$ is the time-derivative of y [12, 48]. The derivatives of y and $\dot{y}$ are needed for the cycle integrator as described below. Therefore, it is only necessary to obtain $\ddot{y}$ in each domain as the derivative of y is simply $\dot{y}$.

In the mass flux dominant domain, the time derivative of $\dot{y}$ is given by

$$\ddot{y} = \frac{\frac{1}{2}C_{\mathrm{D}}\rho \mathrm{v}^2 A_{\mathrm{valve}} + \rho(\mathrm{v}-\dot{x})^2 A_{\mathrm{port}} - k_{\mathrm{valve}} y}{m_{\mathrm{valve}}} \tag{2.61}$$

and in the pressure dominant domain, the time derivative of $\dot{y}$ is given by

$$\ddot{y} = \frac{\frac{1}{2}C_{\mathrm{D}}\rho \mathrm{v}^2 A_{\mathrm{valve}} + (p_{\mathrm{high}} - p_{\mathrm{low}})A_{\mathrm{valve}} - k_{\mathrm{valve}} y}{m_{\mathrm{valve}}} \tag{2.62}$$

The flow velocity v is calculated with the equation for isentropic flow of a compressible ideal gas through a nozzle with throat diameter equal to valve port diameter (velocity is calculated as though the valve plate was not present). The valve is usually constrained by two rigid bodies, the valve seat and the valve stop. If the integration leads to $y < 0$ or $y > y_{\mathrm{stop}}$, the displacement of the valve is set to 0 or y_{stop}, respectively.

The reed valve can be treated as a cantilever beam and its dynamics is characterized by the vibration of the valve plate. By considering the schematic of Figure 2.11, the valve plate is modeled as a beam with a varying width for

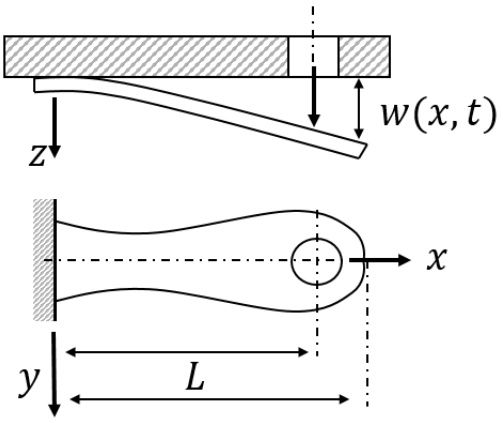

Figure 2.11: Schematic of reed valve described as cantilever beam.

which shear and rotational motion are neglected [46]. Since a plate can be referred to as a shell of zero curvature, shell equations of motion can be applied to the reed valve. In particular, the third equation of motion relates the transverse forces to the deflection. Since twisting of the valve is neglected, i.e., $\partial/\partial y = 0$, the equation of motion for a transversely vibrating beam reduces to [46]:

$$EI\frac{\partial^4 w}{\partial x^4} + \rho A\ddot{w} = q^{'} \tag{2.63}$$

where E is the Young's modulus, I is the moment of inertia of the beam cross-section, ρ is the density of the beam material, A is the beam cross-sectional area and $q^{'}$ is the load per unit length. In order to obtain the transverse displacement $w(x,t)$ which depends on both position and time, proper boundary conditions need to be applied on each edge of the valve. As analytic solutions are difficult to obtain, it is convenient to write the solution in terms of all the natural modes. Thus, the solution of Equation 2.63 can be expressed as the combination of infinite modal series:

$$w(x,t) = \sum_{m=1}^{\infty} q_m(t)\phi_m(x) \tag{2.64}$$

where $\phi_m(x)$ is the valve shape function or natural vibration mode which can be determined from free vibration analysis on a beam and $q_m(t)$ is the generalized coordinate or mode participation factor which can be obtained by integrating the valve dynamics governing equation or from an analytic solution. The m-th natural vibration mode is given by

$$\phi_m(x) = cosh\left(\frac{\lambda_m x}{L}\right) - cos\left(\frac{\lambda_m x}{L}\right) - \alpha_m\left[sinh\left(\frac{\lambda_m x}{L}\right) - sin\left(\frac{\lambda_m x}{L}\right)\right] \tag{2.65}$$

where L is the length of the reed valve and α_m is calculated as

$$\alpha_m = \frac{cosh\lambda_m + cos\lambda_m}{sinh\lambda_m + sin\lambda_m} \tag{2.66}$$

From free vibration analysis, the natural frequency equation

$$cos\lambda_m cosh\lambda_m + 1 = 0 \tag{2.67}$$

has roots $\lambda_{m=1} = 1.875$, $\lambda_{m=2} = 4.694$, $\lambda_{m=3} = 7.855$, etc. By substituting Equation 2.64 inside Equation 2.63 and by applying the condition of orthogonality effect of natural modes, the summations are eliminated by integrating the resulting equation along x, the equation of motion of the generalized coordinate $q(t)$ is obtained:

$$\ddot{q}_m + 2\zeta\omega_m\dot{q}_m + \omega_m^2 q_m = F_m \tag{2.68}$$

with

$$\omega_m = \frac{\lambda_m^2}{L^2}\sqrt{\frac{EI}{\rho A}} \tag{2.69}$$

$$\zeta = \frac{\lambda_m}{2rhoh\omega_m} \tag{2.70}$$

$$F_m = \frac{F_{\text{valve}}}{\rho A \int_x \phi_m^2(x)dx} \tag{2.71}$$

where h is the thickness of the valve, and F_{valve} is the flow force acting on the valve. Equation 2.68 is integrated over time along with the system of equations 2.5 to obtain the transverse displacement of the valve. The valve flow area is determined by

$$A_{\text{valve}} = \pi d_{\text{valve}} w_{\text{valve}} \tag{2.72}$$

As for the one-degree-freedom method, the the vibration valve analysis has two flow dominant regions, pressure dominant region and mass flux dominant region which are identified by the transitional valve plate lift [12]. The mass flow rate through the valve port is calculate by assuming isentropic compressible flow and by applying a proper flow coefficient.

2.6 Overall energy balance

Inside a positive displacement machine, both compression and expansion processes involve a working fluid at relatively high temperature that interacts with the walls of the working chambers as well as with different elements of the shell. In addition, friction losses, motor losses and other forms of mechanical or electrical energy are converted into thermal energy. However, since the structure of the PD machine can be complicated, the temperature distribution inside the

shell is subjected to spatial and temporal variations. Studying the overall heat exchange network inside a compressor or expander is of particular interest in order to accurately predict the performance of the machine. Moreover, some of heat transfer phenomena such as heating up of the suction gas in a compressor can be critical with respect to the decrease in volumetric efficiency.

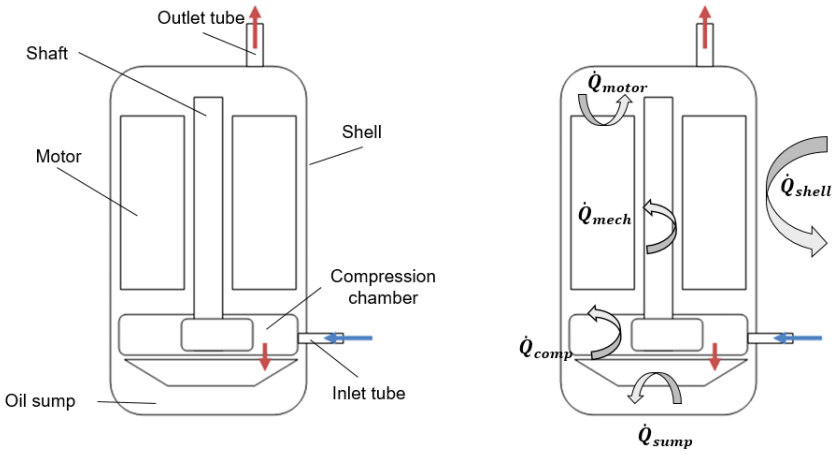

Figure 2.12: Schematic of a general PD compressor and its thermal interactions.

In order to proceed on developing an overall energy balance model, a general compressor schematic and its thermal interactions is considered as an example and it shown in Figure 2.12. In particular, the case of an hermetic compressor is proposed as it includes also the thermal effects associated with the electric motor. In order to simplify the overall heat transfer analysis, the spatial variations of temperatures within the different compressor elements are neglected which implies assuming that thermal gradients inside each solid or oil are relatively small compared to the average temperatures. It follows that temperatures associated with each compressor elements are uniform at any instant during the transient process. Such approach is usually referred to as the lumped capacitance method [49]. By using the lumped capacitance method, a lumped temperature is assigned to each of the compressor components. By referring to Figure 2.12, the following lumped temperatures can be identified:

- T_{comp}: bulk temperature of compressor (working chamber external walls and shaft);
- T_{oil}: bulk temperature of the oil in the sump;
- T_{shell}: bulk temperature of the compressor shell;
- $T_{\mathrm{gas-shell}}$: bulk temperature of the gas within the compressor shell;
- T_{motor}: bulk temperature of the motor. It could be split into stator and rotor,

if a detailed motor model is available.

- $T_{\mathrm{pipe,suc}}$: bulk temperature of the suction pipe;
- $T_{\mathrm{pipe,dis}}$: bulk temperature of the discharge pipe.

Three different heat transfer modes can occur inside a compressor: (i) convection due to gas and oil circulation as well ambient air around the shell ; (ii) conduction between components that are connected and (iii) radiation from internal components to the shell and from the shell to the surroundings. The conservation of energy at any instant of time for each lumped thermal mass can be written as [49]:

$$\frac{d\left(C_{\mathrm{lump}}T_{\mathrm{lump}}\right)}{dt} = \sum_i \left(\dot{Q}_{\mathrm{lump,in,i}} - \dot{Q}_{\mathrm{lump,out,i}}\right) + \dot{Q}_{\mathrm{lump,gen}} \tag{2.73}$$

where C_{lump} is the lumped thermal capacitance, $\dot{Q}_{\mathrm{lump,gen}}$ is the heat rate added to the lump for example by friction losses, and summation term accounts for the thermal interactions between the different lumped elements by means of a heat flow diagram of thermal resistances, as shown in Figure 2.13. The thermal capacitance is usually calculated as $C_{\mathrm{lump}} = c_{\mathrm{p,lump}} m_{\mathrm{lump}}$. Moreover, the lumped masses are usually constant with the exception of the gas and the variation of the specific heat of each material can be neglected. The general heat transfer rate term is expressed as:

$$\dot{Q}_{\mathrm{lump}} = \frac{T_{\mathrm{lump,a}} - T_{\mathrm{lump,b}}}{R_{\mathrm{ab}}} \tag{2.74}$$

where $T_{\mathrm{lump,a}} - T_{\mathrm{lump,b}}$ is the temperature difference between two lumped elements and R_{ab} is the heat transfer thermal resistance. The thermal resistance can be either obtained from experimental data (see examples of scroll [50] and rotary rolling piston [51] compressors) or from empirically correlated average Nusselt numbers for different heat transfer types [52].

It is important to notice that Equation 2.73 describes each compressor lumped temperature as a transient process. However, in most cases, only the steady-state lumped temperatures are of interest. For this reason, it is common practice to drop the time dependent term of Equation 2.73 which reduced to:

$$\sum_i \left(\dot{Q}_{\mathrm{lump,in,i}} - \dot{Q}_{\mathrm{lump,out,i}}\right) + \dot{Q}_{\mathrm{lump,gen}} = 0 \tag{2.75}$$

From the thermal network of resistances, a system of equations can be obtained where the lumped temperatures are the unknowns. Numerical methods to solve the overall energy balance within the overall simulation code are described in Section 2.7.

The overall energy balance can be further simplified by grouping all the elements of the compressor (or expander) into one lumped mass on which an energy balance is enforced. An example of single lumped temperature is shown in

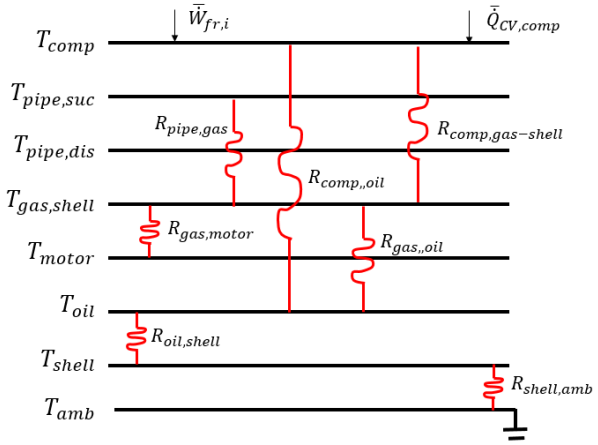

Figure 2.13: Schematic of the thermal resistance network of the overall energy balance of a general compressor.

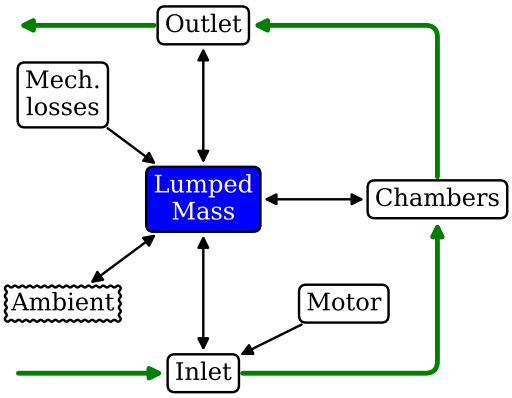

Figure 2.14: Schematic of a single lumped mass compressor energy balance.

Figure 2.14. In this case, thermal interactions between gas and the lumped mass reduce to a single energy balance:

$$\dot{Q}_{\text{amb}} + \dot{Q}_{\text{inlet}} - \overline{\dot{Q}}_{\text{chamber}} + \dot{W}_{\text{mech-loss}} + \dot{Q}_{\text{outlet}} = 0 \tag{2.76}$$

where the friction losses are associated with the mechanical analysis of the compressor motion as well as the corresponding forces and moments induced by the compression process can be estimated by means of different models depending on the specific needs and the level of details required. A simplified classification of friction loss models is presented in Figure 2.15. Examples of detailed mechanical

analyses of positive displacement machines can be found in Ziviani et al. [26].

Single and multi-lumped approaches have been widely used in literature [11,16, 23]. The applicability of the single lumped temperature depends on the positive displacement type and the accuracy expected in predicting the temperatures of the different elements. Both methods are implemented within PDSim. Examples of overall energy balance models are further discussed in Section 2.8.2 and Section 4.8.

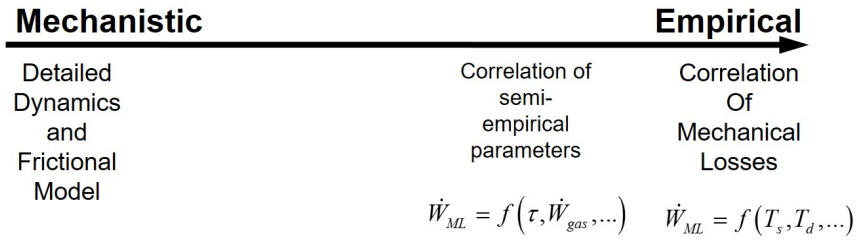

Figure 2.15: Classification of model for estimating the mechanical losses.

2.7 Generalized solution scheme

The simulation of a positive displacement compressor or expander presents several numerical challenges which often are related to the type of geometry considered. However, in general, a mechanistic model is characterized by a number of nested solvers in which the innermost solver passes the outputs to the next outermost solver until the overall compressor energy balance is enforced. In PDSim, the solution scheme is based upon four layers of solvers, as shown in Figure 2.16, which can be identified as:

- preconditioner;
- cycle solver;
- continuity solver;
- overall energy balance solver.

After initializing the simulation model with the necessary data including a guess of the mass flow rate assuming a volumetric efficiency of 100%, the preconditioner is divided into two levels. In the first level, a guess value of the discharge temperature is obtained by assuming a value of the adiabatic efficiency coherent with the machine under analysis. In the second level, one working cycle is run without continuity solver to improve the first set of guess values which allows to initialize the actual full model with values that are closer to the actual solution. A single cycle run is also used for debugging purposes as the reduced computational time facilitate obtaining the results.

Once the preconditioning step is completed and given the guess values for the lumped temperatures, the overall energy balance solver is executed. At each iteration of the overall energy balance solver, the continuity solver is run. The continuity solver ensures that under steady-periodic conditions, the state variables for each control volume will be equal at the beginning and end of the cycle. Within the continuity solver, the working cycle is run a number of times by integrating the set of governing equations until the initial state values are within a tolerance with the end cycle state values.

Due to the hierarchical and nested nature of the solution scheme, the actual numerical methods implemented to ensure the model convergence are discussed in Section 2.7.1 and Section 2.7.2.

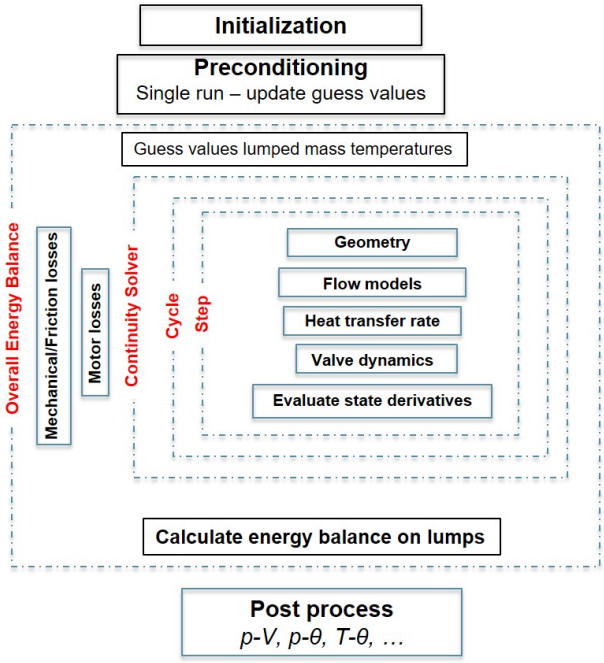

Figure 2.16: Schematic of the multi-layer solver required in a positive displacement machine.

2.7.1 Cycle integrator and stiffness

The cycle solver integrates the differential governing equations over one revolution knowing the initial conditions from the initialization step. In particular, the following steps are taken during the cycle solver, as shown in Figure 2.16:

- mass flow between all the chambers is determined;

- heat transfer between the working chamber and the working fluid is calculated;
- valve dynamics is executed and then integrated along with governing equations;
- a cycle integrator solver is used to predict the property values at the next step.

The integration is carried out simultaneously for each control volume. The behavior of a PD machine is described by a system of differential equations (see Equations 2.5) which are tightly coupled. The set of differential equations as a result of having multiple control volumes can be formulated in functional form as:

$$\vec{\mathbf{f}} = f\left(t, \vec{\mathbf{x}}\right) = \frac{d\vec{\mathbf{x}}}{\mathrm{dt}} \tag{2.77}$$

where t is the variable of integration either time or crank angle and $\vec{\mathbf{x}}$ is the array of variables that needs to be integrated. The array of variables includes both state variables of each control volume, e.g., temperature and density, as well as over variables such as velocity and acceleration of valves.

There a number of numerical integrators that can be used to carry out the integration of the system of non-linear and coupled differential equations [53]. The selection of an integrator suitable for the simulation of PD machines is related to the ability of the solver of handling numerical oscillations and stiffness with reasonable computational effort. It is known that certain compressor geometries such as scroll lead to differential problem that is stiff and for which large number of steps are required in order to avoid numerical oscillations. Although numerical integrators such as Euler and Heun are also available in PDSim, an adaptive method is recommended to solve the system of ODE equations especially when the stiffness is not constant during one cycle. The adaptive step size allows the control of the integration in order to achieve a predetermined accuracy of the solution with minimum computational effort. Te implementation of an adaptive stepsize control requires information about the progress of the integration and an estimation of its truncation error. An adaptive Runge-Kutta (RK) method has been implemented within PDSim. In particular, the embedded Runge-Kutta formulation discovered by Fehlberg is used which leads to a fifth-order method with six function evaluations where another combination of the six functions gives a fourth-order method (embedded fourth-order formula), i.e. RK4/5 [53]. The coefficients found by Cash and Carp [54] are used in the formulation of the method as they are more efficient than Fehlberg's original values. This yields the following algorithm for a general step size h:

$$\vec{f}_1 = f(t_{\mathrm{old}}, \vec{x}_{\mathrm{old}}) \tag{2.78}$$

$$\vec{x}_1 = \vec{x}_{\mathrm{old}} + h\left(\frac{1}{5}\vec{f}_1\right) \tag{2.79}$$

$$\vec{f}_2 = f\left(t_{\text{old}} + \frac{1}{5}h, \vec{x}_1\right) \tag{2.80}$$

$$\vec{x}_2 = \vec{x}_{\text{old}} + h\left(\frac{3}{40}\vec{f}_1 + \frac{9}{40}\vec{f}_2\right) \tag{2.81}$$

$$\vec{f}_3 = f\left(t_{\text{old}} + \frac{3}{10}h, \vec{x}_2\right) \tag{2.82}$$

$$\vec{x}_3 = \vec{x}_{\text{old}} + h\left(\frac{3}{10}\vec{f}_1 - \frac{9}{10}\vec{f}_2 + \frac{6}{5}\vec{f}_3\right) \tag{2.83}$$

$$\vec{f}_4 = f\left(t_{\text{old}} + \frac{3}{5}h, \vec{x}_3\right) \tag{2.84}$$

$$\vec{x}_4 = \vec{x}_{\text{old}} + h\left(-\frac{11}{54}\vec{f}_1 + \frac{5}{2}\vec{f}_2 - \frac{70}{27}\vec{f}_3 + \frac{35}{27}\vec{f}_4\right) \tag{2.85}$$

$$\vec{f}_5 = f(t_{\text{old}} + h, \vec{x}_4) \tag{2.86}$$

$$\vec{x}_5 = \vec{x}_{\text{old}} + h\left(\frac{1631}{55296}\vec{f}_1 + \frac{175}{512}\vec{f}_2 + \frac{575}{13824}\vec{f}_3 + \frac{44275}{110592}\vec{f}_4 + \frac{253}{4096}\vec{f}_5\right) \tag{2.87}$$

$$\vec{f}_6 = f\left(t_{\text{old}} + \frac{7}{8}h, \vec{x}_5\right) \tag{2.88}$$

The new values for the state variables $\vec{x}_{\text{new}}$ are given by

$$\vec{x}_{\text{new}} = \vec{x}_{\text{old}} + h\left(\frac{37}{378}\vec{f}_1 + \frac{250}{621}\vec{f}_3 + \frac{125}{594}\vec{f}_4 + \frac{512}{1771}\vec{f}_6\right) \tag{2.89}$$

and an estimate of the error is given by

$$\frac{\vec{\epsilon}}{h} = -\frac{277}{64512}\vec{f}_1 + \frac{6925}{370944}\vec{f}_3 - \frac{6925}{202752}\vec{f}_4 - \frac{277}{14336}\vec{f}_5 + \frac{277}{7084}\vec{f}_6 \tag{2.90}$$

If the maximum absolute error given by $\epsilon_{\max} = \max(|\vec{\epsilon}|)$ is less than the allowed error per step of $\epsilon_{\text{allowed}}$, the step is accepted, and the step size used was unnecessarily small, so the step size for the next step is increased using

$$h_{\text{next}} = 0.9h\left(\frac{\epsilon_{\text{allowed}}}{\epsilon_{\max}}\right)^{0.2} \tag{2.91}$$

If the error is too large ($\epsilon_{\max} > \epsilon_{\text{allowed}}$), the step must be tried again, but this time with a smaller step. The new step size is obtained from

$$h_{\text{next}} = 0.9h\left(\frac{\epsilon_{\text{allowed}}}{\epsilon_{\max}}\right)^{0.3} \tag{2.92}$$

The parameter 0.9 is a safety factor (usually $\simeq$1) that forces the method to be conservative in its step resizing. The resulting adaptive Runge-Kutta 4/5 method tailors the step-size to the instantaneous requirements in order to maintain the

required error per step with minimum computational effort. A numerical example is proposed to illustrate how the adaptive solver handles stiff problems. Consider the following ODE:

$$\frac{\mathrm{df}}{\mathrm{dt}} = f^2 - f^3, \tag{2.93}$$

which has to be integrated with the initial condition $f(0) = \delta$ over the time integral from $t = 0$ to $t = 2/\delta$ where $\delta = 0.01$. The aforementioned integrators are compared. The results are shown in Figure 2.17. The parameter δ is responsible for the stiffness of the problem. After the transition between 0 to 1, very small steps are required to obtain the correct solution. For smaller values of δ, the situation is worse resulting in overflow. From numerical considerations, it is known that stiffness is a transient phenomenon and in the case of positive displacement machines stiffness is associated with large difference in volumes and flows, variations of thermodynamic properties within relatively small volumes. It is argued that a set of independent thermodynamic properties to define the system of non-linear differential equations could improve the problem. According to Higham and Trefethen [55], a criterion based upon pseudospectra could help quantifying the stiffness and condition the solver accordingly.

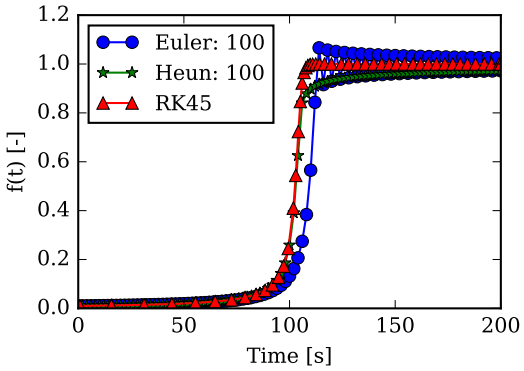

Figure 2.17: Example of numerical integration of a stiff ODE with Newton, Heun and RK45.

The use of an adaptive solver allows handling other numerical challenges such as discontinuities in the chamber volume curves. An example of such discontinuities can be found in spool compressors, as shown in Figure 2.18. At π, both suction and discharge curves have a discontinuity. A numerical procedure has been implemented to recognize the discontinuity in the control volume definitions and to help the adaptive solver to step through by taking a small step in the order of $\Delta\theta = 10^{-10}$ before and after the discontinuity and reassign the control volumes as needed. Similar numerical procedure can be applied in the case of chamber merging or splitting in scroll compressors [11].

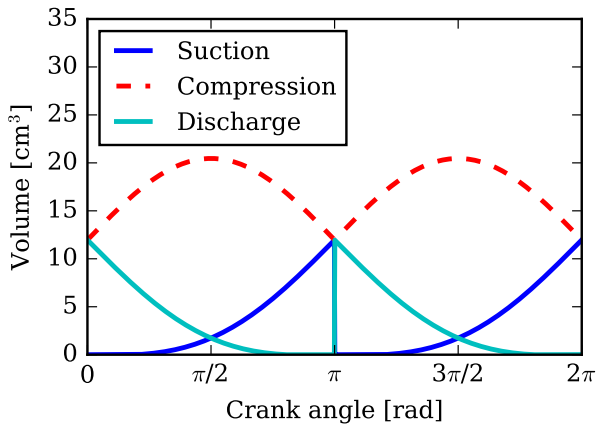

Figure 2.18: Chamber volume definitions of a spool compressor. To be noted is the discontinuity of suction and compression chambers at π [23, 35].

2.7.2 Overall energy balance solver

Once the continuity solver converged by ensuring that the state variables for each control volume and valve variables, if any, are equal at the beginning and at the end of the cycle, a steady-state overall energy balance has to be enforced. In particular, by referring to Figure 2.16, four events need to happen during the execution of the outermost solver:

- calculation of the discharge state;
- calculation of forces and moments to estimate friction losses;
- update the motor rotational speed in hermetic machines;
- calculate the lumped temperatures of the different elements.

Since the integration of the cycle has been completed, the average boundary work rate can be calculated as

$$\overline{\dot{W}}_{pV} = \frac{\omega}{2\pi} \int_0^{2\pi} p(\theta) \frac{\mathrm{dV}}{d\theta} d\theta \tag{2.94}$$

The actual shaft power is obtained by adding or subtracting the mechanical losses from the boundary work rate depending whether it is an expander or a compressor:

$$\dot{W}_{\mathrm{sh}} = \overline{\dot{W}}_{pV} \pm \dot{W}_{\mathrm{mech,loss}} \tag{2.95}$$

where the mechanical losses are obtained by executing the forces and moments analysis. In the case of hermetic compressors, the updated shaft work rate needs

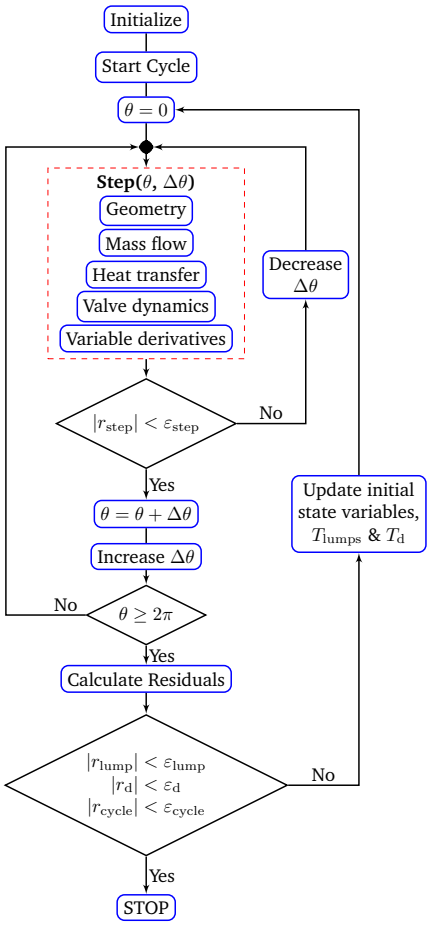

Figure 2.19: Generalized solution scheme for positive displacement model.

to be matched by the electric motor. Thus, the rotational speed of the motor has to be determined iteratively. In PDSim, both motor maps and a detailed single-phase motor model are available. In the case of the detailed single-phase motor model, the approach described by Dutra et al. [56] is implemented which makes use of a Brent's method to bracket the motor slip.

In the simulation, the exhaust pressure is specified, but the discharge temperature (or equivalently, the enthalpy), is unknown, and must be determined iteratively. The discharge temperature (or equivalently the enthalpy) and the lumped temperatures are the independent variables. The discharge state of the fluid leaving the set of chambers is obtained by solving the exhaust flow path backwards by imposing an energy balance. The residual is the difference in the

enthalpy between the back-calculated enthalpy and the outlet enthalpy of the set of chambers from the simulation. This discharge enthalpy from the chambers is calculated by carrying out the integrals in the equation

$$h_{\mathrm{d,chambers}} = \frac{\int_{\mathrm{d}} \dot{m}_i h_i}{\int_{\mathrm{d}} \dot{m}_i} \tag{2.96}$$

over the entire cycle. The new discharge temperature is then updated.

The outlet state from the compressor or expander shell is determined by solving the overall energy balance, see Figure 2.19. In the general case of multi-lumped elements, the number of energy balance equations matches the unknowns. Among multi-dimensional system of equation solvers, a modified Broyden's method [57] is used to minimize the residuals of the system of energy balance equations. A line-search algorithm has been added to ensure the correct direction taken by the solver. When a single lumped temperature is considered, a relaxed secant method is employed to minimize the energy balance residual.

Once both the discharge and lumped temperatures have converged, the comprehensive simulation model is completed.

2.8 Example of comprehensive compressor modeling

The generalized simulation framework developed has been applied to model both compressors of industrial interest and novel compressor types. Examples of simulation results for reciprocating, scroll, rolling piston and Z- compressors are shown in Figure 2.20. The modeling challenges of each compressor type have been addressed in details in Ziviani el al. [26].

In order to show the capabilities of the simulation tool developed, a novel miniature Z-compressor is considered to highlight how different modeling aspects are handled. In particular the following challenging aspects are to be considered for this particular compressor type:

- down-sizing of compressors implies greater influence of leakages and friction losses;
- multiple-control volumes and discontinuities in the volume curves;
- two discharge reed valves;
- multiple leakage paths with both constant and variable gap sizes;
- multiple source of friction losses;
- steady-state overall energy balance with multiple lumped elements.

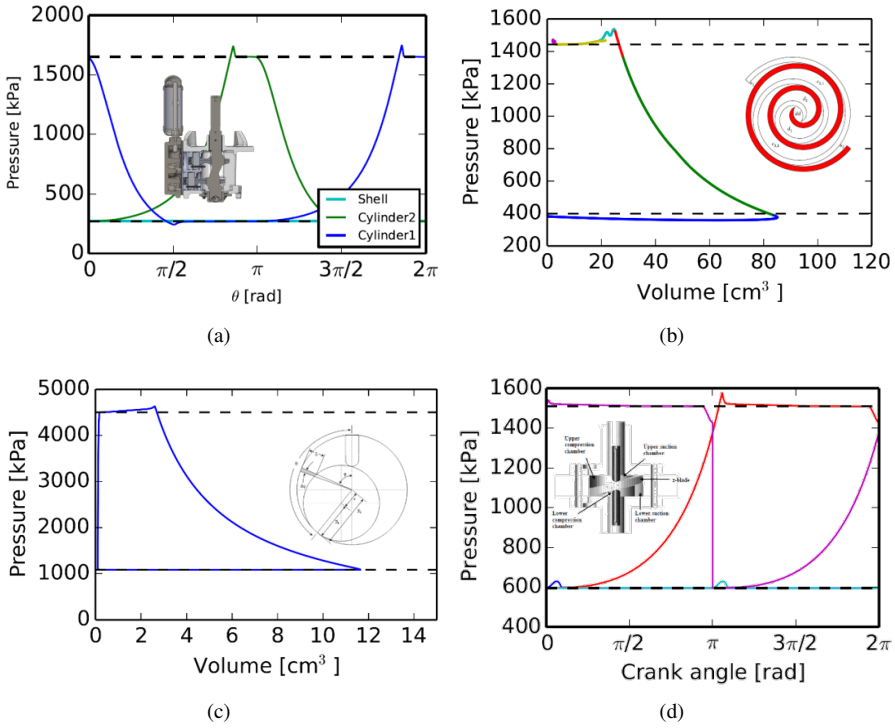

Figure 2.20: Examples of indicated diagrams for different refrigeration compressor types: (a) two-cylinder reciprocating compressor; (b) scroll compressor; (c) rotary rolling-piston compressor; (d) rotary Z-compressor.

2.8.1 Description of a Z-compressor

An air-compressor prototype that is within the family of rotary compressors is considered as an example to apply the generalized approach aforementioned. A cut-away view of the compressor is shown in Figure 2.21. To be noted is that the design concept resembles a two-stage rolling compressor and presents two sets of compression and suction chambers with a half revolution shift between the upper and lower level. The volume of the chambers is the space between inner and outer cylinder walls and the height of the chambers changes periodically as function of the crank angle. The element that separates upper and lower chambers is named blade. Additionally, the chambers on the same side of the blade are separated by means of a point of zero height with the housing and by a sliding vane. Due to the shape of blade and inner cylinder from a front view (see right side of Figure 2.21), the compressor is denoted as Z-compressor. The Z-compressor design considered in this work is an open-drive one. On each side of the compressor

there are two ports allowing for suction and discharge processes. Reed valves are installed on the discharge ports. The main design difference with respect to the original Z-compressor analyzed by Jovane [17] is the blade integrated with the outer cylinder which avoids direct leakage paths from upper to lower chambers and vice-versa as shown in Figure 2.21.

The working process is similar to a twin rolling piston rotary compressor in which two compression processes occur in one rotation. Four working chambers can be identified: upper suction and compression chambers and lower suction and compression chambers as seen in the cutaway view shown in Figure 2.21. Differently from a rolling piston rotary compressor, the Z-blade allows for volume variations. Two sliding vanes separate suction and compression chambers located on the same side of the Z-blade. The volume of each chamber is the space between inner and outer cylinders and the height of the chambers is dictated by the height of the portion of the Z-blade in contact with the vane.

The evolution of the working chamber volumes and their derivatives are shown in Figure 2.22 and they can be integrated into the compression process governing equations.

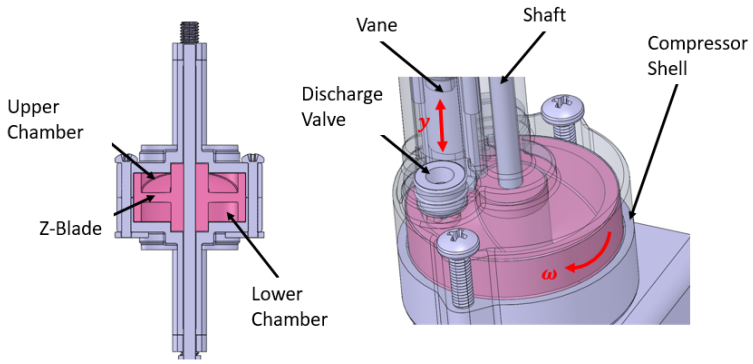

Figure 2.21: Cutaway view (left) and transparent 3D view (right) of the Z-compressor.

2.8.2 Compressor Model

The Z-compressor is divided into five control volumes (CVs) of which four are associated with upper and lower suction and compression chambers and their volumes change according to the rotation angle (see Figure 2.22). A fifth static control volume is introduced to account for the space between the rotating cylinder and the external housing as well as the space where the vanes are installed. A system of conservation equations is applied simoultaneously to each control volume to obtain the change in thermodynamic states. The properties within a control volume are assumed to be uniform, i.e. gradients within compressor

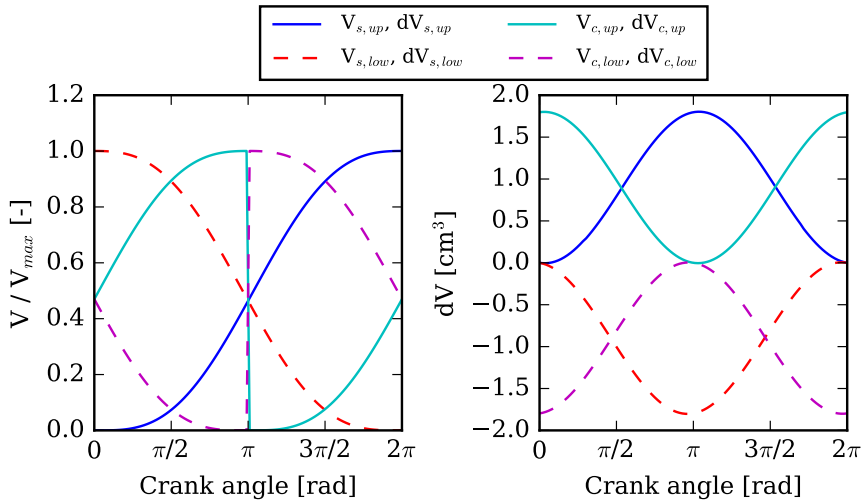

Figure 2.22: Chamber volume curves and their derivatives as function of the crank angle.

chambers are neglected. As CoolProp [30] is used to retrieve the thermophysical properties of air, two independent thermodynamic properties need to be selected to derive the conservation equations of mass and energy. Temperature and density have been chosen. The mass flow rate through the discharge valves are estimated by applying a one-degree-of-freedom dynamic model to the reed valves [14] having two operating modes, i.e., pressure dominant when the net force on the valve is dominated by the pressure difference across the valve, and mass flux dominant when the gas velocity is the dominant force.

As shown in Figure 2.22, the lower chambers are phased by half rotation. As a consequence, there are two discontinuities in the volume curves when the rotation is at π. During the integration of the differential governing equations, such discontinuities would not allow the convergence of the code. This numerical issue has been handled by coupling an adaptive step-size solver with a step-callback function that helps the solver to step through the discontinuity by taking a sufficiently small step before and after the discontinuity. This numerical technique can be applied to other compressor types for example spool compressors [23], where a similar situation occurs. An example of step size variation with the crank angle can be seen in Figure 2.23.

The compressor model is closed by enforcing a steady-state overall energy balance with the shell of the compressor. Two approaches are implemented for the Z-compressor. A single-lumped temperature overall energy balance, as shown

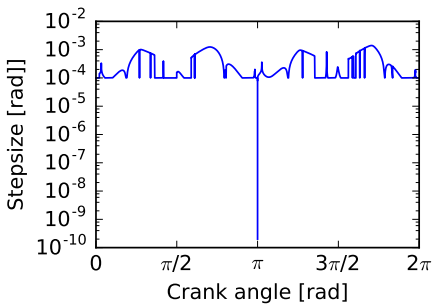

Figure 2.23: Evolution of the integration step size for Z-compressor simulation (T_{in}= 25 °C, p_{in}= 100 kPa, T_{out}= 115 kPa).

in Figure 2.24, is given by:

$$\dot{Q}_{amb} + \sum_i \dot{W}_{i,fr} + \sum_i \dot{Q}_i = \epsilon \tag{2.97}$$

where ϵ is the residual to be minimized, $\dot{Q}_{amb}$ is the heat transfer between the shell and the ambient, $\sum_i \dot{W}_{i,fr}$ is the sum of the mechanical and friction losses and the general $\dot{Q}_i$ term represents the heat transfer interaction between the gas and the shell during suction and compression processes.

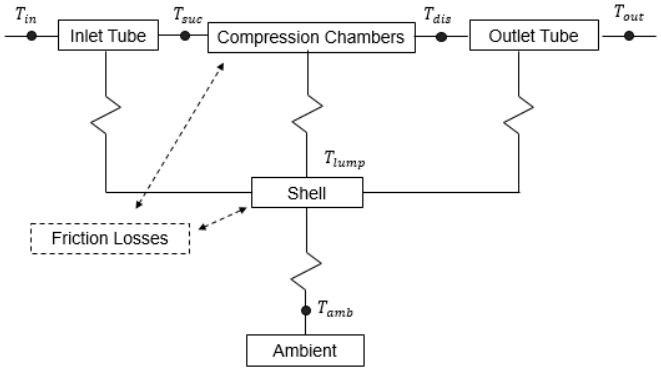

Figure 2.24: Single-lumped temperature overall energy balance applied to a Z-compressor.

A more comprehensive overall energy balance is proposed in Figure 2.25. Four lumped element have been identified and a thermal resistance network can be built as in Figure 2.26.

By applying the energy conservation law to the compressor components, the following system of energy balance equations can be obtained:

$$\overline{\dot{Q}}_{\text{mass,gas}} - \overline{\dot{Q}}_{\text{CV,wall}} - \overline{\dot{W}}_{\text{fr,flat}} - \overline{\dot{W}}_{\text{fr,tip-seal}} - \overline{\dot{W}}_{\text{fr,pt-blade}} = 0 \tag{2.98}$$

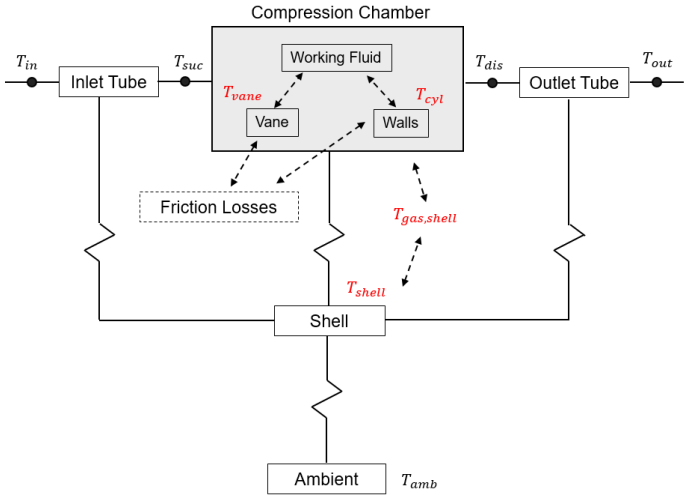

Figure 2.25: Multi-lumped temperature overall energy balance applied to a Z-compressor.

$$\overline{\dot{Q}}_{\text{shell,amb}} - \overline{\dot{Q}}_{\text{gas-shell,shell}} - \overline{\dot{Q}}_{\text{vane,shell}} - \overline{\dot{W}}_{\text{fr,JB}} - \overline{\dot{W}}_{\text{fr,TB}} = 0 \tag{2.99}$$

$$\overline{\dot{Q}}_{\text{vane,shell}} - \overline{\dot{Q}}_{\text{CV,vane}} - \overline{\dot{W}}_{\text{fr,vane-cyl}} = 0 \tag{2.100}$$

$$\overline{\dot{Q}}_{\text{gas-shell,shell}} - \overline{\dot{Q}}_{\text{vane,shell}} = 0 \tag{2.101}$$

2.8.2.1 Leakage Flow Model

The Z-compressor presents several leakage paths. For the current design, the main paths are identified in Figure 5. Furthermore, a more detailed description of each leakage path can be found in Table 2.2. By analyzing the leakage paths, it can be found that most of them present lengths that are relatively long compared to the cross-sectional area. In addition, the leakage path flow area is not always constant. Assuming isentropic flow of perfect gas will overestimate the leakage flows. To improve the leakage flow predictions, a detailed 1D-flow with friction analysis has been employed to obtain the mass flow rate estimations across each path. Coupling the three conservation equations, mass, momentum and energy, a general expression for the system of differential equations along the leakage path can be expressed as in Section 2.5.1. Solving the system of equations shown in (2.55) within the compressor model is computationally very expensive and also makes the convergence of the model more difficult to reach. Therefore, to predict the leakage flows in positive displacement machines, an isentropic flow model is generally adopted as it is simpler. However, it is known that such model can significantly overpredict the flow rate [40]. Therefore, the detailed 1D-flow model

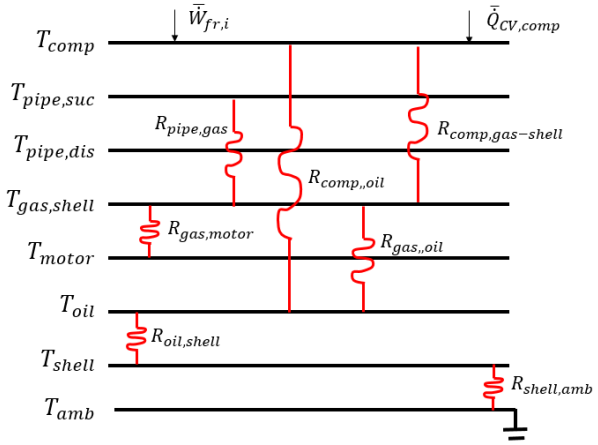

Figure 2.26: Schematic of the thermal resistance network of the overall energy balance of a general compressor.

is used to determine a correction factor between the mass flow rate of leakage using the detailed flow with friction model and the mass flow rate predicted using a simpler isentropic flow model. For a given configuration, the ratio of the isentropic nozzle mass flow rate prediction to that of the detailed model is defined by

$$M = \frac{\dot{m}_{\text{nozzle}}}{\dot{m}_{\text{fr}}} = \frac{a_0 \left(L/L_0\right)^{a_1}}{a_2 \left(\delta/\delta_0\right) + a_3} \left[\xi \left(a_4 Re^{a_5} + a_6\right) + \left(1 - \xi\right) \left(a_7 Re^{a_8} + a_{10}\right)\right] + a_{10} \tag{2.102}$$

where the dimensionless characteristic length and dimensionless gap width are given by $L^* = L/L_0$ and $\delta^* = \delta/\delta_0$ with L_0 and δ_0 being the reference length and gap width values. For brevity, only the case in which the detailed model is applied to the variable leakage path L_4 is shown. In particular, Figure 2.29(a) shows the generated points of the mass flow rate correction factor M for different boundary conditions (pressure ratio across the path) and gap widths as function of the Reynolds number. The calibration results of Equation 2.102 is reported in Figure 2.29(b). The correction factors are then used to compute the mass flow rate in and out each control volume during the integration of of Equation 2.6 and Equation 2.8.

2.8.2.2 Friction Losses

The average total shaft power is given by the sum of the compression power, $\overline{\dot{W}}_{\text{pV}}$, and the total friction power losses, $\overline{\dot{W}}_{\text{fr,tot}}$, due to contacts among the different parts,

$$\overline{\dot{W}}_{\text{sh}} = \overline{\dot{W}}_{\text{pV}} + \overline{\dot{W}}_{\text{fr,tot}} \tag{2.103}$$

Path	Description	Area
L1	Leakage through the clearance of the vane and the bearing slot from the shell to the compression chamber	Constant
L2	Leakage through the clearance of the vane and the bearing slot from the shell to the suction chamber	Constant
L3	Leakage through the flat area of the blade	Constant
L4a,b	Leakages through the clearance of the vane and cylinder	Variable
L5	Leakage through the clearance of the vane and the blade	Variable
Lup	Leakages from the upper compression chamber to the lower suction chamber and from the upper compression chamber to the lower compression chamber	Constant
Ldown	Leakages from the lower compression chamber to the upper suction chamber and from the lower compression chamber to the upper compression chamber	Constant

Table 2.2: Leakage path description.

Detailed force and moments analyses have been included into the model to estimate the friction losses. In particular, once the pressure distribution within the working chambers is known radial and axial loads on blade, shaft and bearings can be obtained as well as the associated frictional torques. Each frictional torque multiplied by the rotational speed gives the friction loss power. Due to the fact that the mathematical formulation of the loads is quite involved, only the general idea is given in this work, as the complete formulation can be found in [17]. The average total friction loss power is given as:

$$\overline{\dot{W}}_{\mathrm{fr,tot}} = \sum_i \overline{\dot{W}}_{\mathrm{i,fr}} = \overline{\dot{W}}_{\mathrm{fr,pt}} + \overline{\dot{W}}_{\mathrm{fr,v}} + \overline{\dot{W}}_{\mathrm{fr,flat}} + \overline{\dot{W}}_{\mathrm{fr,cyl-cyl}} + \overline{\dot{W}}_{\mathrm{fr,cyl-flat}} + \overline{\dot{W}}_{\mathrm{fr,TB}} + \overline{\dot{W}}_{\mathrm{fr,JB-low}} + \overline{\dot{W}}_{\mathrm{fr,JB-up}} \tag{2.104}$$

where $\overline{\dot{W}}_{\mathrm{fr,pt}}$ is the friction power associated with the tangential component of the pressure forces acting on the Z-blade as shown in Figure 2.28, $\overline{\dot{W}}_{\mathrm{fr,v}}$ is the total friction power due to the contact between vane and blade on both sides of the blade, $\overline{\dot{W}}_{\mathrm{fr,flat}}$ is the frictional loss due to the flat portions of the Z-blade, $\overline{\dot{W}}_{\mathrm{fr,cyl-cyl}}$ is the friction loss between the outer cylinder wall and the compressor inner shell, $\overline{\dot{W}}_{\mathrm{fr,cyl-flat}}$ is the friction losses induced by the upper and lower flat circular crowns of the outer cylinder and $\overline{\dot{W}}_{\mathrm{fr,TB}}$, $\overline{\dot{W}}_{\mathrm{fr,JB-low}}$, $\overline{\dot{W}}_{\mathrm{fr,JB-up}}$ are the

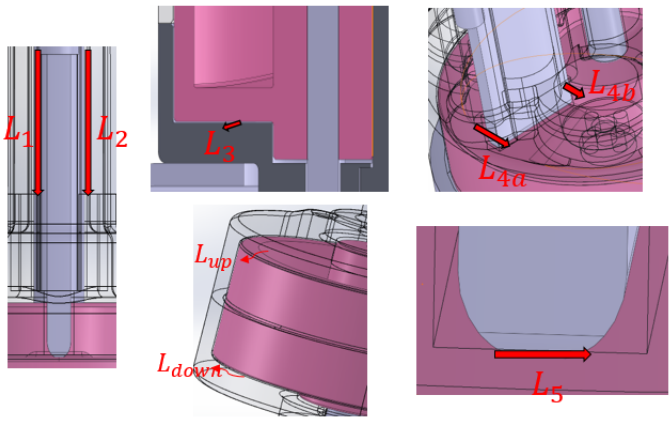

Figure 2.27: Leakage paths of the Z-compressor.

losses related to thrust bearing, lower and upper journal bearings, respectively.

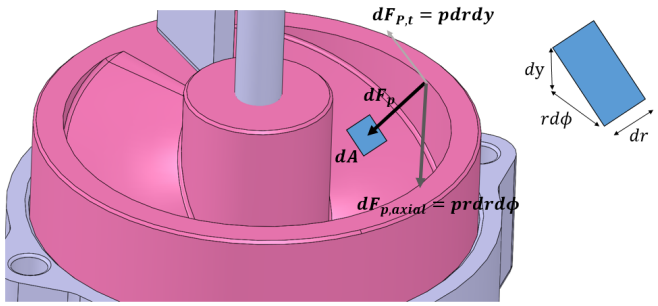

Figure 2.28: Decomposition of the pressure force acting perpendicular to an area element of the Z-blade.

2.8.3 Results and Discussion

The detailed compressor model developed is used as a tool to investigate the internal behavior of the compressor and to quantify the sources of losses. Figure 2.30 shows an example of pressure traces with respect to the rotation angle. The plot of the internal pressure of the compressor during the working process helped adapting the valve parameters to achieve the required operating points.

The baseline design, i.e. #1, has been tested in order to collect experimental data necessary to carry on the validation of the mechanistic model. The comparison between the experimental steady-state points and the model predictions is shown

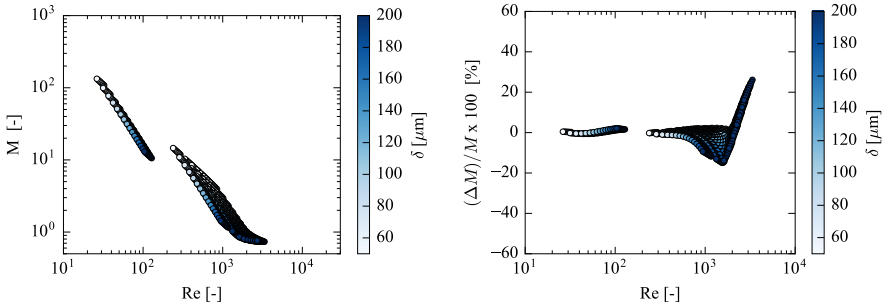

Figure 2.29: (a) Ratio of isentropic nozzle model to detailed model for radial leakage as a function of Reynolds number and gap width (color) ;(b) Error in leakage flow correction term as a function of Reynolds number and gap width (color).

Design	Description
# 1	Baseline (as Figure 2.21)
# 2	Shorter vane geometry and modified shaft configuration (one journal bearing and one thrust bearing); L_1 and L_2 gaps reduced by a factor of 5
# 3	Same as # 2 with thicker vane and minimum gap size everywhere
# 4	Same a #2 ; gaps as baseline and added piston-ring to reduce L_{up} and L_{down}
# 5	Same as # 4 with L_1 and L_2 gaps increased by a factor of 2 compared to baseline

Table 2.3: Description of the different designs analyzed.

in Figure 2.31. In particular, parity plots of mass flow rate, electrical power input, volumetric efficiency and overall isentropic efficiency are reported and the maximum relative errors are indicated on each chart. With the accuracy achieved, the model has been considered validated. Thus, starting from the baseline design, the model has been exercised to improve such design. A total of five possible prototypes have been identified and they are described in Table 2.3. As a first step, the Z-compressor shaft structure has been rethought to reduce friction losses, i.e. design #2. A more compact design led to significantly reduce the friction losses between the vane and the blade as well as eliminating the need for two journal bearings, as shown in Figure 2.32. Next, by keeping the same design configuration as design #2, three additional designs have been defined by considering different clearance gap sizes. A nominal operating point has been chosen to carry out the calculations: suction temperature 23 °C, suction temperature 100 kPa and

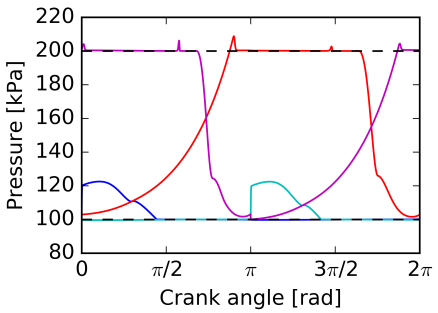

Figure 2.30: Evolution of the pressure within the working chambers throughout one rotation. The colors of the solid lines are identical to the ones in Figure 2.22.

discharge pressure 115 kPa. The results of the average mass flow rates through each path for all the five designs are grouped in Figure 2.33. The different gap sizes are associated with different manufacturing processes and costs. The improvements or degradation of the compressor performance are determined by calculating the volumetric efficiency, as shown in Figure 2.34. In the baseline design, all the gaps are kept the same leading to a volumetric efficiency close to 40%. A new vane design and reduced gaps of L_1 and L_2 of design #2 allowed to improve the volumetric efficiency by almost 50%. The best performance has been obtained with design #3 in which the gaps have been reduced to minimum and with a thicker vane. In the last two designs, a piston-ring has been added to eliminate the leakage flows between upper and lower chambers. However the gap sizes have been relaxed. As a result, design #4 reached a 51% volumetric efficiency while design #5 showed a 15% improvement over the baseline design.

Although the main objective of the study was to improve the flow rate delivered by the machine, the overall performance of the compressor in terms of isentropic efficiency has also been improved significantly, as shown in Figure 2.35.

The parametric analyses have been further used to define a design #6 with tip seals for prototyping.

References

[1] O. Dumont, R. Dickes, and V. Lemert. *Extrapolability and limitations of a semi-empirical model for the simulation of volumetric expanders*. Energy Procedia, 129:315–322, 2017.

[2] W. Soedel. *Introduction to Computer Simulation of Positive Displacement Compressors*. Short Course Text, Ray W. Herrick Laboratories, Purdue University, 1972.

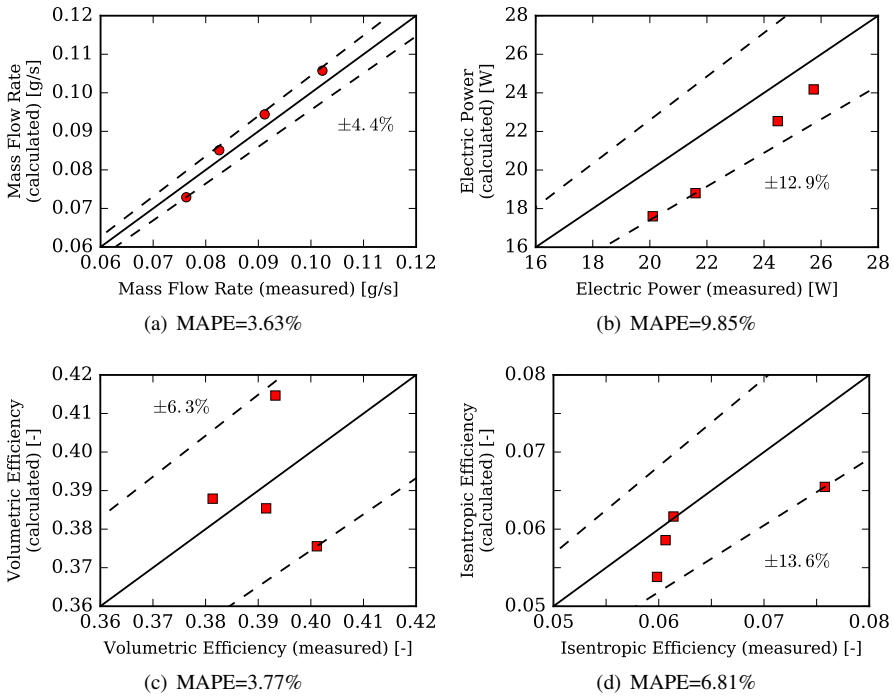

(a) MAPE=3.63% (b) MAPE=9.85%

(c) MAPE=3.77% (d) MAPE=6.81%

Figure 2.31: Z-compressor parity plots: (a) mass flow rate; (b) electric power input; (c) volumetric efficiency; (d) overall isentropic efficiency.

[3] J. F. Hamilton. *Extension of Mathematical Modeling of Positive Displacement Type Compressor*. Short Course Text, Ray W. Herrick Laboratories, Purdue University, 1974.

[4] P. Pandeya. *Performance Analysis of Positive Displacement Refrigerating Compressors*. PhD thesis, Purdue University, 1978.

[5] K.-L. koai. *Mathematical modeling of twin screw compressors with special attention to ga pulsations in three-dimensional gas paths*. PhD thesis, Purdue University, 1990.

[6] Nils Halm. *Mathematical Modeling of Scroll Compressors*. Master's thesis, Purdue University, 1997.

[7] Y. Chen, N.P. Halm, E.A. Groll, and J.E. Braun. *Mathematical Modeling of Scroll Compressor. Part I- Compression Process Modeling*. Int. J. Refrig., 25:731–750, 2002.

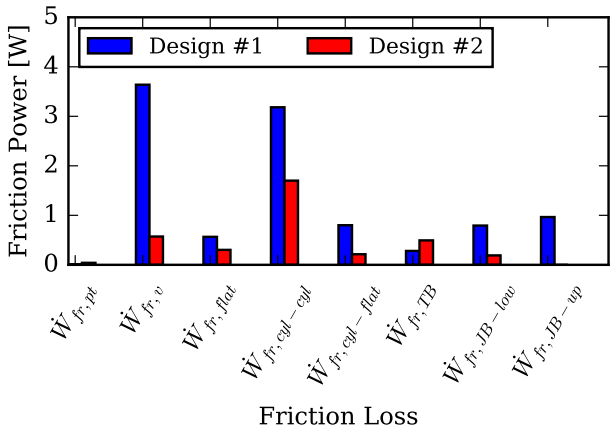

Figure 2.32: Comparison of the friction loss contributions between design # 1 and the improved design # 2. The other designs are equivalent to design # 2 in terms of shaft configuration.

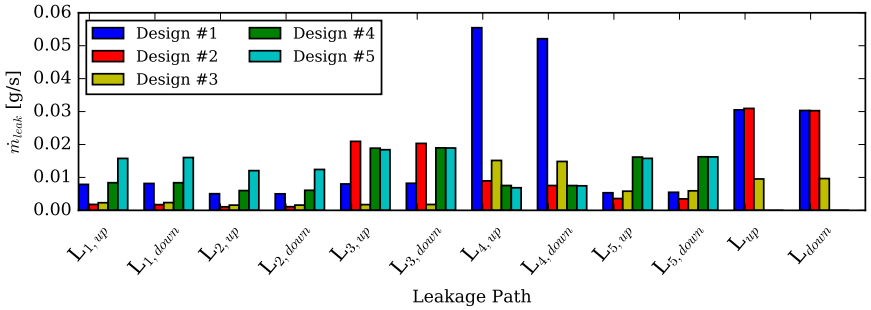

Figure 2.33: Leakage mass flow rate distribution among all the paths for different Z-compressor designs.

[8] Y. Chen, N.P. Halm, E.A. Groll, and J.E. Braun. *Mathematical Modeling of Scroll Compressor. Part II- Overall scroll compressor modeling*. Int. J. Refrig., 25:751–764, 2002.

[9] Vincent Lemort. *Contribution to the Characterization of Scroll Machines in Compressor and Expander Modes*. PhD thesis, University of Liège, 2008.

[10] Vincent Lemort, Ian Bell, Eckhard Groll, and James E. Braun. *Analysis of liquid-flooded expansion using a scroll expander*. In 19th Compressor Engineering Conference at Purdue University, number 1323, 2008.

[11] Ian Bell. *Theoretical and Experimental Analysis of Liquid Flooded Compression in Scroll Compressors*. PhD thesis, Purdue University, 2011.

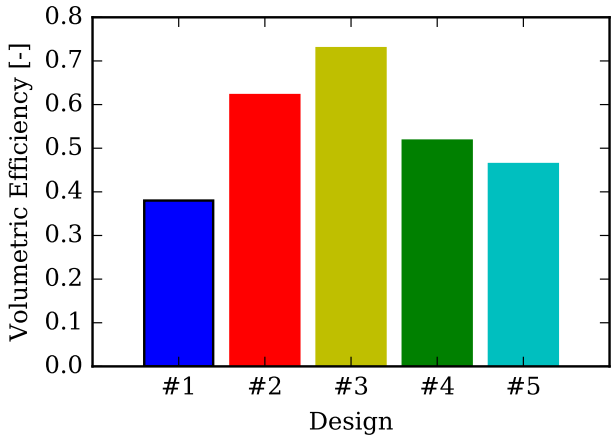

Figure 2.34: Comparison of volumetric efficiency obtained with the different Z-compressor designs.

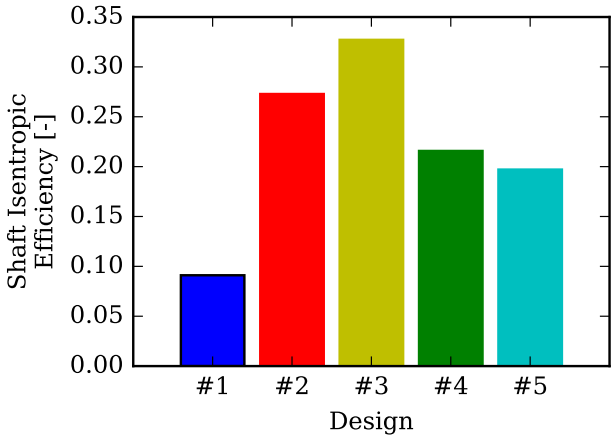

Figure 2.35: Comparison of isentropic efficiency at the shaft (open-drive compressor)obtained with the different Z-compressor designs.

[12] Jun-Hyeung Kim. *Analysis of a Bowtie Compressor with Novel Capacity Modulation*. PhD thesis, Purdue University, 2005.

[13] Craig Bradshaw. *A Miniature-Scale Linear Compressor for Electronics Cooling*. PhD thesis, Purdue University, 2012.

[14] Craig R. Bradshaw, Eckhard A. Groll, and Suresh V. Garimella. *A comprehensive model of a miniature-scale linear compressor for electronics cooling*. International Journal of Refrigeration, 34(1):63 – 73, 2011.

[15] Zhji Liu. *Simulation of a Variable Speed Compressor with Special Attention to Supercharging Effects*. PhD thesis, Purdue University, 1994.

[16] M. M. Mathison, James E. Braun, and Eckhard A. Groll. *Modeling of a Two-Stage Rotary Compressor*. HVAC&R Research, 14:719–748, 2008.

[17] Miguel Jovane. *Modeling and analysis of a novel rotary compressor*. PhD thesis, Purdue University, 2007.

[18] Pawan J. Singh. *A Digital Reciprocating Compressor Simulation Program Including Suction and Discharge Piping*. In International Compressor Engineering Conference at Purdue 1984, 1984.

[19] Bin Yang, C. R. Bradshaw, and E. A. Groll. *Modeling of a semi-hermetic CO_2 reciprocating compressor including lubrication submodels for piston rings and bearings*. International Journal of Refrigeration, 2013.

[20] Thomas W. Bein and James F. Hamilton. *Computer Modeling of an Oil flooded single screw air compressor*. In 1982 International Compressor Engineering Conference at Purdue University, pages 127–134, 1982.

[21] Pawan J. Singh and Ghanshyam C. Patel. *A generalized performance computer program for oil flooded twin-screw compressors*. In International Compressor Engineering Conference at Purdue University, pages 544–553, 1984.

[22] D. Ziviani, I. H. Bell, M. De Paepe, and M. van den Broek. *Comprehensive model of a single screw expander for ORC-systems applications*. In 22th Int.Compressor Engineering Conf. at Purdue, number 1506, 2014.

[23] C. R. Bradshaw and E. A. Groll. *A comprehensive model of a novel rotating spool compressor*. International Journal of Refrigeration, 36:1974–1981, 2013.

[24] I. H. Bell, V. Lemort, E. A. Groll, J. E. Braun, and W. T. Horton. *Development of a generalized steady-state simulation framework for positive displacement compressors and expanders*. In Proceedings of the International Conference on Compressors and their Systems, 2013.

[25] Michael J. Moran and Howard N. Shapiro. *Fundamentals of Engineering Thermodynamics*. John Wiley and Sons, 2008.

[26] D. Ziviani, X. Zhang, I. H. Bell, M. van den Broek, M. De Paepe, E. A. Groll, J. E. Braun, and W. T. Horton. *An open-source simulation framework for positive displacement compressors and expanders*. International Journal of Refrigeration, To be submitted, 2017.

[27] X. Zhang, D. Ziviani, J. E. Braun, and E. A. Groll. *A Numerical Study on Dynamic Characteristics of Linear Compressor for Electronic Cooling*. In 8th International Conference on Compressors and Refrigeration, Xi'an Jiaotong Univerisity, 2017.

[28] Smith, I. K. and Stosic, N. and Aldis, C. A. *Development of the trilateral flash cycle system. Part 3: the design of high-efficiency two-phase screw expanders*. Proc. Instn. Mech. Engrs., Part A: Journal of Power and Energy, 210:75–93, 1996.

[29] N. Stosic, I. K. Smith, A. Kovacevic, and E. Mujic. *Review of Mathematical Models in Performance Calculation of Screw Compressors*. International Journal of Fluid Machinery and Systems, 4(2):271–288, 2011.

[30] Ian H. Bell, Jorrit Wronski, Sylvain Quoilin, and Vincent Lemort. *Pure and Pseudo-pure Fluid Thermophysical Property Evaluation and the Open-Source Thermophysical Property Library CoolProp*. Industrial & Engineering Chemistry Research, 53(6):2498–2508, 2014.

[31] I. H. Bell, V. Lemort, E. A. Groll, J. E. Braun, and G. King. *Liquid-Flooded Compression and Expansion in Scroll Machines - Part I: Model Development*. Int. J. Refrig., 35:1878–1889, 2011.

[32] K. Hanjalic and N. Stosic. *Development and Optimization of Screw Machines With a Simulation Model - Part II: Thermodynamic Performance Simulation and Design Optimization*. Journal of Fluids Engineering, 119:664–670, 1997.

[33] Dmytro Zaytsev. *Development of Wet Compressor for Application in Compression-Resorption Heat Pumps*. PhD thesis, Technische Universiteit Delft, 2003.

[34] D. Chisholm. *Two-Phase flow in pipelines and heat exchangers*. George Goodwin, London, 1983.

[35] M. M. Mathison, J. E. Braun, and E. A. Groll. *Modeling of a novel spool compressor with multiple vapor refrigerant injection ports*. International Journal fo Refrigeration, 36:1982–1997, 2013.

[36] I. K. Smith, N. Stosic, and C.A. Aldis. *Development of a trilateral flash cycle system: Part 3: The design of high-efficiency two-phase screw expanders*. Proceedings of the Institution of Mechanical Engineers. Part A: Journal of Power and Energy, 208(2):135–144, 1996.

[37] N. Stosic, A. Kovacevic, K. Hanjalic, and L. Milutinovic. *Mathematical modelling of the oil influence upon the working cycle of screw compressors*. In International Compressor Engineering Conference at Purdue. Paper 645., 1988.

[38] S.W. Churchill. *Friction factor equation spans all fluid flow regimes*. Chemical Engineering, 84(24):91–92, 1977.

[39] V. Gnielinski. *Neue Gleichungen für den Wärme-und den Stoffübergang in turbulent durchströmten Rohren und Kanälen*. Forschung im Ingenieurwesen, 41(1):8–16, 1975.

[40] I. H. Bell, E. A. Groll, J. E. Braun, and W. T. Horton. *A computationally efficient hybrid leakage model for positive displacement compressors and expanders*. International Journal of Refrigeration, 2013.

[41] Noriaki Ishii, Kenichi Bird, Kiyoshi Sano, Mamoru Oono, Shinji Iwamura, and Takayuki Otokura. *Refrigerant Leakage Flow Evaluation for scroll compressors*. In 1996 Compressor Conference at Purdue University, 1996.

[42] Kazutaka Suefuji, Masao Shiibayashi, and Kenji Tojo. *Performance analysis of hermetic scroll compressors*. In 1992 International Compressor Engineering Conference at Purdue University, 1992.

[43] Kenji Tojo, Masato Ikegawa, Naoki Maeda, Sigeru Machida, Masao Shiibayashi, and Naoshi Uchikawa. *Computer Modeling of scroll compressor with self adjusting back-pressure mechanism*. In 1986 International Compressor Engineering Conference at Purdue University, 1986.

[44] Th. Afjei, P. Suter, and D. Favrat. *Experimental Analysis of an inverter-driven scroll compressor with liquid injection*. In 1992 Compressor Engineering Conference at Purdue University, 1992.

[45] Werner Soedel. *Design and Mechanics of Compressor Valves*. Ray W. Herrick Laboratories, School of Mechanical Engineering, Purdue University, 1984.

[46] Werner Soedel. *Sound and Vibrations of Positive Displacement Compressors*. CRC Press Taylor & Francis Group, 2007.

[47] Robert D. Blevins. *Formulas for Natural Frequency and Mode Shape*. van Nostrand Reinhold Company, 1979.

[48] K. Suefuji and S. Nakayama. *Practical method for analysis and estimation of reciprocating hermetic compressor performance*. In International Compressor Engineering Conference at Purdue University, 1980.

[49] T. L. Berman, A. S. Lavine, F. P. Incropera, and D. P. Dewitt. *Introduction to Heat Transfer*. John Wiley & Sons, Inc., sixth edition edition, 2011.

[50] Yu Chen. *Mathematical Modeling of Scroll Compressors*. PhD thesis, Purdue University, 2000.

[51] S. K. Padhy. *Heat transfer model of a rotary compressor*. International Compressor Engineering Conference at Purdue, page Paper 935., 1992.

[52] Frank P. Incropera and David P. Dewitt. *Fundamentals of Heat and Mass Transfer (5th Edition)*. Wiley, 2002.

[53] Steven C. Chapra and Raymond P. Canale. *Numerical Methods for Engineers*. McGraw-Hill, 2006.

[54] J.R. Cash and Alan H. Karp. *A Variable Order Runge-Kutta Method for Initial Value Problems with Rapidly Varying Right-Hand Sides*. ACM Transactions on Mathematical Software, 16(3):201–222, 1990.

[55] D. J. Higham and L. N. Trefethen. *Stiffness of ODEs*. BIT Numerical Mathematics, 33:285–303, 1993.

[56] T. Dutra and C. J. Deschamps. *A simulation approach for hermetic reciprocating compressors including electrical motor modeling*. International Journal fo Refrigeration, 59:168–181, 2015.

[57] C.G. Broyden. *A class of methods for solving nonlinear simultaneous equations*. Mathematics of Computation, 19:577–593, 1965.

3

Single-Screw Compressor and Expander Geometry

3.1 Introduction

The single-screw concept was first introduced by Bernard Zimmern in early 1960s [1] and consisted of a single six helically grooved central rotor with a cylindrical periphery and a globoid core and two identical 11-teeth starwheels engaging with the rotor [2, 3]. After being rejected several times from French and American companies, a first prototype of single-screw compressor for compressed air applications was built in 1963 and it was licensed two years later. After that point, the development of the single-screw continued and its application was extended to refrigeration within a decade [4–7].

The central position of the rotor in the single-screw potentially leads to different configurations depending on the shape of the grooved rotor and the position of the starwheels. In particular, four main configurations can be distinguished at the moment, as shown in Figure 3.1 [8]:

- Plate-Cylindrical (PC): planar main screw rotor and two cylindrical starwheels. The working process occurs only on the front face of the screw rotor. The starwheels shafts are oriented at opposing angles from the axial face of the main screw.
- Cylindrical-Plate (CP): cylindrical main screw rotor and two planar starwheels. The starwheel shafts are parallel to each other with their rotation

axes perpendicular to the rotation axis of the main screw. The working process occurs within the volume created when the starwheels mesh with the main screw rotor.

- Plate-Plate (PP): planar screw rotor and planar starwheels. The grooves are located on the front and back faces of the main screw rotor. Whereas, two starwheels are employed for each side or the rotor and the rotation axis of their shafts are parallel each other.

- Cylindrical-Cylindrical (CC): cylindrical starwheels and cylindrical screw rotor. The two starwheels are engaged on the top and bottom face of the main screw, respectively. As with the PC design, the starwheel shafts are oriented at opposing angles.

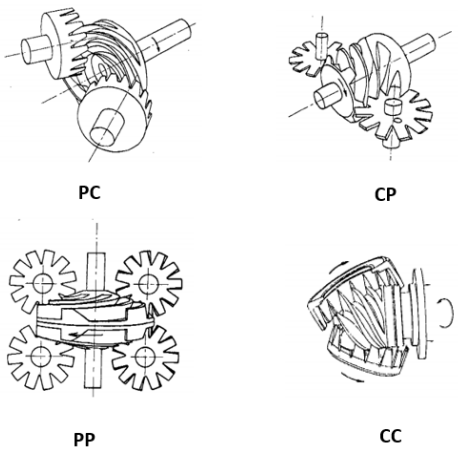

Figure 3.1: Classification of single-screw machines depending on the meshing conditions. Adapted from Zimmern B. [7].

The most common single-screw configuration is the CP-type, which includes as primary components a screw rotor and two starwheels. One of the main reason has to be found in the rising complexity of the manufacturing process of the other configurations, despite a low increase in the efficiency and performance. The other configurations have been investigated mostly numerically and limited work is available on the their manufacturing. Yang S.-C. et al. carried out the analytical modeling of all the different meshing conditions: CP-type [9], CC-type [10], PP-type [11, 12] and PC-type [13].

The improvement of the single-screw design is directly related to the advancements in the manufacturing techniques. Over the years, the accuracy of

the Computer Numerically Controlled (CNC) machines has increased allowing for a better control of the machining process of the main rotor. However, difficulties in the manufacturing process of the grooves still exist [14]. The machining accuracy of the meshing pair is an important aspect and according to Li et al. [15], the average maximum machining error is in the order of two times the design precision required of the single-screw rotor.

Novel manufacturing techniques such as 3-D printing would open the possibility of designing novel types of single-screw meshing configurations that are not cost effective with the current manufacturing processes, such as CC single-screw compressor described by Heidrich and Yang [10, 16]

In this chapter, the geometry of the single-screw machine is described in great details. First, a literature review is proposed to summarize the geometric modeling efforts carried out previously and to highlight the missing aspects. Next, the geometric parameters of the single-screw are described and defined in details. The determination of the meshing equations is also provided for completeness. Last, the geometric relationships are used to calculate the volume and its derivative curves, sealing lines, groove surfaces that will be employed in Chapter 4 to develop a mechanistic model. Additionally, a comparison between different methods for the calculation of the volume curve is proposed.

3.2 Literature review

To analyze a single-screw machine, the relationships among the different dimensions as well as the meshing conditions between main rotor and starwheels need to be established. The majority of the literature available focuses on single-screw compressors (SSC), although in recent years, the interests in single-screw expanders (SSE) for organic Rankine cycle (ORC) system applications is increasing. A typical assembly of an open-drive single-screw machine with the description of each part is proposed in Figure 3.2.

One of the first detailed description of the basic concept and the principle of operation of a SSC was published by J. van Male in 1978 [6], where the so called ”Monoscrew” was first employed as rotary positive displacement refrigerating compressor and designed to operate with refrigerants such as ammonia, R12 and R22. Throughout the market history until nowadays, the design configuration adopted employs a 6-grooved main rotor and 11-teeth starwheel. The reason lies on geometric considerations, leading to variations of swept volume, pressure ratio and the length of leakage paths. Lundberg and Glanvall [17, 18] compared the single-screw geometry with twin-screw design and provided expressions for the different geometric parameters of interest. The groove was unwrapped on a plane to analyze the volume ratio. Chan et al. [19] contributed to the development of a geometry-based model based on the area of the tooth engaged with the groove.

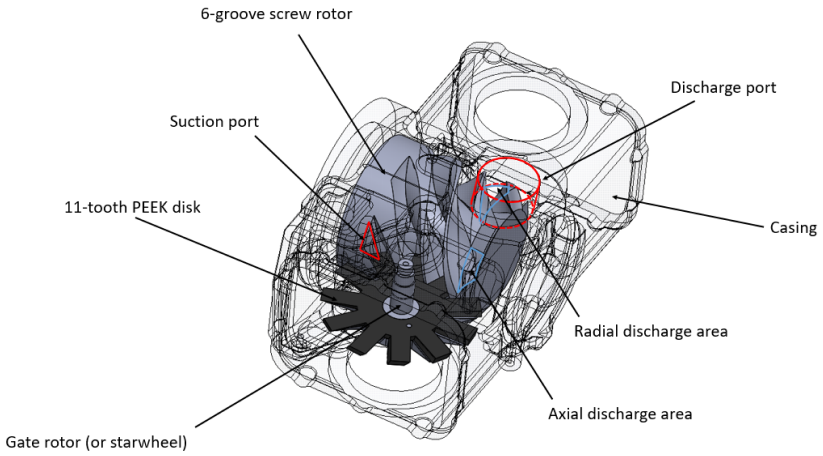

Figure 3.2: Description of a single-screw expander assembly.

Nonetheless, the geometric relationships were not reported. The model was used to investigate different geometric aspects such as degree of penetration of the tooth into the groove, relationship between number of grooves and teeth, effect of the cut-off angle at the beginning of the compression process. The results showed that by decreasing the number of teeth for a fixed 6-grooves main rotor, the swept volume increased significantly with a reduction of the achievable volume ratio. Furthermore, rotors with four grooves rather than six appeared to be a better design choice as it would increase swept volume. However, machining and compression ratio limitations restricted the meshing choices in practice. It was also mentioned that a common factor between the numbers of grooves and teeth would lead to meshing issues.

Similar modeling approach was described in details by Bein and Hamilton [20, 21]. Mathematical expressions of the main rotor design were outlined and the positions of the four corners of each of the engaged teeth were obtained analytically. A polygon approach [22] was used to obtain the engaging tooth area as well as the volume of the groove. Hirai et al. [23] added the description of the sealing lines.

Sun G. [24] proposed a differential approach to describe the engaging area of a tooth with a groove. Analytic expressions were obtained for the groove volume by splitting the groove into two parts depending on the number of corners of the tooth that are engaged. The selection of design parameters were also addressed. An empirical estimation of the maximum groove volume was also obtained. More recently, Jin et al. [25] analyzed the correlation between the starwheel and main rotor diameters ratio as well as the center line spacing.

Currently, the calculation of the volume curve are carried out with both polygon approach and by integration method [26, 27]. However, the latter one has been developed for single-screw compressors and its validity is limited between suction closure and the discharge. If a single-screw expander is considered, such model describes only the volume curve from suction until the discharge opening, excluding the remaining of the discharge process, as shown by Ziviani et al. [28, 29]. Therefore, under- and over-expansion losses cannot be fully captured by the model. Simplified approach has been proposed recently by Wu et al. [30] to describe analytically the decay part of the volume curve in a single-screw expander.

The geometry model of the single-screw is an essential part to determine the meshing conditions and to analyze the manufacturing process. In fact, although the potential of the single-screw technology has been demonstrated over the years with respect to other existing positive displacement (PD) compressor machines in a wide range of applications [31], the reliability of such machine [6, 32] strongly depends on the starwheel tooth flanks wear resistance. Generally, the main rotor is made of cast iron and the starwheels are an assembly of a metal support and a toothed disk made of an anti-wear composed material, e.g., PEEK. The starwheels serve to the sole purpose of sealing compression/expansion chambers and therefore they do not produce any work. As a consequence, only limited amount of work is transmitted to them due to rubbing loads between tooth sides and groove flanks. The uncertainties related to the manufacturing process of the meshing pair and the type of generating profile yield a potential rapid wear of the starwheel tooth flank surfaces meshing with the screw groove flanks. Ultimately, the wear leads to larger gaps which increase the leakages and decreases the volumetric efficiency. The shape of the tooth flanks, the materials and the machining accuracy of the meshing pair represent the important aspects with respect improving the wear resistance. Different geometric meshing conditions have been proposed to achieve a smoother contact during the meshing. The original profile proposed for the single-screw compressor meshing pair was substantially a straight-line envelope mashing pair (SEMP or LEMP) [26]. The contact area between the starwheel tooth flank and the screw rotor is a fixed straight line on the starwheel tooth flank, resulting on a low wear resistance because the contacts are concentrated on a line. The detailed model for LEMP was presented by Yang S.-C. [9]. In order to distribute the contact area into more extensive region and reduce the progressive wearing, a column envelope meshing profile (CEMP) was proposed by Zimmern [3]. A more comprehensive mathematical model of CEMP with design purposes was presented by Wu et al. [33], but due to limitation in machining capabilities, the solution was not suitable for industrial applications. Successively, Wu and Feng [34, 35] improved the feasibility of the column profile by introducing a multi-column (or multi-straight line) approach as well. The proposed approach allows the contact line between

the tooth flak and the groove flank to move back and forth in the whole area of the tooth flank, enhancing the lubrication between tooth and groove flanks and improving the service life. Basically, the meshing area of a multi-column envelope is not continuous but characterized by jumps between one cylindrical segment to another. Furthermore, different curved profiles of the gate-rotor teeth, e.g., elliptical, hyperbolic, or involute, were analyzed by Li et al. [15] in order to enhance the lubrication between tooth and groove flanks. It is possible to find an overview of the different meshing pair profiles in a recent work published by Wu et al. [36]. Conical teeth were also proposed by Yang and Liang [37]. In the open-literature, a comprehensive work that summarizes the geometry modeling of a single-screw is not available. To be precise, although relevant literature exists, such as [38], it is mostly written in Chinese and not publicly available to the Westerner world. In the following sections, the geometry of a single-screw is outlined. Although, a single-screw expander is used as example to carry on the calculations, the methodology is applicable to compressors as well. Only SEMP type of generating profile is considered.

3.3 Geometric characteristics of single-screw machines

To develop a geometry model of the single-screw machine, two steps need to be considered:

- identify the geometric parameters of interest;
- understand and define the meshing process equations.

Therefore, the fundamentals of the single-screw meshing pair will be explained and the main geometric relationships will be developed at first, and then further applied to obtain the groove volume curve and its derivative, the groove surface areas, tooth engaging area and the sealing lines.

Although the single-screw expander is adopted as geometry of reference, the mathematical formulations can be directly applied to a single-screw compressor. The nomenclature and symbols used are in accordance to the open literature in order to facilitate the comparison.

3.3.1 General Parameters

The expansion (or compression) process of the single-screw occurs simultaneously on both sides of the rotor. The inlet flow is split in two parts to reach each of the inlet ports. As shown in Figure 3.3, during the suction process, the groove is filled by working fluid until the left flank of the groove passes the right edge of the triangular-shaped port. At suction closure, the working fluid starts the

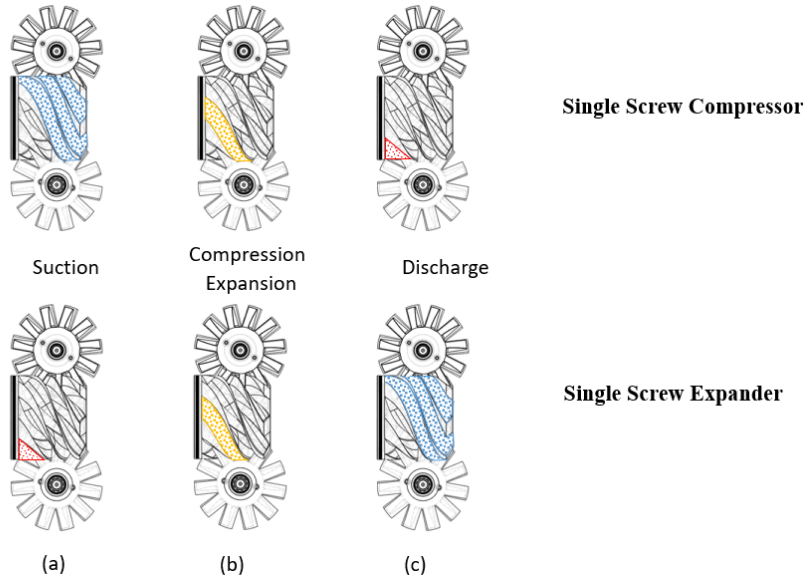

Figure 3.3: Graphic representation of the single-screw expansion and compression processes: (a) suction; (b) closed expansion; (c) discharge. To be noted is that the expansion and compression processes occur simultaneously also on the opposite side of the rotor.

expansion process. When the right side of the engaged tooth begins to leave the groove, the discharge process occurs. Reference studies about the geometry of SSE can be found in literature concerning SSC, for example [19, 21, 23, 24]. However, the formulation is not always comprehensive and many aspects of the design are missing. The geometric description of the SSE involves a large number of variables and parameters. In particular, it is possible to group the variables as [20]:

- independent variables;
- dependent variables;
- limit-set variables.

Besides the variables, a number of empirical design parameters have to be selected. The independent variables include the number of grooves of main rotor, z_{sr}, the number of teeth of the starwheels, z_{sw}, the number of starwheel, N_{sw}, the main rotor diameter, D_{sr}, the starwheel outer and inner diameters, D_{sw}, $D_{\mathrm{sw,in}}$ and the tooth width. The considered SSE has the standard configuration of 6 grooves in the main rotor and 11 teeth in the starwheels, which automatically defines the

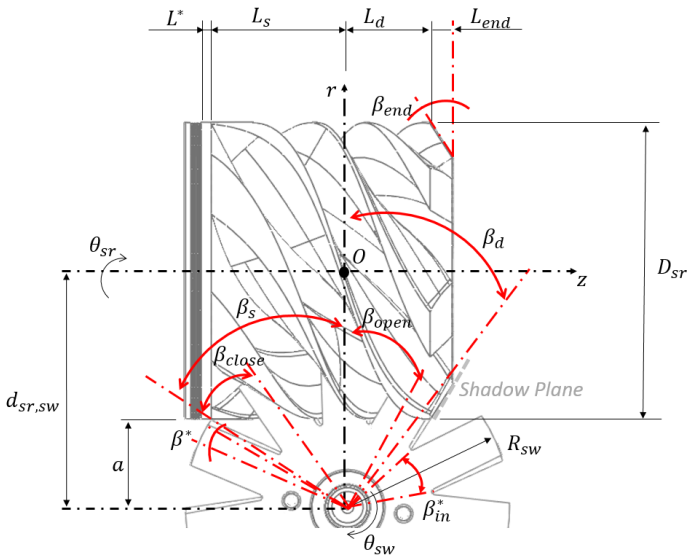

(a)

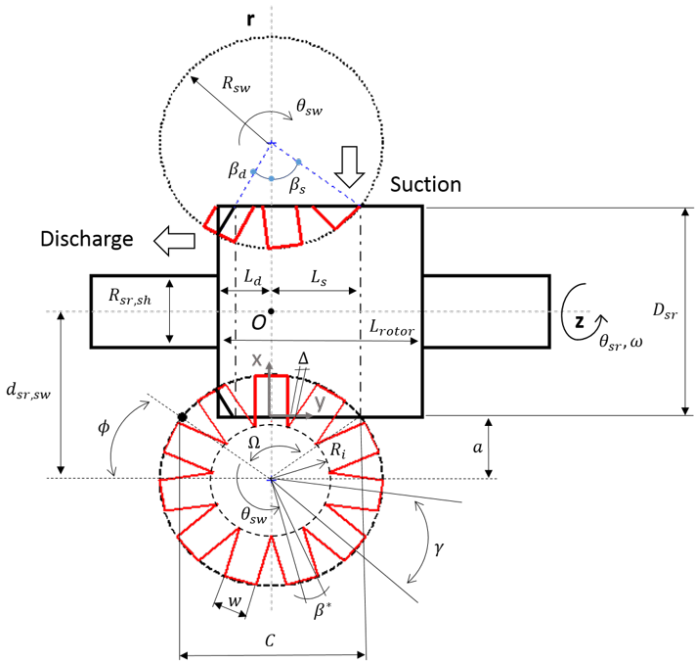

(b)

Figure 3.4: Schematics of the main geometric parameters of the SSE: (a) view of main rotor and starwheel from CAD model; (b) view of the engaging pair obtained from analytic model.

correlation between rotation angle and angular speed of the meshing pair:

$$i = \frac{z_{\mathrm{sw}}}{z_{\mathrm{sr}}} = \frac{\theta_{\mathrm{sr}}}{\theta_{\mathrm{sw}}} = \frac{\omega_{\mathrm{sr}}}{\omega_{\mathrm{sw}}} = \frac{11}{6}. \tag{3.1}$$

where ω_{sr} and ω_{sw} are the angular speeds of main rotor and starwheel, respectively. The number of grooves typically is a multiple of the number of starwheels in order to balance the forces acting on the main rotor. In fact, the expansion or compression process will be symmetric in both sides of the rotor since the same number of grooves are engaged. To be noted is that the number of starwheels and their positions determine the type of configuration of the single-screw machine, i.e. CC, CP, PC, PP [8]. The most common one is Cylinder-Plate (CP) and the reason behind it is explained in the following section dealing with the kinematics of meshing process. The number of teeth of the starwheel should not have a common factor with the number of grooves to guarantee the uniformity of the meshing and control the wear of the teeth. Increasing or decreasing the number of teeth has also the effect of modifying the swept volume [19]. The diameters of main rotor and starwheel are related by a design parameter, $D_{\mathrm{sw}} = \lambda_{\mathrm{d}}\, D_{\mathrm{sr}}$. Normally, D_{sw} is either equal to or slightly larger (up to 10%) than D_{sr}. The diameter of the starwheel and the distance between the center axes of main rotor and starwheel, $d_{\mathrm{sr,sw}}$, influence the maximum groove volume and the degree of penetration of the tooth into the groove:

$$d_{\mathrm{sr,sw}} = \lambda_{\mathrm{opt}} D_{\mathrm{sr}} \tag{3.2}$$

In many cases $d_{\mathrm{sr,sw}} = 0.8\, D_{\mathrm{sr}}$ (see Section 3.4). For obvious structural reasons, the degree of penetration of a tooth into the groove is limited by the main shaft diameter. That is:

$$R_{\mathrm{sr}} - (R_{\mathrm{sw}} - R_{\mathrm{sw,in}}) > R_{\mathrm{sr,sh}} \tag{3.3}$$

Dependent variables are related to the calculation of engaging angles and the length of the rotor sections. By referring to Figure 3.4(a), it is possible to define:

$$\begin{aligned} \beta_{\mathrm{s}} &= \cos^{-1}\left(\frac{d_{\mathrm{sr,sw}} - R_{\mathrm{sr}}}{R_{\mathrm{sw}}}\right) \\ \beta^{*} &= \sin^{-1}\left(\frac{w}{2R_{\mathrm{sw}}}\right) \\ \beta^{*}_{\mathrm{in}} &= 2\sin^{-1}\left(\frac{w}{2R_{\mathrm{sw,in}}}\right), \beta^{*}_{\mathrm{in}} < \frac{2\pi}{z_{\mathrm{sw}}} \end{aligned} \tag{3.4}$$

as well as:

$$\begin{gathered} L_{\mathrm{s}} = R_{\mathrm{sw}} \sin\beta_{\mathrm{s}},\ L_{\mathrm{d}} = R_{\mathrm{sw}} \sin\beta_{\mathrm{d}},\ L^{*} = (0.1 \sim 0.15) D_{\mathrm{sr}} \\ L_{\mathrm{rot,eff}} = L_{\mathrm{s}} + L_{\mathrm{d}} \end{gathered} \tag{3.5}$$

The selection of discharge angle β_{d} is linked to the total engaging angle of the starwheel α_{sw} and typically $\beta_{\mathrm{d}} = 0.7\, \beta_{\mathrm{s}}$. The starwheel engaging angle and the

corresponding groove wrap angle around the main rotor, α_{sr}, have an upper limit established by:

$$\alpha_{\mathrm{sr}} = \alpha_{\mathrm{sw}} \frac{z_{\mathrm{sw}}}{z_{\mathrm{sr}}} < \frac{2\pi}{N_{\mathrm{sw}}} \tag{3.6}$$

Typically, $\alpha_{\mathrm{sw}} \cong 90^{\circ}$ and the explanation is given by the following relationship between the number of teeth engaged simultaneously, $n_{\mathrm{sw,eng}}$, and the angular spacing of the teeth,γ:

$$\begin{aligned} &\alpha_{\mathrm{sw}} = 2\beta^{*} n_{\mathrm{sw,eng}} + 2.5\left(\gamma - 2\beta_{*}\right), \gamma = \frac{2\pi}{z_{\mathrm{sw}}} \\ &\alpha_{\mathrm{sw}} = \beta_{\mathrm{open}} + \beta_{\mathrm{s}} + \beta^{*} \end{aligned} \tag{3.7}$$

where β_{open} represents the point of discharge opening. It is therefore a variable that defines a limit and determines how far the groove wraps around the rotor prior to discharge. In other words, influences the swept volume at the discharge angle and therefore the internal volume ratio. Finally, the tooth width is usually regarded as independent variable. The wider the tooth, the wider is the groove which results in an increased groove volume. However, there is a structural limit related to the minimum groove tip thickness, Δ. The analytic expression of the tooth width w, with the geometry and structural limits is given by:

$$\begin{aligned} &\Delta = \xi\, D_{\mathrm{sr}},\ \xi = 0.017 \sim 0.025 \\ &w = 2\left(d_{\mathrm{sr,sw}} - \frac{D_{\mathrm{sr}}}{2}\right)\sin\frac{\gamma}{2} - \xi\, D_{\mathrm{sr}}\cos\frac{\gamma}{2} \end{aligned} \tag{3.8}$$

A good approximation can also be obtained as $w \approx 0.3\, R_{\mathrm{sr}}$. The geometric relationships can be developed on the basis of a reference system defined as in Fig. 3.4(a). In particular, a set of cylindrical coordinates $(z, r, \theta_{\mathrm{sr}})$ are positioned so that the z axis is coincident with the main rotor rotation axis and the r axis is perpendicular to the z axis and has its origin in correspondence of the perpendicular intersecting line from the starwheel rotation axis. A general point on the starwheel rotates in the z, r plane defined by the main rotor coordinates. On the starwheel an analogous reference system can be defined associated with the rotation angle θ_{sw} (see Figure 3.4(a)).

3.3.2 Meshing profile

The geometry and kinematics of the SSE are directly linked and it is necessary to solve the groove profile generation in order to accurately describe the machine. From the fundamentals of gear kinematics, the single-screw type of meshing can be seen as a double meshing worm gear [39]. The conjugate worm gear surfaces rely on continuous contact lines that ensure the load-transmission. By transferring this concept to an expander (or compressor), the calculation of the contact lines

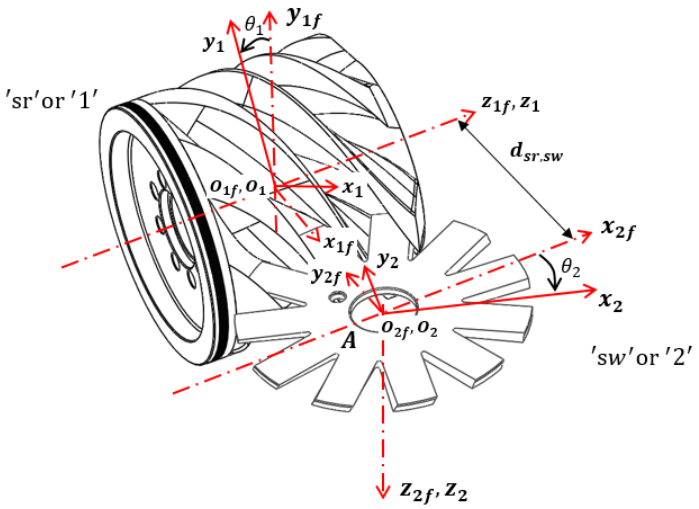

(a)

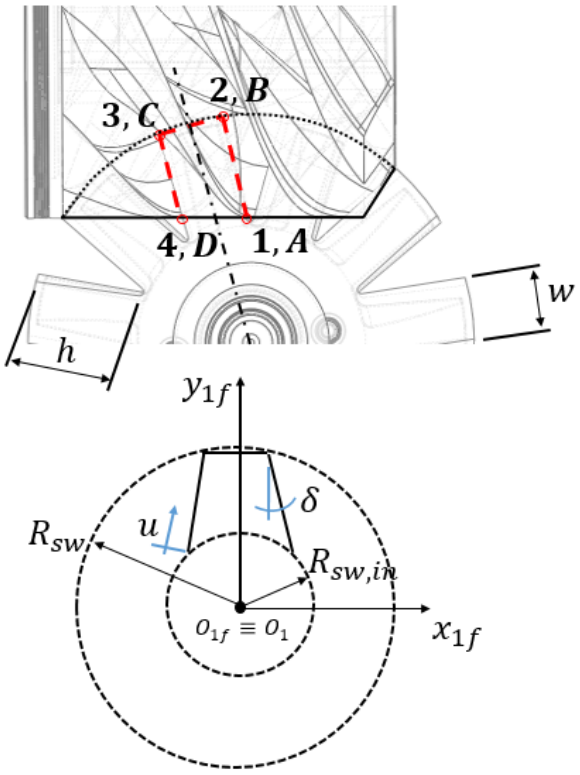

(b)

Figure 3.5: Schematics of the reference systems used to generate the groove profile: (a) main rotor and starwheel fixed and moving reference systems; (b) description of a single engaging tooth into the mating groove.

and the precision during the manufacturing determine the sealing capabilities of the expansion (or compression) chamber. Generally, both the direct and indirect problems have to be solved [39]. In the following, only the direct problem, i.e. the cutting tool (tooth profile in this case) is given and the conjugated groove profile is calculated. Furthermore, different approaches can be used for generating the rotor profile. Three of them are currently investigated in literature: single straight line envelope meshing pair (SSLEMP), multi-straight line envelope meshing pair (MSLEMP) and multi-column envelope meshing pair (MCEMP). The idea is to improve the contact points from a single line to a curved surface to increase the wear resistance of the profile. However, this change to the machining process of the groove also increases the difficulty of manufacture. Many manufacturing companies adopted SSEMP because of its simplicity and acceptable reliability in terms of working hours prior deterioration. Also the SSE considered in this study presents single line profile.

From the gear kinematics theory [39], the meshing process of the screw rotor (*sr*) with two starwheels (*sw*) can be described as an envelope of two-parameter family of surfaces with a cylindrical-plate (CP) configuration. In particular, the generating surface is represented by the starwheel, i.e. plate, (direct problem). The profile of the starwheel is obtained by applying the inverse envelope concept. A right-handed fixed, $O_{\mathrm{i,f}}(x_{\mathrm{if}}, y_{\mathrm{if}}, z_{\mathrm{if}})$, and a rotating, $O_{\mathrm{i}}(x_{\mathrm{i}}, y_{\mathrm{i}}, z_{\mathrm{i}})$, coordinate systems have to be defined for both screw rotor (i = 1) and starwheel (i = 2). Each starwheel tooth engages the mating groove with three sides, identified by segments $\overline{AB}$, $\overline{BC}$ and $\overline{CD}$. The generic representation of a starwheel tooth is proposed in Fig. 3.5(b). A tooth with parallel flanks is obtained by fixing $\delta = 0$. Each segment of the tooth is described by a parameter u. The second parameter is the thickness of tooth, t. By adapting the notation introduced in [39], the starwheel profile is expressed in general terms by:

$$\mathbf{R}_{2\mathrm{j}}(u,t) = \left[\mathbf{R}_{2\mathrm{j,x}}(u,t)\,\mathbf{R}_{2\mathrm{j,y}}(u,t)\,\mathbf{R}_{2\mathrm{j,z}}(u,t)\right]^{T}, \tag{3.9}$$

where $j = \overline{AB}, \overline{BC}, \overline{CD}$. The corresponding family of curves on the main rotor, $\mathbf{R}_{1\mathrm{j}}(u,t,\theta_1)$ are obtained through a rotation matrix $\mathbf{M}_{12}$ and ensuring the meshing condition at each angular position. The meshing equation imposes the sliding velocity between the two bodies in contact as zero, i.e. the cross product between the normal vector to the contact surface, $\mathbf{N}_f^1$, and the relative velocity $\mathbf{V}_f^{(12)}$ is zero. Mathematically, the system of equations that has to be solved simultaneously is given by:

$$\begin{cases} \mathbf{N}_f^{(1)} \cdot \mathbf{v}_f^{(12)} = \left(\frac{\partial \mathbf{R}_{1\mathrm{j}}}{\partial u} \times \frac{\partial \mathbf{R}_{1\mathrm{j}}}{\partial t}\right) \cdot \mathbf{v}_f^{(12)} = 0 \\ \mathbf{R}_{1\mathrm{j}} = \mathbf{M}_{12}\,\mathbf{R}_{2\mathrm{j}} \end{cases} \tag{3.10}$$

where $j = \overline{AB}, \overline{BC}, \overline{CD}$. In particular, the rotation matrix can be expanded as follows:

$$\mathbf{R}_{1j}(u,\theta_1) = \mathbf{M}_{1,1f}\mathbf{M}_{1f,2f}\mathbf{M}_{2f,2}\mathbf{R}_{2\mathrm{j}}(u,\theta_1). \tag{3.11}$$

Usually, to perform coordinate transformations, mixed matrix operations are needed. Homogeneous coordinates can be adopted to include only multiplications [39]. In particular, a general position vector $\mathbf{r}_m = [x_m, y_m, z_m]^T$ in a reference system $O_m(x_m, y_m, z_m)$ can be expressed in terms of homogeneous coordinates by introducing non-zero parameter t^*:

$$x = \frac{x^*}{t^*} \; y = \frac{y^*}{t^*} \; z = \frac{z^*}{t^*} \tag{3.12}$$

For convenience, the parameter is chosen to be unity, or $t^* = 1$:

$$\mathbf{r}_m = \left[x_m \, y_m \, z_m \, 1\right]^T \tag{3.13}$$

Additionally, the general expression of a rotation matrix from a "old" reference system m to a "new" one n is given by:

$$\mathbf{M}_{\mathrm{n,m}} = \begin{bmatrix} (i_n \cdot i_m) & (i_n \cdot j_m) & (i_n \cdot k_m) & (\overline{O_n O_m} \cdot i_n) \\ (j_n \cdot i_m) & (j_n \cdot j_m) & (j_n \cdot k_m) & (\overline{O_n O_m} \cdot j_n) \\ (k_n \cdot i_m) & (k_n \cdot j_m) & (k_n \cdot k_m) & (\overline{O_n O_m} \cdot k_n) \\ 0 & 0 & 0 & 1 \end{bmatrix} \tag{3.14}$$

where $\overline{O_n O_m}$ is the distance between the centers of reference systems. By considering the reference system O_1 on the screw rotor as in Figure 3.5(a), the system of equation of the meshing equation is given by:

$$\begin{cases} x_1 = -x_2 \sin\theta_{sw} \sin\theta_{sr} - y_2 \cos\theta_{sw} \sin\theta_{sr} + z_2 \cos\theta_{sr} + d_{sr,sw} \sin\theta_{sr} \\ y_1 = -x_2 \sin\theta_{sw} \cos\theta_{sr} - y_2 \cos\theta_{sw} \cos\theta_{sr} - z_2 \sin\theta_{sr} + d_{sr,sw} \cos\theta_{sr} \\ z_1 = x_2 \cos\theta_{sw} - y_2 \sin\theta_{sw} \end{cases} \tag{3.15}$$

where the relationship between θ_{sw} and θ_{sr} is given in Equation 3.1. By introducing the parametric curves of the tooth profile, it is possible to obtain a family of meshing curves. As previously mentioned, the meshing equations only consider the plain containing the straight-line profile, shown in Figure 3.6. However, as the tooth slides inside the mating groove, the upper and lower portions of the tooth need to avoid intersecting the groove flanks. A cross-section of a tooth is shown in Figure 3.7 and the sealing line is marked as a red dashed line which also divides the upper (named t) and lower portions of the tooth. In fact, the inclination of the groove, α_{groove}, at each point of contact *M*, varies according the following relationship with the relative velocities of starwheel and rotor:

$$tan\alpha_{\mathrm{groove}} = \frac{\mathrm{v_{sw}}}{\mathrm{v_{sr}}} = \frac{\omega_{\mathrm{sw}} r_{\mathrm{sw,M}}}{\omega_{\mathrm{sr}} r_{\mathrm{sr,M}}} = \frac{z_{\mathrm{sr}} r_{\mathrm{sw,M}}}{z_{\mathrm{sw}} r_{\mathrm{sr,M}}} \tag{3.16}$$

Therefore, three angles need to be defined to comply with meshing and milling requirements:

- α_1,α_2 on the front plane of the tooth;
- α_{11} on root plane of the tooth.

The limiting values of these angles, indicated on Figure 3.7, can be obtained from geometric relationships as:

$$\alpha_{1,\min} = tan^{-1}\left(i\frac{d_{\mathrm{sr,sw}} - R_{\mathrm{sw}}}{R_{\mathrm{sw}}}\right) \tag{3.17}$$

$$\alpha_{2,\max} = tan^{-1}\left(i\frac{R_{\mathrm{sr}}}{R_{\mathrm{sw}}}\right) \tag{3.18}$$

$$\alpha_{11} = tan^{-1}\left(i\frac{R_{\mathrm{sr}}}{d_{\mathrm{sr,sw}} - R_{\mathrm{sr}}}\right) \tag{3.19}$$

The total thickness of the tooth is usually selected from experience and it is typically in the range 6~8 mm. The upper thickness t is related to the manufacturing process in order to guarantee enough space for milling.

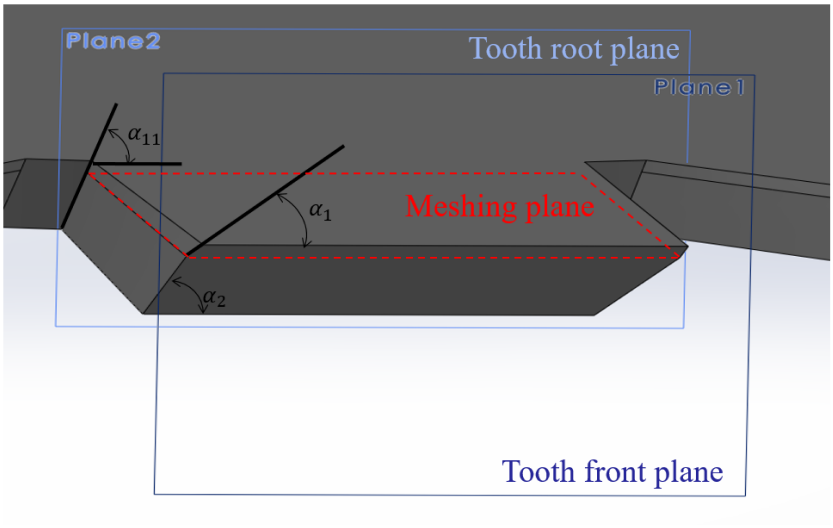

Figure 3.6: Design of tooth with straight-line meshing profile.

Figure 3.8 shows the rotor obtained through 3D cut-sweep by implementing the meshing equation in a parametric form with only one running parameter represented by the angular position. The parametric curve resulting from Equation 3.15 is overlaid in blue. The complete procedure to obtain the 3D rotor from a given tooth profile is explained in Appendix B.

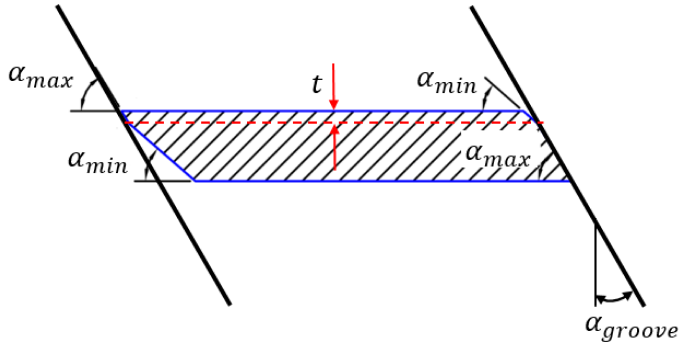

Figure 3.7: Design of tooth with straight-line meshing profile.

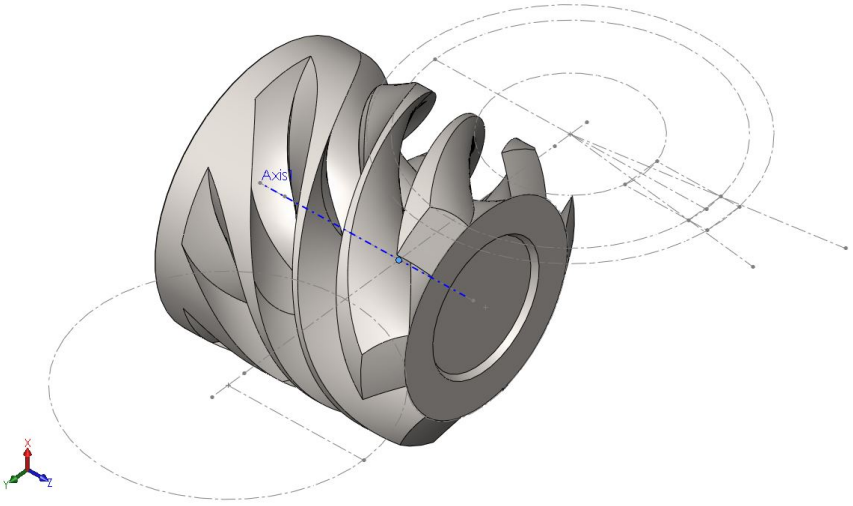

Figure 3.8: Absolute reference system O_1 on the main rotor. The origin is marked with a dot.

3.3.3 Groove Volume Calculation

The geometry of a single-screw machine has been defined and by making use of the relationships developed it is possible to mathematically describe on a 2D-plane the single-screw assembly by means of cylindrical coordinates (z,r), as shown in Figure 3.9. Such graphical representation allows to define three methodologies to obtain the swept volume of the machine as well as the variation of the groove volume over one rotation of the main rotor. In particular, three mathematical approaches are presented and described here with the aim of showing their

limitations, if any. The three methods will be compared in Section 3.4.

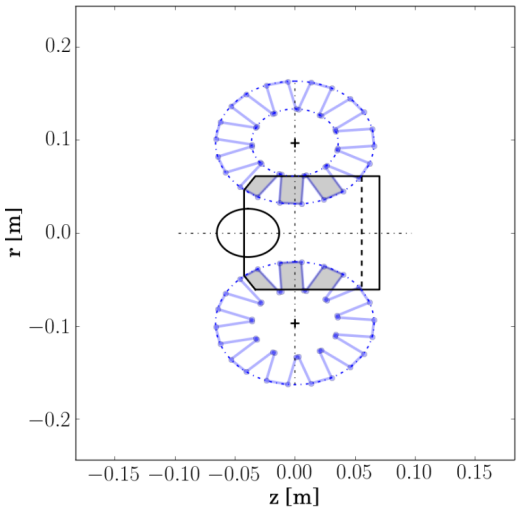

Figure 3.9: Planar representation of single-screw geometry with polygon approach (adapted from [29]).

3.3.3.1 Polygon approach for the calculations of the chamber volume and its derivative

The description of complex geometries by means of polygons has been widely adopted in compressor modeling especially concerning scroll [40] and single-screw types [19, 21, 23]. In the case of single-screw machine, the portion of tooth engaged with the groove can be described analytically by defining the coordinates of the four corner points, which represents the limits of the tooth engaged with the respective groove, as shown in Figure 3.5(b). By considering the reference system (z, r) as in Figure 3.5(b), the analytic expressions for the

$(z,r)_{j=1..4}$ are listed below:

$$
\begin{aligned}
z_1(\theta_{\mathrm{sw}}) &= a \cdot \tan(\theta_{\mathrm{sw}}) - \frac{w}{2\,cos(\theta_{\mathrm{sw}})} \\
r_1(\theta_{\mathrm{sw}}) &= R_{\mathrm{sr}} \\
z_2(\theta_{\mathrm{sw}}) &= R_{\mathrm{sw}} \sin(\theta_{\mathrm{sw}} - \beta^*) \\
r_2(\theta_{\mathrm{sw}}) &= d_{\mathrm{sr,sw}} - R_{\mathrm{sw}} \cos(\theta_{\mathrm{sw}} - \beta^*) \\
z_3(\theta_{\mathrm{sw}}) &= R_{\mathrm{sw}} \sin(\theta_{\mathrm{sw}} + \beta^*) \\
r_3(\theta_{\mathrm{sw}}) &= d_{\mathrm{sr,sw}} - R_{\mathrm{sw}} \cos(\theta_{\mathrm{sw}} + \beta^*) \\
z_4(\theta_{\mathrm{sw}}) &= a \cdot \tan(\theta_{\mathrm{sw}}) + \frac{w}{2\,cos(\theta_{\mathrm{sw}})} \\
r_4(\theta_{\mathrm{sw}}) &= R_{\mathrm{sr}}
\end{aligned}
\tag{3.20}
$$

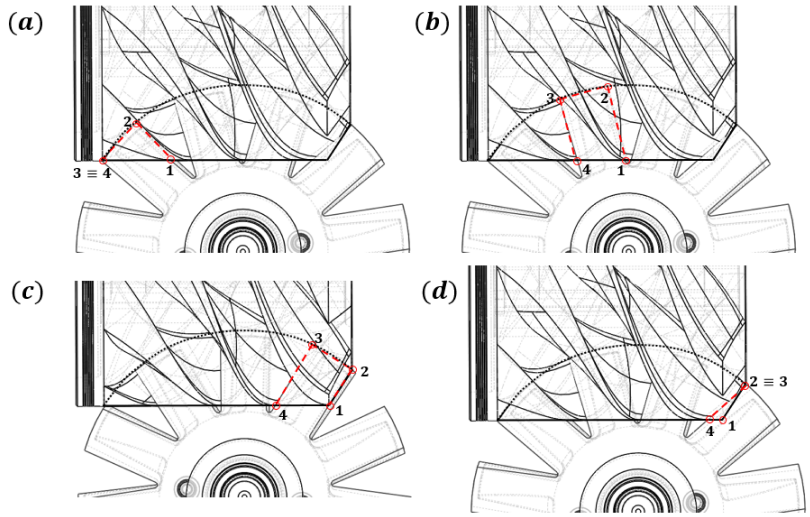

Figure 3.10: Tooth engaging positions in a single-screw expander: (a) during suction process; (b) during closed expansions; (c) discharge opening; (c) discharge process.

However, the tooth engaging process presents at least four general conditions, as shown in Figure 3.10. The analytic descriptions of the four corners of the tooth are valid only from tooth engaging conditions *(a)* through *(c)*. Bein at Hamilton [20] introduced a simplified function to describe the engaging condition *(d)*. Ignatiev [27] extended the polygon description by considering a complete tooth until the starwheel center. A numerical algorithm was developed to numerically obtain the intersecting area between tooth and rotor with particular care on determining whether a point was located inside or outside a polygon as well as the possibility of obtaining multiple polygons. In the present work, the approach proposed by

Ignatiev is extended by describing the rotor and both starwheels as polygons. Boolean operations are employed to obtain the engaged portions of the teeth on both sides of the rotor, as shown in Figure 3.9. There are two main advantages that follows by adopting such generalized approach. First of all, as a tooth is leaving the mating groove, it is possible to account for the fourth tooth that starts engaging. Secondly, once a tooth is completely disengaged, the groove is engaged on the opposite side of the rotor and as the rotation proceeds the groove decreases its volume on one side and simultaneously increases on the other side. Since both starwheels are considered, it is possible to obtain the complete evolution of the groove volume over one complete rotation of the rotor.

The groove volume as well as the porting cross-sectional areas are formed by intermeshing of solid surfaces. Therefore, such quantities (volumes and areas) can be obtained from the description of the solid surfaces (main rotor and starwheels). Green's theorem can be directly applied to this purpose as demonstrated by Ignatiev [27] and Bell et al. [41]. In particular, over a region D in a x-y plane contained in $\mathbb{R}^2$, with boundary ∂D, Green's theorem states:

$$\oint_{\partial D} P(x,y)dx + Q(x,y)dy = \iint_D \left(\frac{\partial Q}{\partial x} - \frac{\partial P}{\partial y}\right) dxdy, \tag{3.21}$$

where the left side is a line integral and the right side is a surface integral and the functions $P(x,y)$ and $Q(x,y)$ have continuous first order partial derivatives on D. The path of integration of the line integral is anticlockwise. It follows that, for example, if $P = x$ and $Q = -y$, the area of D is given by:

$$D = \frac{1}{2} \oint_{\partial D} xdy - ydx \tag{3.22}$$

and it relates the area of a region and the line integral around its boundary. By approximating the integral with a finite difference form, the area of D can be expressed in term of (x,y) coordinates of the boundary ∂D. If the boundary is a polygon then the finite difference form gives the exact solution:

$$D = \frac{1}{2} \sum_{i=1}^{N-1} = (x_{j+1} + x_j)\,(y_{j+1} - y_j) \tag{3.23}$$

to be noted is that in this formulation the area D is signed. Similar procedure can be applied to calculate a volume. By substituting $P = 0$ and $Q = x^2/2$, the volume of a solid in cylindrical coordinates is expressed by:

$$V = 2\pi \oint_{\partial D} \frac{x^2}{2} dy \tag{3.24}$$

In the case of non-axisymmetrical volume computation with $\phi = [\phi_1, \phi_2]$ becomes:

$$V = \int_{\phi_1}^{\phi_2} d\phi \oint_{\partial D} \frac{x^2}{2} dy \tag{3.25}$$

Again, the finite difference formulation can be employed to approximate the integral:

$$V = \sum_{i=1}^{M} \Delta\phi \left[\frac{x_i^2 + x_i x_{i-1} x_{x-1}^2}{6} \left(y_i - y_{i-1}\right) \right]_i \tag{3.26}$$

The obtained finite difference forms can be directly applied to the single-screw geometry problem. In fact, knowing the coordinates of the intersection contour between teeth and main rotor from polygon boolean operations, the appropriate area or volume can be calculated.

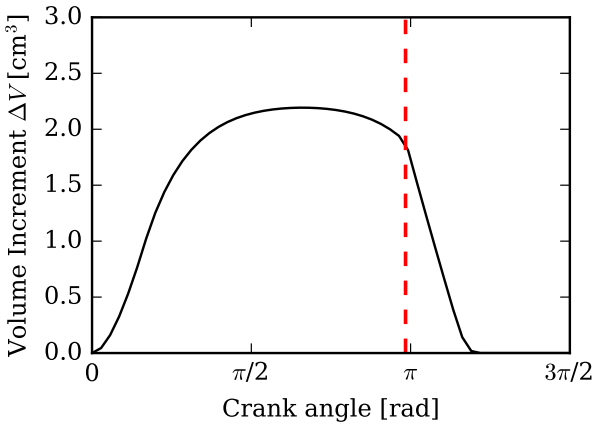

Figure 3.11: Groove incremental volume [23].

The discrete increment of the groove volume is given by the product of the engaging tooth area S and the distance of its centroid from the main rotor axis, c_r, at each rotation angle [19, 21, 27]:

$$\Delta V = A_{\text{tooth}} \left(\Delta\theta_{\text{sw}}\right) c_z \Delta\theta_{\text{sr}} = A_{tooth} \left(\Delta\theta_{\text{sw}}\right) c_z i \Delta\theta_{\text{sw}} \tag{3.27}$$

with:

$$A_{\text{tooth}} = \sum_{j=0}^{n-1} \left| \frac{z_j r_{j+1} - z_{j+1} r_j}{2} \right| \tag{3.28}$$

$$c_r = \frac{1}{6A_{\text{tooth}}} \sum_{j=0}^{n-1} \left(r_{j+1} + r_j\right) \left(z_j r_{j+1} - z_{j+1} r_j\right) \tag{3.29}$$

Equation 3.27 gives the incremental volume of the groove until the tooth disengages completely from the groove. Since the calculation can be performed throughout one rotation of the main rotor, the incremental volume curve of the groove can be obtained without any approximations as shown in Figure 3.11. The total groove volume is calculated as a sum of each discrete volume increment as,

$$V = \sum_{j} \Delta V_j \left(\Delta\theta_{\text{sw}}\right) \tag{3.30}$$

By introducing (3.28) and (3.29) in (3.27), the final expression of the volume can be obtained [27]:

$$V = \sum_{i}^{n_{\text{step}}} \Delta\theta_{\text{sr}} \Big[\sum_{j} \frac{z_j^2 + z_j z_{\text{j-1}} + z_{j-1}^2}{6} \left(r_j - r_{j-1}\right) \Big]_i \tag{3.31}$$

where the running index j represents the number of corner points of the tooth and the index i is the number of angular steps chosen. The volume of the groove over one rotation of the main rotor is obtained as a number of discrete points. Since running the geometry model at each time step would result in high computational time, the discrete points are interpolated by means of cubic spline. The derivative of the volume with respect to the crank angle is obtained by applying a forward difference scheme:

$$\frac{dV}{d\theta} = \frac{V(\theta + \delta) - V(\theta)}{\delta} \tag{3.32}$$

with $\delta = 10^{-4}$ and $dV(\theta = 0) = 0$.

3.3.3.2 Differential approach

The volume of the groove at each starwheel angle (or equivalently main rotor angle) can be calculated by describing the engaging tooth surface with a local reference system $(x_{\text{tooth}}, y_{\text{tooth}})$ on the tooth. In particular, Sun [26] described the procedure to obtain the total groove volume by performing a numerical integration of a function describing the tooth area during the rotation, $A_{tooth}(y, \theta_{\text{sw}})$, over two parts of the groove, i.e. $V_{g,1}(\theta_{\text{sw}})$ and $V_{g,2}(\theta_{\text{sw}})$. In the case of a single-screw expander, the groove volume is given by:

$$V_g(\theta_{\text{sw}}) = \begin{cases} \frac{i}{2} \int_{\beta_s+\beta^*}^{\theta_{\text{sw}}} \int_{-w/2}^{B} A_{\text{tooth}}(y, \theta_{\text{sw}}) dy\, d\theta_{\text{sw}}, & \beta_{\text{s}} + \beta^* \leq \theta_{\text{sw}} \leq \beta_{\text{close}}, \\ V_{\text{g,2}} - \frac{i}{2} \int_{\theta_{\text{sw}}}^{\beta_{\text{d}}} \int_{-w/2}^{w/2} A_{\text{tooth}}(y, \theta_{\text{sw}}) dy\, d\theta_{\text{sw}}, & \beta_{\text{close}} < \theta_{sw} \leq \beta_d, \end{cases} \tag{3.33}$$

with:

$$B = R_{sw} \sin\left[\cos^{-1}\left(\frac{d_{sr,sw} - R_{sr}}{R_{sw}}\right) - \theta_{\text{sw}}\right], \tag{3.34}$$

where V_{g1} and V_{g2} correspond to the description of the volume for three and four corners engaging condition of the tooth respectively, as shown in Fig. 3.5(b). As stated before, by considering the local reference system on the tooth, the infinitesimal area of the tooth engaged in the main rotor groove is $dA_{\text{tooth}} = x dy$ and the coordinate x is defined by a geometric relationship:

$$x = \sqrt{R_{\text{sw}}^2 - y^2} - x \tan\theta_{sw} - \frac{d_{\text{sr,sw}} - R_{\text{sw}}}{\cos\theta_{\text{sw}}} \tag{3.35}$$

The infinitesimal volume of the groove is then

$$dV_{\mathrm{g}} = dA_{\mathrm{tooth}} \frac{R_{\mathrm{sr}} d\theta_{\mathrm{sr}} + \left(R_{sr} - x\cos\theta_{\mathrm{sw}}\right) d\theta_{\mathrm{sr}}}{2} \tag{3.36}$$

where $d\theta_{\mathrm{sr}} = i\, d\theta_{\mathrm{sw}}$. To be noted is that the integration of (3.33) leads to obtain the volume of the groove until the discharge angle β_d.

3.3.3.3 Analytic approach

On the basis of the differential approach described by Sun et al. [26], analytic solutions for the two different parts of the groove V_{g1} and V_{g2} can be obtained. The analytic description of the groove volume was presented by Sun G. [24]. In particular, $V_{\mathrm{g},1}$ represents the groove volume when the tooth is engaged as in case *(a)* of Figure 3.10:

$$\begin{aligned} V_{\mathrm{g1}}\left(\theta_{\mathrm{sw}}\right) = i\Bigg\{ & d_{\mathrm{sw,sr}} \left(R_{\mathrm{sw}}^2 \beta^* + \frac{w}{2}\sqrt{R_{\mathrm{sw}}^2 - \frac{w^2}{4}} \right) \left(\beta_s - \beta^* - \theta_{\mathrm{sw}}\right) \\ & - \left(\frac{R_{\mathrm{sw}}^2 w}{2} - \frac{w^3}{12} \right) \left[sin\left(\beta_{\mathrm{s}} - \beta^*\right) - sin\theta_{\mathrm{sw}} \right] \\ & - \frac{1}{4} \left[\left(d_{\mathrm{sw,sr}} + R_{\mathrm{sr}}\right) aw + \frac{w^3}{12} \right] \left[log\frac{1 + sin\left(\beta_{\mathrm{s}} + \beta^*\right)}{1 - sin\left(\beta_{\mathrm{s}} - \beta^*\right)} - log\frac{1 + sin\theta_{\mathrm{sw}}}{1 - sin\theta_{\mathrm{sw}}} \right] \Bigg\} \end{aligned} \tag{3.37}$$

which is limited by the angle β_*. When the starwheel rotation angle $\beta_* < \theta_{\mathrm{sw}} \leq \beta_{\mathrm{open}}$, the groove volume is expressed by:

$$\begin{aligned} V_{\mathrm{g2}}\left(\theta_{\mathrm{sw}}\right) = & \frac{i\left(\beta_s + \beta^* - \theta_{\mathrm{sw}}\right)^3}{12\beta_*} \left[R_{\mathrm{sw}}^2 \beta_* + \frac{w}{2}\sqrt{R_{\mathrm{sw}}^2 - \frac{w^2}{4}} - aw\frac{1}{cos\left(\beta_{\mathrm{s}} - \beta^*\right)} \right] \\ & \left\{ R_{\mathrm{sr}} - \frac{1}{8\beta^*} \left[R_{\mathrm{sw}} cos\left(\beta_{\mathrm{s}} - 2\beta^*\right) - a \right] \left(\beta_{\mathrm{s}} + \beta^* - \theta_{\mathrm{sw}}\right) \right\} \end{aligned} \tag{3.38}$$

The groove volume at discharge opening is obtained as the sum of the two contributions:

$$V_{\mathrm{g}} = V_{\mathrm{g1}} + V_{\mathrm{g2}} \tag{3.39}$$

3.3.4 Unwrapped groove curves

The geometric parameters of the main rotor have been defined. However, the porting and the sealing lines are still to be determined. Each of the grooves wrap around the cylindrical surface of the main rotor with an angle close to pi.

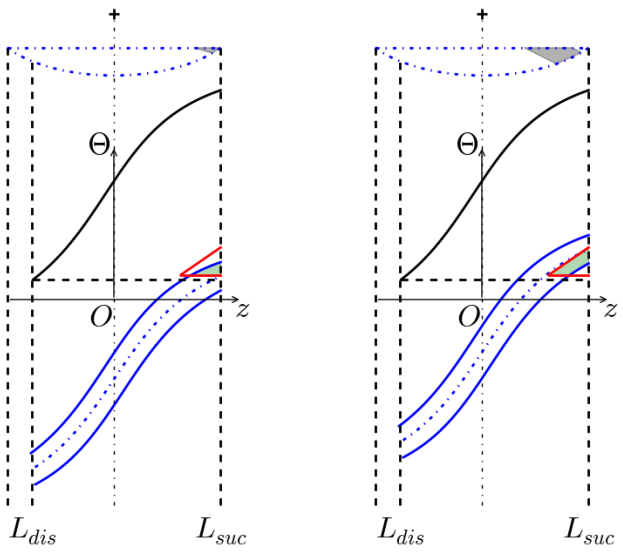

(a) (b)

Figure 3.12: Unwrapped representation of a groove with the suction port over laid.

Therefore, it is possible to derive the helical equation of the groove on a 2D plane in order to obtain its unwrapped description [18]. A local reference system (Θ, z) is introduced to define the groove on a plane where Θ is the unwrapped curvilinear coordinate of the rotor and z is the coordinate along the main rotor axis, as shown in Figure 3.12. In the (Θ, z), the extremities of each groove line have a distance equal to the wrap angle. Mathematically:

$$\begin{cases} \Theta = a\tan\theta_{\mathrm{sw}} \pm \frac{w}{2\cos\theta_{\mathrm{sw}}} & -\beta_{\mathrm{open}} \le \theta_{\mathrm{sw}} \le \alpha_{\mathrm{r}}(\alpha_{\mathrm{l}}) \\ z = R_{\mathrm{sw}} i\left(\theta_{\mathrm{sw}} + \beta_d\right), \end{cases} \tag{3.40}$$
$$\alpha_{\mathrm{r}}(\alpha_{\mathrm{l}}) = \cos^{-1}\left(\frac{d_{\mathrm{sr,sw}} - R_{\mathrm{sr}}}{R_{\mathrm{sw}}}\right) \pm sin^{-1}\left(\frac{w}{D_{\mathrm{sw}}}\right)$$

where the $\pm$ sign is related to the subscripts r, $(+)$, and l, $(-)$, i.e. right and left sides of the groove, β_{open} is the opening angle which is influenced by the rotor end angle, β_{end}. The unwrapped groove is plotted in Figure 3.12. The planar representation of the groove is necessary in order to obtain the suction port area as function of the rotation angle as well the exact suction closure angle which

determined the internal volume ratio.

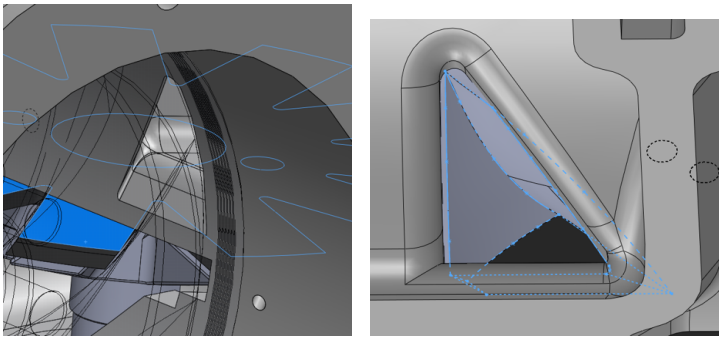

(a) (b)

Figure 3.13: CAD view of the suction port area from (a) inside and (b) from suction pocket.

As show in Figure 3.12, the triangular port shape is overlaid and it is described as a polygon ∂A_{suc}. The suction port polygon can be directly obtained from CAD model as in Figure 3.13 or by approximating the port as a triangle. The actual suction area is obtained by intersecting ∂A_{suc} with the polygon representing the groove ∂G, or:

$$A_{\text{suc}}(\theta_{\text{sr}}) = (\partial G \bigcap \partial A)_{\Delta\theta_{\text{sr}}} \tag{3.41}$$

The discharge process consists of two different porting. When a tooth reaches $\theta_{\text{sw}} = \beta_{\text{open}}$, as illustrated in Figure 3.14, the axial port corresponding to the end of the groove opens. The area can be calculated knowing the distance between the end of groove trailing edge and the meshing plane of the tooth. As the groove further rotates, it intersects with the radial circular discharge port. Polygon clipping can therefore be applied in a similar fashion to the suction port calculations.

Since the groove profile is known in as a discrete set of points, it is straight forward to calculate the groove leading and trailing edge lengths. The length of the groove tip leakage line at each main rotor angular position is given by,

$$L_{leak,tip} = \sum_{i\cdot\beta_s}^{\theta_{sr}} \sqrt{(\Delta\Theta)^2 + (\Delta z)^2} \tag{3.42}$$

The groove sealing lines over one complete rotation are shown in Figure 3.15.

3.3.5 Tooth sealing lines

The tooth sealing lines can be obtained by calculating the distances of each corner of the tooth engaged with the mating groove. In particular, for each engaging conditions (see Figure 3.10) the number of sealing lines varies. As the vertices

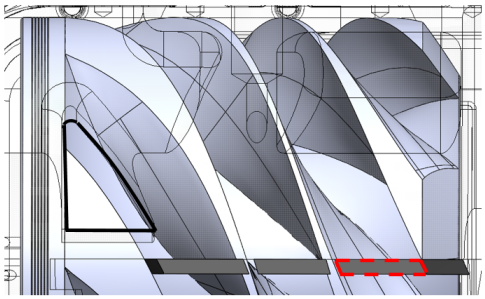

Figure 3.14: 3D view of meshing condition at the beginning of the discharge, i.e. $\theta_{sw} = \beta_{\text{open}}$.

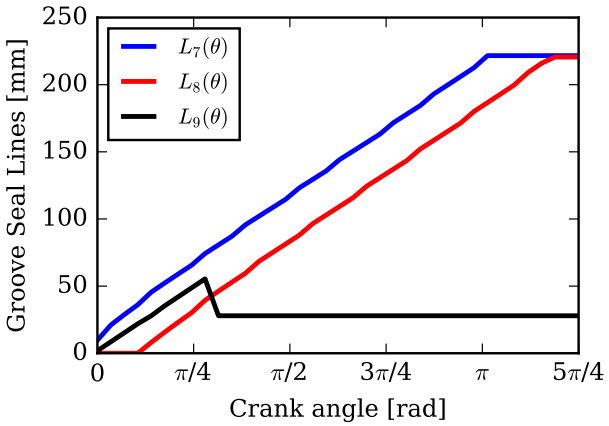

Figure 3.15: Length of the groove sealing lines: leading edge line L_7*, trailing edge line* L_8 *and end-band line* L_9.

of tooth intersected area area known, the sealing lines are obtained by simply calculating the distances between the corners. The sealing line at the root of the tooth corresponds to the gap with the housing which is necessary to allow the rotation of the starwheel. The evolution of the tooth sealing line lengths are shown in Figure 3.16. The perimeter of the tooth is obtained by summing each side of the engaged area in existence at a certain angle.

3.3.6 Calculation of the groove surface area

The groove of main rotor is generated by three contact lines, i.e. sides of the tooth and top of the tooth, Figure 3.17. In order to develop a mechanistic model, the surface of the groove as well as the hydraulic diameter of the cross-section

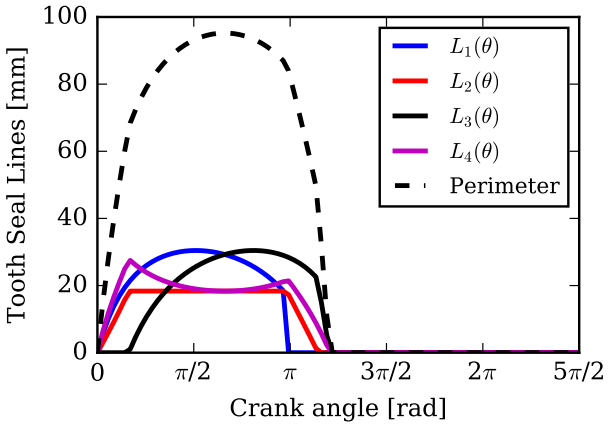

Figure 3.16: Length of tooth sealing lines and groove cross-section perimeter.

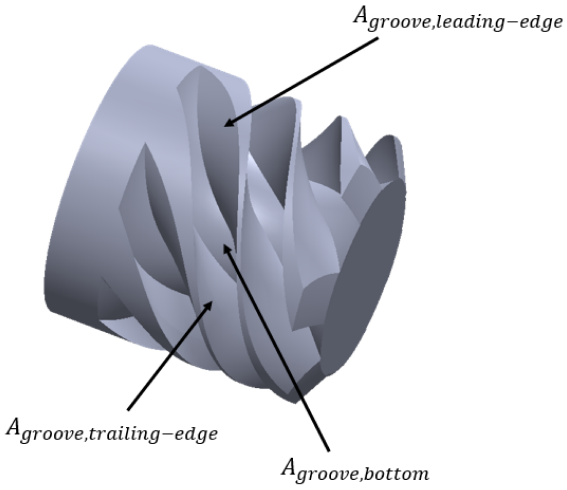

Figure 3.17: Groove surfaces

are to be determined because they are fundamental geometric properties for the estimation of the heat transfer rate during the expansion (or compression) process. Furthermore,by knowing the surface of the groove flanks, the pressure loads can also be computed. By intersecting the tooth polygon with the main rotor, each side of the tooth portion engaged are known.

The surface of the groove can be determined by applying Green's theorem and

by approximating the integral with finite difference form:

$$\begin{aligned} A_{\text{groove}} &= \sum_{i}^{n_{\text{step}}} \Delta\theta_{\text{sr}} \Big[\sum_{j=0}^{n-1} |\partial A_{\text{tooth}}|_{\overline{\text{AB}},\overline{\text{BC}},\overline{\text{CD}}} \Big]_i \\ &= A_{\text{groove,leading-edge}} + A_{\text{groove,trailing-edge}} + A_{\text{groove,bottom}} \end{aligned} \tag{3.43}$$

where $\partial A_{\text{tooth}}$ is the tooth perimeter limited to the three (or two) sides engaged within the groove (see Figure 3.10). Each side of the groove surface and their sum are shown in Figure 3.18.

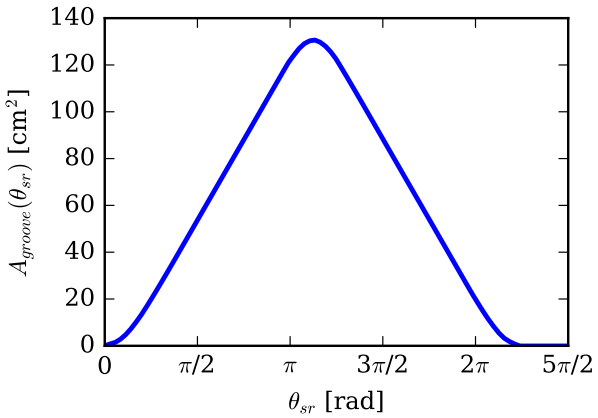

Figure 3.18: Groove surface area as function of main rotor rotation angle.

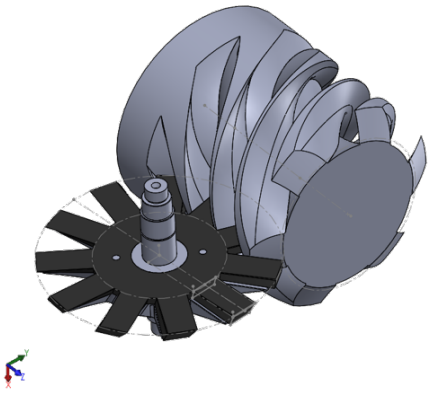

Figure 3.19: 11 kW single-screw expander assembly.

3.4 Geometry model results

The geometry model developed is applied to a single-screw expander whose geometry details are listed in Table 3.1. The assembly starwheel and rotor obtained from the geometry model can be seen in Figure 3.19. In order to develop a mechanistic model, the volume of the groove during one complete rotation needs to be determined.

Parameter	Value	Description
D_{sr}	121.9 mm	Main rotor diameter
D_{sw}	132.0 mm	Starwheel diameter
$d_{sw,sr}$	97.05 mm	Distance main rotor and starwheel
t_{tooth}	5.33 mm	Tooth thickness
L_s	55.25 mm	Rotor length suction side
L_d	42.24 mm	Rotor length discharge side
A_{suc}	303.92 mm^2	Maximum suction port area

Table 3.1: Geometry details of single-screw expander.

In Section 3.3.3, three approaches used in literature have been presented to calculate the volume of the groove. A comparison between the different mathematical models of the groove volume is proposed in Figure 3.20. To be noted is that the volume curves resulting from each method are consistent until the discharge opening. A slight difference, around 3%, exists with respect to the polygonal approach. Beyond that point, only the the polygon method can accurately describe the complete evolution of the groove volume during one rotation of the main rotor. The numerical difference between the numerical integration and the analytic solution is negligible. However, the latter one reduces the overall computational time.

The complete volume curve evolution as well as the areas of suction and discharge ports are reported in Figure 3.21.

The evolution of the suction port area with respect the main rotor rotating is over laid on the same figure. A similar behavior can also be found in [19]. As a consequence, it is possible to optimize the suction process by investigating the shape and the area of the suction port. To be noted is that in Figure 3.22, that at the current position of incipient discharge opening, the groove volume is not at its maximum. This is a characteristic of the single-screw. By delaying the opening (β_{open}) it is possible to adjust the volume at discharge. In general, the swept volume can be defined as a function of D_{sr}^3, [24]. The swept volume is calculated by correlating the engaging tooth area into the corresponding groove and the tooth engaging angle. Additionally, the axial and discharge porting have been calculated. The rotation of the starwheels (see Figure 3.9) and the sliding of the

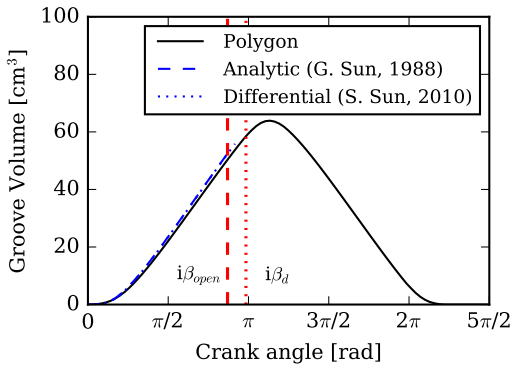

Figure 3.20: Comparison of different methods for calculating the groove volume as a function of the rotating angle of the main rotor.

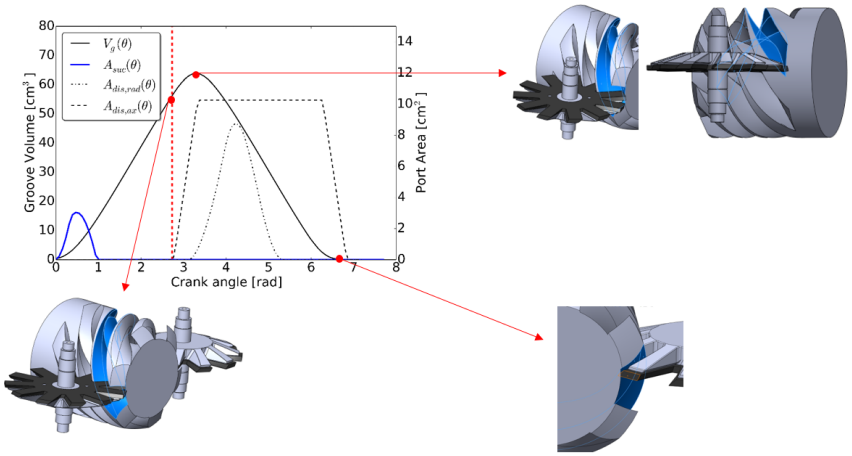

Figure 3.21: Groove volume and port area evolution with respect to the main rotor crank angle. 3D CAD views help visualize discharge opening, maximum groove volume and discharge end situations.

unwrapped groove (see Figure 3.12) are executed simultaneously in the simulation code. Therefore, the model can be used to evaluate the internal built-in volume ratio of the single-screw expander. In fact, by introducing the real geometry of the suction port and its location, the polygon clipping algorithm recognizes when the groove is intersecting the suction port until suction closure, as shown in Figure 3.22. Since the angle at which the discharge process begins can be calculated, β_{open}, the volume ratio can be calculated as:

$$r_{\mathrm{v,built-in}} = \frac{V_{\mathrm{g},2}}{V_{\mathrm{g},1}} = \frac{V_{\mathrm{g}}(\theta_{\mathrm{sw}} = \beta_{\mathrm{open}})}{V_{\mathrm{g}}(\theta_{\mathrm{sw}} = \beta_{\mathrm{s,close}})} \tag{3.44}$$

The calculation of $V_{g,1}$ and $V_{g,2}$ with the polygon method is validated by using the CAD model. In particular, the volume of the grooves at suction closure and discharge opening can be obtained from Solidworks, as shown in Figure 3.23(a) and Figure 3.23(b). The comparison between polygon model and the CAD model is reported in Table 3.2.

Parameter	CAD volume	Polygon volume	Relative error
$V_{g,1}$ [cm^3]	11.056	10.739	2.86%
$V_{g,2}$ [cm^3]	52.714	52.697	0.322%
$V_{g,max}$ [cm^3]	68.396	65.892	3.66%

Table 3.2: Validation of the groove volumes.

The correct estimation of the geometric internal volume ratio allows to analyze the expander and ORC system matching problem that has been described in Section 1.2.2.

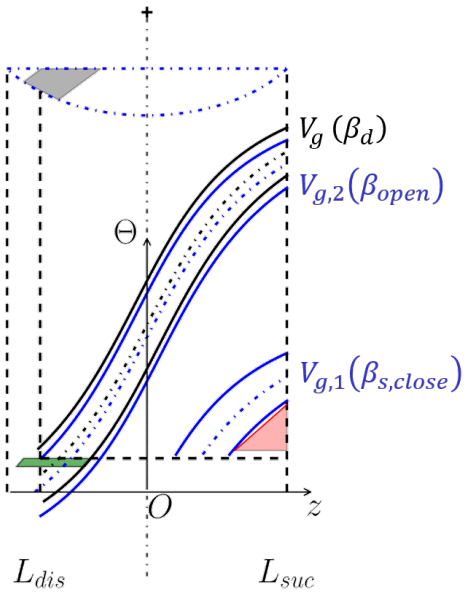

Figure 3.22: Numerical calculation of the internal volume ratio of a single-screw machine.

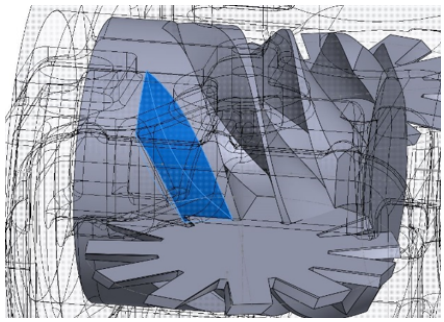

(a)

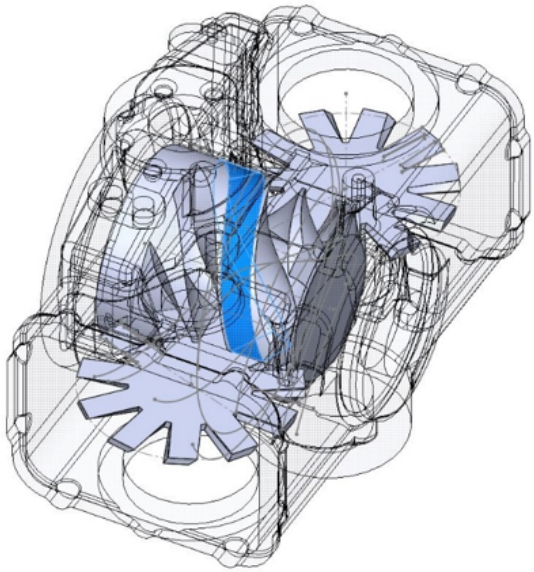

(b)

Figure 3.23: Tridimensional view of groove volume in two particular conditions that defines the internal volume ratio: (a) suction closure; (b) discharge opening.

The theoretical volume flow rate is calculated as:

$$\dot{V}_{\mathrm{th}} = 2z_{\mathrm{sr}} \frac{V_{\mathrm{g},2}}{r_{\mathrm{v,builtin}}} N. \tag{3.45}$$

which suggest that each groove is employed twice per revolution.

Additional consideration can be made on the design configuration of the single-screw. The main rotor is designed with 6 threads and the starwheel with 11 teeth, see Figure 3.19. The number of threads can be determined by the desired compression or expansion ratio [19]. An increase in the number of threads causes

an increase in the compression ratio but also a reduction in the swept volume. Up to a compression ratio of 3 or 4, it is possible to use screws with 4 threads. For higher ratios, ranging from 7 to 10, it is preferable, in order to obtain an optimum thermodynamic efficiency, to use screws with 6 threads. It is possible to obtain higher compression ratios, ranging from 10 to 16, by using screws having 8 threads, or by means of other single-screw design configurations. The number of starwheel teeth and the number of screw threads are to be selected with no common factors so that each tooth sweeps each groove from turn to turn. Thus, it is not necessary in assembling the machine to be concerned with a preferential position of a tooth with respect to a given thread. During early developments of such machine [4], it was found that the minimum dimension of the starwheel should have been substantially equal to that of the main screw. Since 7 teeth resulted in a starwheel which would have meshed with the screw over nearly 180° and would have left no place for the starwheel shaft, the next highest integer having no common factor with 6 was selected, namely 11.

For a fixed 6/11 configuration, the maximum groove volume is influenced by the degree of penetration of the tooth into the groove, h, and by the ratio between starwheel and main rotor diameters, λ_{d}. It can be demonstrated that the degree of penetration is a function of λ_{d} and λ_{opt} which essentially relates the dimensions of the starwheel and main rotor to the distance between the rotation axes:

$$h = \frac{R_{\mathrm{sr}} - (R_{\mathrm{sw}} - a)}{R_{\mathrm{sr}}} = R_{\mathrm{sr}} \left[1 - (\lambda_{\mathrm{d}} - 2\lambda_{\mathrm{opt}} + 1)\right] \tag{3.46}$$

A parametric study is conducted to analyze the effect of the degree of penetration on the maximum groove volume as well as on the tooth dimensions by employing the detailed geometry model developed in the present chapter. In particular, the main rotor diameter is kept fixed as in Table 3.1, and the parameter ζ is chosen equal to 0.017 to ensure the structural integrity of the groove tip. Three values of λ_{d} are selected to be representative of the usual design range: 0.9, 1 and 1.1. The parameter λ_{opt} is bounded between 0.6 and 0.9. The results of calculations are shown in Figure 3.24(a) and Figure 3.24(b). For a given λ_{opt}, as λ_{d} increases (meaning the starwheel diameter is increasing), the tooth width decreases but the maximum groove volume increases. The increase of the degree of penetration is predominant compared to the reduction of tooth width and therefore groove width. The design space of the single-screw lies in the range $\lambda_{\mathrm{d}} = 1 \sim 1.1$. Beyond $\lambda_{\mathrm{d}} = 1.1$, a larger rotor is preferred. For a given λ_{d}, the maximum groove volume increases significantly at first with the simultaneous decrease of tooth width, until the reduction of tooth width outweighs the longer tooth. Depending on the value of λ_{d}, a fairly flat maximum can be identified which represents the design space. It follows that for a given main rotor dimensions, the displacement can be modified by varying the groove dimensions but also the internal volume ratio achievable can be adjusted.

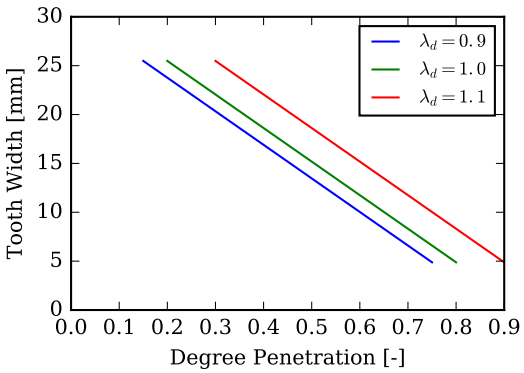

(a)

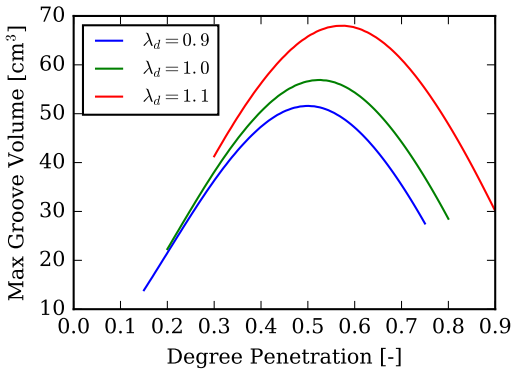

(b)

Figure 3.24: Influence of the degree of penetration of the starwheel into the main rotor on (a) *tooth width and* (b) *maximum groove volume.*

The effect of λ_{opt} on the single-screw design for a fixed λ_{d} is shown in Figure 3.25. In particular, by imposing λ_{d} = 1, three values of λ_{opt} have been considered, i.e. 0.75, 0.8 and 0.85. As λ_{opt} increases the tooth becomes shorter and wider causing a decrease in swept volume. The single-screw expander considered in the present work has λ_{d} = 1.083 and λ_{opt} = 0.796.

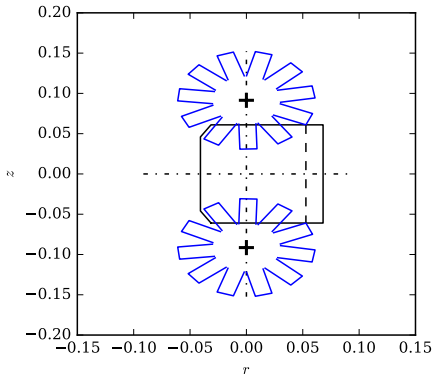

(a) $\lambda_{\text{opt}} = 0.75$

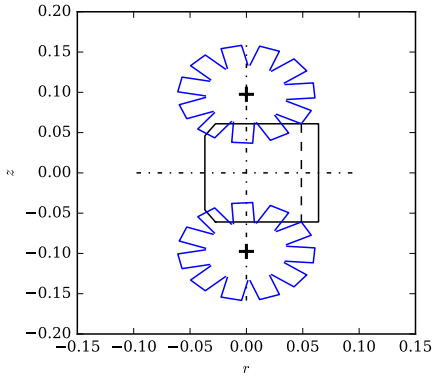

(b) $\lambda_{\text{opt}} = 0.8$

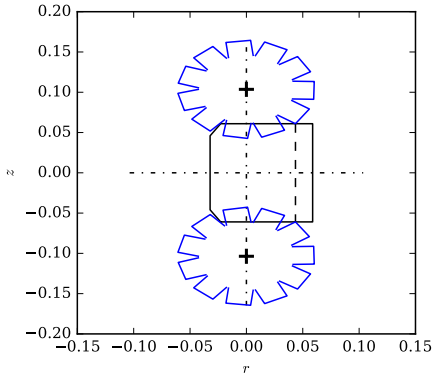

(c) $\lambda_{\text{opt}} = 0.95$

Figure 3.25: Effect of λ_{opt} on the signle-screw design.

References

[1] G. Vrinat. *Helical or screw compressors*. International Journal of Refrigeration, 7(2):107–114, 1984.

[2] B. Zimmern. *Worm rotary compressors with liquid joints*, 1965.

[3] B. Zimmern. *Rotary Injection Worm and Worm Wheel with Specific Tooth Shape*, 1976.

[4] B. Zimmern and G. C. Patel. *Design and Operating Characteristics of the Zimmern Single Screw Compressor*. In International Compressor Engineering Conference, 1972. Paper 16.

[5] J. R. Clark, J. M. Hodge, and B. Hundy, G. F. amd Zimmern. *A new generation of screw compressor for refrigeration*. In Institute of Refrigeration, 1975-1976.

[6] J. van Male. *Monoscrew - A newly developed refrigeration compressor*. International Journal of Refrigeration, 1:242–248, 1978.

[7] B. Zimmern. *From Water to Refrigerant: Twenty Years to Develop the Oil Injection-Free Single Screw Compressor*. In Int. Compr. Eng. Conf. at Purdue, 1984.

[8] M. Masuda, H. Ueno, T. Inoue, K. Hori, and M.A. Hossain. *Effact of variable volume index on performance of single screw compressor*. In Proceedings of 8th Int. Conf. on Compressors and their Systems, City University of London, London, pages 257–264, 2013.

[9] S-C Yang. *A mathematical model of the rotor profile of the single-screw compressor*. Proceedings of IMechE, Part C: J. of Mechanical Engineering Science, 216:343–351, 2002.

[10] S-C Yang. *A mathematical model of a cc-type single-screw compressor*. IMechE Part C: J. Mechanical Engineering Science, 2018:437–448, 2004.

[11] S-C Yang. *Profile generation and analysis of a pp-type single-screw compressor*. Int. J. Adv. Manuf. Technol., 30:789–796, 2006.

[12] S-C Yang and T-L Liang. *Modeling and Manufacturing of PP-Type Single Screw Compressor*. Transactions of the CSME de la SCGM, 31:219–234, 2007.

[13] S-C Yang, T-H Huang, and C-H Lai. *Modeling and Manufacture of a PC-Type Single Screw Compressor Rotor - 2014*. Arabian J. of Science and Engineering, 39:4221–4229, 2014.

[14] W. Wu, J. Li, and Q. Feng. *Simulation of the surface profile of the groove bottom enveloped by milling cutters in single screw compressors*. Computer-Aided Design, 43:67–71, 2011.

[15] J. Li, F. Liu, Q. Feng, and W. Wu. *A New Design of the Tooth Profile for Single Screw Compressors*. In International Compressor Engineering Conference at Purdue, number 1209, 2012.

[16] F. L. Heidrich. *Water Flooded Single Screw (SSP) Compressor Technology*. In International Compressor Engineering Conference at Purdue, pages 145–150, 1996.

[17] A. Lundberg and R. Gianvall. *A Comparison of SRM and Globoid Type Screw Compressors at Full Load*. In International Compressor Engineering Conference, number 288, 1978.

[18] A. Lundberg and R. Gianvall. *A comparison of SRM and globoid type screw compressors*. Int. J. Refrigeration, 2:221–232, 1979.

[19] C. Y. Chan, G. G. Haselden, and G. Hundy. *The HallScrew compressor for refrigeration and heat pump duties*. Int. J. Refrigeration, 4:275–280, 1981.

[20] Thomas W. Bein. *A Computer Model of a Single Screw Air Compressor*. Master's thesis, Purdue Univerisity, 1980.

[21] T. W. Bein and J. F. Hamilton. *Computer modeling of an Oil Flooded Single Screw Air Compressor*. In International Compressor Engineering Conference, 1982. Paper 383.

[22] M. de Berg, O. Cheong, M. van Kreveld, and M. Overmars. *Computational Geometry - Algorithms and Applications*. Springer, third edition edition, 2008.

[23] T. Hirai, S. Noda, Y. Sagara, and K. Tsuzi. *Performance Analysis of OIF Single Screw Compressor*. In International Compressor Engineering Conference, 1986. Paper 520.

[24] G. Sun. *The Investigation of Some Basic Geometric Problems of the Single Screw Co*. In International Compressor Engineering Conference, 1988. Paper 630.

[25] G. Jin, S. Zhang, and X. Yu. *Theoretical Analysis of Diameter Ratio of Engagement Pair for Singe Screw Compressor*. In International Compressor Engineering Conference, 2006. Paper 1831.

[26] S. Sun, W. Wu, X. Yu, and Q. Feng. *Analysis of Oil Film Force in Single Screw Compressor*. In International Compressor Engineering Conference at Purdue, number 2024, 2010.

[27] Kirill Michailovich Ignatiev. *Approach To The Numeric Geometry Analysis of Positive Displacement Compressors, Its Application To A Single Screw Compressor Simulation And Verification By Experiment*. In International Compressor Engineering Conference, number 2059, 2012.

[28] D. Ziviani, I.H. Bell, De Paepe M., and M. van den Broek. *Update on single-screw expander geometry model integrated into an open-source simulation tool*. In 9th Int. Conf. on Compressors and their Systems, City University of London, London, number 39, 2015.

[29] D. Ziviani, I. H. Bell, M. De Paepe, and M. van den Broek. *Mechanistic model of an oil-flooded single-screw expander*. In 23th Int.Compressor Engineering Conference at Purdue, number 1486, 2016.

[30] Y. Wu, R. Zhi, W. Wang, L. Shen, Y. Zhang, B. Lei, J. Wang, and C. Ma. *Mathematical modeling of torque for single screw expanders*. Journal of Mechanical Science and Technology, 31(1):429–436, 2017.

[31] G. G. Haselden. *Potential of the single-screw compressor*. Int, 8:215–220, 1985.

[32] Jin G. and Deng D. *Improvement of the Reliability of a Single Screw Compressor*. In International Compressor Engineering Conference, number 507, 1984.

[33] W. Wu, Q. Feng, J. Xu, and X. Feng. *A Design Method of the Column Envelope Meshing Pair in Single Screw Compressors*. In International Compressor Engineering Conference at Purdue, number 2024, 2010.

[34] W. Wu and Q. Feng. *Column envelope meshing pair and its design method for single screw compressors*. Journal of Zhejiang University, 10:31–36, 2009.

[35] W. Wu and Q. Feng. *A Multicolumn Envelope Meshing Pair for Single Screw Compressors*. Journal of Mechanical Design, 131:1–4, 2009.

[36] W. Wu, X. Hao, Z. He, and J. Li. *Design of the Curved Flank for the Star-Wheel Tooth in Single-Screw Compressors*. Journal of Mechanical Design, 136:1–5, 2014.

[37] S-C Yang and T-L Liang. *Study of a Single Screw Compressor with a Conical Teeth gate rotor*. Transactions of the CSME, 32:333–352, 2008.

[38] Y.-C. Yu. *Positive displacement compressor technical manuals*. Beijing China Machine Press, 2000. (In Chinese).

[39] F. L. Litvin. *Gear Geometry and Applied Theory*. Prentice-Hall, New Jersey, 1994.

[40] I. H. Bell, E. A. Groll, Braun J. E., and G. King. *Update on Scroll Compressor Chamber Geometry*. In 20th International Compressor Engineering Conference at Purdue University, 2010.

[41] I. H. Bell, E. A. Groll, E. Braun J., W. T. Horton, and V. Lemort. *Comprehensive analytic solutions for the geometry of symmetric constant-wall-thickness scroll machines*. International Journal of Refrigeration, 45:223–242, 2014.

4

Single-Screw Expander Overall Mechanistic Model

4.1 Introduction

Deterministic models of single-screw compressors (SSC) have been proposed in literature. Bein and Hamilton [1] developed a computer model of a low pressure oil-flooded single-screw air compressor. An iterative approach based on a polytropic transformation was used to correlate internal predictions with empirical values. Leakage paths were also considered, neglecting the two-phase flow through the gaps. The heat transfer between the air in the compression chamber and oil was neglected. Boblitt and Moore [2] presented a FORTRAN-based computer model of an oil-flooded SSC operating at 100% capacity at matched discharge pressures, meaning the pressure at the end of the compression process corresponded exactly with the discharge pressure. The model is based on two empirical parameters, i.e. polytropic compression efficiency and the discharge flow coefficient. The included leakage model is based on the model proposed by [1], with the addition of the effect of the oil on the volumetric and isentropic efficiency. However, it was assumed that only oil was leaking from the groove tip sealing lines and the refrigerant leakages were restricted to the the discharge port. The heat transfer between the refrigerant and oil in the closed compression process was neglected. The oil injection process was also included in the model. A total of six control volumes were introduced to analyze the overall compression process. Thermal interactions between each control volumes were modeled by means of a

steady-state steady-flow First Law analysis. The closed compression process was divided into a number of steps corresponding to a pressure increment, since the discharge state of a groove had to match the discharge pressure. The main rotor rotation step was a result of the model. Similarly, Wu and Jin [3] developed a SSC model including preheat, pressurization of the gas in the control volume during the suction and closure processes, flow of gas and oil mixture through the discharge port, leakage of gas and oil. Several effects, such as oil-injection rate, clearances and length of leakage paths, discharge port area variation, and oil shear power were included. Hirai et al. [4] proposed a geometry-based model of an oil-free SSC including the analysis of a slide valve mechanism. The theoretical analysis was validated with the pressure-volume diagram obtained from the experimental data. More recently, Wang et al. [5] presented a detailed thermodynamic model of a single-screw compressor with multi-column meshing profile in which continuity and energy conservation eqution were applied to the refrigerant gas and lubricant oil. The control volume analysis was applied to a single working chamber by assuming that all the others behaved in a similar manner. Suction gas heating due to the presence of the motor was also included. A two-phase flow model was employed to calculate the flow rate through the discharge port. A correction coefficient was introduced based upon experimental data. The heat transfer within the working chamber was modeled by including a correction factor to account for the helical shape of the groove. Cooling capacity and shaft power were validated with experimental data. From the literature overview of single-screw compressor modeling, a number of short-comings in the modeling approaches can be identified:

- the compression process has been always considered perfectly symmetric. Limited modeling has been done with respect to single-screw expander;
- instantaneous results from the chamber model, e.g., variation of leakage flow rates, heat transfer rate, pressure trances in all the control volumes, available in literature are scarce;
- the coupling between thermodynamic model and mechanical force analyses on the starwheels and rolling elements is also limited;
- a detailed overall housing energy balance with multi-lumped temperature has never been presented. In order to address these aspects, a comprehensive mechanistic model of a single-screw expander is described in this chapter.

4.2 Non-Symmetric Modeling Approach

As described in Figure 3.3, the operating principle of a single-screw expander is based on the simultaneous filling of the grooves on both sides of the main rotor

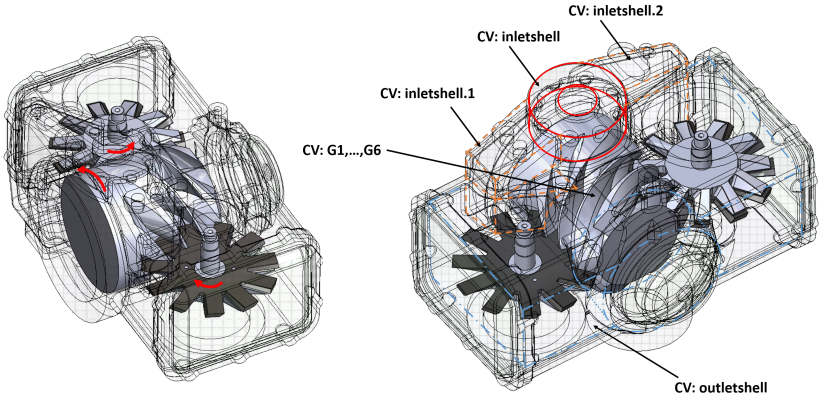

Figure 4.1: Views of the single-screw expander assembly with the direction of rotation of meshing pair (left) and the control volumes (right).

through ports located on the internal cylindrical surface of the housing which hosts the main rotor. As a groove rotates, it is exposed to the suction port until the trailing edge passes over the port. Once the portion of the groove limited by the engaging tooth, by the three sides of the groove and the housing wall is filled with working fluid, the closed expansion occurs until the tooth starts disengaging the groove, when the discharge process begins. Such process occurs on both sides of the main rotor and therefore, when a groove is discharging on one side, it is filling on the other side at the same time. Each groove is employed twice per revolution. By looking at Figure 4.1, the main rotor has six grooves, but due to the fact that two starwheels are engaged at the same time, there are six working chambers on each side of the rotor, as mentioned by Wang et al. [5]. To reduce the complexity of the model, it is common practice to consider only one side of the rotor due to symmetry. A more general approach is adopted in this work. In particular, a non-symmetric description of the machine is considered by computing the expansion process in both sides of the rotor. In order to visualize the internal flow of the machine, 3D-CFD analysis is a viable tool. In collaboration with University of Ferrara, a fluid domain was created from the original single-screw CAD geometry with a non-symmetric inlet ducting (see Figure 4.1). As described in Casari et al. [6] and Ziviani et al. [7], overset grids have been employed to carry on the simulations, after evaluating and comparing different dynamic mesh generation techniques, e.g., dynamic remeshing and key-frame remeshing. The boundary conditions imposed were temperature and pressure at the inlet and pressure at the outlet with a time step of 10^{-6}s. From a preliminary dynamic 3D-CFD simulation conducted on the single-screw expander object of this study, the pressure distributions at the suction ports were slightly different, as shown

in Figure 4.2, suggesting that the internal ducting may lead to different pressure drops and flow fields. Although the convergence of simulation has been checked, numerical effects could also play an important role in estimating the average pressure distributions at the suction ports. The use of internal sensors could certainly help understanding the correctness of such results (see Section 7.3).

In light of these observations, the complexity of the model has been increased. By referring to Figure 4.1, the housing has been divided into four static control volumes (CV) which are associated with the common inlet volume, the two internal ducts that connects the inlet to the suction pockets and shell volume connected to the outlet of the expander. On each side of the rotor, six dynamic control volumes which are changing according to the rotation angle are representative of the six working chambers. The rotation of the main rotor is taken as reference. To relax the notation, the rotation angle of the main rotor, θ_{sr}, will be referred to as θ, unless specified. A summary of the control volume definitions is available in Table 4.1

Type	Description	Geometry
Static	inletshell	V = 69 cm^3, dV = 0 cm^3
	inletshell.1	V = 70 cm^3, dV = 0 cm^3
	inletshell.2	V = 120 cm^3, dV = 0 cm^3
	outletshell	V = 569 cm^3, dV = 0 cm^3
Dynamic	G1,...,G6	V=V(θ), dV=dV(θ) Eq. (3.31) and (3.32)

Table 4.1: Definition of the different control volumes in the single-screw expander.

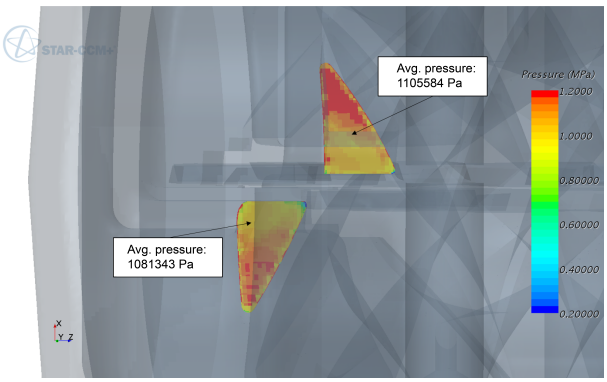

Figure 4.2: Average pressure at the suction ports obtained from a preliminary dynamic CFD simulation on a single-screw expander [8].

The generalized structure of PDSim outlined in Figure 2.2 is used to define and

add each CV to the model. The structure of PDSim allows to define a new control volume instance from a core class which holds an assigned string of the key name of the control volume, a function to calculate the volume and its derivative, the initial thermodynamic state and a string (or list of strings) with the key of the control volume that the current control volume becomes in the next rotation or angle. An example of control volume definition within the Python programming language is proposed below.

```
# Standard PDSim imports
from PDSim.core import ControlVolume
from CoolProp.CoolProp import State

# Create a State class instance for properties
# T[K], P[kPa]
state=State('R245FA',dict(T=383.15,P= 1500))

# The function that will return the volume
# and derivative of volume
def VdV(theta):
        """
        do calculations
        """
        return V,dV

# Create a control volume
CV=ControlVolume('key1',VdV,state,becomes='key1')

# The control volume holds all the thermophysical
# properties. Examples of queries:
h=CV.State.h # specific enthalpy [kJ/kg]
mu=CV.State.visc # dynamic viscosity [Pa-s]
```

By using such approach, each control volume of the single-screw expander can be added to the simulation model. The detailed polygon calculation to obtain the volume curve is carried out once at the beginning of the simulation. The volume of each CV is obtained by simply phasing out the curve by the proper tooth angle γ (see Figure 3.4(b)). The complete evolution of the control volumes over one rotation of one side the main rotor is shown in Figure 4.3. The control volume G_1 is taken as reference. To be noted is that the remaining control volumes G_2 ~ G_6 (solid lines) are phased by $(j\gamma i)_{j=1,2,3,4,5}$ and when each of them complete the revolution, they start wrapping on the opposite of the rotor. At the same time, as new teeth start engaging after G_1, new control volumes form from the groove that ended the expansion process on the other side of the rotor (dashed lines). The present model handles all the CVs on both sides simultaneously with

no simplifications due to symmetry.

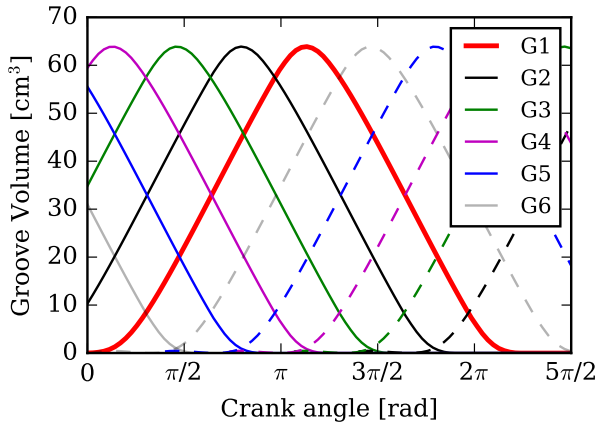

Figure 4.3: Evolution of the main rotor control volumes over one complete rotation for one side of the main rotor.

4.3 Thermodynamic model and thermophysical properties

The geometry model of the single-screw and the volume curves of the control volumes are the first steps in defining a mechanistic model. The governing differential equations of such model have been discussed in depth in Section 2.3. However, additional considerations are made with respect to the type of analysis that it is required for the single-screw expander under investigation. In particular, due to the fact that single-screw expander requires lubrication, the oil-flooded expansion process can be controlled which could result in a decrease of leakages and friction losses and an increase of the boundary work. The mixture of refrigerant and lubricant oil entering the expander is considered to be homogeneous and at same pressure and temperature conditions. Practically, these conditions are realized by mixing the refrigerant and lubricant oil in a static mixer. Due to the highly turbulent mixing of liquid and gas phases in the working chamber, the assumptions of thermal and mechanical equilibrium can be regarded as reasonable [16]. Figure 4.4 illustrates the velocity field inside each working chambers. For a homogeneous mixture, the general mixture thermodynamic property, Ψ_{mix}, is calculated by introducing a liquid mass fraction, x_{L}:

$$\Psi_{\mathrm{mix}} = x_{\mathrm{L}}\Psi_{\mathrm{L}} + \left(1 - x_{\mathrm{L}}\right)\Psi_{\mathrm{r}} \tag{4.1}$$

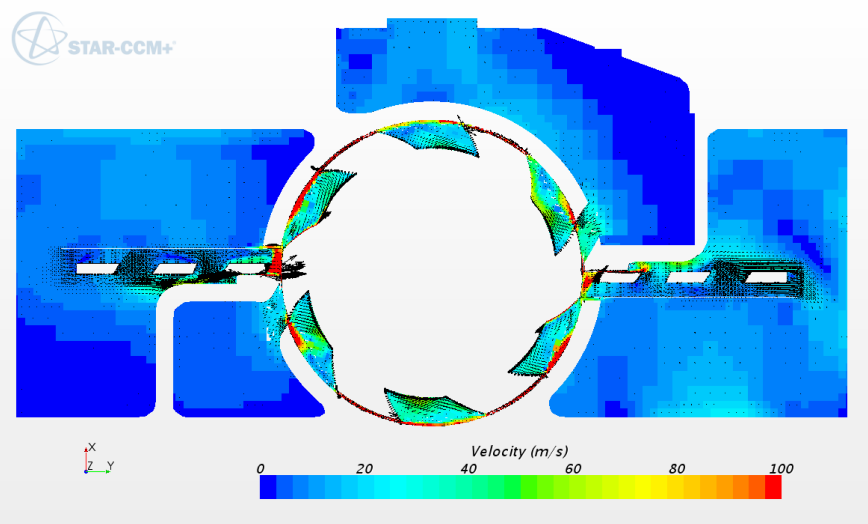

Figure 4.4: Velocity contour obtained a from CFD analysis on a single-screw expander [8].

where Ψ_L and Ψ_r are the properties of lubricant oil and refrigerant, respectively, and with:

$$x_L = \frac{\dot{m}_L}{\dot{m}_L + \dot{m}_r} \tag{4.2}$$

Such formulation is applied to obtain mixture specific internal energy, mixture specific enthalpy, mixture specific heat and mixture specific entropy. The mixture thermal conductivity is calculated as a void-fraction-weighted average of the conductivities of the refrigerant and lubricant oil [9]:

$$k_{mix} = \alpha k_r + (1 - \alpha) k_L \tag{4.3}$$

where α is the void fraction expressed as: [9]:

$$\alpha = \frac{1}{1 + \frac{x_L}{x_r}\frac{v_L}{v_r}K} \tag{4.4}$$

The slip between the phases is not considered and therefore $K = 1$ corresponds to a homogeneous flow. As outlined by Wallis and Chisholm [9,10], different models are available to estimate the viscosity of a mixture that ensure the correct values of for the two phases. McAdams formulation is adopted and it is given by

$$\mu_{mix} = \left(\frac{x_L}{\mu_L} + \frac{x_r}{\mu_r}\right)^{-1} \tag{4.5}$$

Finally, the Prandtl number of the mixture can be obtained straightforward as:

$$Pr_{\text{mix}} = \frac{\mu_{\text{mix}} c_{\text{p,mix}}}{k_{\text{mix}}} \tag{4.6}$$

The thermophysical properties of the refrigerants are retrieved from the CoolProp library [11] by making use of the low-level interface through the *State* class. In the open-literature, lubricant oil property libraries are absent, although lubricant oils are used in most positive displacement compressors and expanders. To close the gap, a *StateFlooded* class derived from the *State* class has been developed and made available open-source within PDSim. Such new class works as a container for all the thermophysical properties of refrigerants, lubricant oils and related homogeneous mixtures. The properties of the lubricant oils have been collected from different published sources [12–16]. An example of pseudo-code in the Python programming language is provided below. In particular, the class is instantiated by specifying two strings representing the refrigerant and lubricant oil, a dictionary[1] data structure with the values of pressure, temperature and liquid mass fraction, and an additional string for the slip ratio model.

```
# Standard PDSim imports
from PDSim.core.stateflooded import StateFlooded

S=StateFlooded('R245fa','POE',dict(T=373,P=200,xL=0.5))
print 'Lubricant oil density:', S.get_rhoL()
print 'Void fraction:', S.get_VoidFrac()
```

The system of governing equations that expresses the conservation of total mass in the control volume, the conservation of the oil mass and the conservation of energy for the general control volume are given as follows:

$$\begin{aligned}
\frac{dm_{CV}}{d\theta} &= \frac{1}{\omega}\sum_i \dot{m}_i \\
\frac{dx_L}{d\theta} &= \frac{1}{m_{CV}}\left[\frac{1}{\omega}\sum_i \dot{m}_i x_{L,i} - x_L \frac{dm_{CV}}{d\theta}\right] \\
\frac{dT}{d\theta} &= \frac{1}{m_{CV} c_{v,mix}}\left\{ -T\left(\frac{\partial p}{\partial T}\right)_{v_{\text{mix}}}\left[\frac{dV}{d\theta} - v\frac{dm_{CV}}{d\theta}\right] - m_{cv}(u_L - u_g)\frac{dx_L}{d\theta} \right. \\
&\qquad \left. -h\frac{dm_{CV}}{d\theta} + \frac{\dot{Q}}{\omega} + \frac{1}{\omega}\sum_i (\dot{m}h)_i \right\}
\end{aligned} \tag{4.7}$$

To be noted is that the term $\left(\frac{\partial p}{\partial T}\right)_{v_{\text{mix}}}$ must be calculated as a numerical derivative and it cannot be obtained directly from the equation of state unless the oil mass

[1] A dictionary is data type built into Python and it can be regarded as an unordered set of key, i.e. value pairs with the requirement that the keys are unique.

fraction is zero. In the system of equations (4.7), sub-models for estimating the flow interactions between the working chambers and heat transfer model are necessary in order to carry on the integration. Such sub-modules will be described in Section 4.4 and Section 4.5.

4.4 Mass Flow Models

In a single-screw expander different flow paths exist that require specific flow models. In particular, the flow paths can be divided into two categories: (i) inlet and outlet flows through porting within the housing; (ii) leakage flows. Moreover, particular attention has to be given to the presence of lubricant oil. In the case that a significant amount of oil (>5% of the total mass flow rate) enters the single-screw expander, the suction and discharge flow paths are described by an adiabatic compressible two-phase flow through a nozzles as proposed by Chisholm [9] and implemented by Lemort and Bell [16, 17] in a oil-flooded scroll expander and compressor, respectively. The mass flow rate expression is based on the conservation of momentum and it is given by:

$$\dot{m} = C_{\text{flow}} A_{\text{suc}} \sqrt{\frac{2\int_{p_{\text{down}}}^{p_{\text{up}}} v_{\text{e}} dp}{v_{\text{e,down}}^2 - \sigma v_{\text{e,up}}^2}} \tag{4.8}$$

where C_{flow} is a flow coefficient, A_{suc} is the suction port area, σ is the ratio between the downstream and upstream flow path areas, v_{e} is the momentum effective specific volume. By considering a separated-flow with the effect of liquid entrainment in the vapor phase (and flowing at the vapor phase velocity), the effective specific volume can be given by:

$$v_{\text{e}} = \left[(1 - x_{\text{L}})\, v_{\text{r}} + K_{\text{e}} x_{\text{L}} v_{\text{L}}\right]\left[\left(1 - x_{\text{L}} + \frac{x_{\text{L}}}{K_{\text{e}}}\right)\right] \tag{4.9}$$

where K_{e} is the effective slip ratio which is a fuction of both entrainment and slip ratio: [9]:

$$K_{\text{e}} = \left[\Psi + \frac{(1 - \Psi)^2}{K - \Psi}\right] \tag{4.10}$$

The slip ratio with entrainment is evaluated from:

$$K = \Psi + (1 - \Psi)\sqrt{\frac{1 + \frac{\Psi x_{\text{L}} v_{\text{L}}}{(1 - x_{\text{L}}) v_{\text{r}}}}{1 + \frac{\Psi x_{\text{L}}}{1 - x_{\text{L}}}}}\sqrt{\frac{v_{\text{r}}}{\text{v}_{\text{L}}}} \tag{4.11}$$

A value of $\Psi = 0.4$ was recommended by Chisholm.

If the amount of oil mixed with the refrigerant is <5% of the total mass flow rate entering the expander, an isentropic, compressible flow through a nozzle is employed and corrected by a flow coefficient to match the experimental data.

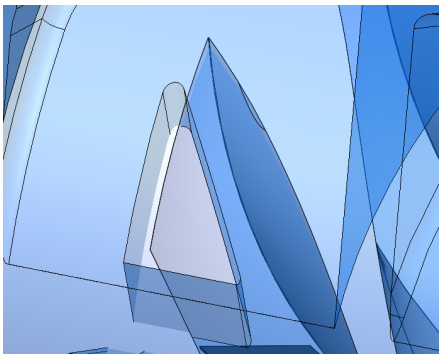

Figure 4.5: Flow path through suction port.

In a single-screw machine multiple leakage paths exist between the meshing pair and the housing and within the meshing pair. By looking at Figure 4.6, nine main leakage paths can be identified which are widely reported in literature [1, 3, 18]. Each path has different geometry and the flow conditions may differ significantly. Therefore, the leakage paths can be divided into three types, depending on geometry of the gap:

- constant clearance gap: gaps between the leading (L_7) and trailing (L_8) edges of the groove and the cylinder walls, gap between the groove end band (L_9) and cylinder walls and gap between upper tooth surface (L_4) and housing;
- variable clearance gap: gaps between the tooth sealing lines (L_1,L_2 and L_3) and the groove flanks and groove bottom surfaces;
- orifice type: blowholes between tooth and groove (L_5 and L_6) due to wear of the profile of inaccuracies in the milling process.

	Starwheel-housing	Screw rotor-housing (on radius)
clearance [mm]	0.02 - 0.06	0.03 - 0.10

Table 4.2: Typical clearance ranges between meshing pair and the housing walls.

The typical range of clearances between the starwheel top surface and the housing as well as the main rotor and the cylinder walls are reported in Table 4.2. In general, the flow through the gaps is expected to have frictional effects as the length of the path is typically several times higher than the gap size. As it is challenging to select the correct flow model for each leakage path, simplified models, such as isentropic compressible flow through a nozzle, are employed and

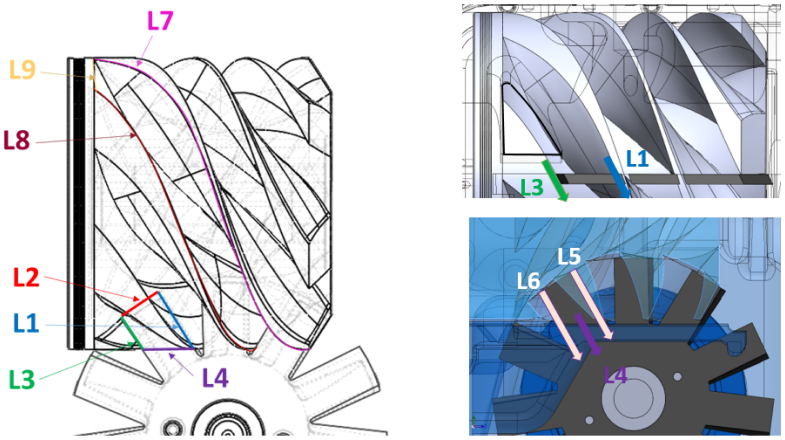

Figure 4.6: Identification of the main leakage paths in a single-screw machine.

then corrected with flow coefficients. This choice is done primarily due to limited computational efforts and limited parameters to be estimated (e.g., throat area). However, it has been shown in literature that such models require large corrections suggesting that they are no appropriate for all the leakage gaps [16]. To this end, the leakage paths o the single-screw expander are first analyzed on a geometric point of view in order to categorize them and then apply proper flow models. The leakage path that involves the leading and trailing edges of the groove presents a variable length due to the shape of the groove. In particular, as expander, the land between two consecutive grooves is larger during the filling and part of the expansion process when the pressure is higher and it decreases while the groove is moving towards the discharge end. Such configuration minimizes the cascade effects and it represents an advantage of single-screw machines compared to twin-screw designs. In the single-screw expander considered in this study with a rotor diameter of 122 mm, the groove land length varies between approximately 20 mm and 2 mm, which represents the minimum structural limit in accordance to Equation 3.8. By considering a clearance of 0.05 mm between the rotor tip and the cylinder walls yields to a length to height ratio between 400 and 40. Thus, the flow though such path can be considered frictional flow between parallel plates. This is also in line with the fact that frictional flow leads to lower mass flow rates estimations compared to an isentropic flow through a nozzle and the longer flow paths should be beneficial to the reduction of leakage flow. Similar considerations apply to the leakage flow through L_4. In fact, the thickness of the cylinder wall is approximately 7.3 mm and the gap is 0.02 mm which results in a length to height ratio of 365. Orifice type of gaps are identified by using the criterion proposed

by Bein [19]. In particular, a flow path is considered a orifice if the ratio of the throttling length to the hydraulic diameter is:

$$\frac{L_{\mathrm{path}}}{D_{\mathrm{h}}} < 2.5 \tag{4.12}$$

Predicting the leakage flows becomes even more challenging due to the presence of oil in the working chambers. As previously mentioned, the refrigerant-oil mixture is considered homogeneous while entering the machine. However, during the expansion process centrifugal forces due to the rotation of the main rotor have the effect of pushing the oil radially. Furthermore, during the rotation, the oil film on the groove surfaces is squeezed by the tooth sides as they sweep through the groove until discharge. This effect is desirable as the oil serves as sealant as long as a stable hydrodynamic lubrication can be established between groove flank and tooth side [20, 21]. Therefore, it follows that oil is present in every leakage path and two-phase flow conditions are established unless only oil is assumed to be leaking (solubility effects being neglected). In literature, leakage flows through the different paths in an oil-flooded single-screw compressor have been handled in different ways. Bein [19] introduced the assumption that only oil leaked through the paths that are on the boundaries of the working chamber control volume due to the fact that during the relative motion of the tooth and the groove, the oil on the surfaces was wiped off by the tooth and collected on the tooth sealing lines as well as blowholes. The gap L_4 between the starwheel upper surface and the housing was considered covered with oil when enough oil was accumulated, i.e., only towards the end of the compression process. During early stages of the compression, also air was assumed to be leaking even though the low pressure in the chamber justified the error introduced by neglecting it. Such assumptions were verified through experimental results. Incompressible flow not considered to be orifice flow was modeled by using Darcy's model. As viscous and non-viscous, e.g., changes in speed and direction of the flow path or thermal deformation of the gaps, effects affected the flow predictions, tuning coefficients were introduced to correct the non-viscous effects which are effected by the relative speed of the meshing pair parts. For constant clearance gaps, the leakage paths were described as flow between parallel plates with a mixed Poiseuille flow and Couette flow with additional non-viscous effects. From experimental observations and available literature, it was concluded that the flow was laminar enough if only oil was leaking [19]. The momentum equations was expressed as:

$$\left(\frac{3}{4}F_{\mathrm{flow}}\right)\mathrm{v}^2 + \frac{32L_{\mathrm{path}}\mathrm{v}\mu_{\mathrm{L}}}{D_{\mathrm{h}}\rho_{\mathrm{L}}} - \frac{\Delta p}{\rho_{\mathrm{L}}} = 0 \tag{4.13}$$

where Δp is the pressure difference between upstream and downstream the path, F_{flow} is the correction factor. The resulting leakage flow rate is obtained by

combining Poiseuille and Couette components:

$$\dot{m}_{\mathrm{leak}} = A_{\mathrm{path}}\rho_{\mathrm{L}}\left(V + \frac{U_{\mathrm{wall}}}{2}\right) \tag{4.14}$$

where U_{wall} is the velocity of the moving wall and A_{path} is the constant cross-sectional area of the path. In the case of variable clearance gaps, a similar approach was used but the Darcy equation was modified to include the variation of the gap in the direction of the flow. Relationships for divergent and convergent-divergent paths were developed. For example, in the case of a divergent leakage path, the Darcy equation became:

$$\frac{\Delta p}{\rho_{\mathrm{L}}} - \frac{\dot{V}^2}{w_{\mathrm{path}}^2}\left[\frac{1}{4\delta_{\mathrm{x=0}}^2} + \frac{1}{4\delta_{\mathrm{x=L}}^2}\right] - \frac{8\mu_{\mathrm{L}}\dot{V}}{w_{\mathrm{path}}}\int_{x=0}^{x=L}\frac{dx}{\delta(x)^3} \tag{4.15}$$

Among the leakage paths, it was found that the starwheel tooth tip gap (L_2) was the most detrimental for the volumetric efficiency. Boblitt and Moore [2] adopted the same assumptions of Bein. The refrigerant leakage was restricted to the discharge port leakage path while only oil was allowed to leak from the groove leading and trailing edges. The refrigerant leakage flow was modeled as adiabatic isentropic flow. In all the cases investigated, the refrigerant leakage flow was chocked. A discharge flow coefficient was introduced. In the case of a 280 mm rotor with an internal volume ratio of 3.5, R12 as working fluid and flow coefficient identified was 0.25. The tooth tip leakage path was found to have a highest influence on the volumetric efficiency if reduced. Wu et al. [3] considered that oil was leaking through the paths except for flow paths L_9 and the discharge port (suction port as expander) where two-phase flow models were applied. In particular, the leakage flow through the end band of the groove was treated as separated and two equations were derived to estimate the oil flow rate and the refrigerant flow rate as function of oil film thickness:

$$\dot{m}_{\mathrm{r,L_9}} = \rho_{\mathrm{r}} w_{L_9}\frac{\delta_{\mathrm{L}}}{6\left(\delta_{\mathrm{r}} + \delta_{\mathrm{L}}\frac{\mu_{\mathrm{r}}}{\mu_{\mathrm{L}}}\right)}\left\{3U + c_{\mathrm{r,CV}}\left[\delta_{\mathrm{r}}^2 + 4\delta_{\mathrm{l}}\left(4\delta_{L_9} - \delta_{\mathrm{L}}\right)\frac{\mu_{\mathrm{r}}}{\mu_{\mathrm{L}}}\right]\right\} \tag{4.16}$$

$$\begin{aligned}\dot{m}_{\mathrm{L,L_9}} = \rho_{\mathrm{L}} w_{L_9}\frac{\delta_{\mathrm{L}}}{6\left(\delta_{\mathrm{r}} + \delta_{\mathrm{L}}\frac{\mu_{\mathrm{r}}}{\mu_{\mathrm{L}}}\right)}\Bigg\{&3U\left(\delta_{\mathrm{L}} + 2\delta_{\mathrm{r}}\frac{\mu_{\mathrm{r}}}{\mu_{\mathrm{L}}}\right) + \\ &c_{\mathrm{L,CV}}\left[\left(3\delta_{L_9} + \delta_{\mathrm{L}}\right)\delta_{\mathrm{r}}\frac{\mu_{\mathrm{r}}}{\mu_{\mathrm{L}}} + \delta_{\mathrm{L}}^2\right]\delta_{\mathrm{L}}\Bigg\}\end{aligned} \tag{4.17}$$

where w_{L_9} is the width of the leakage path, δ_{L_9} is gap clearance, δ_{L} is the oil film thickness, U is wall rotor wall velocity, $c_{\mathrm{L,CV}}$ and $c_{\mathrm{r,CV}}$ are the specific heat at constant pressure for the oil and refrigerant evaluated at the control volume conditions. The oil thickness was calculated as:

$$\delta_{\mathrm{L}} = C_{\mathrm{oil,flow}}\delta_{\mathrm{L_9}} \tag{4.18}$$

where $C_{\mathrm{oil,flow}}$ is the empirical correction factor to estimate the oil film thickness. The leakage flows through the discharge port were assumed to be adiabatic oil-refrigerant homogeneous flow with viscous friction [10], analogously to Bein's approach. With respect to the oil leakage flows, an adiabatic incompressible viscous flow between parallel flat plates was adopted. That is:

$$\dot{m}_{\mathrm{leak,L}} = \rho_{\mathrm{L}} w_{\mathrm{path}} \delta_{\mathrm{path}} \left[\frac{U}{2} + \frac{\delta_{\mathrm{path}} \Delta p_{\mathrm{path}}}{12 \mu_{\mathrm{L}} L_{\mathrm{path}}} \right] \tag{4.19}$$

where L_{path} is length of the leakage path, δ_{path} is the clearance gap and Δp_{path} is the pressure difference between upstream and downstream the path. Wang et al. [18] proposed a detailed analysis of leakage flows in an oil-flooded single-screw compressor with a multi-column tooth profile. Analytic expressions of the flow path areas have been derived and two leakage flow models were proposed for radial ($\mathrm{L_5}$, $\mathrm{L_6}$) and axial ($\mathrm{L_1}$, $\mathrm{L_3}$) flow paths. The refrigerant-oil mixture was treated as homogeneous in both axial and radial gaps and the flow through the leakage path was taken to be isentropic and compressible due to high velocities. With respect to the axial leakage paths, a similar approach to radial leakage flow in rotary compressors was used. In particular, two-phase homogeneous flow was assumed. In order to account for the effects of both pressure difference across the leakage path and the wall velocity, a Couette-Poiseuille flow was used in a similar fashion as Bein [19]. Laminar conditions were considered along with a one-dimensional steady-state flow. In this case, a numerical integration was performed as the gap size had a complex functional form. Whereas, Bein assumed a linear variation of the gap size. Analogously to Bein and Boblitt, the radial leakage flow model was a flow through a orifice. The flow was assumed to be fully turbulent and the oil-refrigerant mixture was considered to be two-phase and homogeneous:

$$\dot{m}_{\mathrm{leak,mix}} = \frac{C_{\mathrm{flow}} \beta A_{\mathrm{path}} \sqrt{2 \Delta p_{\mathrm{path}} \rho_{\mathrm{L}}}}{\left[\lambda_{\mathrm{flow}} + x \left(\frac{\rho_{\mathrm{r}}}{\rho_{\mathrm{L}}} - \lambda_{\mathrm{flow}} \right) \right] \sqrt{1 - \left(\frac{d}{D} \right)^4}} \tag{4.20}$$

where β is the expansion coefficient, C_{flow} is a flow coefficient, λ_{flow} is another flow coefficient determined experimentally, d/D is geometric ratio between the diameter of the orifice and its hydraulic diameter and x is the dryness of the mixture. No information was reported about the magnitude of the flow coefficient. With respect to single-screw expanders, limited literature is available regarding the influence of leakage paths on the performance. Wang et al. [22] performed an experimental study on a single-screw expander with compressed air as working fluid by varying the gas sizes between starwheel and shell and between main rotor and shell. However, no modeling was presented.

The single-screw expander employed in the present work operates with different refrigerants, operating conditions and lubricant oil ratios. In light of the literature

review on single-screw compressors as well as other type of positive displacement machines, a distinction is made based upon the oil fraction entering the machine. If the amount of oil can be considered negligible, leakage flows are assumed to be entirely refrigerant vapor. Furthermore, frictional flow is always considered with the exception of the blowholes (L_5 and L_6). The detailed 1D-flow model described in Section 2.5.1 is applied systematically to each path to determine the proper correction factor with respect to the isentropic compressible flow model. If significant amount of oil floods the expander, the flow through the leakage gaps is considered to be frictional, two-phase and the refrigerant-oil mixture is assumed homogeneous.

4.5 In-groove heat transfer model

The heat transfer process within the grooves of the main rotor is challenging to model because of the presence of refrigerant gas and lubricant oil. In previous works [2, 19] on single-screw compressors, the heat trasfer between the gas and the oil during the closed compression was neglected due to the fact that the compression process occured too quickly (approximately 6 ms at 3000 rpm) for the oil to absorb heat. Wu et al. [3] assumed adiabatic control volumes for the closed compression and discharge control volumes and neglected the heat transfer between gas and oil as well. Li [23] stated that it was reasonable to assume the wall surfaces to be coated by a oil film . Therefore, the refrigerant gas was never in direct contact to the metal walls. Two heat transfer mechanisms were considered within the groove: the first one was between the gas the oil droplets and the second one was between the mixture of refrigerant-oil and the oil film.

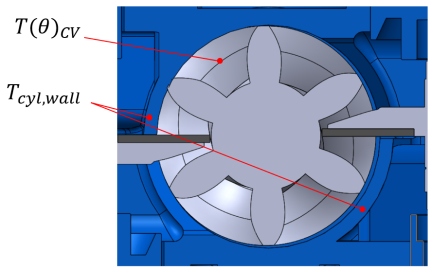

Figure 4.7: Heat transfer between the mixture of refrigerant and oil in the working chambers and the cylinder wall.

In this work, the approach proposed by Wang et al. [5] is considered. By referring to Figure 4.7, the groove is approximated as a helical tube with non-circular cross section. The convective heat transfer coefficient is obtained by correcting the Dittus-Boelter correlation to account for the groove geometry.

Similar approach has been adopted for example by Bell [16] in the case of the spiral geometry of the scroll wraps and by Mathison et al. [24] in the case of curved surfaces in two-stage rotary compressor. The final expression of the heat transfer coefficient is given by:

$$h_{\mathrm{groove}} = 0.023 \frac{k_{\mathrm{mix}}}{R_{\mathrm{sw}} - \frac{d_{\mathrm{sr,sw}}}{cos\theta}} Re_{\mathrm{mix}}^{0.8} Pr_{\mathrm{mix}}^{0.4} \frac{D_{\mathrm{h}}}{d_{\mathrm{eq,groove}}} \left\{ 1 + 1.77 \frac{R_{\mathrm{sw}} - \frac{d_{\mathrm{sr,sw}}}{cos\theta}}{R_{\mathrm{sw}} - \frac{1}{2}\left(R_{\mathrm{sw}} - \frac{d_{rmsr,sw}}{cos\theta}\right)} \right\} \tag{4.21}$$

where $d_{\mathrm{eq,groove}}$ represents the equivalent diameter of the groove and D_{h} is the hydraulic diameter of the groove calculated as:

$$D_{\mathrm{h}} = \frac{4V_{\mathrm{groove}}(\theta)}{A_{\mathrm{groove}}(\theta)} \tag{4.22}$$

The Reynolds number of the mixture in the screw groove is calculated by considering as mean velocity the peripheral velocity evaluated at the groove center radius between tip and bottom. The instantaneous heat transfer rate between the mixture and the cylinder wall is thus obtained as:

$$\dot{Q}_{\mathrm{cyl,wall}}(\theta) = h_{\mathrm{groove}} A_{\mathrm{cyl,wall}}(\theta) \left[T_{\mathrm{cyl,wall}} - T(\theta)\right] \tag{4.23}$$

Finally, the average heat transfer between the mixture in the working chambers and the cylinder walls over one rotation is obtained from:

$$\overline{\dot{Q}}_{\mathrm{cyl,wall}} = \frac{1}{2\pi} \int_0^{2\pi} \left[\sum_{\mathrm{CV}} \dot{Q}_{\mathrm{CV}} \right] d\theta \tag{4.24}$$

where the integration is done numerically with a trapezoidal rule.

4.6 Forces and Moments Analyses

During both expansion and compression processes, the working fluids generates loads on the meshing pair that are ultimately distributed among the mechanical elements of the machine assembly. The mechanical configuration of the single-screw expander object of this study is shown in Figure 4.8. The main rotor is mounted on a shaft which is supported by pair of trust bearings in the front end and a cylindrical roller bearing in the back side of the rotor. Each starwheel shaft is mounted on the housing by means of ball bearings. A detailed analysis of the forces and moments is thus necessary to computed the mechanical torque generated at the shaft as well as the radial and axial forces on the main rotor shaft and on the starwheels that ultimately will result in friction losses through the bearings and the contact between starwheels and main rotor.

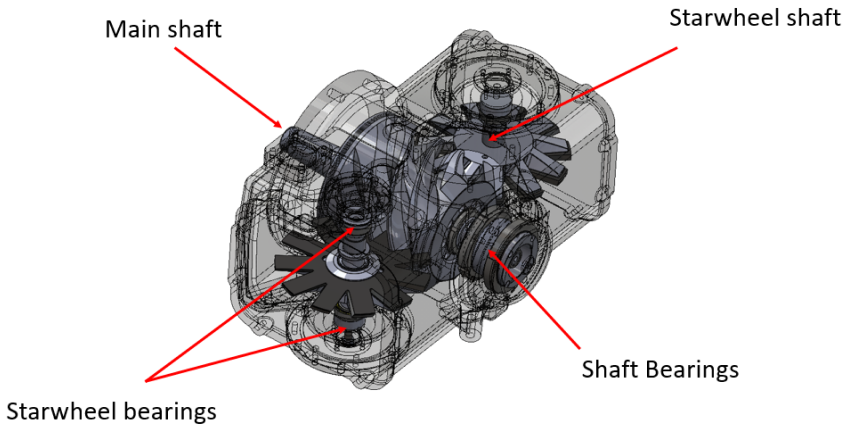

Figure 4.8: Mechanical elements of a single-screw expanders.

4.6.1 Pressure forces and torque

During the working process of the single-screw expander, pressure loads are generated on the groove surface as well as on the starwheel teeth engaged. The pressure distribution on the groove surfaces is responsible for generating the mechanical torque of the shaft. The calculation of the mechanical shaft torque for a single-screw machine has not been fully addressed. Wu et al. [25] considered a simplified approach by calculating the contribution to the mechanical torque of a groove as the product of the gas force applied to the centroid of the portion of the tooth engaged and its distance from the main rotor rotation axis. By summing each contribution, the resulting torque was highly overestimated and a mechanical efficiency was introduced. In the present work, a more rigorous approach is taken by following the methodology applied by Wu and Tran [26] for calculations of the loads on a twin-screw compressor. A schematic of forces on main rotor and starwheels is shown in Figure 4.9. Once the pressure traces of the different control volumes are known at the end of working cycle cycle, the force on each tooth generated by the expansion process is given by:

$$F_{g,i}(\theta) = p_i(\theta)A_i(\theta) \tag{4.25}$$

and it is applied on the centroid of the intersection tooth area (see Section 3.3.3). As there are three or four teeth on each side of the main rotor constantly engaged, the total force due pressure loads is given by summing up each contribution, i.e. $\sum_i F_{g,i}, i = 1, 2, 3, 4$.

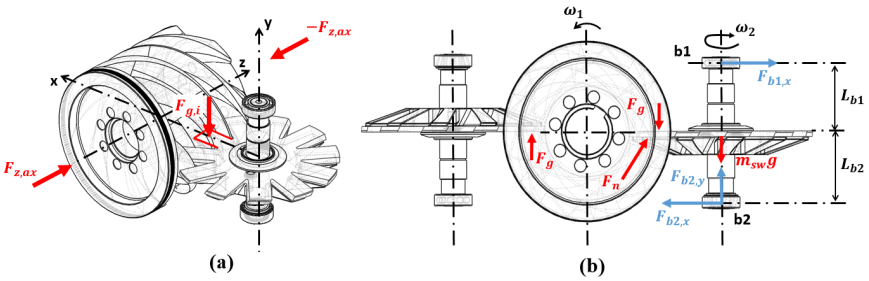

Figure 4.9: Schematic of the forces on main rotor and starwheels.

4.6.2 Load calculations on the starwheels

By referring to Figure 4.9, the groove applies a force F_n which is perpendicular to the groove surface itself and direct to the tooth flank. As a consequence, F_n changes orientation with the helix angle of the groove during the expansion process. For each tooth, a frictional force component of $F_{n,i}$ can be obtained as:

$$F_{f,i} = \mu_g F_{n,i} \tag{4.26}$$

where the friction coefficient μ_g depends on the materials of groove and tooth and the presence of oil. The axial and radial force balances on the starwheel are given by:

$$F_{b2,y} - m_{sw}g - F_g + F_{n,y} = 0 \tag{4.27}$$

$$-F_{b1,x} - F_{n,x} + F_{b2,x} = 0 \tag{4.28}$$

where m_{sw} is the total mass of the starwheel body plus the toothed PEEK disk. By means of a balance of moments around the upper bearing as described by Li et al. [27], the loads on each bearing can be determined and the friction power can also be estimated through the thrust bearing theory.

4.7 Mechanical Losses

The friction losses of dynamic components are coupled into the dynamic analysis of the mechanical components. Examples of such analyses applied to different machines can be found in the open literature:

- Scroll compressor [16, 28]
- Rotary compressor: rolling piston [29, 30]; sliding vane [31]; spool [32]; z-compressor [33]
- Reciprocating compressor [34, 35]
- Screw compressor [26]

PDSim includes the possibility of implementing detailed mechanical analyses to estimate each frictional contribution. The average friction power losses over one working cycle are given as:

$$\overline{\dot{W}}_{\text{friction}} = \sum_i \overline{\dot{W}}_{\text{friction},i} \tag{4.29}$$

In the absence of a mechanistic model for mechanical losses, it is possible to correlate the mechanical losses to the gas compression or expansion power and obtain an empirical relationship for the mechanical efficiency [28]. This correlation is constructed by first running the model with input state points for which experimental data are available, with no mechanical losses or heat transfer. The residual between the model predicted shaft power and the experimental shaft power is then assumed to be due to mechanical losses. A correlation of the form

$$\overline{\dot{W}}_{\text{mech,loss}} = \omega \tau_{\text{mech,loss}} \tag{4.30}$$

is fit to the data for the compressor or expander and the loss coefficient $\tau_{\text{mech,loss}}$ is obtained. From the force and moments analyses carried out for the single-screw expander, the loads on the bearings were determined. For oil-lubricated bearings, their performance can be characterized by numerically solving Reynolds' equation or by adopting known approximated journal bearing solutions [36]. In general, the instantaneous frictional power loss from a bearing is given by

$$\dot{W}_{\text{bearing}} = \vec{\text{F}} \times \vec{v}, \tag{4.31}$$

which is the cross product of the frictional force and the velocity at the point of contact. The magnitude of the friction force is given by a term of a form similar to $|F| = \mu N$ with μ the friction coefficient and N the normal force at the contact point.

Additional viscous losses associated with the presence of oil in flow path gaps can be estimated as proposed by Wu and Jin [3]:

$$\dot{W}_{\text{friction,L}} = L_{\text{path}} w_{\text{path}} U \left(\frac{\mu_{\text{L}} U}{\delta_{\text{path}}} - \frac{1}{2} \frac{\Delta p_{\text{path}} \delta_{\text{path}}}{L_{\text{path}}} \right) \tag{4.32}$$

4.8 Overall energy balance

An overall energy balance of the expander housing is necessary to close the mechanistic model. In particular, thermal interactions occur between the elements of the housing the working fluid during the entire expansion process. Thus, the wall temperatures need to be estimated in order to calculate the associated heat transfer terms. As an example, the cylinder wall temperature that is used to calculate the heat transfer rate within the working chamber (see Section

4.5) is unknown. As outlined in Section 2.6, single-lumped temperature and multi-lumped temperatures are commonly used to enforce the overall energy balance depending on the complexity required. The single-screw expander is an open-drive machine and both approaches are implemented. The validity and limitations of the single-lumped element will be evaluated experimentally by installing multiple thermocouples on the housing surfaces.

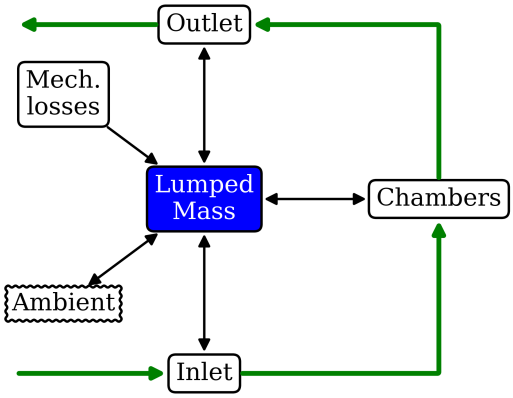

Figure 4.10: Schematic of the single-lump overall energy balance of the open-drive single-screw expander.

4.8.1 Single-lumped Temperature

The overall energy balance based on a single-lumped implied that all the expander elements are grouped into one lumped mass having a temperature T_{lump}. Since spatial gradients are neglected, the lumped temperature is uniform. The working fluid exchanges heat with the lumped mass during suction, closed expansion and discharge processes. The heat generated by friction is also assumed to interact with the lumped mass. Last, the lumped mass exchanges heat with the ambient. The overall energy balance for a single lumped element can be written as,

$$\overline{\dot{W}}_{\text{mech,loss}} + \sum_i \dot{Q}_i(T_{\text{lump}}) = 0 \tag{4.33}$$

where T_{lump} is the mean temperature of the lumped mass of the expander shell and $\dot{Q}_i$ represents all the heat transfer interaction terms between the different parts of the expander and the housing. By referring to Figure 4.10, the overall energy balance for the single-screw expander is given by:

$$\overline{\dot{W}}_{\text{mech,loss}} + \overline{\dot{Q}}_{\text{cyl,lump}} + \dot{Q}_{\text{inletshell,lump}} + \dot{Q}_{\text{outletshell,lump}} + UA_{\text{amb}}\,(T_{\text{lump}}) = 0 \tag{4.34}$$

where the average value of the overall heat transfer coefficient UA_{amb} is obtained from experimental data or assumed accordingly.

4.8.2 Multi-lumped Temperature

In the multi-lumped temperature approach, the entire expander is divided into different elements, i.e., the lumps. It is assumed that there is no temperature gradient in the individual expander elements, i.e., the lumped temperature analysis method is used. The higher the number of elements identified, the more complex the thermal network model becomes. The overall energy balance model developed for the single-screw expander is based on previous models applied to rolling piston, scroll and reciprocating compressors [37–39]. The schematic of the overall energy balance of the single-screw expander and the corresponding thermal resistance network are given in Figure 4.11 and Figure 4.12.

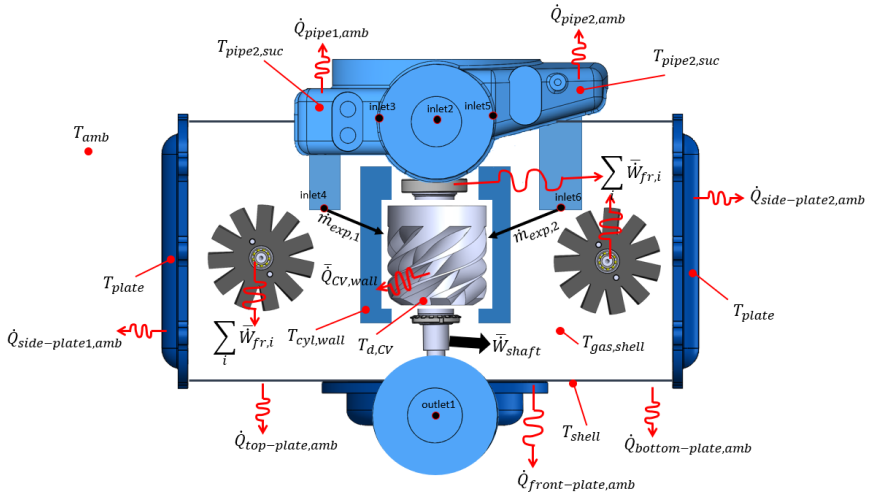

Figure 4.11: Schematic of the overall energy balance of the single-screw expander.

As shown in Figure 4.12, there are six unknown temperatures: the shell temperature, T_{shell}; temperature of refrigerant gas in the housing, $T_{\mathrm{gas,shell}}$; side plate temperatures, T_{plate}; suction temperatures, $T_{\mathrm{pipe1,suc}}$ and $T_{\mathrm{pipe2,suc}}$; cylinder wall temperature, $T_{\mathrm{cyl,wall}}$. To be noted is that the temperature of the gas within the shell corresponds to the temperature associated with the control volume *outletshell*. The amount of heat lost to the environment due to natural convection is dependent on the temperatures of the housing according to Newton's law of cooling. In order to derive the stedy-state energy balance equations for each lumped-element, the following conventions are imposed [40]:

- heat addition to an element is considered positive;

- heat transferred from the element is considered negative;
- internal heat generation which includes frictional heat generation is considered positive.

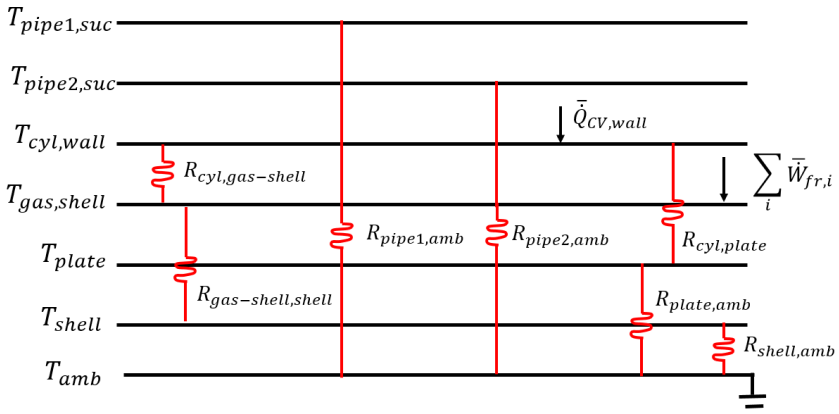

Figure 4.12: Thermal resistance network of the overall energy balance for single-screw expander.

By applying the energy conservation law to each component, the following equations can be derived:

$$\dot{m}_{\mathrm{exp},1}\left(h_{\mathrm{su},2}-h_{\mathrm{su},4}\right)-\dot{Q}_{\mathrm{pipe1,amb}}=0 \tag{4.35}$$

$$\dot{m}_{\mathrm{exp},2}\left(h_{\mathrm{su},2}-h_{\mathrm{su},6}\right)-\dot{Q}_{\mathrm{pipe2,amb}}=0 \tag{4.36}$$

$$\dot{m}_{\mathrm{exp},1}\left(h_{\mathrm{su},4}-h_{\mathrm{dis}}\right)+\dot{m}_{\mathrm{exp},2}\left(h_{\mathrm{su},6}-h_{\mathrm{dis}}\right)=\dot{W}_{\mathrm{pV}}+\dot{Q}_{\mathrm{cyl,wall}} \tag{4.37}$$

$$\dot{m}_{\mathrm{exp}}\left(h_{\mathrm{dis}}-h_{\mathrm{out},1}\right)=\dot{Q}_{\mathrm{friction}}-\dot{Q}_{\mathrm{gas,shell}} \tag{4.38}$$

$$\dot{Q}_{\mathrm{cyl,wall}}-\dot{Q}_{\mathrm{top-plate,amb}}-\dot{Q}_{\mathrm{bottom-plate,amb}} \tag{4.39}$$

$$\dot{Q}_{\mathrm{gas,shell}}-\dot{Q}_{\mathrm{side-plate1,amb}}-\dot{Q}_{\mathrm{side-plate2,amb}}-\dot{Q}_{\mathrm{front-plate,amb}} \tag{4.40}$$

The heat transfer rate terms $\dot{Q}_{\mathrm{pipe1,amb}}$, $\dot{Q}_{\mathrm{pipe2,amb}}$, $\dot{Q}_{\mathrm{top-plate,amb}}$, $\dot{Q}_{\mathrm{bottom-plate,amb}}$, $\dot{Q}_{\mathrm{side-plate1,amb}}$, $\dot{Q}_{\mathrm{side-plate2,amb}}$, $\dot{Q}_{\mathrm{front-plate,amb}}$ and $\dot{Q}_{\mathrm{gas,shell}}$ are expressed in the form:

$$\dot{Q}=\frac{T_{\mathrm{a}}-T_{\mathrm{b}}}{R_{\mathrm{ab}}} \tag{4.41}$$

where, $T_{\mathrm{a}}-T_{\mathrm{b}}$ is the temperature difference between two elements and R_{ab} is the heat transfer thermal resistance. In order to find the thermal resistances, empirically correlated averaged Nusselt numbers are calculated.

The cylinder walls exchange heat with the gas within the shell by free convection as well as with the upper and lower surfaces of the housing by conduction. Thus, the thermal conductance of the heat transfer between cylinder wall and housing is given by:

$$\mathrm{UA}_{\mathrm{cyl-wall,upper-plate}} = \frac{2\pi k_{\mathrm{iron}} L_{\mathrm{upper-plate}}}{log \frac{r_{\mathrm{upper-plate}}}{r_{\mathrm{cyl-wall}}}} \tag{4.42}$$

where k_{iron} is the thermal conductance of the cast iron housing approximated as $70\ \mathrm{W/(mK)}$.

There are five types of free convection heat transfer mechanisms that can be identified on the single-screw housing:

- the heat transfer over the upper surface of a plate,
- over the lower surface of a plate
- along a vertical plate,
- along a horizontal pipe
- and that along a vertical pipe.

For each free convection heat transfer type, adequate correlations for the Nusselt number needs to be defined [41]. In particular, for the free convection over the upper surface of a plate:

(a) hot plate, $T_{\mathrm{s}} > T_{\mathrm{inf}}$

$$\overline{\mathrm{Nu_L}} = 0.54\mathrm{Ra_L^{1/4}} \left(10^4 \leq \mathrm{Ra_L} \leq 10^7\right) \tag{4.43}$$

(b) cold plate, $T_{\mathrm{s}} < T_{\mathrm{inf}}$

$$\overline{\mathrm{Nu_L}} = 0.27\mathrm{Ra_L^{1/4}} \left(10^5 \leq \mathrm{Ra_L} \leq 10^{10}\right) \tag{4.44}$$

For the free convection over a lower surface of a plate:

(a) hot plate, $T_{\mathrm{s}} > T_{\mathrm{inf}}$

$$\overline{\mathrm{Nu_L}} = 0.27\mathrm{Ra_L^{1/4}} \left(10^5 \leq \mathrm{Ra}L \leq 10^{10}\right) \tag{4.45}$$

(b) cold plate, $T_{\mathrm{s}} < T_{\mathrm{inf}}$

$$\overline{\mathrm{Nu_L}} = 0.15\mathrm{Ra_L^{1/3}} \left(10^7 \leq \mathrm{Ra_L} \leq 10^{11}\right) \tag{4.46}$$

Churchill and Chu [42] proposed a correlation to calculate the averaged Nusselt number for the free convective heat transfer along a vertical plate over the entire range of Rayleigh number, $\mathrm{Ra_L}$:

$$\overline{\mathrm{Nu}} = \left\{0.825 + \frac{0.387\mathrm{Ra}_L^{1/6}}{\left[1 + \left(\frac{0.492}{\mathrm{Pr}}\right)^{9/16}\right]^{8/27}}\right\}^2 \tag{4.47}$$

In the case of laminar flow, the following correlation is suggested:

$$\overline{\mathrm{Nu}} = 0.680 + \frac{0.670\mathrm{Ra}_L^{1/4}}{\left[1 + \left(\frac{0.492}{\mathrm{Pr}}\right)^{9/16}\right]^{4/9}} \tag{4.48}$$

For the case of a horizontal pipe

$$\overline{\mathrm{Nu}} = \left\{0.600 + \frac{0.387\mathrm{Ra}_D^{1/6}}{\left[1 + \left(\frac{0.559}{\mathrm{Pr}}\right)^{9/16}\right]^{8/27}}\right\}^2 \quad \mathrm{Nu}_D \leq 10^{12} \tag{4.49}$$

where the subscript D refer to the diameter of the pipe. Sparrow and Gregg [43] suggested using Equation 4.47 to calculate the Nusselt number for the free convection along a vertical pipe if the following condition is satisfied:

$$\frac{D}{L} \geq \frac{35}{\mathrm{Gr}_\mathrm{L}^{1/4}} \tag{4.50}$$

where D is the pipe diameter, L is the pipe length and Gr_L is the Grashof number. The following modification factor should be used to multiply the averaged Nusselt number if the above condition is not satisfied:

$$F = \frac{1}{3}\left[\frac{L/D}{1/\mathrm{Gr}_\mathrm{L}}\right]^{1/4} + 1 \tag{4.51}$$

In all the free convection cases, the so-called film temperature is used to determine the fluid thermal properties which can be defined as:

$$T_\mathrm{f} = \frac{T_\mathrm{s} + T_\mathrm{inf}}{2} \tag{4.52}$$

where T_s is the surface temperature and T_inf is the temperature of the ambient or working fluid depending on the case.

4.9 Solution scheme

From the general structure of the mechanistic model describe in Section 2.7, the solution scheme is based on different layers and therefore different solvers. The flowchart schematic of the solution algorithm is shown in Figure 4.13. Before the simulation can start, the geometric calculations are initialized to store values of volume curve, volume derivative, sealing lines and groove surface for each of the control volumes. At the beginning of the simulation, the mass flow rate is not known along with the discharge temperature and lumped temperatures. For a given

set of boundary conditions, i.e., inlet temperature and pressure, discharge pressure, the discharge temperature of the oil-refrigerant mixture is calculated from:

$$\begin{aligned} h_{\mathrm{d,guess}} = h_{\mathrm{su,mix}}\left(T_{\mathrm{su,exp}}, p_{\mathrm{su,exp}}, x_{\mathrm{L}}\right) \\ -\eta_{ad,exp,guess}\left(h_{\mathrm{su,mix}} - h_{\mathrm{ex,s,mix}}\left(s_{\mathrm{su,exp}}, p_{\mathrm{ex,exp}}, x_{\mathrm{L}}\right)\right) \end{aligned} \tag{4.53}$$

where the adiabatic efficiency of the expander is assumed as 0.7. The mass flow rate through the expander is guessed by assuming a filling factor equal to unity:

$$\dot{m}_{\mathrm{guess}} = 2 z_{\mathrm{sr}} \rho_{\mathrm{su,mix}} V_{\mathrm{g},1} \frac{N_{\mathrm{exp}}}{60} \tag{4.54}$$

Each of the control volumes are initialized with either the inlet conditions or the discharge conditions. At this point, guess values of the lumped temperatures are necessary to begin the integration of the governing equations over one cycle. Before the integration of the differential equations over one revolution can occur, the mass flow between all the chambers, i.e., inlet and outlet flows, leakage flows, and the heat transfer must be calculated. The adaptive solver is used to march through the rotation and to predict the state properties at the next step. Once the cycle is completed, the end cycle callbacks check the continuity of the state variables between beginning of the rotation and the end. The cycle is considered converged if such difference is within a tolerance. At the end of the cycle, a post process functions calculates the instantaneous boundary work, average values of one rotations of mass flow rates and heat transfer rate. The mechanical analysis is then executed to determine the mechanical losses. The discharge state and the overall energy balance residuals are the final requirements to ensure that the model is fully converged. In particular, the discharge enthalpy is obtained by imposing an energy balance that is enforced by solving the exhaust flow path backwards, and back-calculating the enthalpy of the fluid leaving the set of working chambers. The residual is the difference in the enthalpy between the back-calculated enthalpy and the outlet enthalpy of the set of chambers from the simulation. This discharge enthalpy from the chambers is calculated by carrying out the integrals in the equation

$$h_{\mathrm{d,chambers}} = \frac{\int_d \dot{m}_i h_i}{\int_d \dot{m}_i} \tag{4.55}$$

over the entire cycle A relaxed secant solver is used to derive the residual of the exhaust energy balance to zero. The outermost layer of the solution algorithm is the minimization of the overall energy balance residual. In the case of a single-lumped temperature, the solution method is quite straightforward as a simple one-dimensional minimization algorithm can be used. In this case, a relaxed secant solver is employed. If the convergence of the lumped temperature is unstable, other more robust solvers such as Dekker algorithm can be implemented. When a multi-lumped overall energy balance is used, a system of equations is

obtained and has to be solved simultaneously. There are different numerical methods available to solve the system of nonlinear equations either based on gradients, e.g., Newton-Raphson or Broyden's methods, or based on matrix manipulations, e.g., Gauss-Seidel or Gauss-Jordan. The numerical challenges arise from the fact that non-physical solutions of the lumped temperature may exist or the possibility that the solver diverges from the actual solution (wrong direction). In PDSim, a modified Broyden's method and a Gauss-Seidel method have been implemented. The convergence criteria for each residual are listed in Table 4.3.

Residual	Criterion
$\epsilon_{\mathrm{cycle-cycle}}$	0.001
ϵ_{OEB}	0.01
h_{d}	$< 0.1\ \epsilon_{\mathrm{OEB}}$ and $\epsilon_{\mathrm{OEB}} < 0.01$

Table 4.3: Convergence criteria for the residuals of the mechanistic model.

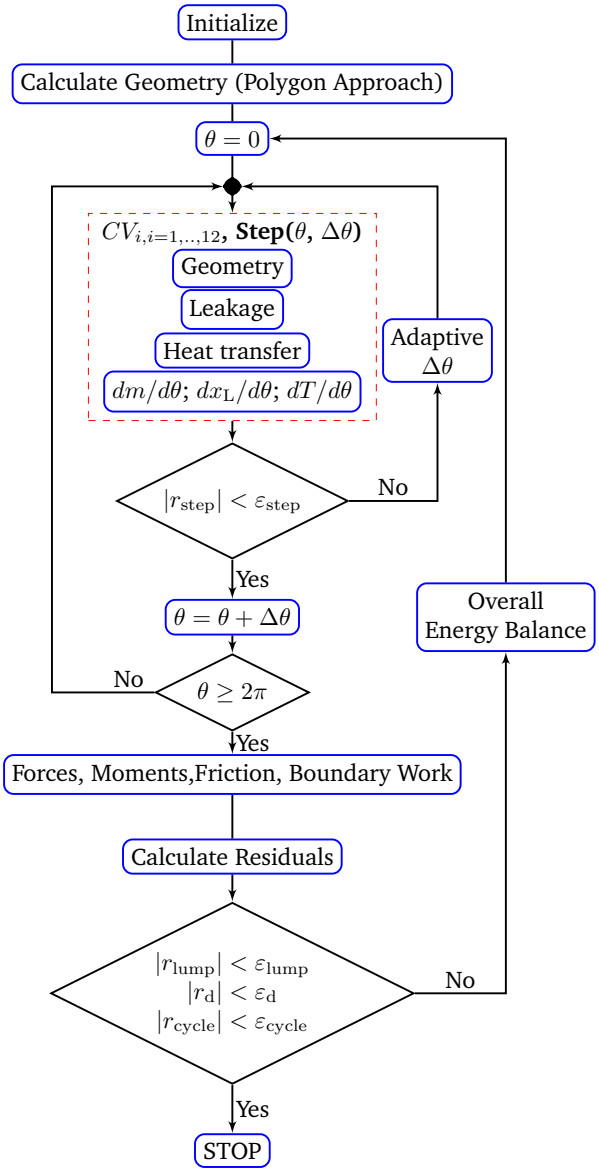

Figure 4.13: Solution algorithm of the single-screw mechanistic model.

References

[1] T. W. Bein and J. F. Hamilton. *Computer modeling of an Oil Flooded Single Screw Air Compressor*. In International Compressor Engineering Conference, 1982. Paper 383.

[2] W. W. Boblitt and J. Moore. *Computer Modeling of Single-Screw Oil Flooded Refrigerant Compressors*. In International Compressor Engineering Conference, number 506, 1984.

[3] J. Wu and G. Jin. *The Computer Simulation of Oil-Flooded Single Screw Compressors*. In International Compressor Engineering Conference, 1988. Paper 646.

[4] T. Hirai, S. Noda, Y. Sagara, and K. Tsuzi. *Performance Analysis of OIF Single Screw Compressor*. In International Compressor Engineering Conference, number 520, 1986. Paper 520.

[5] Z. Wang, Z. Wang, J. Wang, W. Jiang, and Q. Feng. *Theoretical and experimental study on thermodynamic performance of single screw refrigeration compressor with Multicolumn Envelope Meshing Pair*. Applied Thermal Engineering, 103:139–149, 2016.

[6] N. Casari, A. Suman, D. Ziviani, M. van den Broek, M. De Paepe, and M. Pinelli. *Computational Models for the Analysis of positive displacement machines: Real Gas and Dynamic Mesh*. Energy Procedia, 129:411–418, 2017.

[7] D. Ziviani, A. Suman, N. Casari, M. van den Broek, M. De Paepe, and M. Pinelli. *Real gas model and moving mesh in single-screw compressors and expanders*. 3rd Short Course and Forum: Computational Fluid Dynamics in Rotary Positive Displacement Machines, City Univesity of London, 2017.

[8] D. Ziviani, Gabrielloni J. Suman, A., M. Pinelli, M. De Paepe, and M. van den Broek. *CFD Approaches Applied To A Single-Screw Expander*. In 23th Int.Compressor Engineering Conference at Purdue, number 1488, 2016.

[9] D. Chisholm. *Two-Phase flow in pipelines and heat exchangers*. George Goodwin, London, 1983.

[10] G. B. Wallis. *One-dimensional Two-phase Flow*. McGraw-Hill Book Company, 1969.

[11] I. H. Bell, J. Wronski, S. Quoilin, and V Lemort. *Pseudo-pure Fluid Thermophysical Property Evaluation and the Open-Source Thermophysical Property Library CoolProp*. Ind. Eng. Chem. Res., 53:2498–2508, 2014.

[12] Jason Hugenroth. *Liquid Flooded Ericsson Cycle Cooler*. PhD thesis, Purdue University, 2006.

[13] V.P. Zheleznya, Yu.V. Semenyuka, S.N. Ancherbaka, A.J. Grebenkovb, and O.V. Beliayevab. *An experimental investigation and modelling of the solubility, density and surface tension of 1,1,1,3,3-pentafluoropropane (R-245fa)/synthetic polyolester compressor oil solutions*. Journal of Fluorine Chemistry, 128:10291038, 2007.

[14] V. P. Zhelezny, V. V. Sechenyh, Y. V. Semenyuk, A. J. Grebenkov, and O. V¿ Beliayeva. *An experimental investigation and modelling of the viscosity refrigerant/oil solutions*. International Journal of Refrigeration, 32:1389–1395, 2009.

[15] V. P. Zhelezny, S. V. Nichenko, Y. V. Semenyuk, B. V. Kosoy, and R. Kumar. *Influence of compressor oil admixtures on theoretical efficiency of a compressor system*. International Journal of Refrigeration, 32:1526–1535, 2009.

[16] I. H. Bell. *Theoretical and Experimental Analysis of Liquid Flooded Compression in Scroll Compressors*. PhD thesis, Purdue Univeristy, 2011.

[17] Vincent Lemort. *Contribution to the Characterization of Scroll Machines in Compressor and Expander Modes*. PhD thesis, University of Liège, 2008.

[18] Z. Wang, Z. Liu, W. Wu, and Q. Feng. *Research of leakage characteristics of single screw refrigeration compressors with the Multicolumn Envelope Meshing Pair*. International Journal of Refrigeration, 49:1–10, 2015.

[19] Thomas W. Bein. *A Computer Model of a Single Screw Air Compressor*. Master's thesis, Purdue Univerisity, 1980.

[20] W. Post. *The Hydrodynamic Lubrication in a Globoid Wormcompressor*. PhD thesis, Technische Hogeschool Eindhoven, 1983.

[21] T. Li, R. Liu, Z. Huang, F. Liu, and Q. Feng. *Research of the hydrodynamic lubrication characteristcs of different meshing pair profiles in water-flooded single screw compressors*. Proceedings of IMechE, Part A: J. of Power and Energy, 23(2):247–259, 2016.

[22] W. Wang, Y-T Wu, C-F Ma, G-D Xia, and J-F Wang. *Experimental study on the performance of single screw expander by gap adjustment*. Energy, 62:379–384, 2013.

[23] H. Li. *Effects of some key factors on working process of a single screw compressor*. In International Compressor Engineering Conference at Purdue University, number Paper 1078., 1996.

[24] M. M. Mathison, James E. Braun, and Eckhard A. Groll. *Modeling of a Two-Stage Rotary Compressor*. HVAC&R Research, 14:719–748, 2008.

[25] Y. Wu, R. Zhi, W. Wang, L. Shen, Y. Zhang, B. Lei, J. Wang, and C. Ma. *Mathematical modeling of torque for single screw expanders*. Journal of Mechanical Science and Technology, 31(1):429–436, 2017.

[26] Y.-R. Wu and V.-T. Tran. *Dynamic response of a twin-screw compressor with gas-induced cyclic loads based on multi-body dynamics*. International Journal of Refrigeration, 65:111–128, 2016.

[27] T. Li, Wang Z.-L., R. Huang, W.-F. Wu, and Q. K. Feng. *Theoretical analysis of loads on the gate rotor bearings in the single screw compressor*. In Proceedings of International Conference on Compressor and their Systems at the City University of London, pages 219–225, 2013.

[28] Yangguang Liu, Chinghua Hung, and Yuchoung Chang. *Design optimization of scroll compressor applied for frictional losses evaluation*. Int. J. Refrig., 33(3):615 – 624, 2010.

[29] K. Okada and K. Kuyama. *Motion of Rolling Piston in Rotary Compressor*. In International Compressor Engineering Conference at Purdue University, 1982.

[30] T Yanagisawa and T Shimizu. *Friction losses in rolling piston type rotary compressors. III*. Int. J. Refrig., 8(3):159 – 165, 1985.

[31] G. Bianchi and R. Cipollone. *Friction power modeling and measurements in sliding vane rotary compressors*. Applied Thermal, 84:276–285, 2015.

[32] C. R. Bradshaw, G. Kemp, J. Orosz, and E. A. Groll. *Development of a loss pareto for a rotating spool compressor using high-speed pressure measurements and friction analysis*. Applied Thermal Engineering, 99:392–401, 2016.

[33] Miguel Jovane. *Modeling and analysis of a novel rotary compressor*. PhD thesis, Purdue University, 2007.

[34] Pawan J. Singh. *A Digital Reciprocating Compressor Simulation Program Including Suction and Discharge Piping*. In International Compressor Engineering Conference at Purdue 1984, 1984.

[35] R. Link and C. J. Deschamps. *Numerical modeling of startup and shutdown transients in reciprocating compressors*. International Journal of Refrigeration, 34:1398–1414, 2011.

[36] Bernard J. Hamrock, Steven R. Schmid, and Bo O. Jacobson. *Fundamentals of Fluid Film Lubrication*. CRC Press, 2004.

[37] Zhji Liu. *Simulation of a Variable Speed Compressor with Special Attention to Supercharging Effects*. PhD thesis, Purdue University, 1994.

[38] Yu Chen. *Mathematical Modeling of Scroll Compressors*. PhD thesis, Purdue University, 2000.

[39] Jun-Hyeung Kim. *Analysis of a Bowtie Compressor with Novel Capacity Modulation*. PhD thesis, Purdue University, 2005.

[40] S. K. Padhy. *Heat transfer model of a rotary compressor*. International Compressor Engineering Conference at Purdue, page Paper 935., 1992.

[41] Frank P. Incropera and David P. Dewitt. *Fundamentals of Heat and Mass Transfer (5th Edition)*. Wiley, 2002.

[42] S. W. Churchill and H. H. S. Chu. *Correlating equations for laminar and turbulent free convection from a horizontal cylinder*. International Journal of Heat and Mass Transfer, 18:1049–1053, 1975.

[43] E. M. Sparrow and J. L. Gregg. *Laminar free convection heat transfer from the outer surface of a vertical circular cylinder*. Transactions of the ASME, 78:1823–1830, 1956.

5

Experimental Characterization of a Single-Screw Expander

5.1 Introduction

Experimental studies on single-screw expanders (SSE) reported in literature have been carried out by focusing mainly on compressed air type of machines. For instance, Wang et al. [1] evaluated the performances of a SSE prototype by using air as working fluid with a design inlet flow rate of 1.1 Nm^3/min. The experimental tests were carried out at different intake flows, different humidities, constant torque and constant rotational speed. The results showed a maximum power output of 5 kW at 2850 rpm and maximum adiabatic efficiency of 59%. The low adiabatic efficiency value was justified by the poor lubrication system and the use of dry air. Lu et al. [2] investigated a SSE with 175 mm diameter rotor by using a compressed air system. The SSE was able to reach an adiabatic efficiency above 65% with a temperature drop of 70 °C. He et al. [3] analyzed the influence of the intake pressure on the performance of a SSE with 175 mm diameter rotor. The experimental results showed that high values of intake pressure negatively affect the power output. A resonance phenomenon occurred in the range 2000 rpm and 2200 rpm, leading to large leaking. The maximum power output of 22 kW was obtained at 2800 rpm with and the highest adiabatic efficiency was of around 55%. Wang et al. [4] analyzed the influence of the gap size between rotor/shell and starwheel/shell with compressed air as working fluid. Medium size gaps, i.e. 0.04 mm and 0.05 mm, provided the best overall performance with a

maximum expander shaft efficiency of 60% and a maximum volumetric efficiency of approximately 66%. Li et al. [5] developed a 195 mm diameter single-screw expander to recover pressure energy in letdown natural gas stations. Tests were conducted with compressed air instead of natural gas. The results showed a maximum overall expander efficiency of 62.2% obtained at 2800 rpm with an electric power output of 51.1 kW.

Limited work has been done on SSE employed in ORC systems. Zhang et al. [6] developed a SSE with a 155 mm diameter rotor along with an ORC test rig for waste heat recovery from the exhaust of a diesel engine. The working fluid chosen was R123. The main focus was to evaluate the influence of the expander torque and diesel engine loads on the performance of the ORC. A maximum power output of 10.38 kW was achieved with an overall expande efficiency of 57.9%. Yang et al. [7] carried out a similar work by using R245fa as working fluid. A performance map was presented showing the relationship between the expander isentropic efficiency with inlet pressure and rotational speed. The peak of isentropic efficiency was slightly above 65% and it was obtained for an inlet pressure of 1700 kPa (applied pressure ratio of 8) at 3200 rpm. Lei et al. [8] designed a single-screw expander with an internal volume ratio of 4.86 to investigate the effect of large expansion ratio conditions. By using R123 as working fluid, the maximum shaft power output obtained was 8.35 kW with an isentropic efficiency at the shaft of 56%. A total of 21 steady-state points were analyzed under three rotational speeds (2000 rpm, 2500 rpm and 3000 rpm).

In order to assess the potential of SSEs as volumetric expanders for ORC applications, a more in-depth characterization of their performance is required. Currently, several aspects have not been addressed yet in the open-literature. The most important ones, but not limited to, are:

- performance behavior of SSE with different working fluids in an ORC installation;
- relationship between the geometric built-in volume ratio and the applied system pressure ratio as well as the specific expansion ratio;
- quantify the major SSE internal losses and identify design improvements;
- impact of lubricant oil on leakage path and friction losses;
- absence of available experimental data of SSE employed in ORC systems with different working fluids.

The objective of this chapter is to experimentally characterize the single-screw expander shown in Figure 5.1. The chapter is divided into two sections. In Section 5.2, the single-screw expander is installed in a down-scaled industrial regenerative ORC and directly connected to a 11 kWe generator. As the experimental apparatus

has been described in details by Melotte [9] and Lecompte [10], only the main features are reported for completeness. The testing is conducted by employing two working fluids, i.e., SES36 and R245fa. The lubricant oil is Mobil EAL ARTIC 68. In Section 5.3, a numerical analysis is carried out to break down the losses of the expander and to evaluate the impact of design improvements.

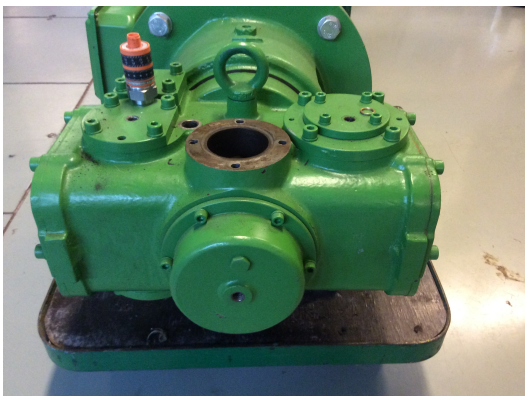

Figure 5.1: View of the single-screw expander used in the present work in its original configuration.

5.2 Industrial ORC Experimental Apparatus

5.2.1 Test setup and Measurement Devices

A standard single-screw air compressor, shown in Figure 5.1, has been converted to operate as expander and installed in a down-scaled industrial ORC unit assembled with off-the-shelf components. Modifications to the compressor unit were necessary to guarantee the proper functionality as expander. In particular, the seals of main shaft, side plates and starwheel bearings caps were substituted to withstand higher temperatures and refrigerant-type of working mediums. The discharge port of the expander (suction port as compressor) has been enlarged to minimize filling losses. Additional oil injection points were added in the housing to ensure proper lubrication of starwheel bearings and main shaft bearings as well as sealing of the gaps. The schematic of the ORC test setup with the installed sensors is shown in Figure 5.2(a). The unit includes three identical brazed plate heat exchangers, a multi-stage centrifugal pump and a buffer tank placed after the condenser. The waste heat source is simulated by means of a 250 kW electric heater with Therminol 66 (T66) as working medium. Both the mass flow rate and the temperature of the thermal oil can be controlled. The heat sink is realized by

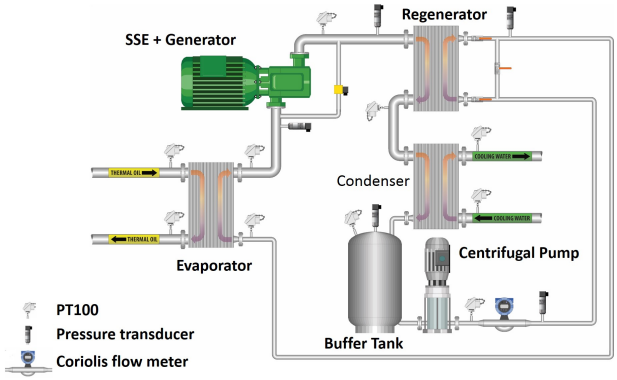

(a)

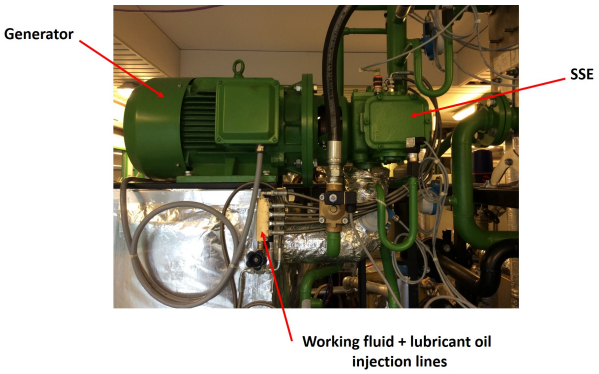

(b)

(c)

Figure 5.2: (a) ORC test rig schematic at Ghent University, Campus Kortrijk; (b) close-up view of the single-screw expander installed and (c) the injection points.

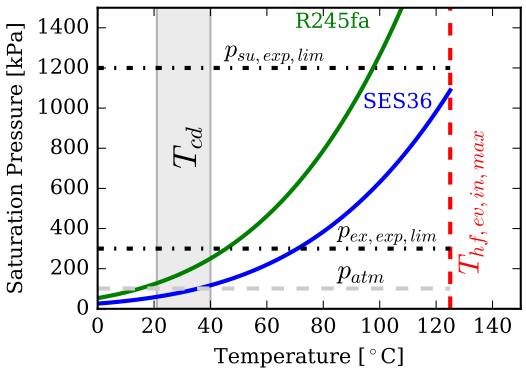

Figure 5.3: Working fluid operating conditions during the tests. Saturation curves are shown for SES36 and R245fa. The expander limit conditions are also overlaid. In particular, the maximum expander inlet pressure is set conservatively to 1200 kPa and the maximum discharge pressure is rated at 250 kPa.

using an intermediate water/ethylene glycol loop with a circulating pump and the heat is rejected to ambient by means of a rooftop air-cooled unit.

The open-drive expander is directly coupled to an asynchronous generator with 11 kWe nominal electric power and a bleeding line after the centrifugal pump provides the lubrication for the expander (mixture of liquid working fluid and up to 3% vol. of Mobil EAL Artic 68). A close-up view of the expander is shown in Figure 5.2(b) and the injection points are visible in FIgure 5.2(c). The geometry details of the expander are summarized in Table 5.1. The electrical power produced by the generator is injected into the electric grid by means of a four-quadrant inverter, which also allows to vary the generator rotational speed from 0 to 3600 rpm. The details of the other main components of the ORC installation are listed in Table 5.2. The ORC working fluids considered during the tests are R245fa and SES36. SES36 is a dry fluid, i.e. positive slope of the vapor saturation curve, instead R245fa is considered an isentropic/dry type of fluid. The main characteristics of the fluids are listed in Table 5.3. Thermodynamic properties are retrieved in real time by using the CoolProp library coupled with LabVIEW [11]. The current expander imposes certain limitations on the range of suitable operating conditions that can be explored. The high-pressure side of the expander can withstand up to 1400 kPa but for safety reasons the limit has been set at 1200 kPa. Similarly, the pressure on the expander discharge side could not exceed 300 kPa. The expander inlet temperature is fixed at 125°C throughout the testing in order to fairly compare the two working fluids. The working conditions as well as the saturation curves of the working fluids are shown in Figure 5.3. To be noted is that the condensing temperature varies significantly during the tests because it is related to the outdoor conditions. Two expander rotational speeds,

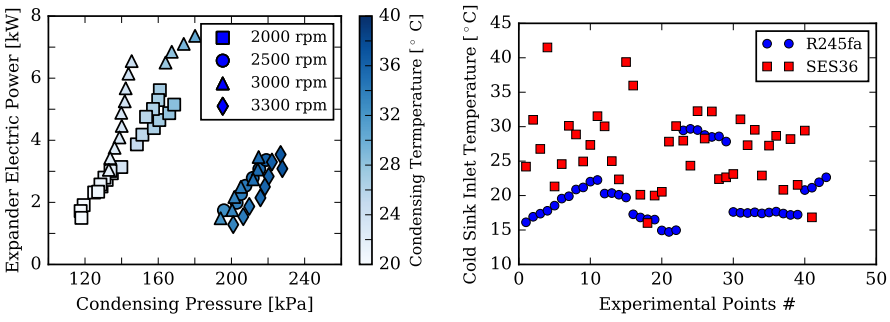

Figure 5.4: (a) Influence of the condensing temperature and pressure on the expander performance for R245fa due to seasonality; (b) variability of the cold sink inlet temperature at the condenser during the testing campaigns.

i.e. 2000 rpm and 3000 rpm (nominal speed of the generator), were initially identified as of interest for the industrial use of the expander. Therefore, both working fluids have been compared based on these rotational speeds throughout the safe operating range. The frequency of the pump has been varied between 25 Hz and 40 Hz. In the case of R245fa, two additional rotational speeds, i.e. 2500 rpm and 3300 rpm, were investigated in order to assess potential influence on the performance. However, due to high external ambient temperatures during the tests, the condensing pressure was very close to the upper limit of 250 kPa which limited the applicable pressure ratio across the expander. As a consequence, the achievable operating points in terms of pressure ratios across the expander were limited in the range of $r_{p,exp} = 3.58 - 4.54$. Under such conditions the expander was working around its internal volume ratio or with slight over-expansion. This fact is shown in Figure 5.4(a). Thus, the variability of the cold source inlet temperature during the different runs can be seen in Figure 5.4(b). For the sake of completeness, all the collected steady-state points are presented in Figure 5.5. In particular, in Figure 5.5(b), all four rotational speeds are distinguished. However, the rotational speeds of 2500 rpm and 3300 rpm will not be considered due to the limited pressure ratio range that was reachable during the experiments.

A number of sensors have been installed in the ORC test rig and their locations are visible in Figure 5.2(a). In particular, absolute pressure senors (APS) and RTDs (resistance temperature detectors) have been placed before and after each component with the exception of the outlet on the regenerator vapor side where only a temperature measurement was installed. A Coriolis flow meter (CFM) is employed to accurately measure the mass flow rate of the working fluid. Temperature and flow rate measurements have been performed also on the cooling and heating loops. Two ultrasonic flow meters (UFM) were used to measure

Engaging ratio	[-]	11/6
D_{sr}	[mm]	122
D_{sw}	[mm]	132
$V_{g,max}$	[cm^3]	57.39
$r_{V,built-in}$	[-]	5.3
L_{rotor}	[mm]	121

Table 5.1: Geometric parameters of 11 kWe single-screw expander [12].

Component	**Type**
Pump	Calpeda MXV 25-214
Expander	BEP 11 kW Single-screw expander
Evaporator	SWEP B200T SC-M (150 plates)
Condenser	SWEP B200T SC-M (150 plates)
Recuperator	SWEP B200T SC-M (150 plates)
Liquid receiver	50 L
Piping	Steel

Table 5.2: Main components of the ORC test setup.

Property	**R245fa**	**Solkatherm® SES36**
Type	pure fluid	azeotropic mixture
Components	pentafluoropropane	R365mfc/ perfluoropolyether (65%-35% by mass)
Molar mass [kg/mol]	0.13404	0.18485
Critical point temperature [K]	427.01	450.7
Critical point pressure [kPa]	3651.0	2849.0
GWP_{100} [-]	1020 [13]	4121 [14]

Table 5.3: Fluid properties of R245fa and SES36.

Variable	Sensor	Range	Uncertainty (k=2)
$\dot{m}_r$	CFM	0-1.8 kg/s	±0.09 %
$\dot{m}_{\mathrm{hf}}$	UFM	0-6 L/s	±0.1 %
$\dot{m}_{\mathrm{cf}}$	UFM	0-6 L/s	±0.1%
T(ORC)	RTD	50-300 °C	±0.2 K
T(T66 loop)	RTD	30-350 °C	±0.2 K
T(heat sink loop)	RTD	0-150	±0.2 K
p	APS	0-1600 kPa	± 1.6 kPa
$\dot{W}_{\mathrm{el,grid}}$,$\dot{W}_{\mathrm{pp,el}}$	Wattmeter	0-100 kW	±0.1 %
$\mathrm{N}_{\mathrm{exp}}$	PLC	-	Neglected

Table 5.4: Operating range and uncertainties of the measurement devices. k indicates the coverage factor.

flow rate of the thermal oil and the water-glycol mediums. The data acquisition system is done through a PLC connected to LabVIEW for control purposes. The measuring range of each sensor and the associated uncertainty are listed in Table 5.4. Steady-state points were detected by following the criteria reported in [15].

5.2.2 Data Reduction and Uncertainty Analysis

The electric power injected into the grid is measured by the inverter. The net power produced by the ORC is obtained by subtracting the pumping power from the expander electric power measured at the grid:

$$\dot{W}_{\mathrm{el,net}} = \dot{W}_{\mathrm{el,grid,exp}} - \dot{W}_{\mathrm{el,pp}} \tag{5.1}$$

Due to the absence of a torque meter to measure the expander shaft power, an overall isentropic efficiency that includes the expander and the generator/inverter is defined as follows:

$$\eta_{\mathrm{is,oa,meas}} = \frac{\dot{W}_{\mathrm{el,grid,exp}}}{\dot{W}_{\mathrm{is,exp}}} = \frac{\dot{W}_{\mathrm{el,grid,exp}}}{\dot{m}_{\mathrm{r,exp}} \left(h_{\mathrm{su,exp}} - h_{\mathrm{ex,is,exp}}\right)} \tag{5.2}$$

In order to obtain the isentropic efficiency at the shaft, the generator efficiency and the inverter effectiveness should be accounted for as follows,

$$\dot{W}_{\mathrm{el,grid,exp}} = \eta_{\mathrm{mech,gen}}\, \varepsilon_{\mathrm{el,inv}} \dot{W}_{\mathrm{sh,exp}} \tag{5.3}$$

and therefore,

$$\eta_{\mathrm{is,sh,exp}} = \frac{\dot{W}_{\mathrm{sh,exp}}}{\dot{W}_{\mathrm{is,exp}}} = \frac{\dot{W}_{\mathrm{el,grid,exp}}}{\eta_{\mathrm{mech,gen}}\, \varepsilon_{\mathrm{el,inv}} \left[\dot{m}_{\mathrm{r,exp}} \left(h_{\mathrm{su,exp}} - h_{\mathrm{ex,is,exp}}\right)\right]} \tag{5.4}$$

Table 5.5: Minimum and maximum values of the measured and derived variables for the single-screw expander with rotational speeds of 2000 rpm and 3000 rpm.

	$p_{su,exp}$ (kPa)	$T_{su,exp}$ (°C)	$p_{ex,exp}$ (kPa)	$T_{ex,exp}$ (°C)	$\dot{m}_r$ (kg/s)	r_p (-)	r_v (-)	$\dot{W}_{exp,el}$ (W)	$\varepsilon_{is,oa,exp}$ (-)	φ_{FF} (-)	$\eta_{ORC,net}$ (-)
SES36											
Min	450	91.7	90.6	73.99	0.15	3.63	3.80	903.8	0.135	0.897	0.010
Max	1028	125	177.9	102.0	0.41	8.83	9.99	6865	0.647	1.117	0.092
R245fa											
Min	566	106.7	120	75.5	0.12	3.71	3.76	1283	0.2058	0.938	0.014
Max	1230	124.9	232	104.6	0.37	7.26	7.74	7364	0.5191	1.231	0.077

Table 5.6: Summary of the uncertainty analysis carried out on the experimental data points.

	$u_{\dot{m}_r}$ (kg/s)	u_{r_p} (-)	u_{r_v} (-)	$u_{\Delta h_{exp}}$ (kJ/kg)	$u_{\dot{W}_{exp,el}}$ (W)	$u_{\varepsilon_{is,oa,exp}}$ (-)	$u_{\varphi_{FF}}$ (-)	$u_{\eta_{ORC,net}}$ (-)
SES36								
Min	0.01354	0.03829	0.04328	194.4	90.38	0.0384	0.07863	0.004494
Max	0.03202	0.1443	0.1693	213.3	685.8	0.08543	0.1036	0.0156
Avg	0.02295	0.08563	0.09723	202.3	379.4	0.07075	0.09176	0.01145
R245fa								
Min	0.01148	0.02885	0.03078	298.7	128.3	0.0277	0.0893	0.003883
Max	0.03406	0.0714	0.07779	316.0	736.4	0.0705	0.1197	0.1431
Avg	0.02223	0.05109	0.05435	307.4	354.9	0.0523	0.1042	0.01376

The correlations for the generator and the inverter efficiency have been obtained from [9] and they are provided in Appendix C.

A volumetric expander is characterized by its built-in volume ratio, $r_{\mathrm{V,built-in}}$. For the single-screw expander, the built-in volume ratio is defined as:

$$r_{\mathrm{V,built-in}} = \frac{V_{\mathrm{g},2}}{V_{\mathrm{g},1}} \tag{5.5}$$

where $V_{\mathrm{g},1}$ and $V_{\mathrm{g},2}$ represent the volume of the main rotor groove at suction closure and at the beginning of the discharge process, respectively. The details of the geometry calculations of the single-screw expander can be found in Chapter 3. The specific volume expansion ratio across the expander, $r_{\mathrm{v,exp}}$, is given by:

$$r_{\mathrm{v,exp}} = \frac{v_{\mathrm{ex,exp}}\left(T_{\mathrm{ex,exp}}, p_{\mathrm{ex,exp}}\right)}{v_{\mathrm{su,exp}}\left(T_{\mathrm{su,exp}}, p_{\mathrm{su,exp}}\right)} \tag{5.6}$$

The volumetric performance of a positive displacement expander is defined by means of the filling factor, φ_{FF}.The filling factor is given by:

$$\varphi_{\mathrm{FF}} = \frac{\dot{m}_{\mathrm{r,exp}} v_{\mathrm{su,exp}}}{\dot{V}_{\mathrm{swept,th}}} = \frac{\dot{m}_{\mathrm{r,exp}} v_{\mathrm{su,exp}}}{2\, z_{\mathrm{sr}}\, V_{\mathrm{g},1}\, \left(N_{\mathrm{rot,exp}}/60\right)} \tag{5.7}$$

Finally, the ORC system net cycle efficiency is obtained by

$$\eta_{\mathrm{ORC,net}} = \frac{\dot{W}_{\mathrm{el,net}}}{\dot{Q}_{\mathrm{r,ev}}} \tag{5.8}$$

where $\dot{Q}_{\mathrm{r,ev}}$ is the heat rate input at the evaporator by considering the working fluid side.

It is known that measured quantities carry uncertainties due to systematic and random errors of the sensors. The measurement uncertainties are then propagated to the calculated quantities. The methodology described by Figliola and Beasley [16] to estimate the propagation of uncertainties is used to compute the uncertainties of calculated results. It is important to notice that the data analysis of the ORC is applied to data sets representing the steady-state conditions. Although, the measured values are not intrinsically constant during the steady state due to random fluctuations, the true state of the system is assumed to be constant. It follows that the average value of a function of interest, e.g., isentropic efficiency, which is a function of a number of measured variables, can be computed by inputting the average value of each measured variable. The true value of a function, f_{true}, over a steady-state interval is given as:

$$f_{\mathrm{true}} = \bar{f} \pm u_f \tag{5.9}$$

where u_f is obtained as:

$$u_f = \sqrt{\sum_{i=1}^{n} \left(\left. \frac{\partial f}{\partial x_i} \right|_{x_i = \bar{x}_i} u_{x_i} \right)^2} \tag{5.10}$$

A confidence band of desired probability of 95% is always considered. Hence, the propagated uncertainty to calculated result also holds with 95% probability . The partial derivatives in Equation 5.10 are calculated using a central difference scheme with a step size equal to the uncertainty of the measured variable. The accuracy of the measuring devices can be obtained from Table 5.4.

The uncertainty analysis has been carried out by using the software EES (Engineering Equation Solver) [17]. The fluid properties and their partial derivatives have been evaluated using the CoolProp database [11].

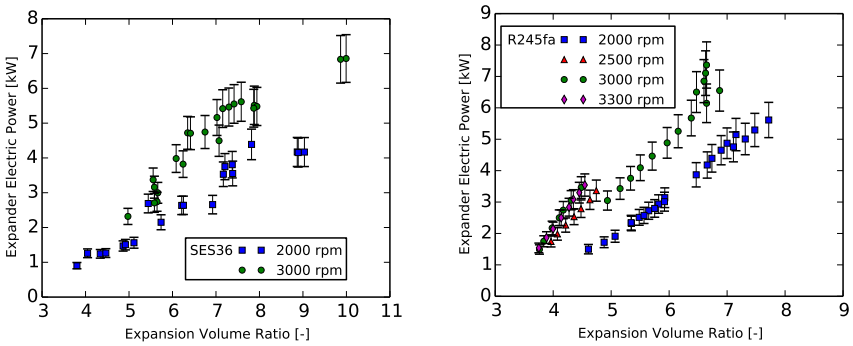

(a) (b)

Figure 5.5: Expander electric power out as function of the expansion volume ratio for SES36 and R245fa at different rotational speeds. All the steady-state points are displayed. Uncertainty bars of the power output are overlaid.

5.2.3 Test Matrix and Results

The performance of the expander is strongly related to the inlet pressure forced by the centrifugal pump. The frequency of the pump is progressively increased from 20 Hz up to 40 Hz with a step size of 0.83 Hz (approximately 50 rpm). The lower value of the frequency is set to avoid low cycle efficiency due to high superheating, whereas the upper value corresponds to safety pressure requirements. As the heat source inlet temperature is fixed at 125 °C, by increasing the pump frequency, the evaporating pressure of the ORC rises and the degree of superheating decreases. The cooling medium flow rate has been kept constant to the maximum value. The pump rotational speed variation has been repeated for two expander rotational

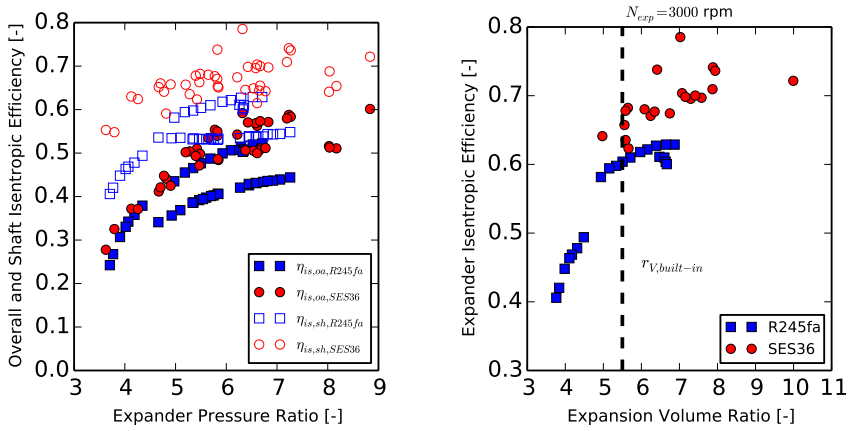

(a) (b)

Figure 5.6: (a) Expander measured overall isentropic efficiency and estimated shaft isentropic efficiency as functions of different pressure ratios, for two rotational speeds:2000 rpm and 3000 rpm; (b) Expander estimated shaft isentropic efficiency at 3000 rpm as a function of the expansion volume ratio. The built-in volume ratio is marked on the plot for reference.

speeds, i.e., 2000 rpm and 3000 rpm. Such test matrix has been used for both working fluids. A total of 59 and 43 steady-state points were obtained for R245fa and SES36. The minimum and maximum values of measured and calculated variables are summarized in Table 5.5. Furthermore, the results of the uncertainty analysis are listed in Table 5.6. The complete set of steady-state data points are available in Table D.1 and in Table D.2.

By comparing the performance obtained with the two working fluids, a higher power output was achieved with R245fa, as seen in Figure 5.5. The peak of electric power output for R245fa was around 7.4 kW with a pressure ratio of 6.3 and a degree of superheating of 26.7 °C, as shown in Figure 5.5(b). In the case of SES36, reported in Figure 5.5(a), the maximum power output achieved was 6.8 kW with a pressure ratio of 8.69 and a degree of superheating of 4.31 °C. For both working fluids, the power output presents a continuously increasing trend with respect to the specific expansion ratio. In fact, as the specific expansion ratio increases, the power generated increases due to the contribution of the under-expansion despite the decrease in efficiency of the expansion process. In the case of SES36 at 3000 rpm, the increase of power output for specific expansion ratios above 8 is reduced and it is related with the fact that the expander inlet conditions are close to saturation. Instead, R245fa would require higher pressure ratios to identify the real maximum in terms of both power output and efficiency. Furthermore, by looking

at the data points of the power output for both fluids, a scattering can be identified due to a variation of the operating conditions for example pressure fluctuations at the expander inlet at given pump rotational speed but different working fluids, or fluctuations of the condensing pressure. A discontinuity in the data trend can be recognized for R245fa at 3000 rpm and a pressure ratio of approximately 4.5 as shown Figure 5.5(b). As the experimental tests were performed in different days to cover the entire operating range, external weather conditions impacted the achievable power output as directly influenced by the air-cooled loop of the condenser. Similar discontinuity can also be seen in the case of the expander efficiency trends.

The expander overall efficiency and its estimated isentropic efficiency are shown in Figure 5.6(a). As a general behavior, the expander overall efficiency, $\eta_{\mathrm{oa,exp}}$, increases with the pressure ratio. The shape of the curve is related to the combined effect of generator and inverter. In fact, the higher the power produced and rotational speed, i.e., higher pressure ratios, the higher is the product $\eta_{\mathrm{mech,gen}} \cdot \epsilon_{\mathrm{el,inv}}$. Both the electro-mechanical efficiency of the generator and the electrical efficiency of the inverter present a log-type of behavior, as expressed by Equation C.1 and C.4. By decreasing the expander rotational speed, the efficiency curve tilts downwards. The effect of the rotational speed is more visible in the case of R245fa. By observing the isentropic efficiency values, they have a more flat behavior in the case of SES36, suggesting that a more optimal pressure ratio has been achieved. The overall expander efficiency is slightly higher for SES36. In fact, SES36 is characterized by a lower condensing pressure than R245fa, for a given condensing temperature, as shown in Figure 5.3. Therefore, since the maximum achievable pressure has an upper limit, SES36 allows higher pressure ratios across the expander which corresponds to higher specific work generated. Besides the pressure ratio across the expander, the imposed expansion volume ratio represents a more meaningful parameter in the case of volumetric expanders because of their fixed built-in volume ratio. Figure 5.6(b) shows the estimated isentropic efficiency at the shaft for R245fa and SES36 at the nominal speed 3000 rpm. The value of the built-in volume ratio is overlaid on the same figure. Qualitatively, the trend of the isentropic efficiency is almost constant between expansion volume ratios 6 and 7.5 which is coherent with the built-in volume ratio. Ideally, it is expected that the maximum occurs at the built-in volume. However, due to the fact that the actual measurements of pressure and temperature are taken externally to the expander on the pipelines, the imposed expansion ratio results always to be slightly larger than the built-in volume ratio in order to compensate internal pressure drops between the suction inlet and expansion chamber pocket as well as on the discharge side. In the case of SES36, the estimated values of the isentropic efficiency might be affected by the correlations used for generator and inverter efficiency. However, it is not clear yet at which expansion volume ratio

the drop-down of the isentropic efficiency occurs.

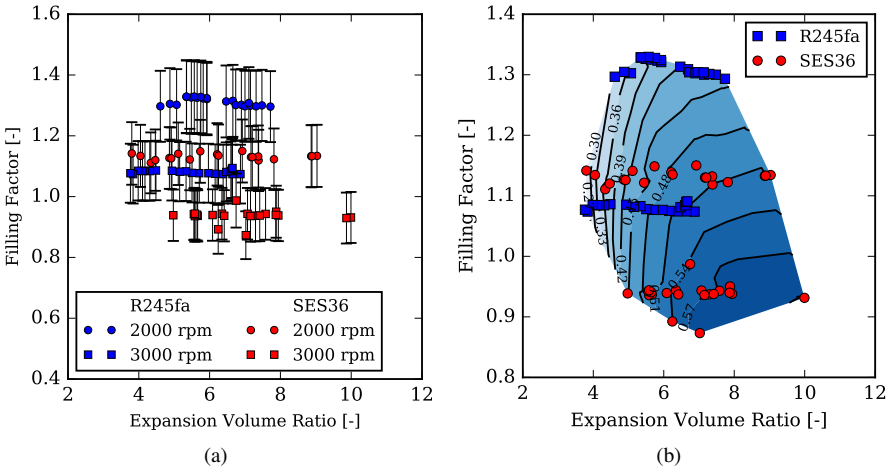

Figure 5.7: (a) Influence of the expander rotational speed and pressure ratio on the filling factor. Uncertainty bars are overlaid; (b) Overall isentropic efficiency as function of the expansion volume ratio and the filling factor. Both working fluid steaty-state points are overlaid.

The built-in volume ratio and the expansion volume ratio are also related to the volumetric performance of the expander in terms of filling factor. As stated by Woodland et al. [18], the isentropic efficiency of a volumetric expander can be fully characterized by its filling factor and expansion volume ratio. The filling factor for R245fa and SES36 and two rotational speeds is shown in Figure 5.7(a). As a general observation, the filling factor is a strong function of the rotational speed. For a certain rotational speed, the filling factor is weakly affected by the expander volume ratio and therefore the pressure difference across the expander. Ideally, the expander should run with a filling factor slightly larger than unity. R245fa at 3000 rpm presents an average filling factor of 1.08 which suggests it is an optimal rotational speed. On the contrary, SES36 seems to experience a slight under-filling. This fact could be related to some uncertainty around the exact internal volume ratio of the expander and possible internal losses that might affect the actual thermodynamic state at the internal suction port. The leakages play a more important role for R245fa. Two reasons can be given: (i) the suction pressure at higher pressure ratios is close to the housing limit; (ii) R245fa has been tested after running the single-screw expander for several hours with SES36. As a consequence, the tooth sealing lines could have been subjected to wear.

The behavior of the expander can be summarized by showing the overall isentropic efficiency as a function of operating conditions such as rotational speed

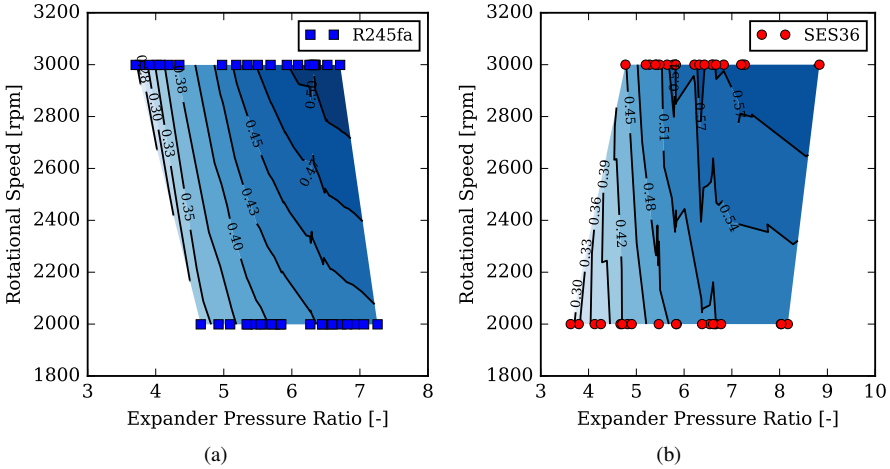

Figure 5.8: Overall isentropic efficiency of the expander as a function of applied pressure ratio and rotational speed (a) *R245fa;* (b) *SES36.*

(controlled variable) and pressure ratio (imposed variable) as well as internal aspects of the machine such as filling factor and expansion volume ratio. In particular, the relationship of the isentropic efficiency with the filling factor and expander efficiency is shown in Figure 5.7(b). Furthermore, the isentropic efficiency as a function of expander rotational speed and applied pressure ratio is reported in Figure 5.8. The experimental points used to generate the contour are also overlaid. The expander isentropic efficiency is maximum for a filling factor close to unity and for and expansion ratio in the range 6.5 to 7.5. A clear global maximum has not been clearly captured which suggests that higher expansion ratios should be explored experimentally. Generally, the peak is expected for a range of filling factor values slightly larger than unity. The reason is to be found in internal pressure drops and to potential leakage flows that still exist. At higher filling factors (meaning lower rotational speeds), the leakages become predominant because the working chamber is overfilled and the working fluid has the time to leak. The isentropic efficiency decreases as a consequence. A steeper decrease of isentropic efficiency occurs for expansion ratios below the built-in volume ratio (over-expansion region) where the isolines are significantly closer to each other. Even more detrimental for the expander performance should be the condition of under-filling and over-expanding which has not been investigated in this work. This fact is shown in Figure 5.9. The plot has been obtained by calibrating Pacejka's equation with experimental data points of R245fa, as described in Ziviani et al. [19], and by exercising the model for different rational speeds and pressure ratios.

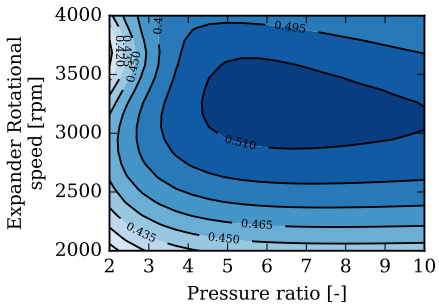

Figure 5.9: Overall isentropic efficiency of the expander as a function of applied pressure ratio and rotational speed (a) *R245fa;* (b) *SES36.*

An overall energy balance on the expander and electric equipment is also performed to gain insights on the electro-mechanical losses and heat losses through the expander housing. From the measurements, the sum of heat losses and electro-mechanical losses can be calculated as:

$$\dot{Q}_{\mathrm{amb,exp,loss}} + \dot{W}_{\mathrm{el-m,loss}} = \dot{m}_r \left(h_{\mathrm{su,exp}} - h_{\mathrm{ex,exp}}\right) - \dot{W}_{\mathrm{el,grid,exp}} \tag{5.11}$$

The left hand side of Equation 5.11 as a function of the pressure ratio is plotted in Figure 5.10(a). The total losses decrease quasi-linearly as the pressure ratio increases. In order to explain in a more accurate way the reason for that behavior, it is necessary to estimate the heat losses through the expander housing. This is accomplished by performing an energy balance only to the expander:

$$\dot{Q}_{\mathrm{amb,exp,loss}} = \dot{m}_r \left(h_{\mathrm{su,exp}} - h_{\mathrm{ex,exp}}\right) - \dot{W}_{\mathrm{sh,exp}} \tag{5.12}$$

The presence of lubricant oil inside the expander is neglected. The heat losses to the ambient represent up to 10% of the shaft power. Although the effect of the heat losses to the ambient on the shaft power is limited, by insulating the expander, the thermodynamic process could slightly improve. The negative values of the heat losses can be explained with an over prediction of the shaft power and due to uncertainties on the measurements as well as the correlations used for the efficiency of generator and inverter. The heat losses decreases with the increase of the pressure ratio. This is true in the range investigated, i.e. small over-expansion. In fact, the increase of pressure ratio corresponds to an increase of isentropic efficiency. In other words, the expansion improves toward an adiabatic transformation. This fact is shown in Figure 5.11(a) and Figure 5.11(b), where the measured inlet and outlet temperatures of the expander are plotted as function of the pressure ratio. For completeness, also the condensing pressure is overlaid. The increase of the condensing pressure is related to the external ambient conditions.

After determining the heat losses, the influence of the losses associated with generator and inverter can be quantified. A break-down of the electro-mechanical

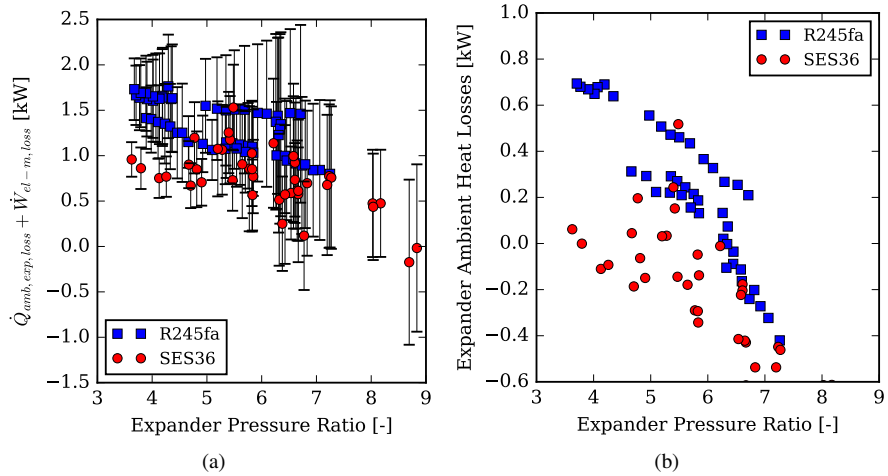

Figure 5.10: (a) Overall energy balance on the expander including generator and inverter. Uncertainty bars of the overall energy balance are overlaid; (b) Estimation of the expander heat losses through the housing.

losses is shown in Figure 5.12(a) for SES36 and in Figure 5.12(b) for R245fa. Each pie chart is representative of the average values for a certain fluid and rotational speed. In the case of SES36, at 2000 rpm the electro-mechanical losses account for 31.8%, indicating that both generator and inverter are operating at non-optimal conditions. In fact, at 3000 rpm the losses decrease to 21.9 % because the shaft power increased. When the ORC is running with R245fa, the power output is generally higher than with SES36. At 2000 rpm, the electro-mechanical losses are around 25.7%. However, at 3000 rpm, even tough the average value of the electro-mechanical losses is decreased by 1.3%, they are higher than the corresponding case of SES36. This is consistent with the fact that R245fa was also tested at low expansion volume ratios (below 5) for 3000 rpm where the power output obtained was below 2 kW.

5.3 Discussion

The actual expander shaft power is affected by internal leakages, heat transfer losses and friction losses, as shown in the energy flow chart of an open-drive expander of Figure 1.3. The electro-mechanical losses associated with the generator and inverter are also accounted for externally to the expander shell. Due to heat losses as well as frictional losses, the adiabatic definition of the isentropic efficiency, i.e. $\eta_{\mathrm{is,ad,exp}} = \Delta h_{exp}/\Delta h_{\mathrm{exp,is}}$ [20], is not representative of the real performance of the machine. In light of the experimental data and the influence

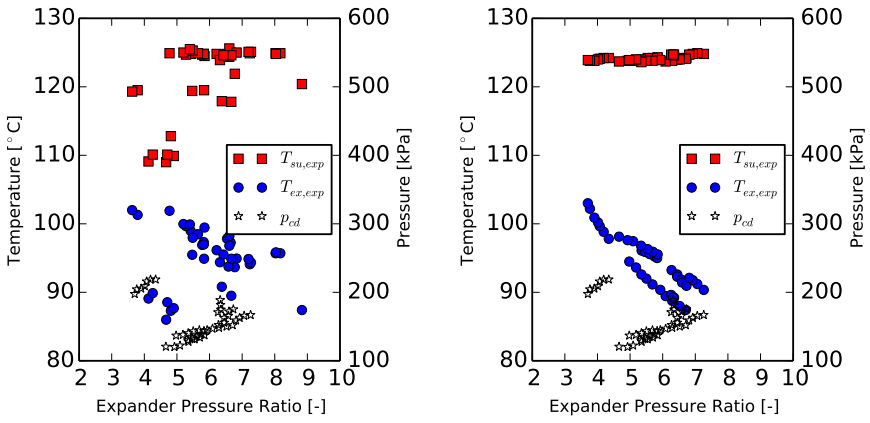

Figure 5.11: Expander suction and discharge temperature at different pressure ratios: (a) SES36; (b) R245fa. In the plots, also the condensing pressure is shown.

of the different loss terms to the expander performance, a calibrated expander semi-empirical model becomes useful to assess potential design improvements by reducing each loss term. The details of the model and its calibration are provided in Appendix D. The expander semi-empirical model is used to quantify the different power and heat rate losses under different pressure ratio conditions. The model has been exercised by fixing the rotational speed at 3000 rpm, the inlet temperature at 125 °C, and by varying the suction pressure in order to simulate a wide range of pressure ratios and consequently expansion ratios. The discharge pressure for each working fluid is defined as the average value of experimental data. The discharge pressures are set to 150 kPa and 110 kPa for R245fa and SES36, respectively.) The evolution of the expander power output and the different loss terms with respect the applied expansion ratio is displayed in Figure 5.13(a) and Figure 5.13(b). On the graphs, the shaft isentropic efficiency and overall isentropic efficiency are also overlaid. It can be noted that the term associated with friction and electro-mecanical losses is predominant. The contribution of solely electric equipment can be seen by comparing the trends of shaft power, $\dot{W}_{sh,exp}$ and electric power, $\dot{W}_{el,exp}$. The friction losses of the current expander can be related to the lack of minimum lubrication required due to partial occlusion of the injection orifices observed during the maintenance of the machine. By comparing the magnitude of the friction losses, the expander running with R245fa has higher values. This can be attributed by the amount of hours that the single-screw has accumulated during the testing with SES36. A more accurate estimation of the internal mechanical/friction losses can be done by installing a torque meter.

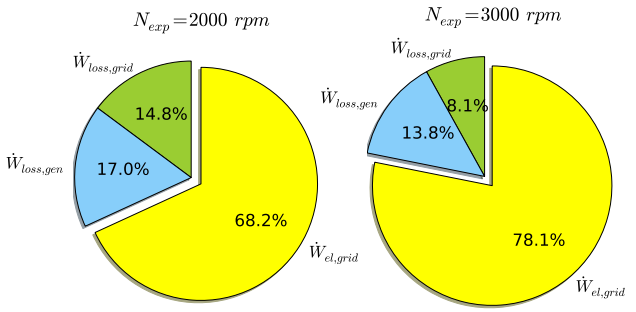

(a)

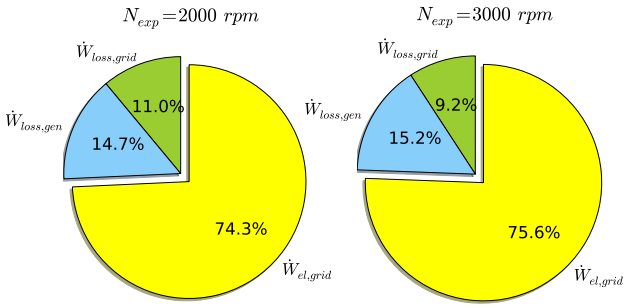

(b)

Figure 5.12: Contribution of the electro-mechanical losses on the total expander power output at the shaft. The inlet temperature is fixed at 125 °C: (a) SES36; (b) R245fa (adapted from Ziviani et al. [19]).

The second major contribution to the expander losses is the leakage term which represents between 10% and 15% of the shaft power.

SSE running with R245fa has been identified as the test case since the pressure ratio applied to the machine was not optimized due to structural limitations. Such parametric analysis is carried out by first selecting the best experimental steady-state point measured as the reference condition, i.e., suction pressure and temperature of 1020 kPa and 124.1 °C, discharge pressure 152 kPa and rotational speed of 3000 rpm. Secondly, part of the calibrated parameters (listed in Table D.3) related to design features are varied to assess the sensitivity of

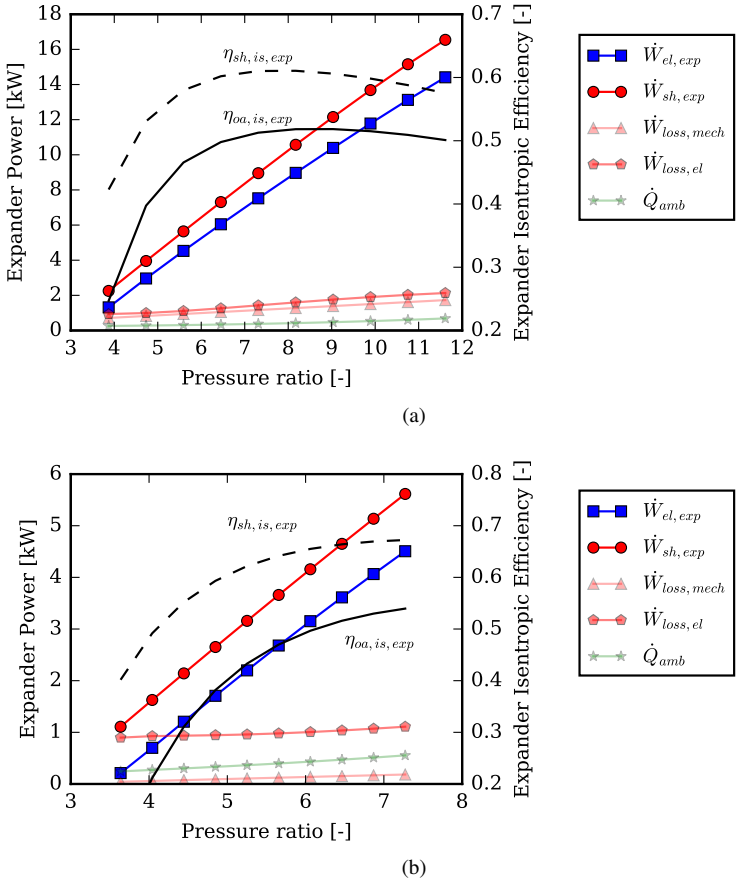

Figure 5.13: Numerical results of the semi-empirical model: (a) influence of the electro-mechanical losses, leakage and heat losses on the expander power outputs with R245fa. The inlet temperature is fixed at 125 °C and the condensing pressure is set at 150 kPa. The suction pressure is varied between 600 kPa and 1800 kPa. The expander rotational speed is 3000 rpm.; (b) influence of the electro-mechanical losses, leakage and heat losses on the expander power outputs with SES36. The inlet temperature is fixed at 125 °C and the condensing pressure is set at 110 kPa. The suction pressure is varied between 400 kPa and 1000 kPa. The expander rotational speed is 3000 rpm.

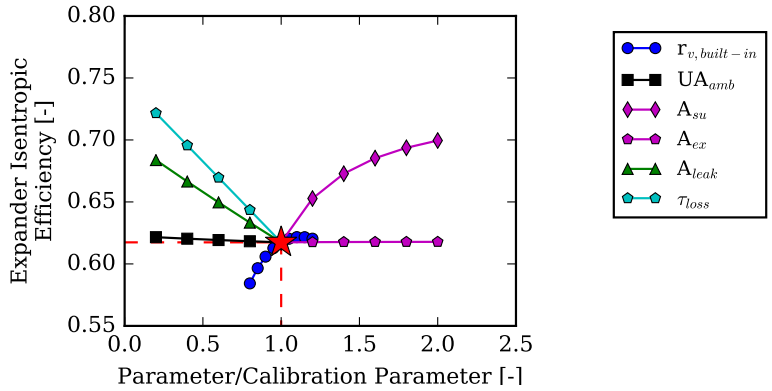

Figure 5.14: Evaluation of potential improvements on the single-screw expander. The reference condition is marked with a star and it represents the best operating point measured, i.e. $T_{su,exp}$ = 124.1 °C, $p_{su,exp}$ = 1020 kPa, $p_{ex,exp}$ = 152 kPa at 3000 rpm. The isentropic efficiency is plotted as a function of different model parameters normalized with respect the calibrated values.

the expander performance with these parameters. The list of parameters are reported in the legend of Figure 5.14. Each of them have been varied one at the time in the direction that has engineering relevance, for example the loss related coefficient is decreased, the suction port pressure drop throat area is increased, and the built-in volume ratio is increased and decreased. The range in which the parameters are varied is determined as follows: if a parameter is a loss (τ_{loss}, UA_{amb}, A_{leak}), the ratio parameter/calibrated parameter ranges from 1 (original value) to 0.1 (up to 90% decrease in losses). From a practical point of view, losses cannot be zero. If a parameter is associated with a design modification ($r_{\text{V,built-in}}$), A_{suc}, A_{ex}), engineering considerations are made in order to vary the parameters in the proper direction. For example, the built-in volume ratio has been increased and decreased to capture the overall trend. In fact, in a positive displacement expander, over-expansion losses are detrimental to its performance. In the reference condition, the pressure ratio applied is r_p = 6.71. Decreasing the built-in volume ratio (up to 30% reduction) results in a rapid decrease of the overall isentropic efficiency. Since the actual volume ratio of the expander considered in this work is approximately 5.5, there is a slight improvement on the expander efficiency by increasing the built-in volume ratio (up to 20%). For the single-screw expander, built-in volume ratio above 6 would result in a very small triangular suction port. There is a trade-off between increasing the volume ratio and limiting suction pressure drops. The throat areas at suction and discharge have been increased to reduce the pressure drops. While, the discharge area has no tangible effects, the suction area plays a key role for an expander. The throat area has been

increased up to twice the original value to achieve a sort of asymptotic behavior. The results of the parametric study is presented in Fig. 5.14. The plot shows the expander isentropic efficiency as function of normalized parameters with respect each calibration value. The reference condition (1,0.622) is also shown. It can be noted that under such pressure ratio, an increase of built-in volume ratio, $r_{\mathrm{V,built-in}}$, has small influence on the performance which means the expander is operating at proper pressure ratio with respect the internal design. However, if the built-in volume ratio is reduced, there is a rapid degradation of the performance. The effect of the ambient losses, UA_{amb}, on the efficiency seems to be limited. However, the heat losses can be reduced by properly insulating the expander shell. By reducing both the mechanical losses, τ_{loss}, and the equivalent leakage area, A_{leak}, the efficiency increases by approximately 20%. The equivalent leakage area accounts for manufacturing defects, wearing of the profiles, thermal effects on the rotor. Leakages and mechanical friction losses can be reduced by improve the lubrication. Furthermore, the expander performance could also be improved by enlarging the equivalent suction area, A_{suc}, to limit flow blockage. On the other hand, the discharge port area, A_{ex}, has no significant effects under the current operating point. Large under-expansion conditions might require adaptations to the discharge port area. By improving the design of the expander, the maximum isentropic efficiency achievable is in the order of 72.5%.

References

[1] W. Wang, C.F. Wu, Y.T.and Ma, L.D. Liu, and J. Yu. *Preliminary experimental study of single screw expander prototype*. Applied Thermal Engineering, 31:3684 3688, 2011.

[2] Y. Lu, W. He, Y. Wu, W. Ji, C. Ma, and H. Guo. *Performance study on the compressed air refrigeration system based on single screw expander*. Energy, 55:762–768, 2013.

[3] W. He, Y. Wu, Y. Peng, Y. Zhang, C. Ma, and G. Ma. *Influence of intake pressure on the performance of single screw expander working with compressed air*. Applied Thermal Engineering, 51:662 669, 2013.

[4] W. Wang, Y-T Wu, C-F Ma, G-D Xia, and J-F Wang. *Experimental study on the performance of single screw expander by gap adjustment*. Energy, 62:379–384, 2013.

[5] G. Li, Y. Wu, Y. Zhang, R. Zhi, J. Wang, and C. Ma. *Performance Study on a Single-Screw Expander for a Small-Scale Pressure Recovery System*. Energies, 10(6):1–14, 2017.

[6] Y-Q Zhang, Y-T Wu, G-D Xia, C-F Ma, W-N Ji, S-W Liu, K. Yang, and F-B Yang. *Development and experimental study on organic Rankine cycle system with single-screw expander for waste heat recovery from exhaust of diesel engine*. Energy, 77:499–508, 2014.

[7] K. Yang, H. Zhang, S. Song, J. Zhang, a d Zhang Y. Wu, Y., H. Wang, Y. Chang, and C. Bei. *Performance Analysis of the vehicle diesel engine-ORC combined system based on a screw expander*. Energies, 7:3400–3419, 2014.

[8] B. Lei, Y.-T. Wu, C.-F. Ma, J.-F. Wang, L. Zhang, C. Li, Y.-K. Zhao, and R.-P. Zhi. *Development and experimental study on single screw expander integrated into an Organic Rankine Cycle*. Energy, 116:43–52, 2016.

[9] N. Melotte. *Experimental study and dynamic modeling of a Waste Heat Recovery Organic Rankine Cycle*. Master's thesis, University of Liege, 2012.

[10] S. Lecompte. *Performance Evaluation of Organic Rankine Cycle Architectures: Application to Waste Heat Valorisation*. PhD thesis, Ghent Univesity, 2016.

[11] I. H. Bell, J. Wronski, S. Quoilin, and V. Lemort. *Pure and Pseudo-pure Fluid Thermophysical Property Evaluation and the Open-Source Thermophysical Property Library CoolProp*. Industrial & Engineering Chemistry Research, 53(6):2498–2508, 2014.

[12] D. Ziviani, I. H. Bell, M. De Paepe, and M. van den Broek. *Update on single-screw expander geometry model integrated into an open-source simulation tool*. In 9th Int. Conf. on Compressors and their Systems, City University of London, London, number 39, 2015.

[13] R. Akasaka, Y. Higashi, A. Miyara, and S. Koyama. *A fundamental equation of state for cis-1,3,3,3-tetrafluoropropene (R-1234ze(Z))*. International Journal of Refrigeration, 44:168–176, 2014.

[14] V. Apostol, H. Pop, A. Dobrovicescu, T. Prisecaru, A. Alexandru, and M. Prisecaru. *Thermodynamic Analysis of ORC Configurations Used For WHR from a Turbocharged diesel engine*. Proceedia Engineering, 100:549–558, 2015.

[15] B. J. Woodland, J. E. Braun, E. A. Groll, and W. T. Horton. *Experimental Testing of an Organic Rankine Cycle with Scroll-type Expander*. In International Refrigeration and Air Conditioning Conference at Purdue, number 2505, 2012.

[16] R. S. Figliola and D. E. Beasley. *Theory and Design of Mechanical Measurements*. John Wiley & Sons, Inc., 5th edition edition, 2011.

[17] S. A. Klein. *Engineering Equation Solver Software (EES) - F-Chart*.

[18] B. J. Woodland. *Methods of increasing net power output of organic Rankine cycles for low-grade heat recovery with a detailed analysis using a zeotropic working fluid mixture and scroll expander*. PhD thesis, Purdue University, 2015.

[19] D. Ziviani, A. Desideri, V. Lemort, M. De Paepe, and M. van den Broek. *Low-order models of a single-screw expander for organic Rankine cyle applications*. In 9th Int. Conf. on Compressors and their Systems, City University of London, London, number 38, 2015.

[20] J-C Chang, T-C Hung, Y-L He, and W. Zhang. *Experimental study on low-temperature organic Rankine cycle utilizing scroll type expander*. Applied Energy, 155:150–159, 2015.

6

Single Screw Expander Analysis and Optimization

6.1 Introduction

A comprehensive mechanistic model of the single-screw expander has been described in Chapter 4. The phenomenological nature of the model allows to investigate the impact of different losses on the performance of the machine. At first, the experimental results obtained are used to validate the model. Then the mechanical losses estimated are used to carry on an optimization of the operation of the ORC with a single-screw expander.

6.2 Model validation

The mechanistic model is employed here to estimate the mechanical shaft power and to obtain the actual mechanical efficiency by including the friction power losses associate with the bearings and friction contacts between teeth and grooves. Therefore the mechanistic model is first validated with a set of experimental data. In particular, R245fa has been used for validation purposes due to the absence of transport properties for SES36 in CoolProp (in REFPROP 9.1.1 such fluid is not available), which are necessary for calculating the heat transfer coefficients in the overall energy balance as well as during the integration of the governing equations. The resulting parity plots between calculated and experimental points are shown

in Figure 6.1.

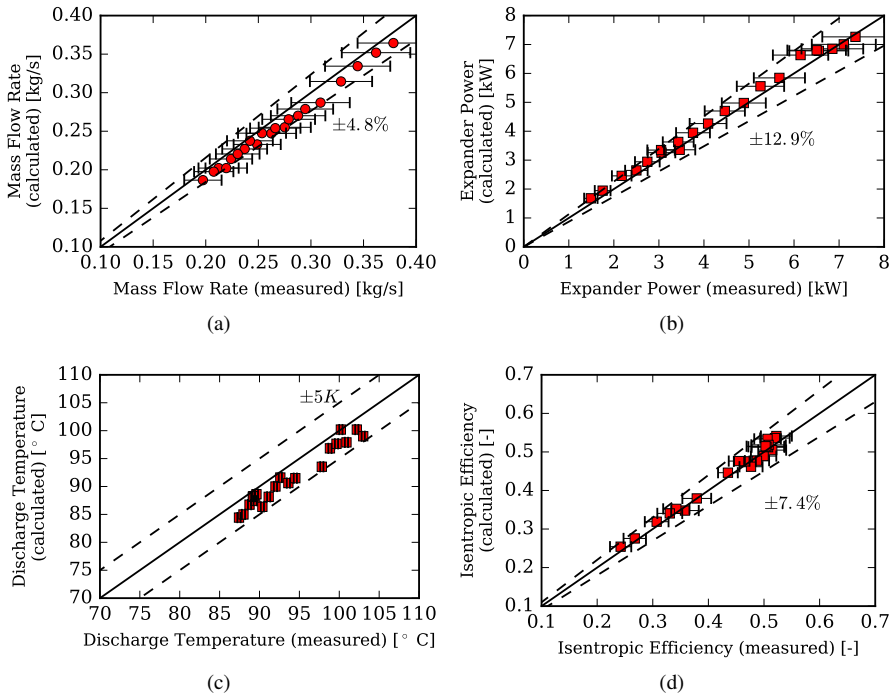

Figure 6.1: Non-symmetric single-screw expander model parity plots: (a) mass flow rate; (b) electric power output; (c) expander discharge temperature; (d) overall isentropic efficiency. A total of 21 steaty-state points are shown at 3000 rpm. Uncertainty bars are over laid. The maximum relative error is reported in each plot.

In Figure 6.2, the model has been exercised to obtain the p-V diagrams in both cases of under- and over-expansion. In particular, the inlet pressure and temperature are fixed at 800 kPa and 100 °C, the rotational speed of the main rotor is 3000 rpm and lubricant oil mass fraction is 0.01. Two values of the discharge pressure have been considered: 150 kPa (case with under-expansion) and 200 kPa (case with over-expansion). These values are also representative of the experimental operating conditions investigated (see Chapter 5). By comparing the two p-V diagrams, it can be noted that the over-expansion, shown in Figure 6.2(b), is particularly detrimental for the performance of the machine with respect to under-expansion. Under the specified conditions, the slight over-expansion caused a 17% decreased in power output. Due to the fact that the internal volume ratio of the expander is around 5.3, the peak of isentropic efficiency was obtained for an applied pressure ratio between 6 and 8.

The validated model has been exercised to calculate the boundary work rate

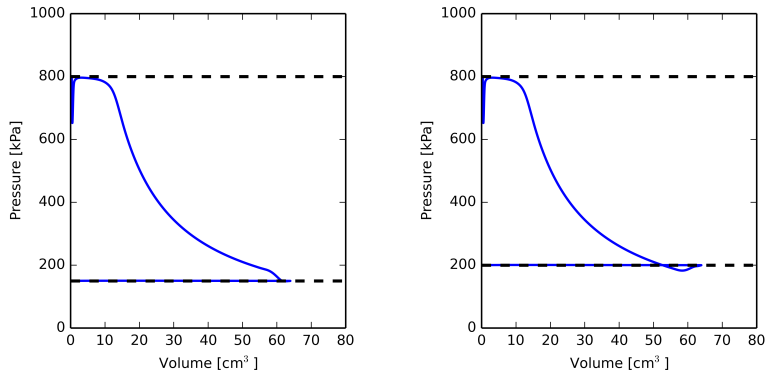

Figure 6.2: Pressure versus groove volume of single-screw expander (p_{su}= 800 kPa, T_{su}= 100 °C, x_L = 0.01, N = 3000 rpm): (a) under-expansion (p_{ex}= 150 kPa); (b) over-expansion (p_{ex}= 200 kPa).

and the friction losses for each of experimental conditions. The average boundary work rate generated by the expander is calculated as:

$$\overline{\dot{W}}_{pV} = \frac{\omega}{2\pi}\int_0^{2\pi} p(\theta)\frac{\mathrm{dV}}{d\theta}d\theta \tag{6.1}$$

The average mechanical power output of the expander is obtained by subtracting the mechanical losses from the boundary work rate:

$$\dot{W}_{\mathrm{sh,exp}} = \overline{\dot{W}}_{pV,exp} - \overline{\dot{W}}_{\mathrm{mech,loss}} \tag{6.2}$$

where the mechanical losses are obtained by solving the forces and moments balance equations for starwheel and main rotor. Thus, the mechanical efficiency of the expander is calculated as the ratio of the mechanical shaft power to the boundary work rate (or indicated power):

$$\eta_{\mathrm{mech,exp}} = \frac{\dot{W}_{\mathrm{sh,exp}}}{\overline{\dot{W}}_{pV,exp}} \tag{6.3}$$

The results are reported in Figure 6.3(a). In particular, the filled markers represents the calculated boundary work rate for two rotational speeds (2000 rpm and 3000 rpm) based on the actual experimental boundary conditions, i.e. inlet temperature and pressure and discharge pressure. To be noted is that the different trends of the boundary work rate at 3000 rpm are related to the fact that the condensing pressure is constantly varying during the testing, as already mentioned in Section 5.2.

By applying Equation 6.1, suction pressure losses are accounted for. The indicated efficiency contributions can be estimated by including the leakage losses. The total friction losses are overlaid in the same figure with empty markers. To be noted is that the friction losses represent a significant contribution to decrease the expander power output. In fact, the mechanical efficiency is estimated to be around 70% for expander pressure ratios between 5 and 7, near optimum operating conditions for the given internal volume ratio and internal pressure drops. Such high friction losses have been associated with the non-sufficient lubrication between tooth and starwheel as well as the bearings. After a detailed inspection, the injection orifices were found partially occluded. Additionally, the tooth profiles were worn out, suggesting high wear.

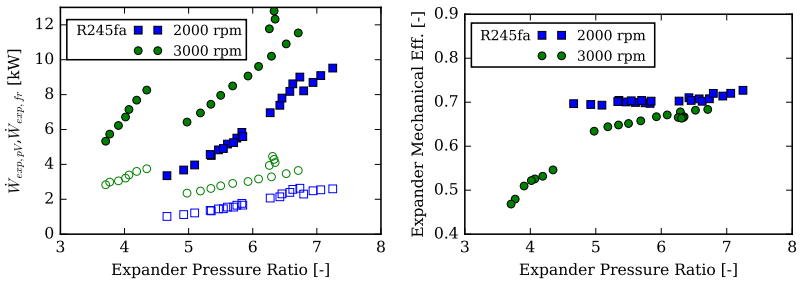

Figure 6.3: (a) Calculated boundary work rate (filled markers) and friction power losses (empty markers) as a function of the applied pressure ratio; (b) calculated mechanical efficiency of the expander.

To further validate the mechanistic model, dynamic pressure transducers have been installed in different points of the housing to capture the entire expansion process. The experimental work is currently ongoing on a new set of rotor and meshing pair of starwheels.

6.3 Optimizing the operation of a single-screw expander

A volumetric expander can be fully characterized by its overall isentropic efficiency, filling factor and specific expansion ratio. The performance and operating conditions of the single-screw expander with the two working fluids are summerized in Figure 6.4. The peak of overall isentropic efficiency is achieved for a filling factor close to unity (3000 rpm) and an imposed specific volume ratio between 8 and 10 and with SES36 as working fluid. However, during the operation of an ORC, both system and expander performance should be optimized

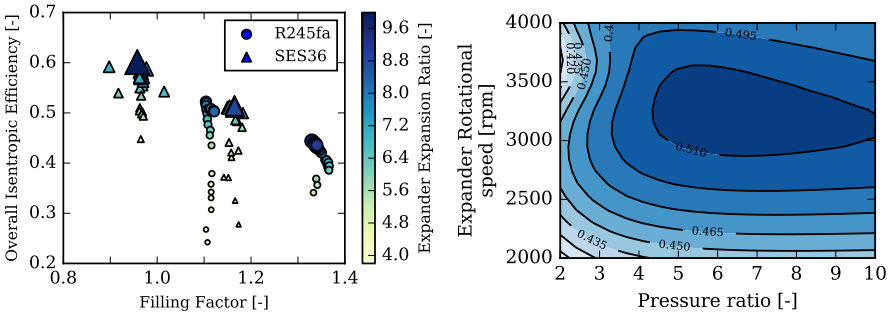

(a) (b)

Figure 6.4: Expander overall isentropic efficiency as function of the filling factor and specific expansion ratio. The marker size is proportional to the specific expansion ratio.

simultaneously. This aspect is analyzed by making use of the experimental data obtained and numerically by means of a cycle model. The ORC system can be considered as a heat engine with heat source having a finite capacity. Therefore, it is useful to assess the thermal performance against the theoretical maximum heat that can be recovered given by the Second Law of Thermodynamics. The Second Law efficiency in the case of an ORC system with a finite heat capacity heat source can be written as:

$$\eta_{II,finite} = \frac{\dot{W}_{el,net}}{\dot{m}_{hf} \int_0^{hf,in} \left(1 - \frac{T_0}{T}\right) \delta q} \tag{6.4}$$

where the denominator represents the thermal exergy of the heat source with a finite heat capacity and it can be expressed by:

$$\begin{aligned} \dot{m}_{hf} \int_0^{hf,in} \left(1 - \frac{T_0}{T}\right) \delta q = \\ \dot{m}_{hf} \Big\{ \left(h_{in}\left(T_{hf,in}, p_{hf,in}\right) - h_0\left(T_0, p_{hf,in}\right)\right) - \\ T_0 \left(s_{in}\left(T_{hf,in}, p_{hf,in}\right) - s_0\left(T_0, p_{hf,in}\right)\right) \Big\} \end{aligned} \tag{6.5}$$

The integral of the Carnot efficiency over the heat source profile limits has been calculated neglecting the contributions of kinetic energy and potential energy. Thus, since the thermal oil used as hot source is incompressible, any contribution associated to the pressure being slightly higher than the atmospheric one is neglected (the piping system is not pressurized). The dead state temperature is chosen to be the coldest temperature within the ORC system, i.e., the cooling medium entering the condenser, $T_{cf,in}$. If the heat source is fixed, then the

denominator of Equation 6.4 is independent of the cycle configuration or working fluid, which allows to fairly compare the performance of a certain system with different working fluids. To be noted is that, for a fixed heat source, maximizing $\eta_{II,finite}$ also means maximizing $\dot{W}_{el,net}$. Given a certain ORC installation, two performance indexes are introduced to characterize the matching between the expander performance and the ORC system efficiency. Such indexes are defined as normalized ratios of the overall isentropic efficiency and the Second Law efficiency calculated as in Equation 6.4 with respect to a reference condition. For a set of experimental data, the reference condition is chosen to be the maximum measured value of each quantity, i.e., $\eta_{II,finite,max}$ and $\eta_{is,oa,max}$. Mathematically, the indexes are given by:

$$\eta^*_{is,oa} = \frac{\eta_{is,oa}}{\eta_{is,oa,max}} \tag{6.6}$$

$$\eta^*_{II,finite} = \frac{\eta_{II,finite}}{\eta_{II,finite,max}} \tag{6.7}$$

Being the indexes independent from the working fluid adopted and the cycle architecture (e.g., subcritical, supercritical, trilateral flash cycle, partial-evaporating cycle, etc.) [1], it is suitable to compare the overall performance of the system with respect to the installed expander efficiency.

In the case of $\eta^*_{is,oa} = \eta^*_{II,finite} = 1$, both the system and the expander are operating at their best performance point with respect the set of measured values considered. Any deviation from the unity means that either the expander or the system operating point is moving toward lower efficiency. For a given ORC system, there exists a suitable range in which a reasonable high matching between system and expander performance is guaranteed. Additional information can be obtained regarding the part-load operation of the expander in terms of performance degradation.

The definition of $\eta^*_{is,oa}$ and $\eta^*_{II,finite}$ become more interesting if the optimum values of the finite Second Law efficiency, $\eta_{II,finite,opt}$, and expander isentropic efficiency, $\eta_{is,oa,opt}$, can be predicted by means of a model for a given set of operating conditions. If $\eta^*_{is,oa,opt} = \eta^*_{II,finite,opt} = 1$ then there is a perfect match between the system and the expansion machine. Typically, this occurs if the internal volume ratio of the expander is chosen to match the system specific volume ratio across the expander.

By analyzing Figure 6.5(a) and Figure 6.5(b). In particular, the plots show, for each working fluid, the relationships between the normalized indexes $\eta^*_{is,oa}$ and $\eta^*_{II,finite}$ and the expander pressure ratio. The nominal speed of 3000 rpm is considered. In the case of R245fa, Figure 6.5(a), for the working points at which the cycle Second Law efficiency reaches values close or equal to the maximum value measured, the expander works only around 82% of the maximum

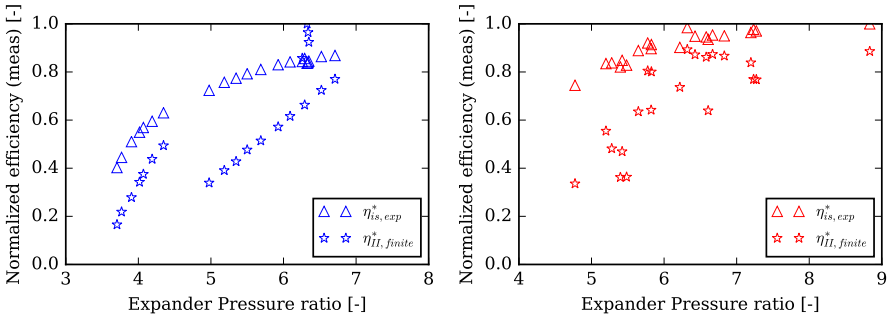

Figure 6.5: Normalized indexes $\eta^*_{is,exp}$ and $\eta^*_{II,finite}$ versus expander pressure ratio at 3000 rpm. (a) R245fa; (b) SES36.

isentropic efficiency. On the contrary, with SES36, the expander works for the large majority above 85% of the maximum isentropic efficiency because of higher pressure ratios allowed by the working fluid. Furthermore, the maximum cycle First Law efficiency is achieved by SES36 and the reason is that despite the lower power output generated, the heat rate recovered is significantly lower than in the case of R245fa due to the lower working fluid mass flow rate. However, the maximum cycle Second Law efficiency is achieved with R245fa because of the higher power generated with respect to the total exergy rate available from the heat source (Equation 6.4). As a consequence, the ORC running with R245fa should be further investigated to estimate the optimum operating point to maximize both the expander and cycle performance, which is covered in the second part of this work. The ORC unit running with R245fa has potential margin of improvement by increasing the pressure ratio. Practically, higher pressure ratios could be achieved with the current installation by improving the structural resistance of the expander. In order to optimize the ORC system to maximize the power output, the heat rate recovered has to be controlled by imposing the proper evaporating pressure which determines a certain superheating level. Thus, the recoverable heat is constrained by the presence of a pinch point temperature difference which is related to design of the evaporator. In particular for subcritical cycle, the location of pinch point can exist either at the exit of working fluid side of evaporator while the slope of curve of heat source is small (the heat capacity rate ratio of the heat source and cold sink is much higher than unity), or incipient boiling point of working fluid while the slope of curve of heat source is large (finite heat capacity). A control strategy can be developed on the basis of known inlet heat source and cold sink conditions. The pump frequency can be adjusted, and as a consequence the superheating level, to achieve the optimal evaporating pressure, under the given

boundary conditions, that maximizes the power output. In fact, in many stationary ORC installations for waste heat recovery, the heat source availability is known in advance. Therefore, it is possible to predict optimal set points of the ORC unit depending on full-load capacity or part-load operations. Heat source and superheating can be correlated by means of a performance map and for a given heat source rate available, the optimum superheating level that maximized the Second Law efficiency can be determined (set point for the feed pump). Two example of operating maps are shown in Figure 6.6. Such maps have been obtained by fixing the heat sink temperature at 20 °C, the heat source inlet temperature at 125 °C and by varying the hot medium flow rate between 0.5 kg/s and 3 kg/s. Such boundary conditions are representative of the working conditions of the ORC unit tested in Chapter 5. The experimental data points for both SES36 and R245fa are overlaid. To be noted is that in the case of R245fa, see Figure 6.6(b), the operation is not optimized for the given hot source conditions. Significant increase of Second Law efficiency could be achieved by increasing the pressure ratio of the system which is also consistent with the fact that the single-screw expander requires higher pressure ratios.

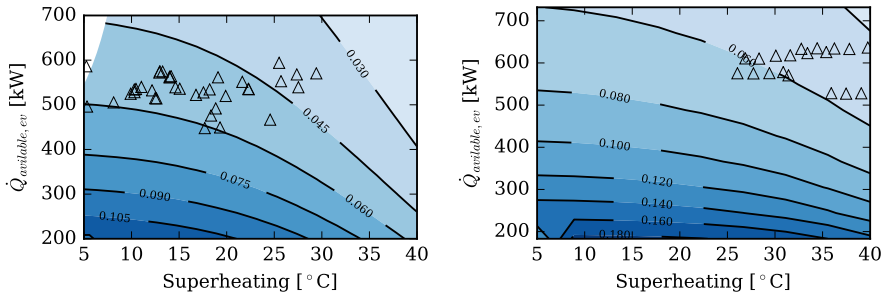

(a) (b)

Figure 6.6: Optimization of superheating level for different heat input availability: (a) SES36; (b) R245fa. The contours show the global efficiency of the ORC system. The heat source inlet temperature is kept constant at 125 °C. The experimental data obtained is overlaid.

6.4 Proposed Design

The experimental and numerical analyses led to a deep understanding of the single-screw machine that can be applied to both ORC applications but also to vapor compression systems where the majority of such machines are currently employed.

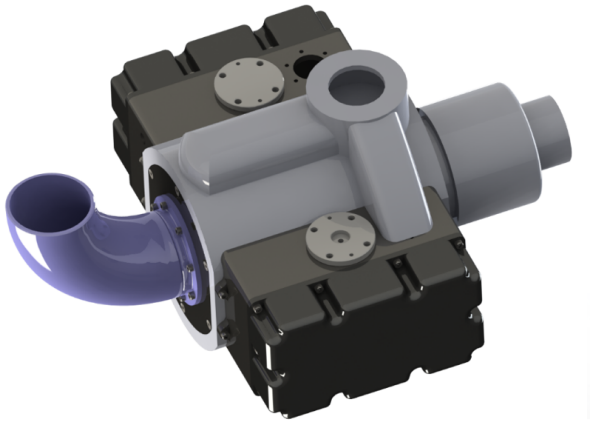

Figure 6.7: 3D-view of the new single-screw expander design. Design created in collaboration with Claudio Pavan, Ph.D., Solid Energy (cpavan@solidenergy.it).

By focusing on ORC applications, the design of a proper expander has at least four technological requirements:

- control of the tolerances which affect the leakages;
- accessibility and maintenance;
- part-load control;
- low cost of manufacturing.

As a result of the experience gained with the single-screw expander tested, a prototype-oriented design has been developed aiming to effectively solve a number of technical issues encountered with the ultimate goal of proposing the first single-screw expander designed for ORC applications.

The proposed design is shown in Figure 6.7 and its exploded view is shown in Figure 6.8. The majority of single-screw machines present a housing which is obtained by casting. The fine control over internal tolerances become complicated as milling tools have a difficult access especially in the cylindrical portion of the housing that hosts the main rotor. The starwheel are mounted on each side of the housing. Due to the narrow space available, the access to the starwheels for inspection can be difficult, especially in single-screw machines with lower power output, as shown in Figure 6.9. The vertical alignment of the starwheel with respect to the main rotor and the positioning of the main rotor are crucial to ensure the correct rotation of the meshing pair. A different approach is introduced with the new design. In fact, the housing has been divided into three parts: a cylindrical central part where the rotor is installed and two lateral parts that hold the starwheels. The side plates have been substituted by side shells which allow to expose the starhweels once removed. Each of the parts of the housing

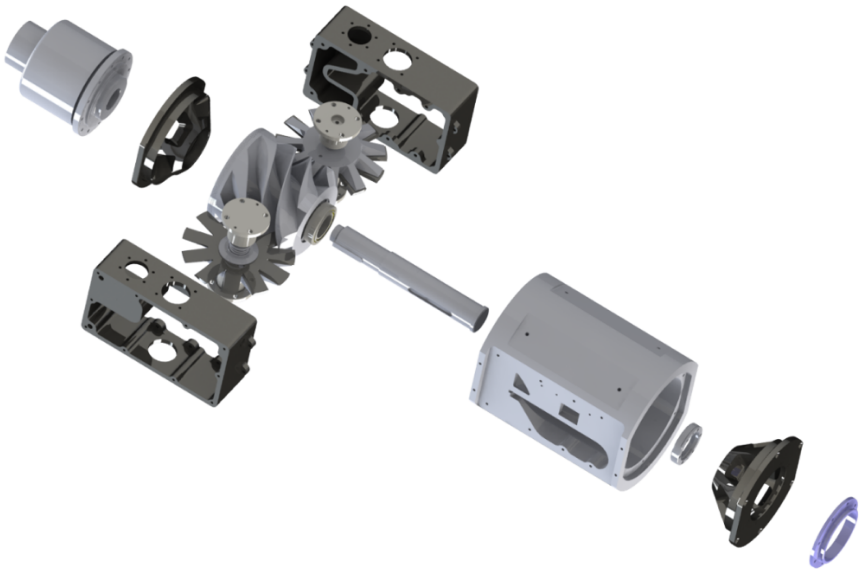

Figure 6.8: Exploded view of the design. Design created in collaboration with Claudio Pavan, Ph.D., Solid Energy (cpavan@solidenergy.it)

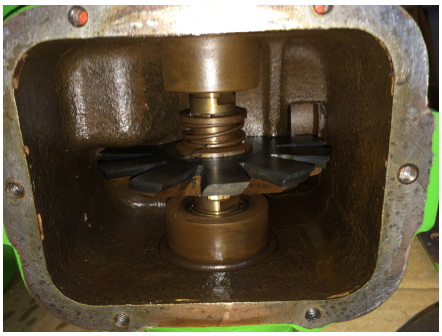

Figure 6.9: Side view of the starwheel assembly.

can be easily machined ensuring high accuracy on the tolerances. The sealing between each housing element is obtained by gaskets and the contact surfaces are polished accordingly. Since the expander is an open-drive machine, the shaft seal is important to limit refrigerant leaks. To avoid the use of shaft seals, a magnetic coupling assembly has been added. The central rotor is held into place with two conically shaped elements at each side of the central cylinder that host also the bearings. Such configuration allows to have an axial outlet port from the housing. The shaft configuration is considerably simplified compared to the original one.

In a single-screw expander, there is a common inlet and the flow is distributed

between the two sides of the rotor by means of internal channels. A CFD analysis has been carried out to visualize the flow stream. The result of the analysis is shown in Figure 6.10. To be noted is that there are areas of the internal ducts where the flow is separated which is not optimal for pressure drops. In the new housing, the inlet ducts have been shaped to minimize the flow losses, as show in Figure 6.7. Furthermore, a rotating valve is used to by-pass the flow to the discharge end if required during the start-up procedures.

The lubrication of the main shaft is achieved with a single port on each side of housing. A close-view of the lubrication inlet port is visible in Figure 6.11.

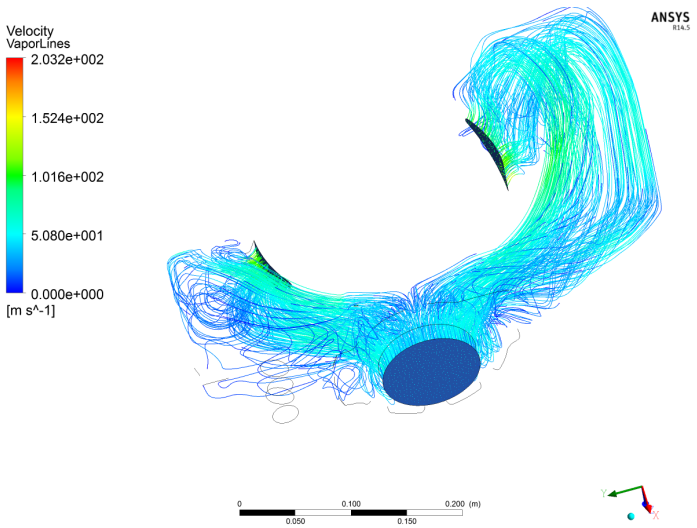

Figure 6.10: Flow visualization of the inlet cavities of the original single screw housing.

During the development of the new housing, part-load behavior has also been considered. By referring to Figure 6.12, the total length of the rotor and the diameter have a fixed ratio that is decided in the design phase. The length interested during the expansion process has been defined as effective length (sum of suction side L_{s} and discharge side L_{d}). Due to the fact that the single-screw expander is a volumetric machine, the theoretical pressure ratio can be calculated by knowing the internal volume ratio:

$$r_{\mathrm{p}} = r_{\mathrm{v,built-in}}^{n} \tag{6.8}$$

where n is the polytropic index that depends on the type of fluid and thermodynamic process. The closed expansion occurs from the moment of suction closure until the beginning of the discharge process. The main rotor rotation angle at which the closed expansion occurs corresponds to a certain length and axial

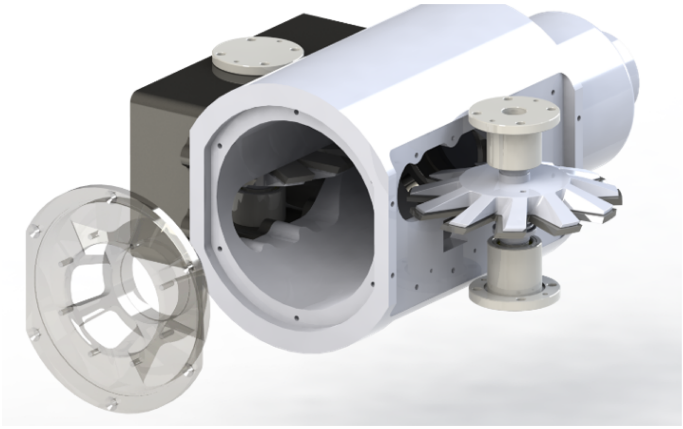

Figure 6.11: Close view to the new design with single port for lubrication purposes. Design created in collaboration with Claudio Pavan, Ph.D., Solid Energy (cpavan@solidenergy.it)

position of the rotor. Therefore, it is possible to calculate where the expansion process is at a certain type along the main rotor axis. In fact, from the geometry model the relationship between pressure $p(\theta)$ and chamber volume $V(\theta)$ with respect to the rotation angle is known. It has been shown that until the discharge angle an analytic form of the swept volume can be used. It follows that a general mathematical formulation of the control system can be derived:

Input : Geometry and ORC pressure ratio

function **Control** (geo,r_p):
 time constant→ τ
 if $r_{v,exp} < (r_{v,exp})_{nom}$ **then**
 $L'\left(\theta, (r_{v,exp})_{part-load}\right) \propto L'(\theta, V_{2,part-load})$
 $\widetilde{x} \propto L'$
 return $f(\widetilde{x}, \tau)$
else
 return $f(\widetilde{x} = 0, \tau)$
end

Output: Actuator law

algorithm 1: Single-screw expander part-load pseudo-algorithm.

If the pressure ratio of the ORC system is below the nominal one, the length of the expansion process can be controlled by creating a channel that communicated with the discharge side. The new expansion ratio is obtained by identifying the the

position of the rotor $L^{'}$ at which corresponds the groove volume $V_{2,\mathrm{part-load}}$. By determining a lumped dynamic time constant of system τ, the general mechanical actuator law $f(\widetilde{x}, \tau)$ can be obtained, where $\widetilde{x}$is the control motion coordinate. The details of the mechanical system that allows the part-load control are not included in the present work. However, the location of the secondary opening port can be seen on the cylindrical part of the housing in Figure 6.8.

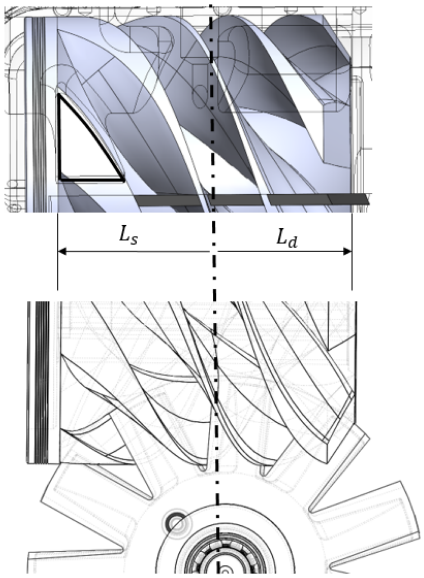

Figure 6.12: Schematic of the proposed part-load principle in a single-screw expander.

References

[1] S. Lecompte, H. Huisseune, M. van den Broek, B. Vanslambrouck, and M. De Paepe. *Review of organic Rankine (ORC) architectures for waste heat recovery*. Renewable and Sustainable Energy Reviews, 47:448–461, 2015.

[2] B. J. Woodland, A. Krishna, E. A. Groll, J. E. Braun, W. T. Horton, and S. V. Garimella. *Thermodynamic comparison of organic Rankine cycles employing liquid-flooded expansion or a solution circuit*. Applied Thermal Engineering, 61:859–65, 2013.

[3] M. Imran, M. Usman, Park B-S, and D-H Lee. *Volumetric expander for low grade heat and waste heat recovery applications*. Renewable and Sustainable Energy Reviews, 57:1090–1109, 2016.

[4] B. J. Woodland, E. A. Groll, J. E. Braun, and W. T. Horton. *Performance Benefits for Organic Rankine Cycles with Flooded Expansion and Internl Regeneration*. In International Refrigeration and Air Conditioning Conference at Purdue, number 2462, 2010.

[5] E. Georges. *Investigation of a Flooded Expansion Organic Rankine Cycle System*. Master's thesis, University of Liege, 2012.

[6] J. J. Hugenroth. *Liquid Flooded Ericsson Cycle Cooler*. PhD thesis, Purdue University, 2006.

[7] I. H. Bell, E. A. Groll, J. E. Braun, G. B. King, and W. T. Horton. *Optimization of a scroll compressor for liquid flooding*. Int. J. of Refrigeration, 35:1901–1913, 2012.

[8] E. W. Lemmon, I. H. Bell, M. L. Huber, and M. O. McLinden. *NIST Standard Reference Database 23: Reference Fluid Thermodynamic and Transport Properties-REFPROP, Version 9.1.1, National Institute of Standards and Technology*, 2016.

[9] I. H. Bell. *ACHP - http://achp.sourceforge.net*, 2011.

[10] V. P. Zhelezny, V. V. Sechenyh, Y. V. Semenyuk, A. J. Grebenkov, and O. V¿ Beliayeva. *An experimental investigation and modelling of the viscosity refrigerant/oil solutions*. International Journal of Refrigeration, 32:1389–1395, 2009.

7 Conclusions

7.1 Summary

Organic Rankine cycles have assumed an important role as a waste heat recovery technology which is applicable to a wide range of heat source profiles. Although the ORC technology can be considered mature, there are still fundamental aspects that require further research in order to obtain better thermodynamic performance and financial profit. The major aspects, but not limited to, are the cycle architectures, the components and the control strategies. The conversion of thermal energy carried by the working fluid into mechanical energy first and then to valuable electrical power occurs by means of an expander. It has been shown how positive displacement expanders are suitable devices in the medium to low power range due to the trade-off between performance and cost. The majority of positive displacement machines are available from the refrigeration industry. However, commercially available expanders are still limited. Among the positive displacement machines, screw-type of expanders are particularly attractive in the medium power range due to high performance and the adoption of such machine in the medium to low power range (10-200 kW) is of particular interest. Single-screw machines present a number of design characteristics that are potentially advantageous in ORC applications such as balanced loading on the main rotor (major difference with twin-screw type), minimized cascading effects between working chambers, low noise and vibrations, high volume ratios and part-load internal control capabilities. Nonetheless the research on such

machine as employed expander in ORC applications is still at early stages and limited results are available on its characterization with different working fluids and working conditions. In order contribute to the field, both numerical and experimental aspects have been investigated in the present work. The first step undertaken was the enhancement of a generalized simulation framework for the detailed modeling of positive displacement expanders as well as compressors. In the open-literature, this is a major contribution to both academia and industry. The mechanistic model of a novel Z-compressor served as an example of design optimization study. Successively, the geometry of the single-screw expander was integrated into the tool along with a detailed mechanistic model which included leakage effects, heat transfer interactions, presence of lubricant oil and mechanical losses. Furthermore, numerical methods were developed to design the meshing pair. In order characterize experimentally the single-screw expander, a down-scaled industrial ORC was used as a test-rig and two working fluids were investigated. A total of 102 steady-state points were obtained and further used to carry on the analyses. The single-screw prototype achieved a maximum overall isentropic efficiency around 62% with SES36 as working fluid. By analyzing the experimental data, it emerged that the matching between the expander and ORC performance was not optimal in the case of R245fa. Performance maps were obtained to define the relationship between heat rate available, optimum superheating and maximum Second Law efficiency for a finite heat source capacity, which it has been shown corresponding to the maximum net power output. From the numerical analysis of the single-screw expander, a reduction in leakage flows and friction losses up to 50% could improve the isentropic efficiency up to from 0.6 (experimental value) to 0.72. A means of achieving such reduction in internal losses is the control of the lubricant oil flow rate. The numerical and experimental results obtained in this work showed the potential of such machine as a expander in ORC applications. As the research is progressing towards novel cycle architectures such as partial-evaporating ORCs, single-screw expanders could be employed as a promising technology. The knowledge gained during this research resulted a new design with internal control mechanism to modulate the expander under part-load conditions.

7.2 Achieved performance and critical sources of losses

An overview of the best performance achieved by the single-screw expander tested is proposed in Table 7.1.

The single-screw expander has been tested extensively with two working fluids. The meshing profile on the starwheel teeth worn out over time, as shown in Figure

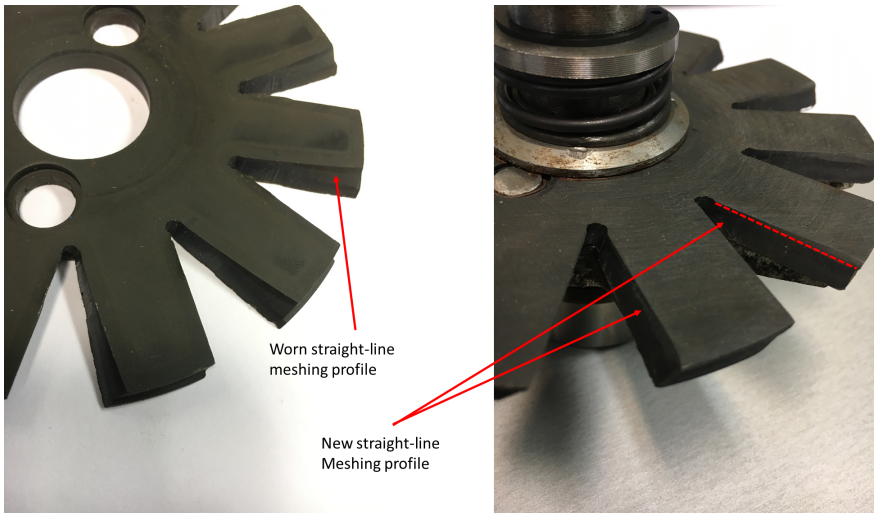

Figure 7.1: Comparison between worn starwheel profile and new straight-line meshing profile.

7.1 during an inspection after the completion of the tests. The groove lands on the rotor were also slightly damaged probably due to contact with the housing because of thermal expansion or metal chips and lack of proper lubrication. The straight-line profile is marked in red for clarity and it is essential to guarantee sealing between sides of the tooth and mating groove flanks. The wear of the meshing pair caused an increase in leakage losses. The lubrication system was not effective enough to seal the gaps and reduce the friction losses. Structural limits of the housing prevented reaching higher pressure ratios. Therefore two major aspects have been identified as potential design improvements: (i) control over the tolerances and lubrication; (ii) improve the structure of the housing. Both aspects have been solved with newer housing design as shown in Section 6.4.

Working fluid	y_{oil} (-)	r_{p} (-)	N_{exp} (-)	ϕ_{FF} (-)	$\eta_{\mathrm{is,sh,exp}}$ (-)	$\eta_{\mathrm{mech,exp}}$ (-)	$\eta_{\mathrm{oa,exp}}$ (-)
R245fa	<0.05	6.71	3000	1.07	0.692 (calc)	0.720 (calc)	0.522 (meas)
SES36	<0.05	8.69	3000	0.923	0.726 (calc)	0.763 (calc)	0.606 (meas)

Table 7.1: Summary of the best single-screw expander performance achieved with three working fluids.

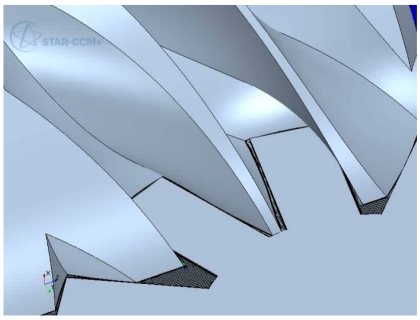

(a)

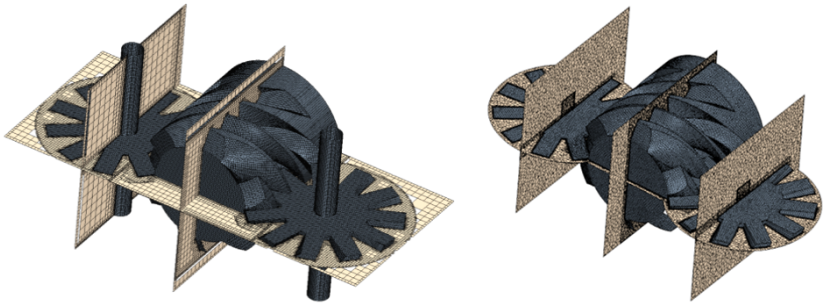

(b)

Figure 7.2: (a) Close-up view of meshing pair with a numerical mesh; (b) examples of overset meshes.

7.3 Research Perspectives

The numerical methods developed in this work concerning the kinematics and geometry of the single-screw machines as well as the mechanistic modeling can be further used to tackle Computational Fluid Dynamics (CFD) simulations in such machines which is an open topic in literature till nowadays. The complexity of such problem comes from the configuration of meshing pair that has perpendicular rotation axes, as shown in Figure 7.2(a), unlike twin-screw machines where the rotors have parallel rotation axes. The knowledge of the kinematics of single-screw meshing pair has been used to develop preliminary grid generation methods by making use of commercial software as well as by developing as-hock Python codes couple of OPENFoam, as shown in Figure 7.2. The ability of simulating complex rotor configurations, such as the single-screw, is of particular interest both on academic point of view as well as industry. An example of pressure trace obtained from CFD simulation is shown in Figure 7.3. Another benefit of solving the CFD problem is related to the extension of the mechanistic model developed

in this thesis. In particular, the CFD results can be coupled with the chamber model to investigate the effect of suction and discharge ports and pulsating flow. Additionally, the CFD results can be used to calibrate the mechanistic model especially when lubricant oil is present in the gaps.

The comprehensive mechanistic model with thermal network requires an in-depth validation. A dedicated ORC test-bench has been designed and built with an independent lubrication oil loop which allows to control the flooding ratio of the expander and it is described in details in Appendix E. The single-screw expander investigated in this thesis has been equipped with internal pressure and temperature sensors and also thermocouples on the external housing, as it is shown in Figure 7.4. Such setup can be used to investigate internal performance of the machine as well as novel ORC cycle configurations such as partial-evaporating ORC which opens research opportunities on the fundamentals of two-phase expansion. As part of the development of mechanistic model, gas pulsations should be included in the inlet ducting to understand the influence of the non-symmetric configuration and validations could be carried out by having dynamic pressure transducers installed.

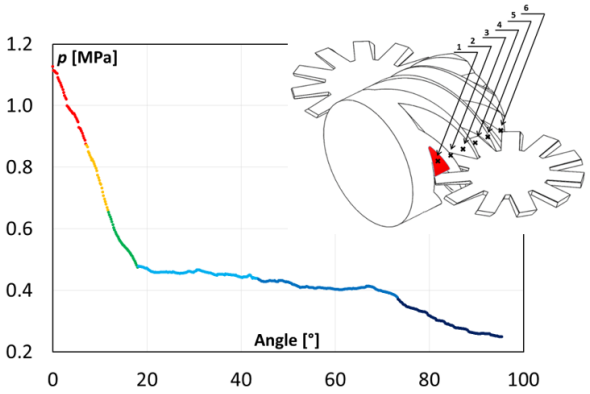

Figure 7.3: Example of pressure trace obtained from CFD Simulation (from Ziviani et al. "Real gas model and moving mesh in single-screw compressors and expanders", 3^{rd} Short Course and Forum Computational Fluid Dynamics in Rotary Positive Displacement Machines, 9^{th} to 10^{th} September 2017, City University of London).

Figure 7.4: View of the modified single-screw expander with internal and external sensors.

A

Publications

Related publications as first author in peer-reviewed international journals

Ziviani D., Zhang X., Bell I.H., De Paepe M., van den Broek M., Groll E.A., Braun J.E., Horton W.T. *An open-source simulation framework for positive displacement compressors and expanders: Applications*, Internationa Journal of Refrigeration (2017). To be submitted.

Ziviani D., Groll E.A., Braun J.E., De Paepe M., van den Broek M., *Analysis of an organic Rankine cycle with liquid-flooded expansion and internal regeneration (ORCLFE)*, Energy (2017). Under review.

Ziviani D., Gusev S., Lecompte S., Groll E. A., Braun J.E., Horton W.T., van den Broek M., De Paepe M., *Optimizing the performance of a small-scale organic Rankine cycle that utilizes a single-screw expander*, Applied Energy, 189(2017), 416-432.

Ziviani D., Gusev S., Lecompte S., Groll E. A., Braun J.E., Horton W.T., van

den Broek M., De Paepe M., *Characterizing the performance of a single-screw expander in a small-scale organic Rankine cycle for waste heat recovery*, Applied Energy, 181(2016), 155-170. Citing articles: 6

Ziviani D., Woodland B.J., Georges E., Groll E.A., Braun J.E., Horton W.T., van den Broek M., De Paepe M., *Development and validation of a charge sensitive organic Rankine cycle (ORC) simulation tool*, Energies 9(2016),389. Citing articles: 3

Ziviani D., van den Broek M., De Paepe M., *Geometry-based modeling of single screw expander for organic Rankine cycle systems in low-grade heat recovery*, Energy Procedia, 61(2014), 100-103. Citing articles: 3

Ziviani D., Suman A., Lecompte S., De Paepe M., van den Broek M., Spina P.R., Pinelli M., Venturini M., Beyene A., *Comparison of a single-screw and a scroll expander under part-load conditions for low grade heat recovery systems*, Energy Procedia, 61(2014), 117-120. Citing articles: 4

Other publications as first author in peer-reviewed international journals

Ziviani D., Beyene A., Venturini M, *Advances and challenges in ORC systems modeling for low grade thermal energy recovery*, Applied Energy, 121 (2014), 79-95. Citing articles: 42

Publications as co-author in peer-reviewed international journals

Bell, I.H., Ziviani D., Lemort V., Bradshaw C.R., Mathison M., Groll E.A., Braun J.E., Horton W.T., *A general quasi-steady modeling approach for positive displacement compressors and expanders: PDSim*, International Journal of Refrigeration (2017). To be submitted.

Suman A., Ziviani D., Gabrielloni J., Pinelli M., De Paepe M., van den Broek M., *Different numerical approaches for the analysis of a single screw expander*, Energy Procedia 101(2016), 750-757.

Lecompte S., Ameel B., Ziviani D., van den Broek M., De Paepe M., *Exergy analysis of zeotropic mixtures as working fluids in Organic Rankine Cycles*, Energy Conv. Manag., 85(2014), 727-739. Citing articles: 7

Publication as co-author in books

CRC Handbook of Thermal Engineering, Second Edition. Chapter 4.11 Compressors Bach C.K., Bell I.H., Craig B.R., Groll E.A., Krishna A., Kurtulus O., Mathison M., Shaffer B., Yang B., Zhang X., Ziviani D., 2017. (In Press)

Related publications as first-author in proceedings of international conferences

Ziviani D., Zhang, X., Groll E.A., PDSim: A Generalized Modeling Platform to Predict the Performance of Positive Displacement Compressors, Keynote Speech at 8th International Conference on Compressors and Refrigeration, Xian Jiaotong University, July 20-22, 2017.

Ziviani D., Kim D., Subramanian S.N., Braun J.E., Groll E.A., Feasibility Study of IEC Bottoming ORC with Water/EG Mixture as Working Fluid, IV International Seminar on ORC Power Systems, ORC2017, 13-15 September 2017, Milano, Italy. Energy Procedia.

Ziviani D., Gusev S., Schuessler S., Achaichia A., Braun J.E., Groll E.A., De Paepe M., van den Broek M., Employing a Single-Screw Expander in an Organic Rankine Cycle with Liquid Flooded Expansion and Internal Regeneration, IV International Seminar on ORC Power Systems, ORC2017, 13-15 September 2017, Milano, Italy. Energy Procedia.

Ziviani D., Groll E. A., Modeling and analysis of an open-drive Z-compressor, International Conference on Compressors and their Systems 2017, 11-13 September 2017, London UK.

Ziviani D., Groll E.A., Braun J.E., Horton W.T., De Paepe M., van den Broek M., Non-symmetric approach to single-screw expander and compressor modeling, International Conference on Compressors and their Systems 2017,

11-13 September 2017, London UK.

Ziviani D., Kim D., Subramnian N., Braun J.E., Groll E.A., Affordable Rankine Cycle (ARC) for Heavy-Duty Truck Waste Heat Recovery, Proceeding of ECOS 2017, July 2-6, 2017, San Diego, CA, USA.

Ziviani D., Suman A., Gabrielloni J., Pinelli M., De Paepe M., van den Broek M., CFD Approaches Applied to a Single-Screw Expander, 23rd International Compressor Engineering Conference at Purdue, July 11-14, 2016.

Ziviani D., Bell I.H., De Paepe M., van den Broek M., Mechanistic model of an oil-flooded single-screw expander, 23rd International Compressor Engineering Conference at Purdue, July 11-14, 2016.

Ziviani D., Dickes R., Quoilin S., Lemort V., De Paepe M., van den Broek M., Organic Rankine cycle modeling and the ORCmKit library: analysis of R1234ze(Z) as drop-in replacement of R245fa for low-grade waste heat recovery, Proceeding of ECOS 2016, June 19-23, 2016, Portoroz, Slovenia.

Ziviani D., Woodland, B.J., Georges E., Groll E.A., Braun J.E., Horton W.T., De Paepe M., van den Broek M., ORCSIM: a generalized organic Rankine cycle simulation tool, 3rd International Seminar on ORC Power Systems, October 12-14, 2015, Brussels, Belgium. Paper 30.

Ziviani D., Bell I.H., De Paepe M., van den Broek M., Update on single-screw expander geometry model integrated into an open-source simulation tool, IOP Conference Series: Materials Science and Engineering, vol. 90, 2015. Paper 012064.

Ziviani D., Desideri A., Lemort V., De Paepe M., van den Broek M., Low-order models of a single-screw expander for organic Rankine cycle applications, IOP Conference Series vol. 90, 2015. Paper 012061.

Ziviani D., Woodland B.J., Georges E., Groll E.A., Braun J.E., De Paepe M., van den Broek M., Development of a general organic Rankine cycle simulation tool: ORCSIM, Proceedings of ECOS 2015: the 28th int. Conf. on Efficiency, Cost, Optimization, Simulation and Environmental Impact of Energy Systems, Pau (France), June 30th July 3rd, 2015. Paper 50942.

Ziviani D., Bell I.H., van den Broek M., De Paepe M., Comprehensive Model of a Single Screw Expander for ORC-Systems, 22nd International Compressor

Engineering Conference at Purdue, Herrick Laboratories Purdue University, July 2014. Paper 1548. Downloads: 1959

Ziviani D., Lecompte S., van den Broek M., De Paepe M., Geometry-based Modeling of Single-Screw Expander for Organic Rankine Cycle System for low-grade Heat Recovery, ICAE 2014 Taipei, Taiwan.

Ziviani D., Suman A., Lecompte S., De Paepe M., van den Broek M., Spina P.R., Pinelli M., Venturini M., Beyene A., Comparison of a Single-Screw and Scroll-Expander under Part-load Conditions for Low-grade Heat Recovery ORC Systems, ICAE 2014 Taipei, Taiwan.

Related publications as co-author in proceedings of international conferences

Zhang, X., Ziviani D., Groll E.A., A Numerical Study on Dynamic Characteristic of Linear Compressor for Electronics Cooling, 8th International Conference on Compressors and Refrigeration, Xian Jiaotong University, July 20-22, 2017

Lavernia A., Ziviani D., Shaffer B., Bansal K., Groll E.A., optimization of an organic Rankine cycle as bottoming cycle of a 1 kWe GENSET for residential applications, IV International Seminar on ORC Power Systems, ORC2017, 13-15 September 2017, Milano, Italy. Energy Procedia.

Kim D., Ziviani D., Subramanian S.N., Braun J.E., Groll E.A., A Moving Boundary Modeling Approach for Heat Exchangers with Binary Mixtures, IV International Seminar on ORC Power Systems, ORC2017, 13-15 September 2017, Milano, Italy. Energy Procedia.

Casari N., Suman A., Ziviani D., van den Broek M., De Paepe M., Pinelli M., Computational Models for the Analysis of positive displacement machines: Real Gas and Dynamic Mech, IV International Seminar on ORC Power Systems, ORC2017, 13-15 September 2017, Milano, Italy. Energy Procedia.

Yang B., Ziviani D., Groll E.A., Comprehensive Model of a Hermetic Reciprocating Compressor, International Conference on Compressors and their Systems 2017, 11-13 September 2017, London UK.

Casari N., Suman A., Ziviani D., Morini M., Pinelli M., Virtual model for ORC Whole ORC Modeling: WOM, Proceeding of ECOS 2017, July 2-6, 2017, San Diego, CA, USA.

Gusev G., Ziviani D., van den Broek M., Solar Driven Water Circulation and Aeration System for Aquaculture, Proceeding of ECOS 2017, July 2-6, 2017, San Diego, CA, USA.

Gusev S., Ziviani D., De Viaene J., Derammelaere S., van den Broek M., Modelling and Preliminary Design of a Variable-BVR Rotary Valve Expander with an Integrated Linear Generator, 23rd International Compressor Engineering Conference at Purdue, July 11-14, 2016.

Liu, F., Xie J., Ziviani D., Feng Q., van den Broek M., De Paepe M., Analysis on Lubricant Film Force for Two Types of Meshing Pair Profile in Single Screw Compressor, 23rd International Compressor Engineering Conference at Purdue, July 11-14, 2016.

Dickes R., Ziviani D., De Paepe M., van den Broek M., Quoilin S., Lemort V., ORCmKit: an open-source library for organic Rankine cycle modelling and analysis, Proceeding of ECOS 2016, June 19-23, 2016, Portoroz, Slovenia.

Gusev, S., Hernandes A., Ziviani D., van den Broek M., Modeling of a Variable-BVR Free Piston Expander/Compressor, Latin American Conference on Automatic Control (CLCA), October 13-15, 2016 Medellin, Colombia.

Suman A., Ziviani D., Gabrielloni J., Pinelli M., De Paepe M., van den Broek M., Different Numerical Approaches for the Analysis of a Single-Screw Expander, 71st Conference of the Italian Thermal Machines Engineering Association, ATI2016, 14-16 September 2016, Turin, Italy.

Gusev S., Ziviani D., van den Broek M., Experimental comparison of a single-screw expander under different operating conditions and working fluids, 3rd International Seminar on ORC Power Systems, October 12-14, 2015, Brussels, Belgium. Paper 163.

Gusev S., Ziviani D., Bell I.H., De Paepe M., van den Broek M., Experimental Comparison of Working Fluids for Organic Rankine Cycle with Single-Screw Expander, 15th International Compressor Engineering Conference at Purdue, Herrick Laboratories Purdue University, July 2014. Paper 2356. Downloads: 671

Awards

3^{rd} Place Student Paper at 23^{rd} International Compressor Engineering Conference Student Paper Competition, 2016 Purdue Conferences for the paper: Mechanistic Model of an Oil-Flooded Single-Screw Expander

2013 Research scholarship of the ASME IGTI ORC Power Systems committee. Awarded with the amount of 10,000 €for a research stay at Purdue University from May 1^{st} to October 30^{th} 2014 in order to perform the research project titled Organic Rankine Cycle with Liquid Flooded Expansion (ORCLFE) using a Screw Expander and Internal Heat Regeneration for Waste Heat Recovery

B

3D Design of Single-Screw Meshing Pair

B.1 Example: 122 mm main rotor

For the sake of completeness, the rotor will be generated by considering the opposite starwheel with respect to Figure 3.5. The reference system used in the following design procedure as well as the engaging pair rotor and starwheel are shown in Figure B.1. The meshing equation can be adapted from Equation B.1, by modifying the signs in accordance with the right-hand unit vectors rules (see Equation 3.14).

$$\begin{cases} x_1 = -\left[-x_2 \sin\theta_{sw} \sin\theta_{sr} - y_2 \cos\theta_{sw} \sin\theta_{sr} + z_2 \cos\theta_{sr} + d_{sr,sw} \sin\theta_{sr}\right] \\ y_1 = -\left[-x_2 \sin\theta_{sw} \cos\theta_{sr} - y_2 \cos\theta_{sw} \cos\theta_{sr} - z_2 \sin\theta_{sr} + d_{sr,sw} \cos\theta_{sr}\right] \\ z_1 = x_2 \cos\theta_{sw} - y_2 \sin\theta_{sw} \end{cases} \tag{B.1}$$

where $\theta_{sr} = 11/6\theta_{sw}$ and $\theta_{sw} = [0, \pi]$. The geometric details can be found in Table B.1.

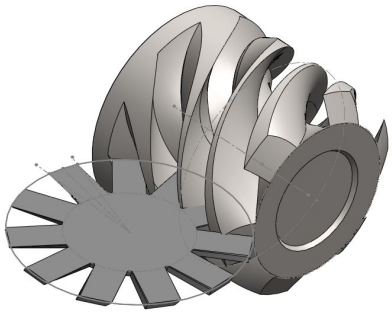

Figure B.1: Engaging pair.

Engaging ratio	[-]	11/6
D_{sr}	[mm]	122
D_{sw}	[mm]	132
$d_{sw,sr}$	[mm]	96
L_{rotor}	[m]	120.25
L_s	[m]	55.25
L_d	[m]	42.25

Table B.1: Geometric parameters of 11 kWe single-screw expander .

B.2 Design procedure in SOLIDWORKS

The different steps that are required in order to obtain the main screw rotor from a given tooth profile are described in this section.

- *Preliminary drawings.* Figure B.2
- *Tip and hub tooth profiles*. Figure B.3, Figure B.4(a), Figure B.4(b)
- Projection of the tooth profile points. Each point of the tooth profile must be projected by using Equation B.1. The X and Z coordinates can be obtained from CAD coordinates directly. The Y coordinate corresponds to the range $[-w/2, w/2]$ and the zero is set on the centerline of the tooth width, i.e., according to the absolute reference system $[X, Y, Z] = [0, -d_{sr,sw}, 0]$.
- *Generate surfaces*. Generate the surfaces corresponding to each side. The surfaces are ruled by the straight lines of the tooth flanks. Once all the surfaces have been generated for a particular cut to be performed, they can be knitted together and then a solid can be generated by filling in the closed surface, as shown in Figure B.6.

- *Intersection with D_{sw}.* The solid generated in the previous step needs to be trimmed to the right dimensions of the starwheel diameter to ensure the right penetration of the tooth in to the rotor. Undercutting can be controlled as a consequence as well as the bottom of the groove. A revolved surface is generated from a sketch having radius $D_{\mathrm{sw}}/2$, Figure B.7(a). An intersection operation is then performed to obtain the right solid part, as shown in Figure B.7(b).

- *Circular pattern and first cut.* The solid obtained in the previous step is multiplied by $z_{\mathrm{sr}} = 6$ around the main rotor axis. Through a boolean operation, the six bodies are subtracted from the main rotor. The first cut is accomplished.

- *Second and third cuts.* The previous steps must be repeated for the upper and bottom parts of the tooth.

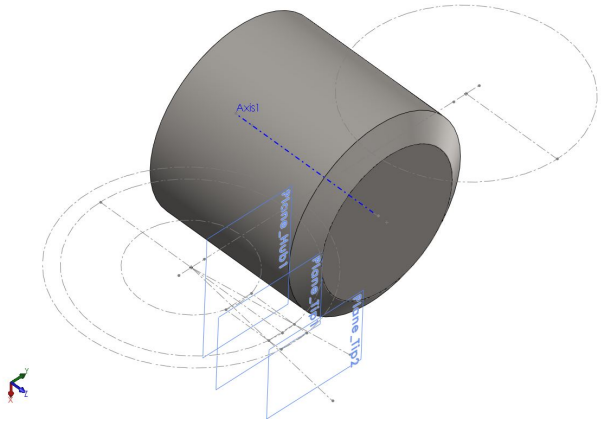

Figure B.2: Preliminary sketches and rotor.

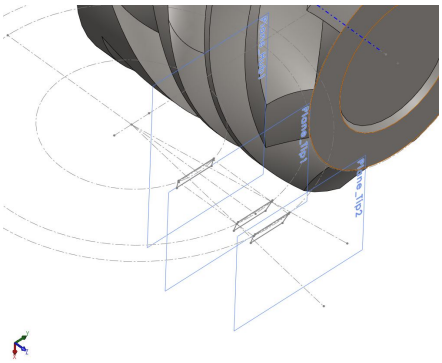

Figure B.3: Tip and hub tooth profiles sketches.

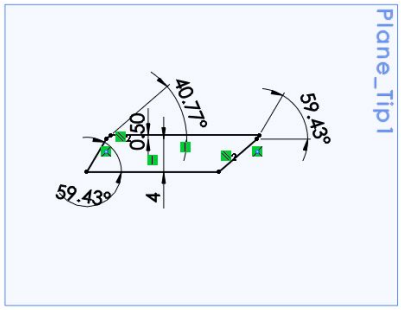

(a)

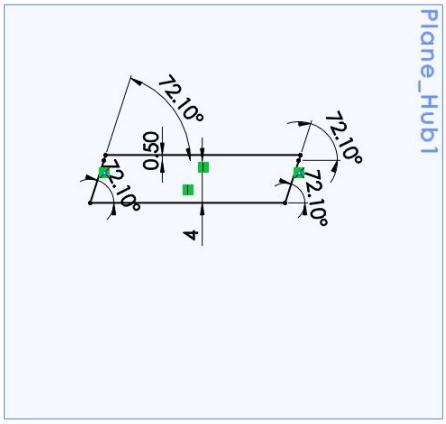

(b)

Figure B.4: (a) *Sketch of tooth tip profile;* (b) *Sketch of tooth hub profile.*

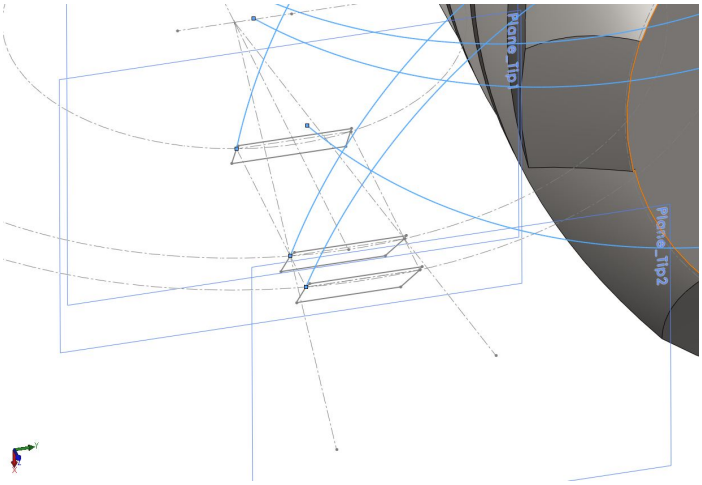

Figure B.5: Examples of projecting the tooth profile points over the meshing line by means of parametric curves.

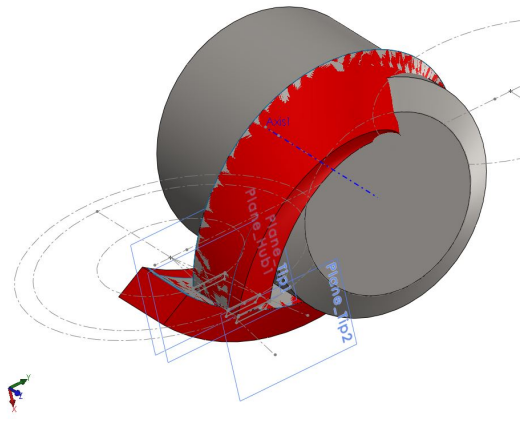

Figure B.6: Examples of projecting the tooth profile points over the meshing line by means of parametric curves.

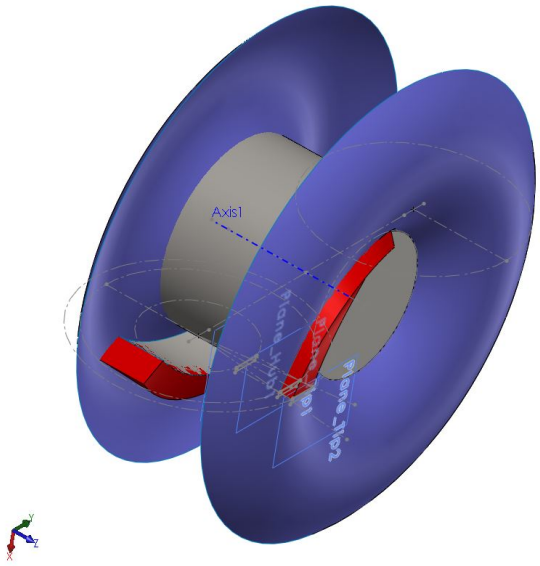

(a)

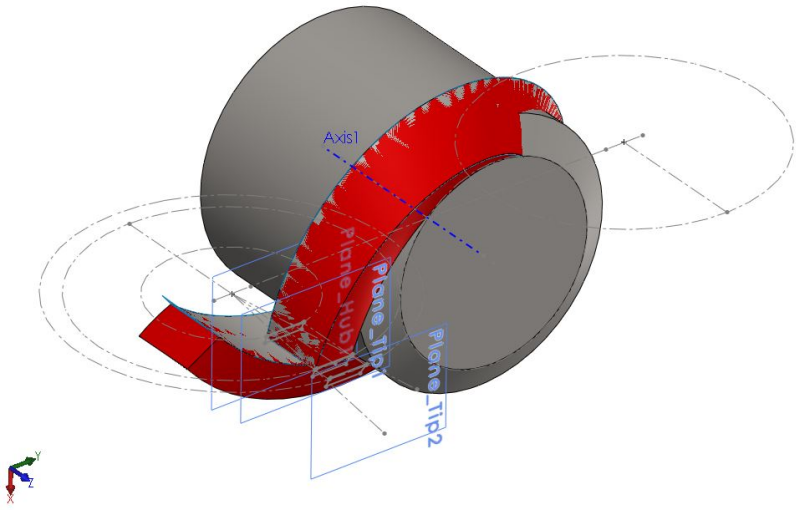

(b)

Figure B.7: (a) *Sketch of tooth tip profile;* (b) *Sketch of tooth hub profile.*

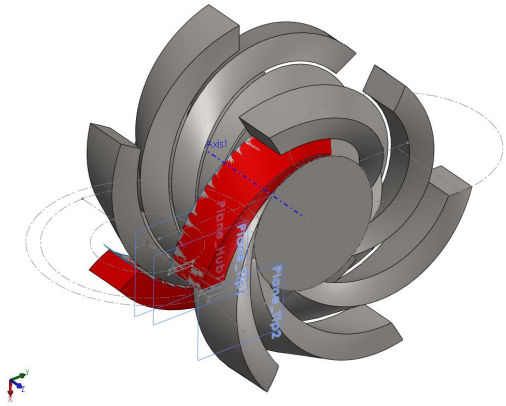

Figure B.8: Circular pattern.

C

Correlations for generator and inverter efficiency

The electrical efficiency of the inverter, $\eta_{el,inv}$, is expressed as a function of the expander rotational speed and power generated:

$$\eta_{el,inv} = a_0 + a_1 \cdot ln_N + a_2 \cdot ln_N^2 + a_3 \cdot ln_N^3 + a_4 \cdot ln_W + a_5 \cdot ln_W^2 + a_6 \cdot ln_W^3 \quad \text{(C.1)}$$

where:

$$ln_N = ln\left(\frac{N_{exp}}{N_{exp,nom}}\right) \quad \text{(C.2)}$$

$$ln_W = ln\left(\frac{\dot{W}_{el,exp}}{\dot{W}_{el,nom}}\right) \quad \text{(C.3)}$$

with $N_{exp,nom}$ = 2930 rpm and $\dot{W}_{el,nom}$ = 11 kW. The coefficients $a_0, ..., a_6$ are listed in Table C.1.

The electro-mechanical efficiency of the generator, $\eta_{el-mech,gen}$, is given as a function of the expander rotational speed and the torque at the shaft:

$$\begin{aligned}\eta_{el-mech,gen} = {} & b_0 + b_1 \cdot ln_N + b_2 \cdot ln_N^2 + b_3 \cdot ln_N^3 + b_4 \cdot ln_\tau + b_5 \cdot ln_\tau^2 + b_6 \cdot ln_\tau^3 \\ & + b_7 \cdot ln_N \cdot ln_\tau + b_8 \cdot ln_N \cdot ln_\tau^2 + b_9 \cdot ln_\tau \cdot ln_N^2 + b_{10} \cdot ln_\tau^2 \cdot ln_N^2\end{aligned} \quad \text{(C.4)}$$

a_0	$9.55726922 \cdot 10^{-1}$
a_1	$2.60983262 \cdot 10^{-2}$
a_2	$2.42349302 \cdot 10^{-2}$
a_3	$1.21191602 \cdot 10^{-2}$
a_4	$4.94828374 \cdot 10^{-2}$
a_5	$3.34143316 \cdot 10^{-2}$
a_6	$2.27446360 \cdot 10^{-2}$

Table C.1: Coefficients of the inverter electrical efficiency.

b_0	$8.93747915 \cdot 10^{-1}$
b_1	$3.23048796 \cdot 10^{-2}$
b_2	$-1.91761519 \cdot 10^{-2}$
b_3	$1.52204756 \cdot 10^{-2}$
b_4	$7.32867448 \cdot 10^{-3}$
b_5	$-3.17061820 \cdot 10^{-2}$
b_6	$2.16415080 \cdot 10^{-2}$
b_7	$1.63125253 \cdot 10^{-2}$
b_8	$4.37556935 \cdot 10^{-3}$
b_9	$-4.11952262 \cdot 10^{-2}$
b_{10}	$-1.62681324 \cdot 10^{-2}$

Table C.2: Coefficients of the generator electro-mechanical efficiency.

where:

$$ln_\tau = ln\left(\frac{\tau}{\tau_{nom}}\right) \tag{C.5}$$

and

$$\tau_{nom} = \frac{\dot{W}_{el,nom}}{\omega_{nom}} = \frac{\dot{W}_{el,nom}}{\frac{2\pi N_{exp,nom}}{60}} \tag{C.6}$$

The coefficients $b_0, ..., b_{10}$ are listed in Table C.2.

D

Single-Screw Expander Semi-Empirical Models

D.1 Experimental steady-state data points for SES36 and R245fa

The steady-state experimental data points collected with the downsized 11 kWe industrial organic Rankine cycle test rig is provided in Table D.1 and Table D.2. The data is also available as an electronic annex of Ziviani et al. [1].

Table D.1: Steady-state points obtained for SES36.

Run #	$T_{su,ev}$ (°C)	$p_{su,exp}$ (kPa)	$T_{su,exp}$ (°C)	$p_{ex,exp}$ (kPa)	$T_{ex,exp}$ (°C)	$\dot{m}_r$ (kg/s)	T_{cd} (°C)	N_{exp} (rpm)	$\dot{Q}_{T66,in}$ (kW)	$\dot{W}_{el,grid}$ (kW)	$\dot{W}_{el,pp}$ (kW)	$\eta_{is,oa,exp}$ (-)	η_{ORC} (-)
1	76.34	520.2	109.0	108.1	86.0	0.151	37.3	2000	28.5	1.469	0.970	0.135	0.0175
2	79.61	533.7	109.1	126.0	89.09	0.154	41.9	2000	27.9	1.243	0.963	0.647	0.0100
3	79.58	786.3	117.8	116.3	89.5	0.243	39.2	2000	42.9	3.553	1.570	0.647	0.0462
4	79.17	816.8	112.8	168.0	87.31	0.266	50.8	2000	45.3	2.690	1.566	0.647	0.0248
5	77.65	508.5	109.9	101.6	87.68	0.150	35.4	2000	27.9	1.562	0.889	0.647	0.0241
6	78.45	517.7	110.1	107.2	88.55	0.150	36.9	2000	27.8	1.507	0.910	0.647	0.0214
7	79.72	526.1	110.1	120.9	89.88	0.153	40.5	2000	28.5	1.265	0.886	0.647	0.0133
8	86.29	842.8	125.0	124.6	97.25	0.258	40.9	2000	46.3	3.806	0.800	0.647	0.0648
9	88.12	674.1	124.5	112.4	99.45	0.195	38.0	2000	36.1	2.635	0.600	0.647	0.0563
10	86.58	795.1	124.8	119.9	97.83	0.240	39.7	2000	43.3	3.531	0.700	0.647	0.0653
11	83.1	931.6	121.9	136.1	93.67	0.300	43.5	2000	51.1	4.389	1.000	0.647	0.0662
12	80.87	837.9	117.9	129.9	90.81	0.268	42.0	2000	45.3	3.750	0.800	0.647	0.0650
13	84.22	672.1	119.5	112.4	94.9	0.198	37.9	2000	35.3	2.638	0.600	0.647	0.0577
14	84.54	589.5	119.4	164.0	95.48	0.171	35.6	2000	31.1	2.151	0.500	0.647	0.0529
15	91.57	633.8	119.5	149.8	101.3	0.186	50.4	2000	31.7	1.259	0.500	0.647	0.0239
16	89.17	556.7	119.3	104.6	102.0	0.160	47.5	2000	28.1	0.903	0.400	0.647	0.0178
17	83.92	820.8	124.9	101.1	95.7	0.252	33.7	2000	45.1	4.172	0.800	0.647	0.0748
18	85.71	614.7	124.4	90.7	98.2	0.177	30.9	2000	34.3	2.658	0.500	0.647	0.0629
19	83.7	826.0	124.9	99.3	95.7	0.252	33.5	2000	45.0	4.169	0.800	0.647	0.0747
20	84.0	825.2	124.8	101.1	95.8	0.252	34.0	2000	45.1	4.154	0.800	0.647	0.0744
21	84.77	787.2	124.8	124.1	96.2	0.308	40.4	3000	51.6	4.745	0.800	0.647	0.0764
22	82.93	864.1	123.9	134.3	94.4	0.309	42.7	3000	56.7	5.162	0.600	0.647	0.0801
23	86.19	733.9	124.8	124.1	97.3	0.257	40.9	3000	47.9	3.822	0.400	0.647	0.0713

Table D.1: Steady-state points obtained for SES36 (Continued).

Run #	$T_{su,ev}$ (°C)	$p_{su,exp}$ (kPa)	$T_{su,exp}$ (°C)	$p_{ex,exp}$ (kPa)	$T_{ex,exp}$ (°C)	$\dot{m}_r$ (kg/s)	T_{cd} (°C)	N_{exp} (rpm)	$\dot{Q}_{T66,in}$ (kW)	$\dot{W}_{el,grid}$ (kW)	$\dot{W}_{el,pp}$ (kW)	$\eta_{is,oa,exp}$ (-)	η_{ORC} (-)
24	87.55	617.5	124.8	111.5	98.9	0.218	37.9	3000	40.2	2.997	0.300	0.647	0.0670
25	85.58	829.0	124.7	141.0	96.9	0.316	44.5	3000	54.7	4.721	0.800	0.647	0.0717
26	88.4	666.7	124.7	123.5	99.7	0.238	41.1	3000	43.3	3.159	0.600	0.647	0.0590
27	85.69	833.1	124.8	140.6	97.0	0.315	44.5	3000	54.6	4.710	0.800	0.647	0.0715
28	82.12	805.1	124.9	109.3	94.1	0.306	35.8	3000	55.3	5.513	0.900	0.647	0.0834
29	82.33	811.4	125.1	109.8	94.3	0.306	35.9	3000	54.7	5.480	0.900	0.647	0.0837
30	82.9	811.1	125.1	111.1	94.9	0.307	36.6	3000	54.1	5.429	0.460	0.647	0.0919
31	88.87	709.6	125.0	133.9	100.0	0.259	43.4	3000	45.0	3.373	0.600	0.647	0.0615
32	85.68	592.9	124.9	120.9	101.9	0.207	40.3	3000	37.9	2.319	0.500	0.647	0.0479
33	87.29	746.4	124.9	129.9	98.5	0.275	42.0	3000	48.0	3.982	0.700	0.647	0.0683
34	84.91	732.5	125.6	108.9	96.8	0.269	36.6	3000	44.5	4.495	0.700	0.647	0.0853
35	82.99	863.6	125.0	124.5	94.9	0.333	40.5	3000	53.4	4.495	0.900	0.647	0.0883
36	82.62	866.2	124.4	129.5	93.8	0.333	41.8	3000	52.9	5.615	0.900	0.647	0.0862
37	85.41	572.2	125.3	102.7	97.9	0.201	35.3	3000	33.1	5.463	0.500	0.647	0.0677
38	83.11	866.7	124.6	127.9	94.9	0.334	41.3	3000	52.3	2.741	0.900	0.647	0.0889
39	84.58	603.7	125.5	104.6	99.9	0.202	35.9	3000	31.9	5.552	0.500	0.647	0.0691
40	83.98	869.7	124.6	132.9	95.5	0.334	42.4	3000	52.2	2.707	0.900	0.647	0.0865
41	75.38	885.9	120.4	98.6	87.4	0.349	31.4	3000	66.6	5.418	1.000	0.647	0.0879
42	74.87	882.7	119.3	99.9	86.6	0.350	31.7	3000	65.1	6.858	1.000	0.647	0.0890
43	76.73	892.5	119.2	110.4	88.1	0.356	35.9	3000	63.8	6.835	1.000	0.647	0.0875

Table D.2: Steady-state points obtained for R245fa.

Run #	$T_{su,ev}$ (°C)	$p_{su,exp}$ (kPa)	$T_{su,exp}$ (°C)	$p_{ex,exp}$ (kPa)	$T_{ex,exp}$ (°C)	$\dot{m}_r$ (kg/s)	T_{cd} (°C)	N_{exp} (rpm)	$\dot{Q}_{T66,in}$ (kW)	$\dot{W}_{el,grid}$ (kW)	$\dot{W}_{el,pp}$ (kW)	$\eta_{is,oa,exp}$ (-)	η_{ORC} (-)
1	73.8	700.1	123.8	127.9	96.1	0.162	20.4	2000	41.0	2.318	0.598	0.386	0.0419
2	75.7	739.1	123.9	132.2	95.9	0.172	21.2	2000	42.3	2.513	0.600	0.392	0.0452
3	77.5	776.1	124.0	135.5	95.6	0.181	21.8	2000	44.3	2.723	0.623	0.398	0.0474
4	79.2	813.4	124.1	138.5	95.2	0.191	22.4	2000	46.2	2.937	0.700	0.403	0.0484
5	80.8	852.6	124.2	143.4	95.0	0.201	23.4	2000	48.2	3.138	0.727	0.406	0.0501
6	77.1	971.1	123.9	152.2	93.2	0.233	25.0	2000	54.6	3.838	0.900	0.421	0.0544
7	77.8	1020.0	124.0	155.7	96.2	0.247	25.5	2000	55.9	4.180	1.000	0.426	0.0569
8	77.6	1064.9	124.0	162.6	92.3	0.259	26.6	2000	58.4	4.393	1.098	0.429	0.0564
9	77.4	1107.0	124.2	165.7	91.8	0.270	27.1	2000	61.0	4.651	1.101	0.431	0.0582
10	77.0	1150.0	124.1	172.1	91.4	0.285	28.0	2000	63.4	4.873	1.200	0.431	0.0579
11	76.7	1191.0	124.2	175.2	90.9	0.297	28.5	2000	65.5	5.149	1.300	0.434	0.0587
12	75.8	1230.0	124.8	166.9	90.3	0.305	27.2	2000	66.9	5.613	1.335	0.444	0.0640
13	76.7	1187.0	124.9	165.7	91.2	0.293	27.0	2000	64.5	5.295	1.300	0.439	0.0619
14	77.1	1140.0	124.8	162.8	91.7	0.281	26.5	2000	61.5	5.008	1.200	0.437	0.0619
15	77.3	1100.0	124.7	158.9	92.1	0.268	25.9	2000	60.4	4.756	1.100	0.436	0.0605
16	79.3	818.7	124.3	137.3	95.5	0.192	22.2	2000	46.1	3.012	0.700	0.406	0.0501
17	77.7	780.2	124.2	134.0	95.9	0.183	21.6	2000	43.7	2.797	0.610	0.401	0.0500
18	76.0	744.1	124.2	131.4	96.3	0.173	21.1	2000	41.9	2.575	0.600	0.394	0.0471
19	74.2	708.9	124.0	130.0	96.8	0.164	20.9	2000	40.8	2.343	0.580	0.386	0.0433
20	70.6	627.9	123.8	122.3	97.5	0.143	19.2	2000	37.2	1.911	0.500	0.369	0.0379
21	69.0	596.7	123.8	120.3	97.6	0.136	18.8	2000	35.4	1.720	0.400	0.356	0.0373
22	67.3	566.9	123.7	120.7	98.1	0.128	18.9	2000	33.6	1.500	0.400	0.341	0.0327
23	79.4	776.9	124.2	199.7	102.1	0.203	7865	2500	46.4	1.745	0.600	0.286	0.0247

Table D.2: Steady-state points obtained for R245fa (Continued).

Run #	$T_{su,ev}$ (°C)	$p_{su,exp}$ (kPa)	$T_{su,exp}$ (°C)	$p_{ex,exp}$ (kPa)	$T_{ex,exp}$ (°C)	$\dot{m}_r$ (kg/s)	T_{cd} (°C)	N_{exp} (rpm)	$\dot{Q}_{T66,in}$ (kW)	$\dot{W}_{el,grid}$ (kW)	$\dot{W}_{el,pp}$ (kW)	$\eta_{is,oa,exp}$ (-)	η_{ORC} (-)
24	80.08	821.9	124.2	206.4	101.5	0.217	7865	2500	48.7	1.985	0.600	0.302	0.0284
25	81.27	858.4	124.2	208.9	100.7	0.228	7865	2500	51.1	2.268	0.700	0.322	0.0306
26	82.32	895.2	124.0	211.5	99.8	0.241	7865	2500	53.5	2.534	0.717	0.336	0.0340
27	83.13	934.1	124.0	215.7	99.2	0.253	7865	2500	55.9	2.788	0.800	0.347	0.0355
28	84.2	973.0	123.9	218.2	98.5	0.265	7865	2500	57.7	3.072	0.881	0.360	0.0380
29	84.68	1010.0	124.0	222.0	97.8	0.277	7865	2500	60.1	3.364	0.900	0.373	0.0410
30	83.6	950.9	124.2	218.8	97.8	0.288	35.4	3000	62.9	3.461	0.900	0.379	0.0407
31	82.9	915.9	124.2	218.6	98.83	0.275	35.3	3000	60.5	3.058	0.800	0.358	0.0373
32	82.2	878.3	124.1	215.9	99.65	0.262	35.0	3000	57.5	2.743	0.800	0.342	0.0338
33	80.9	838.8	124.0	208.9	100.2	0.249	34.1	3000	55.2	2.500	0.700	0.331	0.0326
34	79.4	802.7	123.8	205.5	100.9	0.237	33.5	3000	53.4	2.174	0.700	0.307	0.0276
35	78.1	770.3	123.8	204.4	102.2	0.224	33.4	3000	50.4	1.751	0.600	0.268	0.0228
36	77.04	732.2	123.9	197.6	103.0	0.212	32.4	3000	48.6	1.489	0.600	0.242	0.0183
37	73.1	1020.0	124.1	152.0	87.4	0.309	24.4	3000	70.6	6.550	1.100	0.522	0.0772
38	73.6	978.6	124.0	150.0	88.0	0.295	24.1	3000	68.1	6.145	1.000	0.520	0.0756
39	74.7	932.8	123.8	148.3	88.8	0.279	23.8	3000	64.2	5.675	0.970	0.515	0.0733
40	75.4	895.1	123.7	146.9	89.4	0.266	23.7	3000	61.6	5.255	0.900	0.506	0.0707
41	74.1	857.5	123.9	144.7	90.4	0.254	23.4	3000	59.1	4.885	0.800	0.499	0.0691
42	77.2	822.9	123.8	144.7	91.1	0.242	23.4	3000	57.1	4.4463	0.800	0.487	0.0641
43	76.1	787.1	123.8	143.1	92.0	0.230	23.2	3000	54.6	4.092	0.700	0.477	0.0621
44	76.1	750.4	123.6	140.3	92.6	0.220	22.7	3000	52.6	3.757	0.700	0.466	0.0581
45	74.8	715.4	124.0	138.0	93.6	0.208	22.2	3000	50.8	3.429	0.600	0.455	0.0557
46	73.3	681.1	123.9	136.9	94.5	0.197	22.0	3000	48.2	3.048	0.600	0.435	0.0508

Table D.2: Steady-state points obtained for R245fa (Continued).

Run #	$T_{su,ev}$ (°C)	$p_{su,exp}$ (kPa)	$T_{su,exp}$ (°C)	$p_{ex,exp}$ (kPa)	$T_{ex,exp}$ (°C)	$\dot{m}_r$ (kg/s)	T_{cd} (°C)	N_{exp} (rpm)	$\dot{Q}_{T66,in}$ (kW)	$\dot{W}_{el,grid}$ (kW)	$\dot{W}_{el,pp}$ (kW)	$\eta_{is,oa,exp}$ (-)	η_{ORC} (-)
47	74.9	1070.0	124.7	170.9	89.6	0.329	27.7	3000	72.7	6.502	1.200	0.507	0.0729
48	74.4	1110.0	124.7	174.8	89.2	0.344	28.3	3000	74.9	6.851	1.203	0.508	0.0755
49	74.2	1150.0	124.6	181.6	89.16	0.362	29.3	3000	77.8	7.105	1.300	0.504	0.0746
50	74.5	1190.0	124.7	188.6	89.2	0.378	30.3	3000	80.4	7.364	1.400	0.503	0.0742
51	83.8	975.1	124.4	227.0	98.5	0.230	36.4	3300	64.0	3.299	0.900	0.351	0.0374
52	84.4	1009.0	124.3	231.3	98.2	0.310	37.0	3300	65.4	3.542	0.900	0.361	0.0403
53	84.4	972.1	124.2	232.2	99.5	0.298	37.1	3300	63.6	3.085	0.9	0.335	0.0343
54	83.4	930.2	124.3	225.1	100.2	0.284	36.1	3300	60.1	2.836	0.800	0.326	0.0339
55	82.5	893.3	124.2	222.5	101.0	0.271	35.9	3300	57.7	2.500	0.798	0.305	0.0295
56	81.2	856.4	124.2	220.2	102.1	0.259	35.5	3300	58.9	2.146	0.700	0.279	0.0258
57	79.6	815.1	124.1	214.9	102.7	0.246	34.7	3300	53.5	1.868	0.669	0.259	0.0224
58	78.5	776.0	124.4	211.2	103.9	0.232	34.2	3300	51.2	1.539	0.600	0.231	0.0183
59	77.2	738.5	124.3	205.9	104.6	0.221	33.4	3300	48.8	1.283	0.600	0.205	0.0140

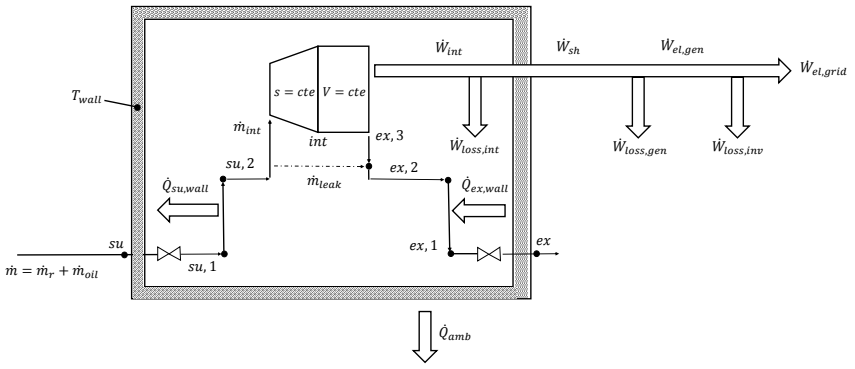

Figure D.1: Schematic representation of the open-drive expander semi-empirical simulation model.

D.2 Semi-empirical model of the single-screw expander

The single-screw expander is modeled by decomposing the entire expansion process in different steps as originally proposed by Winandy et al. [2]. The present expander is an open-drive machine connected directly to a generator by means of jaw couplings and the actual electrical power output is measured through the inverter. For this reason, the electro-mechanical losses are accounted for by introducing two correlations for the generator and inverter efficiency. By referring to Fig. D.1, the working fluid entering the expander undergoes to: an adiabatic pressure drop (su-su_1) and a cool down due to heat transfer with the expander housing during the suction process (su_1-su_2); an isentropic expansion due to the built-in volume ratio (su_2- int); an adiabatic expansion at constant volume (int-ex_3); an adiabatic mixing with the internal leakage flows (ex_3-ex_2); a heat transfer with the housing (ex_2-ex_1) and pressure drop during the discharge process (ex_1-ex). A lumped isothermal wall is used to imposed an overall energy balance of the expander which includes the expander internal mechanical losses, $\dot{W}_{loss,int}$, heat transfer rate with the expander shell, $\dot{Q}_{su,wall}$ and $\dot{Q}_{ex,wall}$, and heat losses to the ambient $\dot{Q}_{amb}$ [3]. The energy balance is expressed by:

$$\dot{Q}_{su,wall} - \dot{Q}_{ex,wall} + \dot{W}_{loss,int} - \dot{Q}_{amb} = 0 \tag{D.1}$$

The model also includes the presence of lubricant oil which is mixed with the working fluid. The working fluid and lubricant oil are considered to be in thermal

and mechanical equilibrium so that a homogeneous mixture model can be applied. The total mass flow rate entering the expander is given by

$$\dot{m}_{exp} = \dot{m}_r + \dot{m}_{oil} = (1 + y_{oil})\,\dot{m}_r \tag{D.2}$$

where y_{oil} represents the ratio between the oil mass flow rate to the working fluid mass flow rate. The leakage model considers an adiabatic compressible flow of working fluid through a nozzle where the equivalent throat area, $A_{r,leak}$, determined empirically. The presence of lubricant oil affects the actual leakage area and therefore, the total throat area can be expressed as:

$$A_{r,leak} = A_{tot,leak} - A_{oil,leak} = A_{tot,leak} - y_{oil} A_{r,leak} \frac{v_{oil,up}}{v_{r,thr,leak}} \tag{D.3}$$

where $A_{oil,leak}$ represents the portion of area sealed by the lubricant oil. The working fluid leakage flow rate is expressed by:

$$\dot{m}_{r,leak} = C_{r,thr,leak} \frac{A_{r,leak}}{v_{r,thr,leak}} \tag{D.4}$$

As described before, the total work consists of an isentropic and constant volume contributions. The internal isentropic specific work of the oil and working fluid mixture is given by:

$$w_{int,is} = h_{r,su2} - h_{r,int} + x_{oil}\,(h_{oil,su2} - h_{oil,int}) \tag{D.5}$$

where the specific entropy of the mixture defined as $s_{mix,int} = s_{r,int} + x_{oil} s_{oil,int}$ is kept constant. An effective built-in volume ratio can be defined as:

$$r^*_{v,int} = \frac{v_{r,int}}{v_{r,su2}} \tag{D.6}$$

The work associated with the expansion at constant machine volume is given by:

$$w_{int,V} = (p_{r,int} - p_{r,ex2})\,(v_{r,int} + x_{oil} v_{oil,su2}) \tag{D.7}$$

where implicitly it is assumed that $p_r = p_{oil}$.

The heat transfer during suction ad discharge process are calculated by using the ϵ-NTU method. The overall thermal conductance is given by:

$$UA_i = UA_{n,i} \left(\frac{\dot{m}_{i,exp}}{\dot{m}_{n,exp}} \right)^n \tag{D.8}$$

where the index i stands for suction and discharge conditions, $UA_{n,i}$ and $\dot{m}_{n,exp}$ represent the nominal thermal conductance at suction and discharge and

the nominal mass flow rate, respectively. The power coefficient n is usually chosen to be equal to 0.8 by assuming the Reynolds heat transfer analogy of fully developed turbulent flow, as reported by various authors and for different volumetric machines of both expanders and compressors [4–6]. The exponent n has been bounded between 0.6 and 0.8 in order to verify such assumption. The heat transfer rate to the ambient is calculated by assuming a constant UA_{amb} value:

$$\dot{Q}_{amb} = UA_{amb}\left(T_{wall} - T_{amb}\right) \tag{D.9}$$

where T_{wall} is the lumped expander shell temperature and T_{amb} is the ambient temperature.

The total internal mechanical losses of the expander are defined by a term proportional to the internal power output and a term associated with mechanical and friction losses. In particular,

$$\dot{W}_{loss,int} = \alpha_{loss}\dot{W}_{int} + \dot{W}_{loss,mech} \tag{D.10}$$

where $\dot{W}_{loss,mech}$ is calculated by means of constant friction torque, τ_{loss}:

$$\dot{W}_{loss,mech} = \dot{W}_{loss,0} + 2\pi\tau_{loss}\frac{N_{exp}}{60} \tag{D.11}$$

Finally, the electro-mechanical losses of the generator and inverter are estimated by:

$$\dot{W}_{loss,gen} = \left(1 - \eta_{el-m,gen}\right)\dot{W}_{sh,exp} \tag{D.12}$$

$$\dot{W}_{loss,inv} = \left(1 - \eta_{el,inv}\right)\dot{W}_{el,gen} \tag{D.13}$$

A total of 11 parameters needs to be identified upon the experimental results obtained. A genetic algorithm is used to minimize an objective function which depends on the sum of relative errors between the calculated and measured values of the expander mass flow rate, discharge temperature and electric power output. More details about the minimization process can be found in [7]. The objective function is defined as follows:

$$\begin{aligned} obj^2 = \sum_i \left(\frac{\dot{m}_{calc} - \dot{m}_{meas}}{\dot{m}_{meas}}\right)^2 + \sum_i \left(\frac{T_{ex,calc} - T_{ex,meas}}{T_{ex,max} - T_{ex,min}}\right)^2 \\ + \frac{1}{\sqrt{2}}\sum_i \left(\frac{\dot{W}_{el,exp,calc} - \dot{W}_{el,exp,meas}}{\dot{W}_{el,exp,meas}}\right)^2 \end{aligned} \tag{D.14}$$

where the running index i is the total number of experimental points. The resulting calibrated coefficients for both working fluids are reported in Table D.3. The

Parameter	R245fa	SES36
$\dot{m}_{n,exp}$ [kg/s]	0.51	0.47
UA_{suc} [W K^{-1}]	$25.75\left(\frac{\dot{m}_{exp}}{\dot{m}_{n,exp}}\right)^{0.8}$	$27.19\left(\frac{\dot{m}_{exp}}{\dot{m}_{n,exp}}\right)^{0.8}$
UA_{ex} [W K^{-1}]	$15.44\left(\frac{\dot{m}_{exp}}{\dot{m}_{n,exp}}\right)^{0.8}$	$16.19\left(\frac{\dot{m}_{exp}}{\dot{m}_{n,exp}}\right)^{0.8}$
UA_{amb} [W K^{-1}]	11.63	5.85
A_{suc} [m^2]	7.45e-5	8.63e-5
x_{leak} [-]	0.0	0.0
A_{leak} [m^2]	8.7e-6	3.27e-6
A_{ex} [m^2]	58.27e-5	12.66e-4
y_{oil} [-]	0.01	0.01
α_{loss} [-]	0.05	0.05
$\dot{W}_{loss,0}$ [W]	350.59	62.17
τ_{loss} [N m]	6.75	5.32

Table D.3: Identified parameters of the expander semi-empirical model for both working fluids.

Variable	**MAPE**	**Max RE**	**Min deviation**	**Max deviation**	**Standard deviation**
R245fa					
$\dot{m}_{r,exp}$	1.48%	2.22 %	-0.0073 kg/s	0.0050 kg/s	0.056 kg/s
$\dot{W}_{el,exp}$	5.11%	10.50 %	-609.78 W	1156.46 W	1770.78 W
$T_{ex,exp}$	0.42%	0.93%	-7.66 K	1.62 K	6.28 K
$\eta_{oa,exp}$	6.14%	12.31%	-0.093 (-)	0.105 (-)	0.094 (-)
SES36					
$\dot{m}_{r,exp}$	2.79%	8.90 %	-0.00714 kg/s	0.02288 kg/s	0.0629 kg/s
$\dot{W}_{el,exp}$	10.72%	22.09 %	-598.15 W	775.81 W	1541.38 W
$T_{ex,exp}$	1.002%	2.35%	-8.64 K	2.93 K	6.95 K
$\eta_{oa,exp}$	11.59%	26.05%	-0.1285 (-)	0.0846 (-)	0.0860 (-)

Table D.4: Summary of the relative and absolute errors on semi-empirical model prediction for R245fa and SES36.

verification of the semi-empirical model is presented as parity plots of mass flow rate, power output, discharge temperature and overall isentropic efficiency. The results are shown in Figure D.2 and Figure D.3. A summary of the error analyses on the results is reported in Table D.4.Finally, a sensitivity study on the identified parameters is shown in Figure D.4.

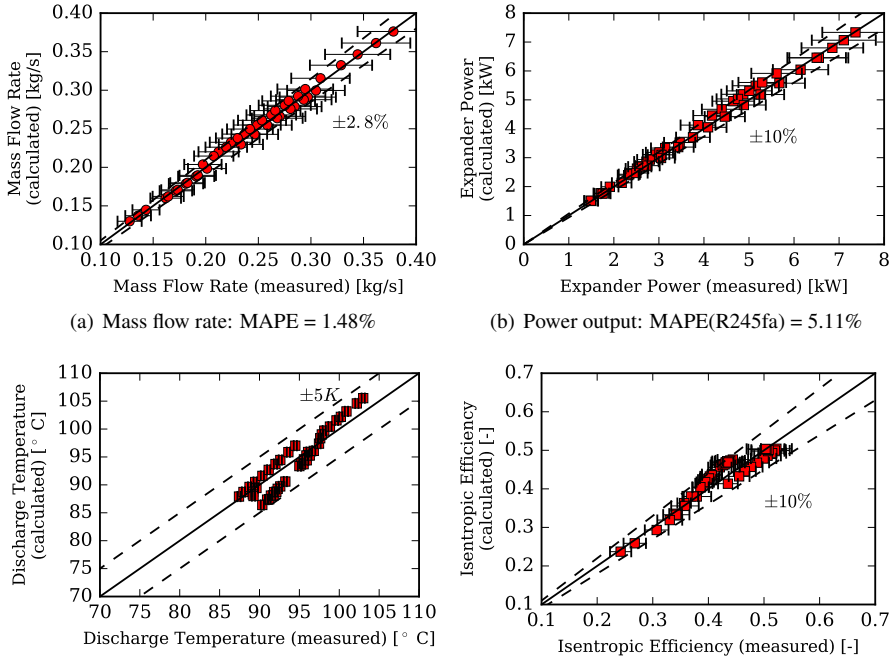

(a) Mass flow rate: MAPE = 1.48%

(b) Power output: MAPE(R245fa) = 5.11%

(c) Discharge temperature: MAPE(R245fa) = 0.42%

(d) Isentropic efficiency: MAPE(R245fa) = 6.14%

Figure D.2: Comparison between measured and predicted values with the semi-empirical model for the scroll and single-screw expanders: (a) refrigerant mass flow rate; (b) power output; (c) discharge temperature; (d) isentropic efficiency. In the parity plots, all the steady-state points are shown.

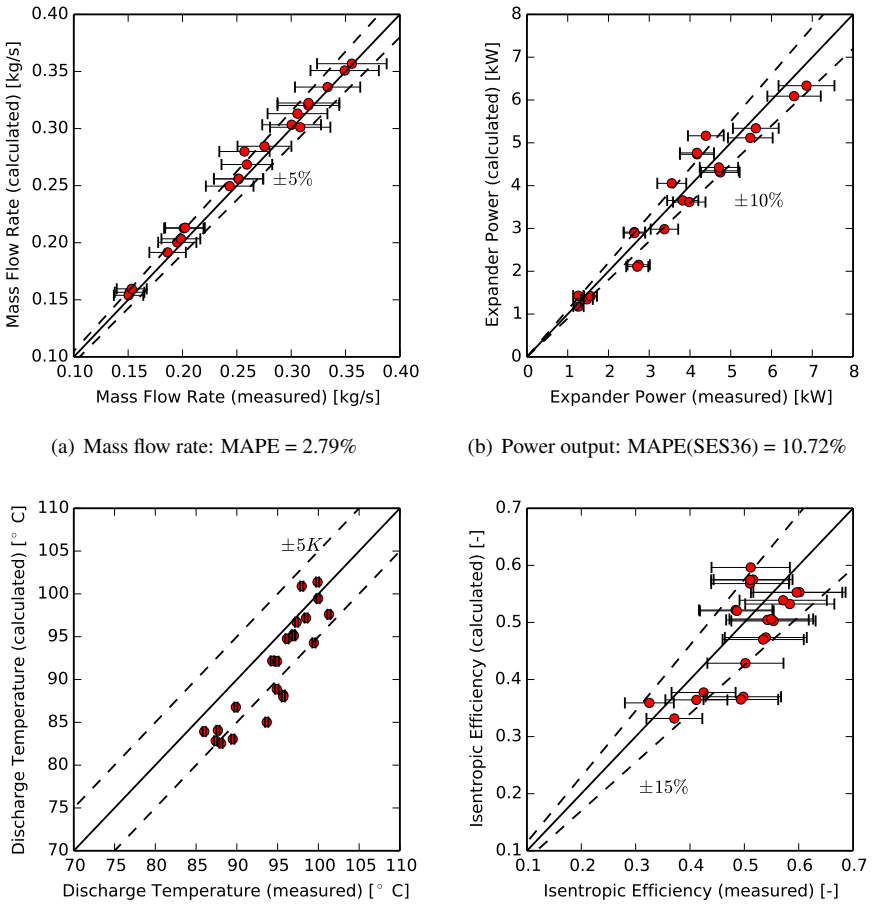

(a) Mass flow rate: MAPE = 2.79%

(b) Power output: MAPE(SES36) = 10.72%

(c) Discharge temperature: MAPE(SES36) = 1.00%

(d) Isentropic efficiency: MAPE(SES36) = 11.59%

Figure D.3: Comparison between measured and predicted values of SES36 with the semi-empirical model for the single-screw expanders: (a) refrigerant mass flow rate; (b) power output; (c) discharge temperature; (d) isentropic efficiency. In the parity plots, only the steady-state points used for validation are shown.

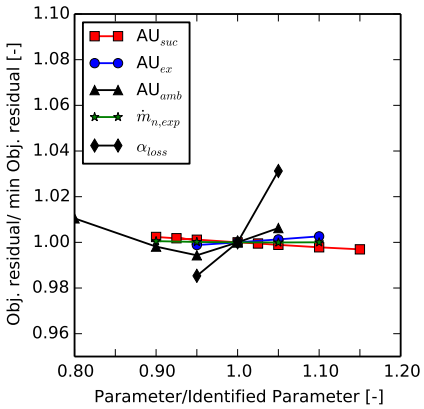

Figure D.4: Sensitivity analysis on the semi-empirical model of the single-screw expander.

References

[1] D. Ziviani, S. Sergei, S. Lecompte, E. A. Groll, J. E. Braun, W. T. Horton, M. van den Broek, and M. De Paepe. *Characterizing the performance of a single-screw expander in a small-scale organic Rankine cycle for waste heat recovery*. Applied Energy, 181:155–170, 2016.

[2] E. Winandy, C. Saavedra, and J. Lebrun. *Simplified modeling of an open-drive reciprocating compressor*. International Journal of Thermal Sciences, 42:183–192, 2002.

[3] V. Lemort, S. Declaye, and S. Quoilin. *Experimental characterization of a hermetic scroll expander for use in a micro-scale Rankine cycle*. Proc. of Institution of Mechanica Engineers, Part A: Journal of Power and Energy, 226:126–136, 2012.

[4] A. Giuffrida. *Modelling the performance of a scroll expander for small organic Rankine cycles when changing the working fluid*. Applied Thermal Engineering, 70:1040–1049, 2014.

[5] L. Dardenne, E. Fraccari, A. Maggioni, L. Molinaroli, L. Proserpio, and E. Winandy. *Semi-empirical modeling of a variable speed scroll compressor with vapor injection*. International Journal of Refrigeration, 54:76–87, 2015.

[6] A. Giuffrida. *A semi-empirical mmethod for assessing the performance of an open-drive screw refrigeration compressor*. Applied Thermal Engineering, 93:813–823, 2016.

[7] N.A. James, J.E. Braun, E. A. Groll, and W. T. Horton. *Semi-empirical modeling and analysis of oil flooded R410A scroll compressors with liquid injection for use in vapor compression systems*. Int. J. Refrig., In Press, 2016.

E

ORC with Liquid Flooded Expansion and internal regeneration (ORCLFE)

E.1 Introduction

Screw-type of expanders can potentially reach isentropic efficiency above 80% [2]. Since, usually, these machines require active lubrication systems, i.e., dedicated lubrication loops with multi-injection ports, the concept of liquid flooded expansion can be explored to achieve two goals:

- improve the expansion process towards an isothermal transformation to increase the potential power output and favor the use of internal regeneration;
- use the flooding medium (typically lubricant oil) to minimize the friction losses and leakage flows.

From previous numerical analyses [3, 4], it has been shown how positive displacement expanders with larger internal volume ratios are favored for investigating flooded expansion. For this reason, a single-screw expander

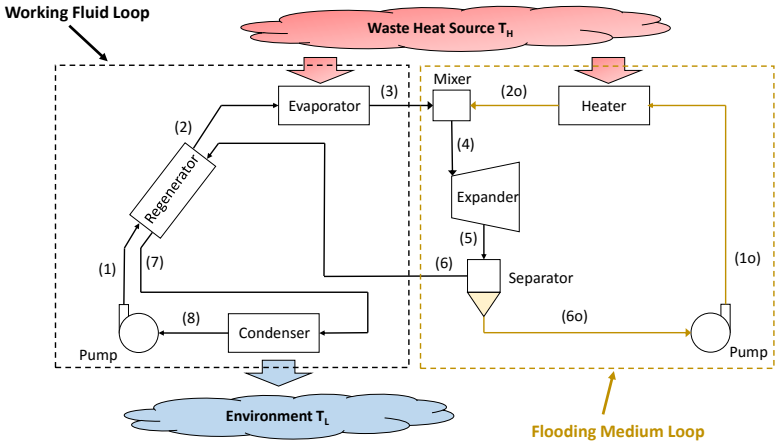

Figure E.1: Schematic representation of ORCFLE (Adapted from Woodland et al. [1]).

represents a suitable candidate. Hence, organic Rankine cycle with liquid flooded expansion (ORCLFE) and internal regeneration is proposed to investigate such aforementioned benefits.

An ORCLFE test rig has been designed and built to extend the testing capabilities of the previous industrial prototype (see Section 5) in order to better characterize the performance of expanders. The characterization of single-screw expander with R245fa and SES36 without significant amount of lubricant oil has been presented in Section 5.2. The setup is used to assess the benefits of a controlled flooded expansion as well as to compare R245fa and its potential replacement R1233zd(E). A synthetic POE lubricant oil, ACD100FY, is used as flooding medium.

E.2 ORCLFE thermodynamic analysis

By considering the cycle schematic of the ORCLFE system architecture depicted in Figure E.1, both the primary working fluid (1) and the flooding medium (1o) are pumped to the high system pressure. While the flooding medium is heated up directly by the heater (11), the working fluid is first preheated inside the internal regenerator (2) and then vaporized and superheated by the evaporator (3). The finite heat source is used to heat up the primary working fluid and the flooding medium. State (3) and state (2o) are assumed to be at the same temperature and pressure conditions. The two fluids undergo a mixing process (4) prior to

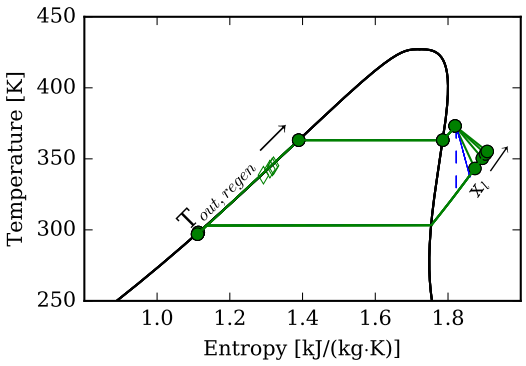

(a)

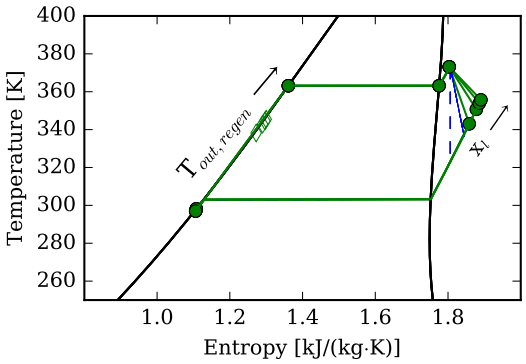

(b)

Figure E.2: Thermodynamic plot of ORC with liquid flooded expansion and internal regeneration for different flooding ratios:(a) *R245fa;* (b) *R1233zd(E).*

entering the expander. In the mixing section, a homogeneous mixture is ideally achieved. After the expansion process occurs (5), the vapor phase of the working fluid is separated from the flooding medium inside a oil separator. The flooded expansion,guarantees a significant degree of superheating of the working fluid at the expander outlet which represents a favorable condition for the internal regeneration. The working fluid vapor phase (6) is used to regenerate (7) before it is condensed in the condenser (8). The portion of flooding medium separated is then pumped back to the high pressure side and the cycle is repeated. In Figure E.2, the effect of flooded expansion is shown for R245fa and R1233zd(E). As the flooding ratio increases, the discharge temperature of the expander is closer to an isothermal. At the same time, the higher discharge temperature allows for internal regeneration which improves the thermodynamic cycle efficiency.

Challenges arise when designing an ORCLFE system. In particular, three main aspects should be considered that limit the theoretical performance of the proposed ORC enhancement:

- possible flashing of the flooding medium into its two-phase region which could cause a temperature drop, i.e. the flooding medium would also be expanding;
- irreversibilities due to the mixing of primary working fluid and flooding medium as well as solubility of refrigerant into the flooding medium;
- additional flooding medium pump and heat exchanger that increase the cost of the system.

In order to analyze the proposed system, an ORCLFE cycle model was developed that partially includes the aforementioned aspects. The following assumptions were made:

- real gas model for the working fluid;
- the liquid is considered incompressible and non volatile;
- the ideal mixture model is used;
- pressure drops in the heat exchangers and line sets are neglected;
- liquid and gas flows are assumed to be in thermal and mechanical equilibrium;
- perfect mixing;
- perfect separation process (i.e., no solubility effects) in the oil separator except where specified;
- fixed volumetric displacement rate for the expander with a filling factor equal to unity.

Besides the potential performance improvements over the baseline ORC, the model is used to assess the impact of the expander internal volume ratio on the liquid-flooded expansion performance as well as on the overall cycle performance.

E.2.1 Effective volume internal volume ratio

A positive displacement expander is characterized by a fixed internal volume ratio related to the ratio of the discharge volume of the expansion chamber to the volume

Description	Value
Reference temperature, T_0	25 °C
Condenser outlet subcooling	5 °C
Cold sink temperature	20 °C
Minimum temperature difference in heat exchangers (approach or pinch)	5 °C
Heat source temperature	100-150 °C
Heat source mass flow rate	1 kg/s
Flooding ratio	0-1
Regenerator effectiveness (if not specified)	0.9
Pump isentropic efficiency	0.5
Pump electric motor efficiency	0.9
Expander isentropic efficiency	Calculated
Expander mechanical effciency (if not specified)	0.8
Expander ambient heat transfer (UA_{amb})	0.01 kW/(m^2 K)
Negligible pressure drop in linesets, separator, mixer and heat exchangers	-
Negligible heat loss in linesets, separator, mixer, pumps	-

Table E.1: List of assumptions made in the cycle and component models.

of the expansion chamber at suction closure (or the displaced volume). That is:

$$r_{v,built-in} = \frac{V_{ex,exp}}{V_{su,exp}} \tag{E.1}$$

Due to the presence of a flooding medium (generally an incompressible liquid) in the expansion chamber, the volume ratio that the working fluid sees is higher and it can be defined as the effective built-in volume ratio $r^*_{v,built-in}$ [5]. Its mathematical definition is related to the liquid volume fraction existing in the chamber:

$$a_l = \frac{V_{\mathrm{l,in}}}{V_{\mathrm{s,exp}}} \tag{E.2}$$

It can be demonstrated that the effective volume ration is given by:

$$r^*_{\mathrm{v,built-in}} = \frac{r_{\mathrm{v,built-in}} - a_{\mathrm{l}}}{1 - a_{\mathrm{l}}} \tag{E.3}$$

It can be noted that as the liquid volume fraction increases, the effective volume ratio increases moderately until approximately 0.8, then more sharply in the range 0.8 - 0.9 and approaching infinity for $a_{\mathrm{l}} \rightarrow 1$. This fact is shown in Figure E.3 where the effective volume ratio is reported as a function of the liquid volume fraction in the working chamber for different geometric built-in volume ratios (2-6). In particular, built-in volume ratios >3.5 are characteristic of screw

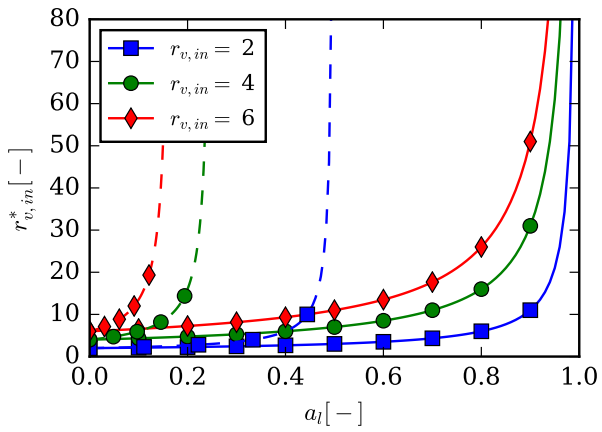

Figure E.3: Expander (solid lines) and compressor (dashed lines) effective volume ratios as a function of the flooding medium volume fraction for different geometric built-in volume ratios.

machines. For a certain liquid volume fraction, the higher the fixed volume ratio of the expander, the higher is the effective volume ratio achievable. In the case of a compressor, similar liquid volume fractions lead to more significant changes in the effective volume ratio (shown as dotted lines). The optimal volume ratios needed for liquid-flooded expansion (or compression) are in general larger with respect to dry-running expanders. For instance, Bell et al. [6] optimized a scroll compressor for liquid-flooding. Starting from a baseline compressor design with a built-in volume ratio of 1.8, the optimized geometry for flooded compression resulted to have an internal volume ratio of 2.7.

E.2.2 Thermo-physical properties

Modeling the ORC with flooded expansion requires the knowledge of the flooding medium properties during the expansion process and in the flooding loop in addition to the working fluid properties. REFPROP 9.1.1 [7] is used to retrieve the thermophysical properties of the working fluids. An additional property wrapper has been developed to calculate both the properties of the lubricant oils and the mixture of oil and working fluids. Many of the oil properties were obtained from open literature [8,9], as already mentioned in Section 4.3. Additional assumptions are introduced in order to evaluate the mixture properties. Besides the fact that oil and working fluid are in thermal and mechanical equilibrium, it is assumed that both phases have the same temperature and pressure. As aforementioned,

it is generally assumed that the phases exiting the oil separator are completely separated. However, during normal operation, working fluid can be dissolved in the oil flow stream and oil droplets are entrained in the working fluid vapor stream leaving the separator. Solubility effects can be accounted for if the solubility of the mixture oil-working fluid is known at the temperature and pressure values of interest for a certain application. In order to perform the cycle analysis, the mixture enthalpy and mixture entropy as functions of temperature and pressure must be determined. An oil mass flow ratio, y_{l}, is defined as

$$y_{\mathrm{l}} = \frac{\dot{m}_{\mathrm{l}}}{\dot{m}_{\mathrm{r}}} \tag{E.4}$$

where $\dot{m}_{\mathrm{r}}$ and $\dot{m}_l$ are the mass flow rates of working fluid and lubricant oil, respectively. With respect to a mixture of oil and working fluid, the oil mass fraction is obtained from:

$$x_{\mathrm{l}} = \frac{\dot{m}_{\mathrm{l}}}{\dot{m}_{\mathrm{r}} + \dot{m}_{\mathrm{l}}} = \frac{1}{\frac{1}{y_{\mathrm{l}}} + 1} \tag{E.5}$$

and the working fluid mass fraction is obtained as $x_{\mathrm{r}} = 1 - x_{\mathrm{l}}$.

The generic mixture thermodynamic property, Ψ_{mix}, such as specific heats, specific enthalpy, specific internal energy, specific exergy, is calculated assuming ideal mixing rule as,

$$\Psi_{\mathrm{mix}} = \Psi_{\mathrm{r}} + y_{\mathrm{l}}\Psi_{\mathrm{l}} \tag{E.6}$$

As far as the specific entropy is concerned, when a mixture is formed from pure fluids at constant temperature and pressure, entropy is generated. For an ideal mixture, the specific entropy is obtained as:

$$s_{\mathrm{mix}} - \sum_i w_i s_{\mathrm{i}} = \Delta s_{\mathrm{mix}} \tag{E.7}$$

where w_i is the mass fraction of the *i-th* component of the mixture.

The mixture density is calculated based on the void fraction weighted average [10]:

$$\rho_{\mathrm{mix}} = \alpha\rho_{\mathrm{r}} + (1 - \alpha)\,\rho_l \tag{E.8}$$

where the void fraction, α is given by:

$$\alpha = \frac{1}{1 + \left[\frac{1}{x_{\mathrm{r}}} - 1\right] S\frac{\rho_{\mathrm{r}}}{\rho_{\mathrm{l}}}} \tag{E.9}$$

with the slip ratio S equal to unity for homogeneous flow. Transport properties are not used in the current cycle model.

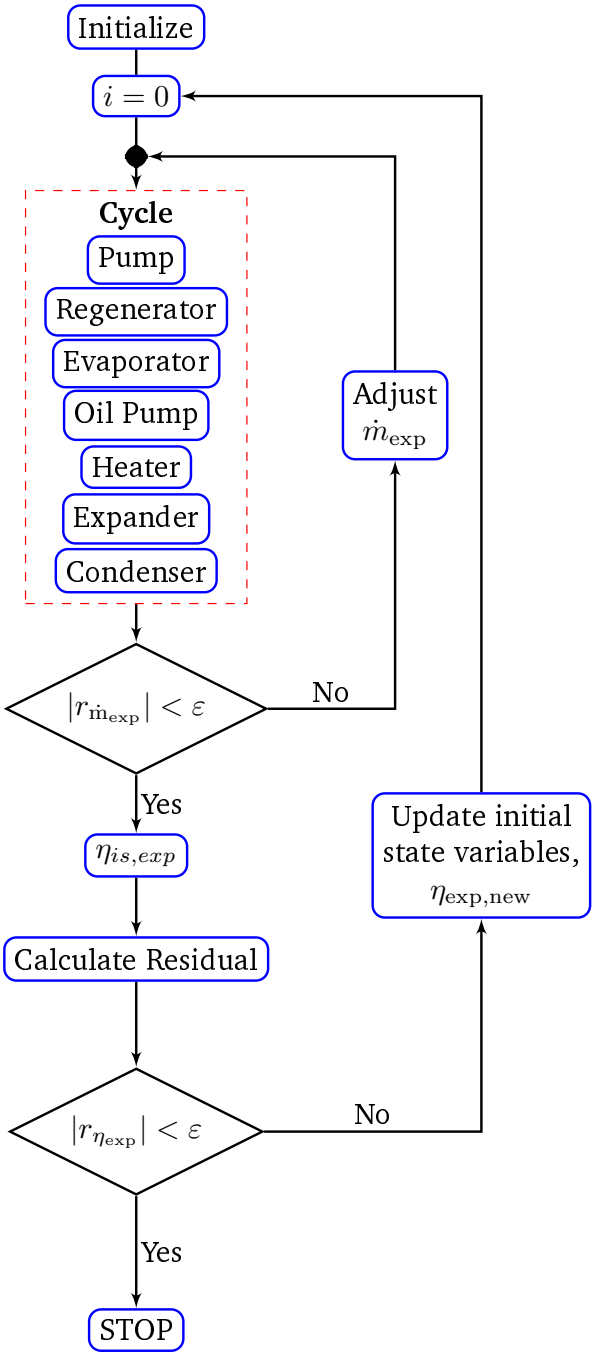

Figure E.4: Overall cycle solution scheme.

E.2.3 Overall cycle model

A cycle model is developed to simulate and optimize the ORCLFE. All cycle components are visible in Figure E.1. The heat source and cold sink temperatures have fixed values of T_H and T_L, respectively. The heat exchangers are modeled by considering pinch points and by assuming a counterflow arrangement. Such modeling approach allows to predict the achievable heat transfer rates between two fluids without the complexity of a particular heat exchanger geometry, the calculation of heat transfer coefficients and pressure drops. The maximum heat transfer rate between two fluids is defined as:

$$\dot{Q}_{\max} = min\Big(\dot{m}_c \left(h_c \left(T_{h,su}, p_c\right) - h_c \left(T_{c,su}, p_c\right)\right), \\ \dot{m}_h \left(h_h \left(T_{h,su}, p_h\right) - h_h \left(T_{c,su}, p_h\right)\right)\Big) \quad \text{(E.10)}$$

where c and h represent the cold and hot fluid streams. In the case of the condenser, both the pinch point temperature difference and the degree of subcooling are imposed. The condensing pressure is assumed to be constant as the pressure drops in the condenser are neglected. Furthermore, pressure drops associated with linesets, separator and regenerator are also not considered. It follows that $p_{cd} = p_5 = p_6 = p_{6o} = p_7 = p_8$. The condenser irreversibility rate is calculated as:

$$\dot{E}_{cd} = T_0 \left[\dot{m}_r \left(s_8 - s_7\right) + \frac{\dot{Q}_{cd}}{T_L}\right] \quad \text{(E.11)}$$

The pumps pressurized the subcooled working fluid from state (8) to state (1) and the flooding medium from (6o) to (1o) at the same pressure value. A constant isentropic efficiency is adopted to model the pumps. In the case of the flooding medium pump, the specific work is calculated as

$$w_{pump,l} = v_l \Delta p \quad \text{(E.12)}$$

The irreversibility rates of the pumps are given by:

$$\dot{E}_{pump} = T_0 \, \dot{m}_r \left(s_2 - s_1\right) \quad \text{(E.13)}$$

$$\dot{E}_{pump,l} = T_0 \, \dot{m}_l \left(s_{1o} - s_{6o}\right) \quad \text{(E.14)}$$

A constant effectiveness models is used for the regenerator. In particular, the maximum enthalpy difference allowed in the regenerator is defined as:

$$\Delta h_{reg,\max} = min\left(h_6 - h(T_1, p_6), h(T_6, p_1) - h_1\right) \quad \text{(E.15)}$$

By introducing the effectiveness, the actual enthalpy difference can be calculated:

$$\Delta h_{\mathrm{reg}} = \epsilon_{reg} \Delta h_{\mathrm{reg,max}} \tag{E.16}$$

The enthalpy at states (2) and (7) can then be obtained. The irrevesibility rate of the regenerator is:

$$\dot{E}_{\mathrm{reg}} = T_0 \, \dot{m}_{\mathrm{r}} \left[(s_2 + s_7) - (s_1 + s_6) \right] \tag{E.17}$$

The outlet temperature of the evaporator, T_3, is obtained by imposing the superheating and the evaporating pressure (or the system pressure ratio) is a degree of freedom in the cycle model to be optimized, since only the pinch point temperature difference is specified (see Table E.1). Regarding the flooding medium, the outlet temperature of the heater is equal to the one of the evaporator, i.e. $\mathrm{T_{2o}} = \mathrm{T_2}$. Similarly to the condensing side, the pressure drops across the evaporator and heater are neglected and therefore $p_1 = p_2 = p_3 = p_{1\mathrm{o}} = p_{2\mathrm{o}} = p_{\mathrm{ev}}$. The irreversibility rate of evaporator and heater are:

$$\dot{E}_{\mathrm{ev}} = T_0 \left[\dot{m}_{\mathrm{r}} \left(s_3 - s_2 \right) - \frac{\dot{Q}_{\mathrm{ev,r}}}{T_{\mathrm{H}}} \right] \tag{E.18}$$

$$\dot{E}_{\mathrm{heater}} = T_0 \left[\dot{m}_{\mathrm{l}} \left(s_{2\mathrm{o}} - s_{1\mathrm{o}} \right) - \frac{\dot{Q}_{\mathrm{heater,l}}}{T_{\mathrm{H}}} \right] \tag{E.19}$$

The working fluid and the oil are mixed together at constant pressure to obtain an homogeneous mixture. Assuming the mixer to be adiabatic, the energy balance is given by

$$\dot{m}_{\mathrm{r}} h_3 + \dot{m}_{\mathrm{l}} h_{2\mathrm{o}} - \left(\dot{m}_{\mathrm{r}} + \dot{m}_{\mathrm{l}} \right) h_4 = 0 \tag{E.20}$$

Although the mixture of oil and working fluid is considered ideal, entropy is generated during the mixing process, i.e. entropy of mixing Δs_{mix}. Therefore, the mixture specific entropy at the outlet of the mixture is given by:

$$s_{4,\mathrm{mix}} - \left(s_3 + x_{\mathrm{l}} s_{2\mathrm{o}} \right) = \Delta s_{\mathrm{mix}} \tag{E.21}$$

with $\Delta s_{\mathrm{mix}} > 0$. The entropy of mixing is calculated as an ideal mixture at constant temperature and pressure.

The expander model has been already described in details in Section 1.2.1. An expander isothermal efficiency is also defined to provide additional information on the performance of the expander with respect to actually achieving an isothermal expansion:

$$\eta_{exp,isoth} = \frac{\dot{W}_{\mathrm{sh,exp}}}{\dot{m}_{\mathrm{r}} w_{isoth,exp} + \dot{m}_{\mathrm{l}} v_{4\mathrm{o}} \left(p_4 - p_5 \right)} \tag{E.22}$$

with:

$$w_{isoth,exp} = h_4(T_4, p_4) - h_{5,isoth}(T_4, p_5) - T_4 \left(s_4(T_4, p_4) - s_{5,isoth}(T_4, p_5)\right) \quad \text{(E.23)}$$

The irreversibility rate of the expander is calculated as

$$\dot{E}_{\text{exp}} = T_0 \, \dot{m}_{\text{exp}} \left(s_{5,mix} - s_{4,mix}\right) \quad \text{(E.24)}$$

After the expansion process, i.e. state (5), the mixture of oil and working fluid enters the oil separator. In an ideal separation process, the mixture of oil and working fluid is completely separated into two phases. In practice, a fraction of the working fluid is dissolved in the oil phase as well as droplets of oil are entrained in the working fluid vapor phase. The oil separator model assumes no heat losses or pressure drops, i.e. T_5=T_6 =T_{6o}, and only the solubility of working fluid in oil is considered using an available correlation. In the general case, the mass fraction of refrigerant dissolved in the liquid flowing in the flooded medium loop of Figure E.1 is defined by:

$$x_{\text{r,sol}} = \frac{\dot{m}_{\text{r,sol}}}{\dot{m}_{\text{r,sol}} + \dot{m}_l} \quad \text{(E.25)}$$

Hence, the actual oil mass fraction exiting the separator is

$$x_{\text{l,sol}} = 1 - x_{\text{r,sol}}, \quad \text{(E.26)}$$

which has to be updated at the mixing section. The oil separator irreversibility is neglected, i.e. $\dot{E}_{\text{sep}}$=0.

Lastly, the cycle thermodynamic performance is evaluated by means of both First and Second Laws of Thermodynamics. The cycle thermodynamic efficiency is given as the ratio of the net power output to the total heat rate input:

$$\eta_{\text{ORCLFE}} = \frac{\dot{W}_{\text{net}}}{\dot{Q}_{\text{in}}} = \frac{\dot{W}_{\text{exp}} - \dot{W}_{\text{pp,r}} - \dot{W}_{\text{pp,l}}}{\dot{Q}_{\text{ev,r}} + \dot{Q}_{\text{heater,l}}} \quad \text{(E.27)}$$

The Second Law efficiency is defined as the thermal (First Law) efficiency divided by the theoretical maximum (Carnot) efficiency, in accordance with [1]:

$$\eta_{\text{II,ORCLFE}} = \frac{\eta_{\text{ORCLFE}}}{\eta_{\text{Carnot}}} \quad \text{(E.28)}$$

where η_{Carnot} is defined as a function of T_{H} and T_{L}.

The flowchart of the cycle model solution scheme is represented in Figure E.4. Two main residual functions are minimized to obtain the desired convergence

of the model. The simulation is initialized by guessing the values for the working fluid mass flow rate, expander isentropic efficiency and the internal thermodynamic state (in). Once the overall expander energy balance (Equation 1.7) is satisfied, the actual overall isentropic efficiency is calculated using Equation 1.9 and it is compared with the initial guess value. The iteration process continues until the convergence criteria is met. Furthermore, the working fluid mass flow rate is adjusted to ensure the imposed pinch point temperature difference in the heat exchangers.

Fluid	MM (kg kmol^{-1})	T_{crit} (°C)	p_{crit} (kPa)	Safety Group	AL (yr.)	ODP (-)	$GWP_{100yr.}$ (-)
R245fa	134.05	153.9	3651.0	B1	7.6	0.0	1020
R1234ze(Z)	114.04	153.7	3533.0	AL2	0.027-0.049	0.0	>3
R1233zd(E)	130.49	166.5	3623.6	A1	0.071	0.0	1
R1336mzz(Z)	164.06	171.3	2900.0	A1	0.060	0.0	2

Table E.2: Summary of thermophysical properties, safety and environmental data of the working fluids considered in the present study.

E.2.4 Flooded expansion with a single-screw expander

The cycle model has been exercised over a range of flooding ratios and expander volume ratios to investigate the impact on the power output and cycle efficiency improvements over the baseline ORC. At first, R245fa is considered as the primarily working fluid. The inlet heat source temperature is fixed at 120 °C, unless specified. Under the specified conditions, the degrees of freedom are internal volume ratio of the expander and the evaporating temperature. The ORCLFE architecture is compared to the baseline ORC with internal regeneration. In particular, the baseline ORC is defined as a conventional ORC with pump, evaporator, expander, condenser and internal regenerator without any significant flooding. The results are presented in Figure E.5(a) and Figure E.5(b). In particular, for a given pressure ratio of 7, by increasing the expander internal volume ratio, the specific work increases significantly due to the reduced under-expansion losses. The flooding ratio has a limited impact on the actual expander specific work, as shown in Figure E.5(a), but it has a more significant impact on the cycle efficiency. For a expander internal volume ratio of 6, the cycle efficiency relative improvements to the baseline cycle with internal regeneration is as high as 4%. As shown in Figure E.5(b), ORCLFE allows to improve the cycle thermodynamic efficiency. However, as also outlined by Georges [4],

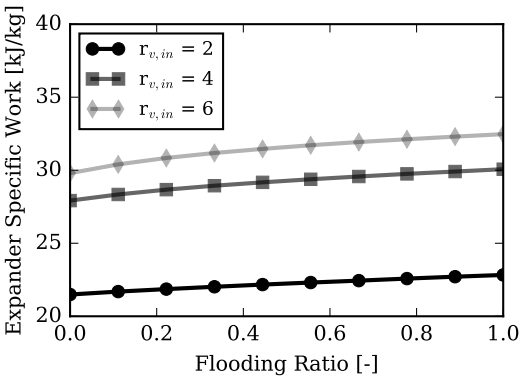

(a)

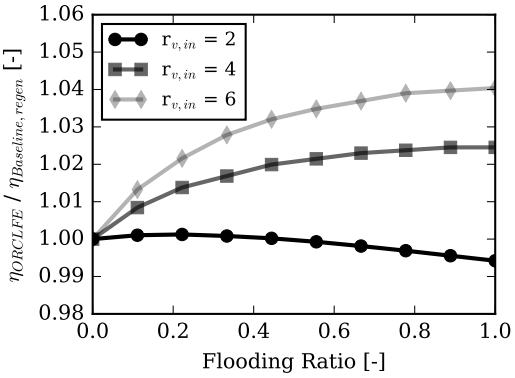

(b)

Figure E.5: (a) *Influence of the built-in volume ratio on the specific expander work for a given working condition at different flooding ratios. The working fluid is R245fa and the imposed pressure ratio is 7;* (b) *Ratio of ORCLFE cycle efficiency to the baseline ORC with regeneration assuming an effectiveness of 0.8. The working fluid is R245fa. Imposed pressure ratio is 7 and superheating 10* $^{\circ}C$.

R245fa does not allow for a significant increase in the expander specific work. For the heat source temperature range considered, different working fluids can be considered as potential candidates for ORCLFE. Among all the working fluids available, the selection has been limited to those that have near-zero GWP and zero ODP. The three candidates selected as possible replacements of R245fa are HFOs R1234ze(Z), R1233zd(E) and R1336mzz(Z). The working fluid characteristics are summarized Table E.2.

The efficiency of the expansion process for a given expander is related to the properties of the working fluid in terms of enthalpy difference between suction

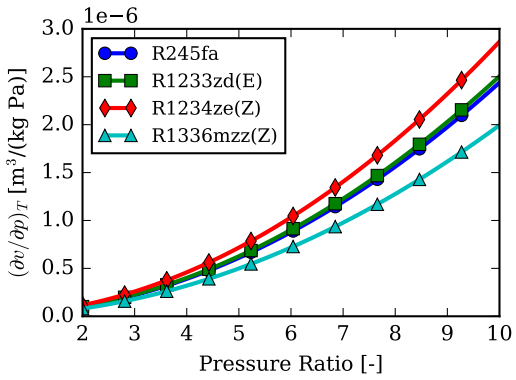

Figure E.6: Variation of $\partial v/\partial p$ with the pressure ratio under isothermal conditions for different working fluids.

and discharge conditions and the increase of specific volume with respect to the decrease of pressure, i.e. $\partial v/\partial p$. By assuming an isothermal expansion from (T_1,p_1) to (T_2=T_1,p_2=p_1/r_p), the quantity $\partial v/\partial p$ at constant temperature can be evaluated at the discharge conditions for different pressure ratios. As shown in Figure E.6, R1234ze(Z) presents the highest values of $\partial v/\partial p$ while R1336mzz(Z) the lowest. As a result, R1234ze(Z) should allow to obtain higher specific work output for the investigated conditions.

As outlined in the previous analysis, a volumetric expander with a volume ratio between 4 and 6 is desirable to benefit from the presence of large amount of oil in the working chamber. To this end, a single-screw expander with an internal volume ratio of 5.3 is considered. From the experimental characterization carried out in Section 5.2.3, the mechanical losses were estimated by considering a fictitious torque, τ_{loss} to calculate the shaft power and estimate the mechanical efficiency:

$$\dot{W}_{\text{sh,exp}} = \dot{W}_{\text{in,exp}} - 2\pi\tau_{\text{loss}}\frac{N_{\text{exp}}}{60} \tag{E.29}$$

The expander is assumed to be well insulated with an improved overall heat transfer coefficient to the ambient from approximately 11 kW/(m^2 K) to 0.01 kW/(m^2 K). The total mass flow rate is imposed by the displacement of the machine:

$$\dot{V}_{swept,exp} = 2z_{\text{r}}\frac{V_{g,ex}}{r_{\text{v,in}}}\frac{N_{\text{exp}}}{60} = \dot{m}_{\text{exp}}v_{4,\text{mix}} \tag{E.30}$$

where z_r is the number of grooves (i.e., 6), N_{exp} is the expander rotational speed fixed at 3000 rpm and $V_{g,ex}$ is the chamber volume at the discharge opening. Finally, suction and discharge two-phase pressure drops are not considered, i.e., the ports are properly designed to minimize such losses.

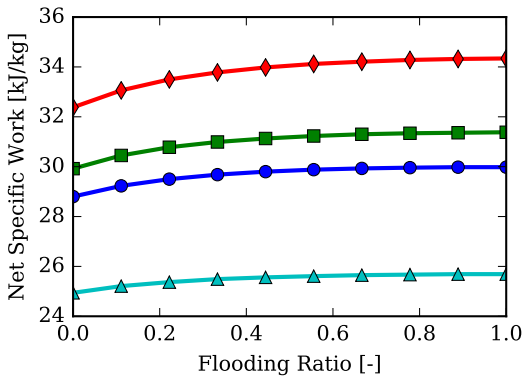

(a)

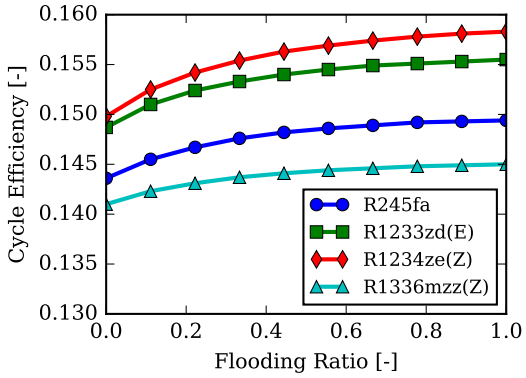

(b)

Figure E.7: (a) Net specific work output as function of flooding ratio; (b) Cycle thermodynamic efficiency as function of flooding ratio. The legend is shared. Heat source temperature fixed at 120°C, imposed pressure ratio is 7 and expander internal volume ratio is 6.

At first, to understand the behavior of each working fluid, a sweep of the flooding ratio for a fixed heat source inlet temperature of 120 °C is performed. The pressure ratio and the superheating are optimized to maximize the Second Law efficiency. The net specific work and the cycle thermodynamic efficiency as a function of the flooding ratio are plotted in Figure E.7(a) and Figure E.7(b), respectively. Under such applied boundary conditions, R1234ze(Z) achieves higher work output as well as higher cycle efficiency. While, R1336mzz(Z) showed poor performance when compared to the other working fluids. The main reason for these results is related to the critical point conditions of each working fluid with respect to the heat source inlet temperature. It follows that the expander volume ratio is not optimized for each working fluid. Nonetheless, this analysis is useful

to understand the different trends before carrying out an optimization study. Additional considerations of the impact of isothermal expansion on the expander performance are given next. In Figure E.8, the expender isothermal efficiency is plotted as a function of the flooding ratio. As the flooding ratio increases, the expansion process moves towards an isothermal process and the isothermal efficiency increases up to 10.4% in the case of R1234ze(Z).

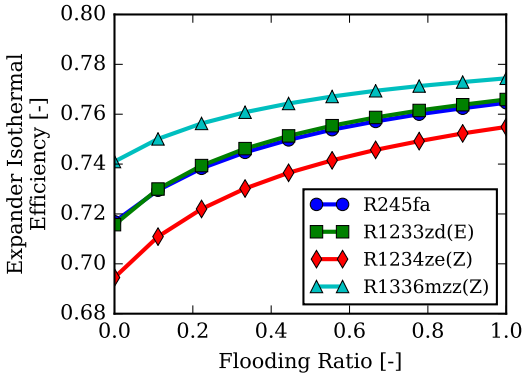

Figure E.8: Evolution of expander isothermal efficiency as function of flooding ratio for different working fluids.

The irreversibility rate for each component at different flooding ratios are reported in Figure E.9. The flooding ratio has a relative small impact on the total irreversibility rate as shown in Figure E.10. By increasing the flooding ratio, the irreversibilities associated with the evaporator, condenser and expander decrease more significantly in comparison to the increased irreversibilities of the oil pump, oil heater and regenerator. In Figure E.11, the Second Laws efficiency is plotted as a function of the flooding ratio. It can be seen that increasing the flooding ratio improves the Second Law efficiency. In particular, R1234ze(Z) benefits the most from the increase in flooding ratio. Furthermore, it can also be noted that the values of Second Law efficiency for R245fa are comparable to the ones obtained by Woodland et al. [1] under the same heat source inlet temperature of 120 °C.

To evaluate the theoretical performance improvements of ORCLFE employing a single-screw expander over the baseline cycle, an optimization study has been carried out for each working fluid by considering three hot source inlet temperatures, i.e. 100 °C, 120 °C and 150 °C. Three degrees of freedom were identified: pressure ratio across the expander, superheating and flooding ratio. For each of the independent variables, upper and lower bounds were set. In particular, the superheating has been limited between 0 °C and 30 °C. Whereas the upper bound of the pressure ratio has been set accordingly for each working fluid to

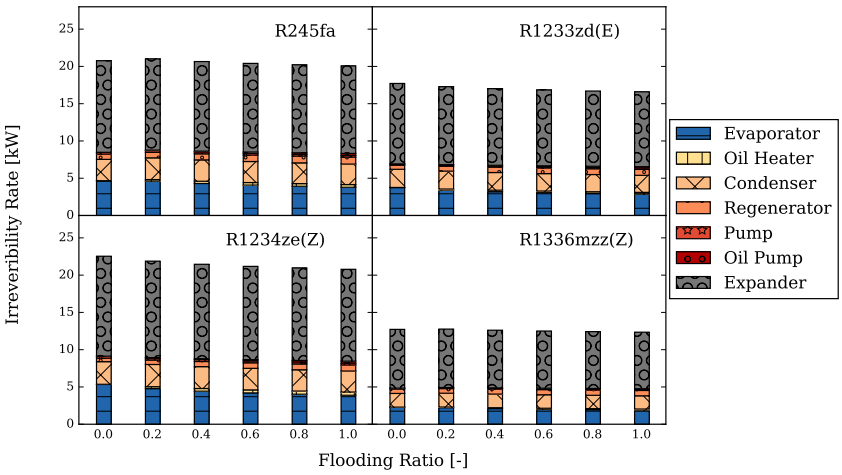

Figure E.9: Breakdown of the irreverisibilities for each ORCLFE system components and different working fluids as a function of the flooding ratio. The heat source inlet temperature is fixed equal to 120 °C and both superheating and pressure ratio are optimized.

ensure a sub-critical type of cycle. The net power output has been chosen as an objective function to be maximized.

The results of the optimization and the comparisons between the working fluids are shown in Figure E.12(a) and Figure E.12(b) as well as reported in Table E.3. The performance of the baseline ORC with internal regeneration are overlaid on the plots and indicated with black solid bars for a direct comparison. The flooded expansion increases both the power output of the expander as well as the oil pump input power. The actual benefit of the quasi-isothermal expansion on the net power is within a few percentage points if the single-screw expander mechanical losses are kept the same as the case of non-flooded expansion. The exception is R1234ze(Z), for which the flooded expansion led to a increased net power of 4.6% at 100°C, 1.8% at 120°C and 8.61% at 150°C, respectively. However, the cycle efficiency improves for all the cases considered due to higher potential for internal regeneration with the flooded cycle. For example, the relative cycle improvement for R245fa is up to 7.8% at 150°C, which is in line with the results obtained by Woodland et el. [3]. By flooding the expander with lubricant oil, it is expected that the losses associated with leakages and friction can be reduced. To account for this aspect, the optimization has been redone by halving the frictional torque used in Equation E.29. The results are shown in both Figure E.12(a)

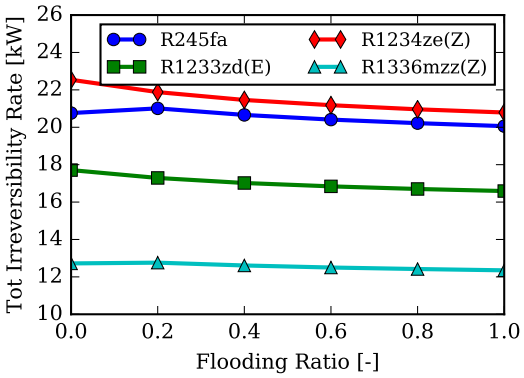

Figure E.10: Total irreversibility rate as function of flooding ratio for different working fluids. The heat source inlet temperature is fixed equal to 120 °C and both superheating and pressure ratio are optimized.

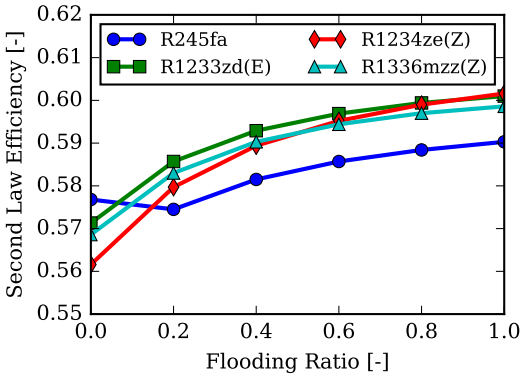

Figure E.11: Second Law efficiency of ORCLFE as a function of flooding ratio for different working fluids. The heat source inlet temperature is fixed equal to 120 °C and both superheating and pressure ratio are optimized.

and Figure E.12(b) with shaded bars. The reduction of mechanical losses due to flooded expansion allows to increase the net power output significantly which also is responsible for the improvements in cycle efficiency. In particular, each working fluid shows further improvements between 6.8% (R1234ze(Z) at 150°C) and 27.7% (R1336mzz(Z) at 100°C) with respect to the optimized ORCLFE. In the considered analysis, R1234ze(Z) and R1233zd(E) are the better candidates to implement the flooded expansion with single-screw expander.

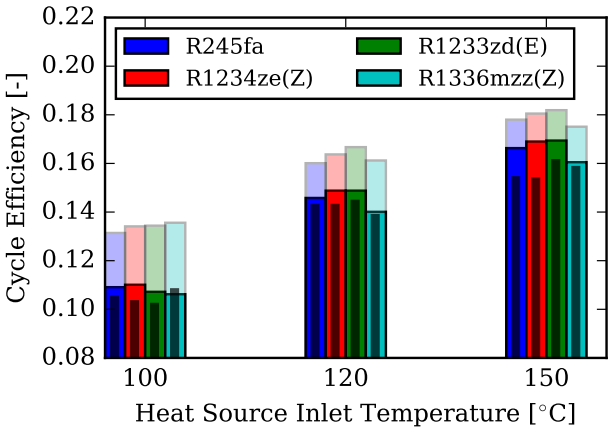

(a)

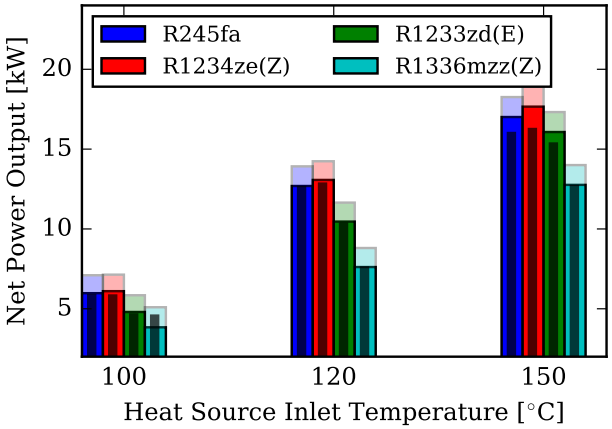

(b)

Figure E.12: ORCLFE optimization results for three heat source inlet temperatures and different working fluids. Deep colored bars represent ORCLFE performance, the shaded bars are the results of ORCLFE with reduced mechanical losses and the black bars are the ORC with internal regeneration results: (a) thermodynamic cycle efficiency; (b) net power output.

Fluid	T_H (°C)	y_l (-)	p_{cd} (kPa)	r_p (-)	$\dot{W}_{net}$ (kW)	η_{ORCLFE} (-)
R245fa	100	0.3293	177.8	4.873	5.977 (2.05%)	0.1091 (+3.81%)
	120	0.1761	177.8	7.131	12.69 (+0.47%)	0.1458 (+2.03%)
	150	1.00	177.8	9.839	17.01 (+6.25%)	0.1663 (+7.77%)
R1234ze(Z)	100	0.4409	210.2	4.437	6.103 (+4.66%)	0.1101 (+6.58%)
	120	0.2939	210.2	6.392	13.07 (+1.79%)	0.1488 (+4.13%)
	150	1.00	210.2	8.778	17.66 (+8.61%)	0.169 (+9.88%)
R1233zd(E)	100	0.3885	154.6	4.839	4.799 (+3.31%)	0.1072 (+4.89%)
	120	0.244	154.6	7.088	10.46 (+1.26%)	0.1488 (+2.90%)
	150	0.4711	154.6	9.265	16.07 (+4.69%)	0.1694 (+5.02%)
R1336mzz(Z)	100	1.00	89.01	5.494	3.839 (-16.03%)	0.1062 (-1.85%)
	120	0.167	89.01	8.912	7.598 (-0.39%)	0.1405 (+1.01%)
	150	0.130	89.01	12.31	12.76 (-0.‘55%)	0.1605 (+1.26%)

Table E.3: Comparison between ORC baseline and optimized ORCLFE for different heat source inlet temperatures.

E.2.5 Effect of oil solubility

The ORCLFE includes an oil separator after the expander. In this component, due to the combination of temperature and pressure and the separation process, the chemical equilibrium of the two phases results in solubility of working fluid in oil. As a consequence, the dissolved working fluid flows through the oil pump and oil heater affecting the cycle efficiency. For this analysis, R245fa is used as the working fluid since the solubility of R245fa in ACD100FY is available in [8, 11]. The solubility as a function of temperature and pressure is shown in Figure E.13.

The heat source inlet temperature is fixed as 120 °C while the cold sink is kept

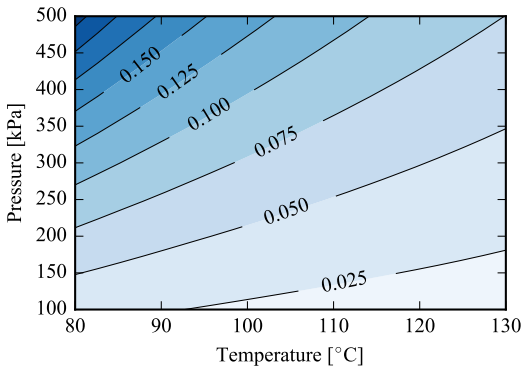

Figure E.13: Solubility of R245fa in polyolester (POE) lubricant oil ACD100FY [8].

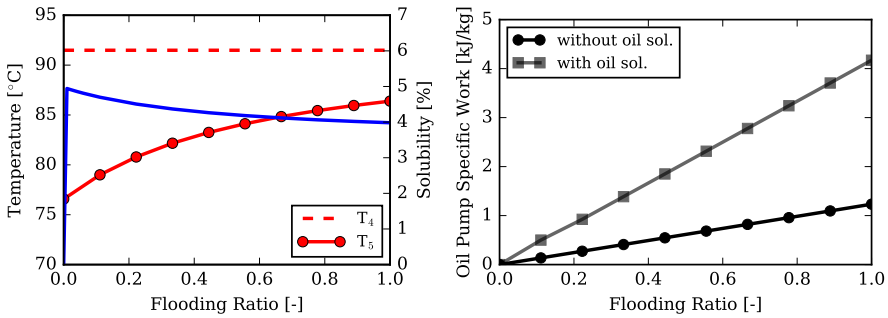

Figure E.14: (a) Effect of the oil solubility on the oil pump specific work for different flooding ratios; (b) Effect of the oil solubility on the oil pump specific work for different flooding ratios.

as specified in Table E.1. The single-screw expander with an internal volume ratio of 5.3 is employed. A simulation is carried out by varying the flooding ratio between 0 and 1 at a fixed pressure ratio of 7 and superheating level of 10 °C. As the flooding ratio increases, the expander discharge temperature approaches the inlet temperature. Since the condensing pressure is imposed by the cold sink temperature, higher discharge temperature implies lower solubility fraction, as shown in Figure E.14(a). The flooded expansion is beneficial in this aspect. However, as the flooding ratio increasing, the oil pump specific work increases, as expected. If the working fluid is dissolved into the lubricant oil, the pumping work increases significantly, as reported in Figure E.14(b). The optimal amount of oil flooding is directly linked with the solubility fraction which is related to the operating conditions at the expander discharge. Solubility should be at minimum

to avoid an increase of oil pump work and, consequently, a decrease of net power output.

E.3 ORCLFE Test Setup Architecture

An overview of ORCLFE system built along with the description of the main components is shown in Figure E.15. The experimental test stand can be divided into four main loops according to the hydraulic scheme of Figure E.16:

1. hot source loop;
2. cold source loop;
3. working fluid loop;
4. active oil circulation loop.

Heating and cooling loops are the two main external loops to the ORCLFE. In particular, the heating source loop consists of an electric heater with a maximum heating capacity of 250 kWe. Therminol 66 is employed as thermal oil. The maximum thermal oil flow is 14 m^3/h at a maximum temperature of 340 °C. A roof-top air cooled condenser with a rated capacity of 480 kW at 20 °C ambient is used as cooling loop. The cooling medium is a mixture of water and ethylene-glycol (33 vol%). The temperature of the water-glycol mixture that enters the condenser depends directly on the external ambient conditions. The mass flow rate of both external loops are controlled by three way valves. The electric heater and the rooftop cooling unit are visible in Figure E.17.

The working fluid loop and active oil circulation loop are part of the ORC unit. Two three-piston diaphragm pumps are used to pressurize the fluids in the working fluid and lubricant oil loops. Auxiliary filters are installed on the pump discharge lines that can be used to remove unwanted particles coming from heat exchangers and expander.

Plate heat exchangers are employed as evaporator, heater, regenerator and condenser. The mixing between working fluid and lubricant oil is realized by means of a static mixer in stainless-steel. The internal patterns of the mixer have been optimized to minimize the pressure drop and guarantee an homogeneous lubricant oil-refrigerant mixture at the expander inlet. The design of the static mixer is shown in Figure E.18(a). Wheres, a top view of the assembly static mixer and expander is visible in Figure E.18(b). A gravity separator is installed on the

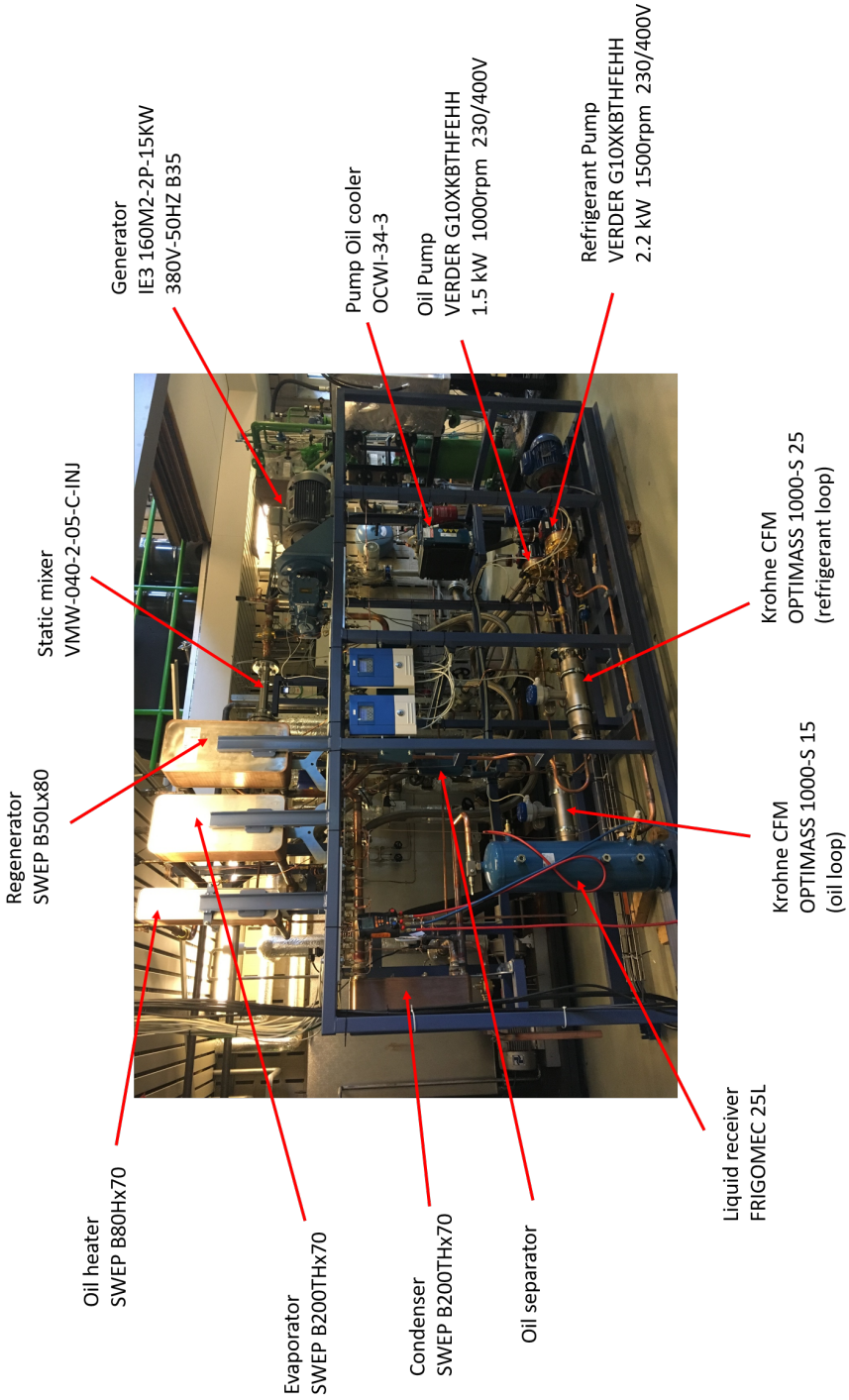

Figure E.15: View of ORCLFE test rig. The main components are indicated and described.

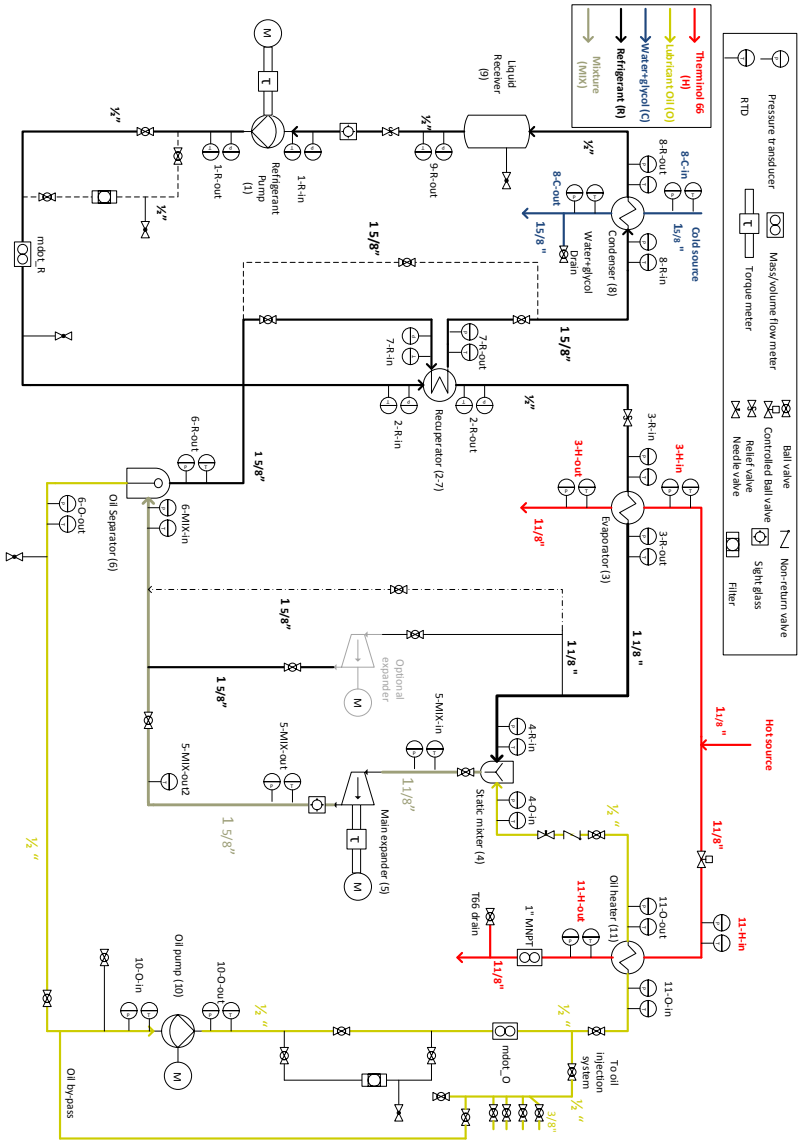

Figure E.16: Detailed schematic of ORCFLE installation.

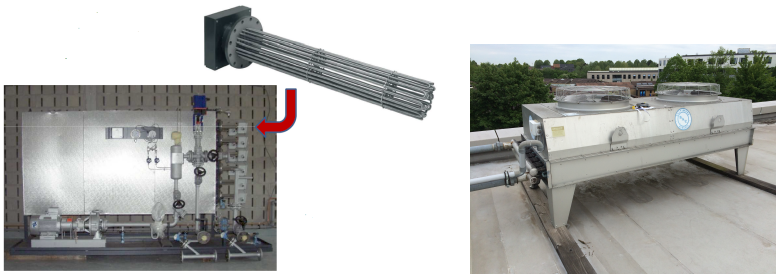

(a) (b)

Figure E.17: View of (a) *Maxxtec electric oil heater and* (b) *rooftop cooling unit.*

discharge line of the expander which separates the working fluid vapor from the lubricant oil. The lubricant oil then returned to the oil pump while the working fluid vapor is directed to either the regenerator or condenser depending on the cycle configuration. A liquid receiver is placed after the condenser with three different purposes: (i) ensure a minimum liquid level on the pump suction line; (ii) in case of over-pressure, a relief valve on the discharge line of the pump will release the liquid inside the receiver; (iii) serve as charging point to the installation.

The installation is controlled by means of a PLC. Each pump has a dedicated VFD which is connected to the PLC via MODBUS protocol. A 15 kW regenerative drive is used to control the expander generator. The PLC is connected to LabVIEW via ethernet connection. From the PLC MODBUS, rotational speed, power and torque from each drive are monitored and acquired. Both cooling and heating loops are controlled in a similar way with a separate PLC. The hot loop temperature set-point is maintained with a PI controller. The ORC control cabinet is shown in Figure E.19.

E.3.1 Single-Screw Expander Tested

The single-screw expander used during the first experimental campaign (see Figure 5.1) underwent significant modifications to improve its performance. After disassembling the housing and the meshing pair, a thorough inspection revealed that the meshing profile on the starwheel teeth was worn out, as shown in Figure E.20. The groove lands on the rotor were also slightly damaged probably due to contact with the housing and lack of proper lubrication. For these reasons, the meshing pair has been replaced with a new straight-line profile,shown in Figure E.20 as well. The straight-line profile is marked in red for clarity and it is essential

Table E.4: List of sensors installed on the ORCLFE test bench.

Measurement	Manufacturer	Model	Description
Temperature	TC-Direct	514-942	∅6mm PT100
Pressure	Wika	A-10/S-20	Absolute pressure transducers
Dynamic pressure	Stekon	Kulite XTE-190(M)	Miniature ruggedized high temperature pressure transducers
Mass flow rate (hot source)	Rosemount	3051	Pressure orifice
Mass flow rate (cooling loop)	Siemens	Sitrans FUS 380	Ultrasonic flow meter
Mass flow rate (working fluid)	Khrone	OPTIMASS 1000-S 25	Coriolis mass flow sensor
Mass flow rate (lubricant oil)	Khrone	OPTIMASS 1000-S 15	Coriolis mass flow sensor
Torque	Omega	TQ513-500-EN1024-MB	Rotating torque sensor for expander with encoder
Torque	Omega	TQ513-200-MB	Rotating torque sensor for working fluid pump

Table E.5: Operating range and uncertainties of the measurement devices. k indicates the coverage factor.

Variable	Sensor	Range	Uncertainty (k=2)
$\dot{m}_r$	CFM	0-1.8 kg/s	±0.09 %
$\dot{m}_o$	CFM	0-1.8 kg/s	±0.09 %
$T_{exp,su}$,$T_{exp,ex}$	RTD	50-300 °C	±0.2 K
T_{exp}	TC-type T	50-300 °C	±0.2 K
$p_{exp,su}$,$p_{exp,ex}$	APS	0-1600 kPa	± 1.6 kPa
τ_{exp}	Torque meter	0-53 Nm	±0.1 %
$\tau_{pp,r}$	Torque meter	0-22 Nm	±0.1 %
N_{exp}	PLC	-	Neglected

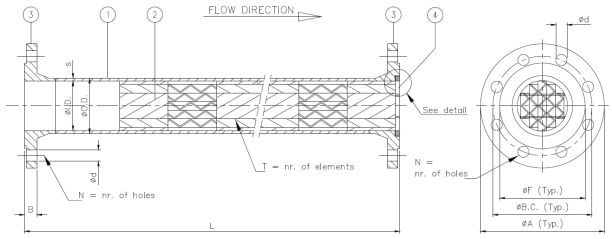

(a)

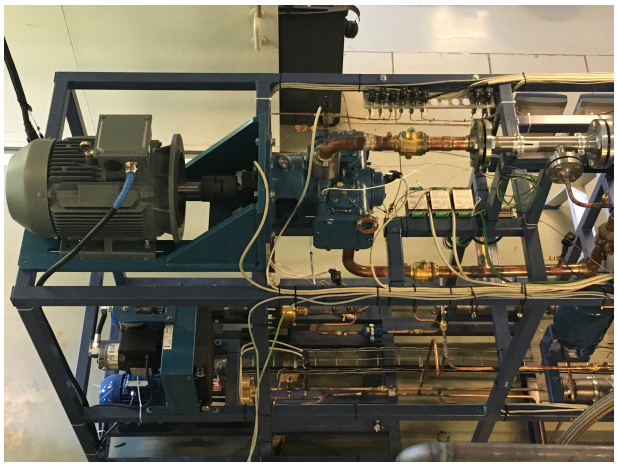

(b)

Figure E.18: (a) Static mixer design; (b) top view of static mixer and expander assembly.

to guarantee sealing between sides of the tooth and mating groove flanks. The main rotor has also been replaced to ensure the meshing with the new mating starwheels. The shaft-rotor assembly is shown in Figure E.21(a). The thrust bearing element at the front of the rotor has been kept the same. However, the journal bearing installed on the open-drive side of the shaft as well as on the starwheels have been replaced. A PTFE rotary shaft seal was installed to avoid leakages.

Besides the meshing pair, also the housing needed several improvements. One of the element of concern was the sealing capabilities of the current housing as well as the possibility of running at higher pressures. To this end, suction and discharge flanges, the end plates and the front circular cap were re-engineered by using stainless steel plates and flanges. By polishing the contact surfaces on the housing, copper gaskets with a thickness of 2 mm were installed in every connection. A close view of the side place installation is shown in Figure E.21(b).

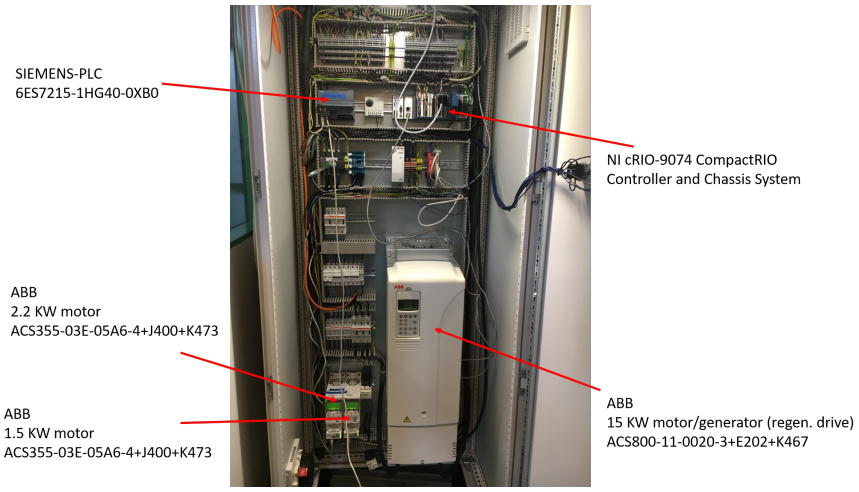

Figure E.19: View of Rittal IP66 enclosure with installed drives, control system and DAQ.

The stainless steel flanges on the suction and discharge ports of the expander were then soldered with the copper piping. Such arrangement allowed to install RTDs and pressure transducers capillary tubes both at suction inlet and discharge outlet of the expander. The complete installation of the expander is visible in Figure E.22. To be noted is that, at the discharge side of the expander, the new flange was properly designed to have a measuring point connection to evaluate the discharge state of the working fluid as accurate as possible.

In order to characterize the internal performance of the expander, dynamic pressure transducers and thermocouples were installed on the housing. As marked in Figure E.23, six pressure ports were drilled on the housing to capture both the in-groove expansion process as well dynamic phenomena in both internal suction pockets. A dynamic pressure sensor was also placed on the front of the housing the capture the discharge process. in addition to the pressure ports, eight compression fittings have been installed in several locations of the housing to be able to measure the temperature evolution during the expansion process as well the temperature surrounding the different mechanical elements. Surface thermocouples were installed to quantify the heat losses to the ambient. The details of the installed sensors and locations will be discussed in Section E.3.2.

The expander shaft was connected to the generator by means of a torque meter in order to obtain an accurate estimation of the mechanical power generated by the expander and to obtain the shaft angular position which is necessary to align the pressure traces of the dynamic sensors.

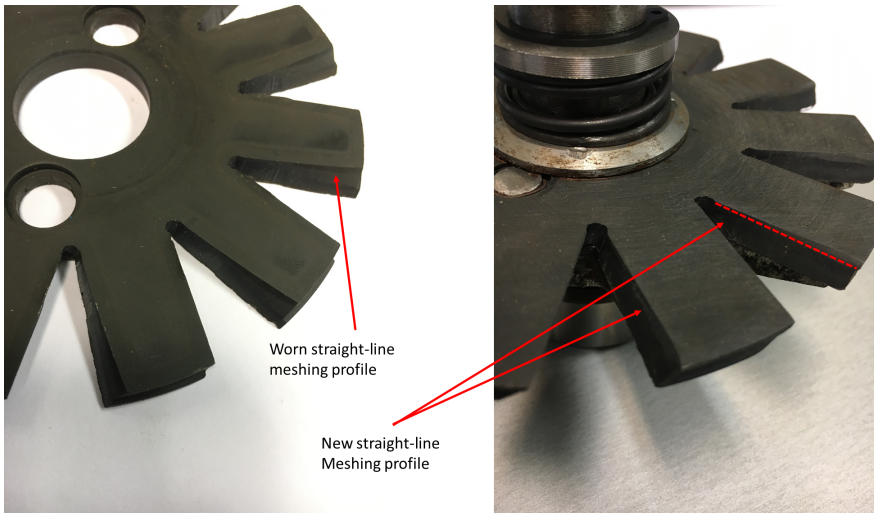

Figure E.20: Comparison between worn starwheel profile and new straight-line meshing profile.

E.3.2 Sensor installation

By referring to Figure E.16, the ORCLFE test-rig is equipped with temperature and pressure measurements at the inlet and exit of each component with the exception of the pipe line connecting the condenser outlet to the liquid receiver inlet, which is quite short. At each measuring point, tee connections have been soldered onto the copper piping to facilitate the installation of both RTDs and capillary tubes for the pressure transducers. An example of tee connection at the expander inlet is shown in Figure E.24(a). Due to the significant amount of sensors, the pressure transducers are installed in arrays on aluminum plates at the same height and grouped conveniently by location. In Figure E.24(b), it is possible to see the pressure sensor arrangement for one of the locations. Moreover, such arrangement minimized the thermal drift error for the pressure transducers which heavily affects the calculations of enthalpy and entropy at the expander inlet and outlet conditions.

Two Coriolis flow meters are used to measure the mass flow rate of working fluid and lubricant oil.

Torque sensors are installed on expander and working fluid pump shafts. For both torque sensors, a shaft alignment tool has been used to ensure the correct alignment between expander and pump shaft with the corresponding drives.

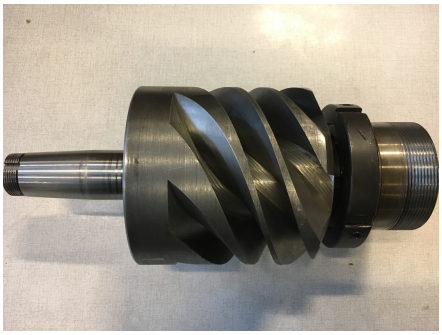

(a)

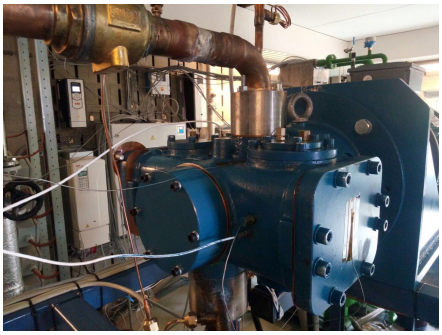

(b)

Figure E.21: (a) Single-screw expander shaft-rotor assembly; (b) close view to the re-engineered side plates, front cylindrical cap and new copper gaskets.

Dynamic pressure transducers with high natural frequency are necessary in order to capture the fast expansion process. Six miniature ruggedized absolute pressure transducers for high temperature are employed. In particular, Kulite XTE-190(M)-17 bar(a) have been selected with a M5 threaded connection. Such sensors presents a full scale ouput (FSO) of 100 mV (nominal) with a combined non-linearity, hysteresis and repeatability uncertainty of ±0.1% FSO (best fit straight line or BFSL). In order to acquire such signals, amplifiers are required to condition the signals and to obtain ouput signals either as 0-10 V or 4-20 mA which are commonly used in DAQ boards. To this end, three Tasar AW980-2K signal conditioners have been selected, as shown in Figure E.25(a) . Each amplifier has two independent channels so that two Kulite sensors can be configured within one device. In Figure E.25(b), two Kulite sensors represented by their serial numbers are associated with the two channels. The Tesar channels and the Kulite 4-wire connections are reported in Table E.6. Each Kulite sensor has been calibrated with the associated Tesar signal conditioner and the dynamic pressure is obtained by

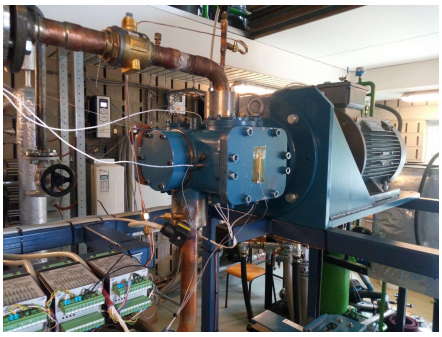

Figure E.22: View of the upgraded expander installed in the ORC.

knowing the sensor sensitivity as:

$$p_{\mathrm{dynamic}} = \frac{V_{\mathrm{read}} - V_{\mathrm{zero}}}{\Delta_{\mathrm{sensor}}} \tag{E.31}$$

where Δ_{sensor} is the sensitivity obtained from the calibration process with units mV/bar. The internal impedance is used to calculate the signal output in mA. The signal outputs from the Tesar devices are then acquired by mean of National Instruments NI-9203 current module.

The expander internal and surface temperature measurements are performed by means of mineral insulated thermocouples type-K with pot seal. These semi-rigid thermocouples have insulated junctions and allows to be shaped to fit the particular surface of interest. The junction diameter is 1 mm to ensure fast response. The thermocouples are inserted into the housing through compression fittings. A total of six thermocouples are installed on the expander. The labeling of the thermocouples on the installation is shown in Figure E.23. The thermocouples are connected to DIN-rail mounted connector modules as shown in Figure E.26 and their locations are listed in Table E.7.

A detailed description of the sensors installed can be found in Table E.4 and their uncertainties are listed in Table E.5.

E.3.3 Data Reduction and Uncertainty Analysis

In order to characterize the performance of the expander, steady-state experimental points are identified by following the criteria proposed by Woodland et al. [12] and already employed in Section 5.2.3. The thermodynamic properties of R1233zd(E)

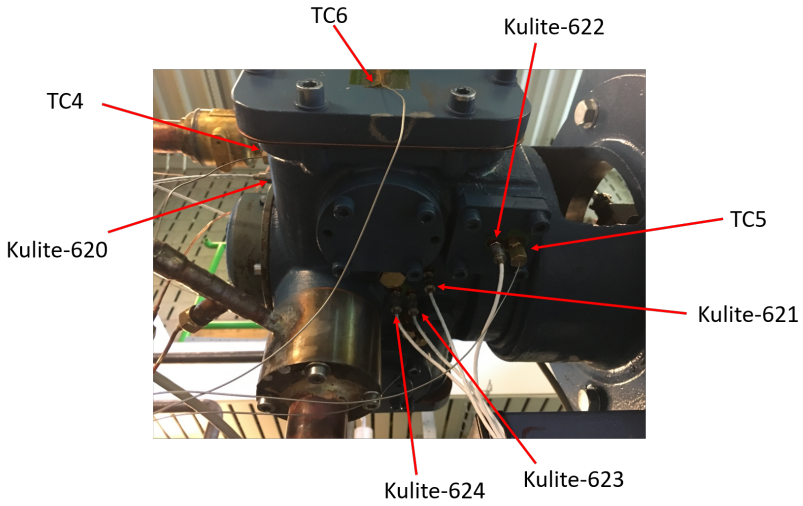

(a)

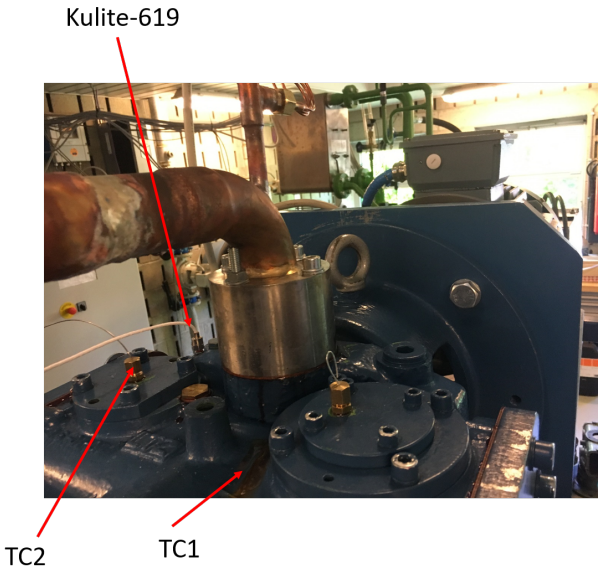

(b)

Figure E.23: Overview of the thermocouples and pressure transducers installed on the expander.

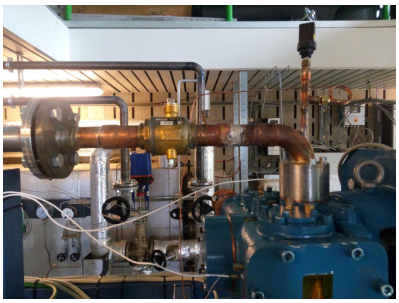

(a)

(b)

Figure E.24: (a) Installation of pressure and temperature sensors by means of tee connections; (b) Installation of pressure transducers in arrays.

Chn. 1	Chn. 2	Kulite wires	Power supply	Output signal	Other
1	22	WHITE			
2	21	RED			
3	20	GREEN			
4	19	BLACK			
5	18				Not used
6	17				Not used
7	16			0(4)-20 mA	
8	15			Output ground	
9	14				0-10 V Not used
10	13		+24 VDC		
11	12		Ground		

Table E.6: Connections of the Tesar amplifiers as shown in Figure E.25(b).

Thermocouple #	Location
TC1	Upper hosing surface
TC2	Top left bearing slot
TC3	Rotor
TC4	Discharge right side
TC5	Bottom suction pocket
TC6	Side plate surface

Table E.7: Location of the thermocouples on the expander housing as shown in Figure E.23.

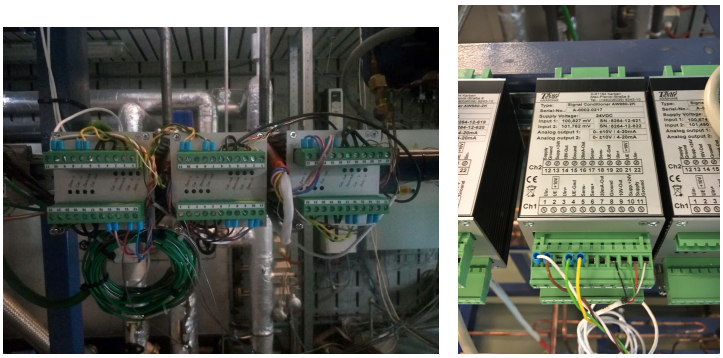

(a) (b)

Figure E.25: (a) Tesar amplifiers for the Kulite pressure transducers mounted on din-rail; (b) Tesar connections and Kulite sensors channel assignment.

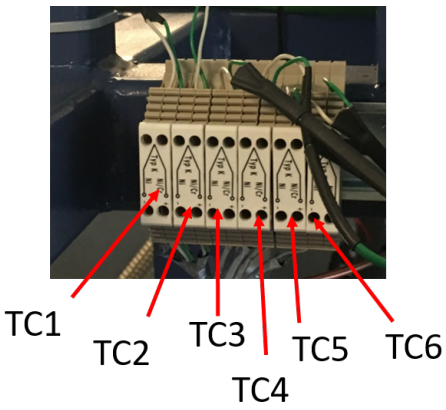

Figure E.26: Channel assignment of thermocouple modules.

are retrieved from CoolProp [13]. The general properties of the working fluid are listed in Table E.8. When compared to R245fa, R1233zd(E) presents a higher critical point temperature but lower critical point pressure. The molar mass is approximately 2.6% lower. A comparison between the thermodynamic plots is shown in Figure E.27. The equation of state implemented has been developed by Mondjar et al. [14]. The properties of ACD100FY has been obtained from Zhelezny et al. [8]. The uncertainty analysis is carried out by using the methodology described by Figliola and Beasley [15]. As outlined in Section 5.2.3, the true value of a function, f_{true}, over a steady-state interval is given as:

$$f_{\text{true}} = \bar{f} \pm u_f \tag{E.32}$$

where u_f is obtained as:

$$u_f = \sqrt{\sum_{i=1}^{n} \left(\left. \frac{\partial f}{\partial x_i} \right|_{x_i = \bar{x}_i} u_{x_i} \right)^2} \tag{E.33}$$

A confidence band of desired probability of 95% is always considered. Hence, the propagated uncertainty to calculated result also holds with 95% probability . The partial derivatives in Equation 5.10 are calculated using a central difference scheme with a step size equal to the uncertainty of the measured variable. As stated by Woodland [16], Equation E.33 assumes that systematic uncertainties are uncorrelated. Such assumption is generally true but does not apply to the concentration of a binary mixture. In fact, as already discussed in Section 4.3, the oil-refrigerant mixture is treated as a homogeneous mixture. The liquid mass fraction is calculated by measuring the mass flow rates of refrigerant and lubricant oil with the Coriolis flow meters. That is:

$$x_{\mathrm{L}} = \frac{\dot{m}_{\mathrm{L}}}{\dot{m}_{\mathrm{L}} + \dot{m}_{\mathrm{r}}} \tag{E.34}$$

The uncertainty in the lubricant oil concentration at inlet and outlet of the expander is considered the same. Thus, this uncertainty is correlated. In such case, a correction for correlated systematic errors is used according to Figliola and Beasley [15]. The inlet and outlet thermodynamic states of the expander are determined by knowing temperature and pressure measurements. The inlet enthalpy is calculated as:

$$h_{\mathrm{su,exp}} = f\left(T_{\mathrm{exp,su}}, p_{\mathrm{exp,su}}, x_{\mathrm{L,su}}\right), \tag{E.35}$$

and the outlet enthalpy can be obtained in the same fashion. The isentropic outlet enthalpy is given by:

$$h_{\mathrm{ex,exp,s}} = f\left(s_{\mathrm{exp,su}}, p_{\mathrm{exp,ex}}, x_{\mathrm{L,su}}\right) \tag{E.36}$$

Therefore the isentropic specific work is calculated as:

$$w_{\mathrm{exp,s}} = h_{\mathrm{su,exp}} - h_{\mathrm{ex,exp,s}} \tag{E.37}$$

Due to the fact that the oil concentration is the same and also that the inlet entropy is also a function of the inlet measurements, the calculation of the isentropic specific work uncertainty reduces to a function of four measured quantities:

$$w_{\mathrm{exp,s}} = f\left(T_{\mathrm{exp,su}}, p_{\mathrm{exp,su}}, x_{\mathrm{L,su}}, p_{\mathrm{exp,su}}\right) \tag{E.38}$$

Equation E.33 is applied to Equation E.38 and not directly to the individual enthalpies. Therefore, the isentropic work rate and its total uncertainty are expressed by:

$$\dot{W}_{\mathrm{exp,is}} = \left(\dot{m}_{\mathrm{L}} + \dot{m}_{\mathrm{r}}\right) w_{\mathrm{exp,s}} \tag{E.39}$$

$$u_{\dot{W}_{\mathrm{exp,is}}} = \left\{ \left(\sum_{i=L,r} \frac{\partial \dot{W}_{\mathrm{exp,is}}}{\partial \dot{m}_{\mathrm{i}}} u_{\dot{m}_{\mathrm{i}}} \right)^2 + \sum_{\mathrm{i=su,ex}} \left(\frac{\partial \dot{W}_{\mathrm{exp,is}}}{\partial T_{\mathrm{i}}} u_{T_{\mathrm{i}}} \right)^2 + \left(\frac{\partial \dot{W}_{\mathrm{exp,is}}}{\partial p_{\mathrm{su}}} u_{p_{\mathrm{su}}} \right)^2 + \left(\frac{\partial \dot{W}_{\mathrm{exp,is}}}{\partial x_{\mathrm{L}}} u_{x_{\mathrm{L}}} \right)^2 \right\}^{\frac{1}{2}} \tag{E.40}$$

The machanical shaft power of the expander is given by:

$$\dot{W}_{\mathrm{shaft,exp}} = \tau_{\mathrm{mech}} \frac{2\pi N_{\mathrm{exp}}}{60} \tag{E.41}$$

and the associated total uncertainty is calculated as:

$$u_{\dot{W}_{\mathrm{shaft,exp}}} = \sqrt{\left(\frac{\partial \dot{W}_{\mathrm{shaft,exp}}}{\partial \tau_{\mathrm{mech}}} u_{\tau_{\mathrm{mech}}} \right)^2 + \left(\frac{\partial \dot{W}_{\mathrm{shaft,exp}}}{\partial N_{\mathrm{exp}}} u_{N_{\mathrm{exp}}} \right)^2} \tag{E.42}$$

where the total uncertainty of the torque measurement, $u_{\tau_{\mathrm{mech}}}$, is obtained by combining the total systematic uncertainty on the calibration and uncertainty due to thermal shift since the sensor is compensated in the temperature range 21 ° and 76 °:

$$u_{\tau_{\mathrm{mech}}} = \sqrt{u^2_{\mathrm{sys,calibration}} + u^2_{\mathrm{thermal}}} \tag{E.43}$$

The overall energy balance of the expander is given by:

$$\dot{W}_{\mathrm{shaft,exp}} = \left(\dot{m}_{\mathrm{L}} + \dot{m}_{\mathrm{r}}\right)\left(h_{\mathrm{su,exp}} - h_{\mathrm{ex,exp}}\right) - \dot{Q}_{\mathrm{amb}} \tag{E.44}$$

The isentropic efficiency at the shaft and its uncertainty are calculated as:

$$\eta_{rms,shaft} = \frac{\dot{W}_{\mathrm{shaft,exp}}}{\dot{W}_{\mathrm{exp,s}}} \tag{E.45}$$

$$u_{\eta_{rms,shaft}} = \sqrt{\left(\frac{\partial \eta_{rms,shaft}}{\partial \dot{W}_{\mathrm{shaft,exp}}} u_{\dot{W}_{\mathrm{shaft,exp}}} \right)^2 + \left(\frac{\partial \eta_{rms,shaft}}{\partial \dot{W}_{\mathrm{exp,s}}} u_{\dot{W}_{\mathrm{exp,s}}} \right)^2} \tag{E.46}$$

An overall isentropic efficiency is also defined by measuring the electrical power output of the generator:

$$\eta_{\mathrm{s,oa}} = \frac{\dot{W}_{\mathrm{el,exp}}}{\dot{W}_{\mathrm{exp,s}}} \tag{E.47}$$

The boundary work rate is estimated by using the internal pressure sensors. Each pressure sensors is aligned with rotation by using the optical encoder of the torque meter (alternatively the drive of the generator can be used through the PLC). The average boundary work rate generated by the expander is calculated generally given as:

$$\overline{\dot{W}}_{pV} = \frac{\omega}{2\pi} \int_0^{2\pi} p(\theta) \frac{\mathrm{dV}}{d\theta} d\theta \tag{E.48}$$

The integration is approximated with a trapezoidal rule and the derivative of the volume with respect to the rotation angle is obtained from the geometry model.

The mechanical losses of the expander are then computed as:

$$\dot{W}_{\mathrm{mech,loss}} = \overline{\dot{W}}_{pV} - \dot{W}_{\mathrm{shaft,exp}} \tag{E.49}$$

Thus, the mechanical efficiency of the expander is calculated as the ratio of the mechanical shaft power to the boundary work rate:

$$\eta_{\mathrm{mech}} = \frac{\dot{W}_{\mathrm{mech}}}{\overline{\dot{W}}_{pV}} \tag{E.50}$$

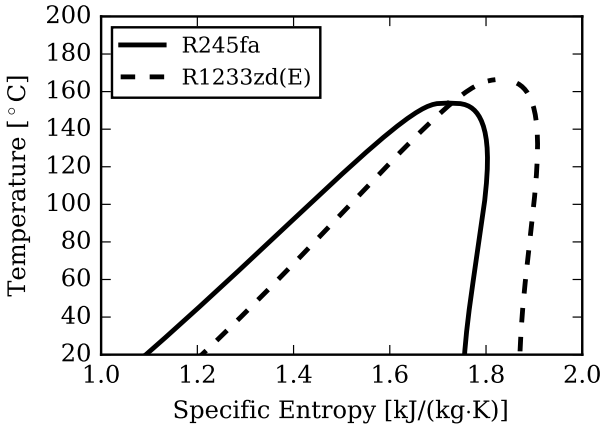

Figure E.27: Comparison between R245fa and R1233zd(E) domes.

Property	**R245fa**	**R1233zd(E)**
Type	pure fluid	pure fluid
Components	pentafluoropropane	trans-1-Chloro-3,3,3-trifluoropropene
Molar mass [kg/mol]	0.13404	0.13049
Critical point temperature [K]	427.01	435.69
Critical point pressure [kPa]	3651.0	3623.6
GWP_{100} [-]	1020	1

Table E.8: Fluid properties of R245fa [17] and R1233zd(E) [18].

References

[1] B. J. Woodland, A. Krishna, E. A. Groll, J. E. Braun, W. T. Horton, and S. V. Garimella. *Thermodynamic comparison of organic Rankine cycles employing liquid-flooded expansion or a solution circuit*. Applied Thermal Engineering, 61:859–65, 2013.

[2] M. Imran, M. Usman, Park B-S, and D-H Lee. *Volumetric expander for low grade heat and waste heat recovery applications*. Renewable and Sustainable Energy Reviews, 57:1090–1109, 2016.

[3] B. J. Woodland, E. A. Groll, J. E. Braun, and W. T. Horton. *Performance Benefits for Organic Rankine Cycles with Flooded Expansion and Internl Regeneration*. In International Refrigeration and Air Conditioning Conference at Purdue, number 2462, 2010.

[4] E. Georges. *Investigation of a Flooded Expansion Organic Rankine Cycle System*. Master's thesis, University of Liege, 2012.

[5] J. J. Hugenroth. *Liquid Flooded Ericsson Cycle Cooler*. PhD thesis, Purdue University, 2006.

[6] I. H. Bell, E. A. Groll, J. E. Braun, G. B. King, and W. T. Horton. *Optimization of a scroll compressor for liquid flooding*. Int. J. of Refrigeration, 35:1901–1913, 2012.

[7] E. W. Lemmon, I. H. Bell, M. L. Huber, and M. O. McLinden. *NIST Standard Reference Database 23: Reference Fluid Thermodynamic and Transport Properties-REFPROP, Version 9.1.1, National Institute of Standards and Technology*, 2016.

[8] V.P. Zheleznya, Yu.V. Semenyuka, S.N. Ancherbaka, A.J. Grebenkovb, and O.V. Beliayevab. *An experimental investigation and modelling of*

the solubility, density and surface tension of 1,1,1,3,3-pentafluoropropane (R-245fa)/synthetic polyolester compressor oil solutions. Journal of Fluorine Chemistry, 128:10291038, 2007.

[9] I. H. Bell. *Theoretical and Experimental Analysis of Liquid Flooded Compressor in Scroll Compressors*. PhD thesis, Purdue Univeristy, 2011.

[10] D. Chisholm. *Two-phase flow in pipelines and heat exchangers*. George Godwin, London and New York, 1983.

[11] V. P. Zhelezny, V. V. Sechenyh, Y. V. Semenyuk, A. J. Grebenkov, and O. V. Beliayeva. *An experimental investigation and modelling of the viscosity refrigerant/oil solutions*. International Journal of Refrigeration, 32:1389–1395, 2009.

[12] B. J. Woodland, J. E. Braun, E. A. Groll, and W. T. Horton. *Experimental Testing of an Organic Rankine Cycle with Scroll-type Expander*. In International Refrigeration and Air Conditioning Conference at Purdue, number 2505, 2012.

[13] I. H. Bell, J. Wronski, S. Quoilin, and Lemort V. *Pseudo-pure Fluid Thermophysial Property Evaluation and the Open-Source Thermophysical Property Library CoolProp*. Ind. Eng. Chem. Res., 53:2498–2508, 2014.

[14] M. E. Mondejar, M. O. McLinden, and E. W. Lemmon. *Thermodynamic Properties of trans-1-Chloro-3,3,3-trifluoropropene (R1233zd(E)): Vapor Pressure, (p, ρ, T) Behavior, and Speed of Sound Measurements, and Equation of State*. J. Chem. Eng. Data, 60(8):2477–2489, 2015.

[15] R. S. Figliola and D. E. Beasley. *Theory and Design of Mechanical Measurements*. John Wiley & Sons, Inc., 5th edition edition, 2011.

[16] B. J. Woodland. *Methods of increasing net power output of organic Rankine cycles for low-grade heat recovery with a detailed analysis using a zeotropic working fluid mixture and scroll expander*. PhD thesis, Purdue University, 2015.

[17] R. Akasaka, Y. Higashi, A. Miyara, and S. Koyama. *A fundamental equation of state for cis-1,3,3,3-tetrafluoropropene (R-1234ze(Z))*. International Journal of Refrigeration, 44:168–176, 2014.

[18] J. R. Hulse, R. S. Basu, R. R. Singh, and R. H. P. Thomas. *Physical Properties of HCFO-1233zd(E)*. J. Phys. Chem., 57:3581–3586, 2012.